SUSY Higgs Boson Searches at LEP and SUSY Parameter Measurements at TESLA

Dissertation
zur Erlangung des Doktorgrades
des Fachbereichs Physik
der Universität Hamburg

vorgelegt von
Philip Bechtle
aus Bietigheim-Bissingen

Hamburg
Juli 2004

Gutachter der Dissertation	:	Univ. Prof. Dr. R.-D. Heuer Univ. Prof. Dr. P. Schleper Univ. Prof. Dr. J. Kalinowski
Gutachter der Disputation	:	Univ. Prof. Dr. R.-D. Heuer Univ. Prof. Dr. B. Naroska
Datum der Disputation	:	09.09.2004
Vorsitzender des Prüfungsausschusses	:	Univ. Prof. Dr. G. Heinzelmann
Vorsitzender des Promotionsausschusses	:	Univ. Prof. Dr. R. Wiesendanger
Dekan des Fachbereichs	:	Univ. Prof. Dr. G. Huber

Nicht von Beginn an enthüllten die Götter uns Sterblichen alles;
Aber im Laufe der Zeit finden wir, suchend, das Bess're.
Diese Vermutung ist wohl, ich denke, der Wahrheit recht ähnlich.
Sichere Wahrheit erkannte kein Mensch und wird keiner erkennen
Über die Götter und alle die Dinge, von denen ich spreche,
Selbst wenn es einem einst glückt, die vollkommene Wahrheit zu künden,
Wissen kann er es nie: Es ist alles durchwebt von Vermutung.

Xenophanes [1]

Abstract

Using data collected with the OPAL detector at LEP at e^+e^- centre-of-mass energies up to 209 GeV, the search for Higgs bosons in the Minimal Supersymmetric Standard Model (MSSM) in the pair production channel is investigated and the results are interpreted in CP-conserving and, for the first time experimentally, CP-violating scenarios. New scenarios are also included, which aim to set the stage for Higgs searches at future colliders. The data are consistent with the prediction of the Standard Model with no Higgs boson produced. Model-independent limits are derived for the cross-sections of a number of event topologies motivated by predictions of the MSSM. Limits on Higgs boson masses and other MSSM parameters are obtained for a number of representative MSSM benchmark scenarios. For example, in the CP-conserving scenario "$m_{\mathrm{h}}-$max" where the MSSM parameters are adjusted to predict the largest range of values for m_{h} at each $\tan\beta$, Higgs boson mass limits of $m_{\mathrm{h}} > 84.5$ GeV and $m_{\mathrm{A}} > 85.0$ GeV are obtained at the 95% confidence level. For a top quark mass of 174.3 GeV, this translates into an excluded domain in $\tan\beta$ of $0.7 < \tan\beta < 1.9$, which is decreased to $1.0 < \tan\beta < 1.3$ for a top quark mass of 179.3 GeV. For the CP-violating benchmark scenario CPX which, by construction, enhances the CP-violating effects in the Higgs sector, the domain $\tan\beta < 2.8$ is excluded but no universal limit can be set on the Higgs boson masses.

Provided that Supersymmetry (SUSY) is realized, the future Linear Collider will most likely provide a wealth of precise data from SUSY processes. An important task will be to extract the Lagrangian parameters. On this basis it will be possible to uncover the underlying symmetry breaking mechanism from the measured observables. In order to determine the SUSY parameters, the program Fittino has been developed. It uses an iterative fitting technique to determine the SUSY parameters directly from the observables, using all available loop-corrections to masses and couplings. As fit result, a set of parameters including the full error matrix and two-dimensional uncertainty contours are obtained. Pull distributions can automatically be created and allow an independent cross-check of the fit results and possible systematic shifts in the parameter determination. This method is used successfully in first general MSSM fits for the SPS1a scenario. The results underline the importance of having both access to a large part of the supersymmetric particle spectrum (as provided by the Linear Collider and the Large Hadron Collider LHC together) and – at least partly – very precise measurements of SUSY observables (as obtained at a future Linear Collider).

Zusammenfassung

Unter Verwendung der Daten des OPAL-Experiments am e^+e^- Beschleuniger LEP bei Schwerpunktsenergien von bis zu 209 GeV wird die Suche nach Higgs-Bosonen im Minimal Supersymmetrischen Standardmodell (MSSM) im Paarproduktionsprozess vorgestellt. Die Resultate werden in CP-erhaltenden und CP-verletzenden MSSM-Szenarien interpretiert, wobei letztere erstmals experimentell untersucht werden. Neue MSSM-Szenarien, die den Rahmen für Higgs-Boson-Suchen an zukünftigen Beschleunigern vorgeben, sind mit eingeschlossen. Die Ergebnisse sind mit der Vorhersage des Standardmodells ohne Higgs-Boson konsistent. Für eine Reihe von MSSM-motivierten Ereignistopologien werden modellunabhängige Grenzen auf die Produktionswirkungsquerschnitte gesetzt. Im Rahmen repräsentativer MSSM "benchmark"-Szenarien werden Grenzen auf MSSM-Parameter hergeleitet. Im Rahmen des "$m_{\mathrm{h}}-$max" MSSM-Szenarios, in dem alle Parameter so gewählt sind, daß sie für jeden Wert von $\tan\beta$ den maximalen Bereich von Higgs-Boson-Massen m_{h} liefern, sind folgende Bereiche mit einem Vertrauensniveau von 95 % erlaubt: $m_{\mathrm{h}} > 84.5$ GeV und $m_{\mathrm{A}} > 85.0$ GeV. Für eine Masse des Top-Quarks von 174.3 GeV läßt sich dies in einen ausgeschlossenen Bereich von $0.7 < \tan\beta < 1.9$ des Parameters $\tan\beta$ übersetzen. Für eine Top-Quark-Masse von 179.3 GeV schrumpft dieser ausgeschlossene Bereich auf $1.0 < \tan\beta < 1.3$. Im Rahmen des CP-verletzenden MSSM-Szenarios CPX, in dem die Effekte der CP-Mischung im Higgs-Sektor maximiert werden, ist der Bereich $\tan\beta < 2.8$ ausgeschlossen. Es kann aber keine allgemeine Grenze auf die Masse des leichtesten Higgs-Bosons gesetzt werden.

Unter der Voraussetzung, daß Supersymmetrie (SUSY) in der Natur realisiert ist, wird der zukünftige Linearbeschleuniger höchstwahrscheinlich eine große Menge an präzisen Meßdaten von SUSY-Prozessen liefern können. Auf Basis der Parameter der Niederenergie-SUSY-Lagrangedichte, die aus den Meßdaten extrahiert werden kann, sollte es möglich sein, die Mechanismen der SUSY-Brechung zu untersuchen. Das Programm Fittino wurde entwickelt, um die Parameter der SUSY-Lagrangefunktion zu bestimmen. Es verwendet eine iterative Fitmethode, um unter Verwendung präziser Vorhersagen mit allen verfügbaren Schleifenkorrekturen direkt von den Observablen auf die Parameter zu schließen. Als Resultat der Prozedur werden die an die Observablen angepaßten Parameter inklusive ihrer Korrelationen ausgegeben. Die Berechnung von Pull-Verteilungen erlaubt die unabhängige Überprüfung der Resultate der Anpassung. Diese Methode wird verwendet, um eine generelle Bestimmung der MSSM-Parameter im SPS1a-Szenario durchzuführen. Die Resultate unterstreichen die Wichtigkeit, sowohl ein breites Teilchenspektrum von SUSY-Teilchen untersuchen zu können (wie etwa am zukünftigen Linearbeschleuniger und am LHC zusammen), als auch sehr präzise Informationen über Teile des SUSY-Teilchenspektrums aus den Daten des zukünftigen Linearbeschleunigers zu erhalten.

Contents

1 Introduction **1**

2 Theoretical Context **5**
2.1 Foundations of the Standard Model 5
2.2 The Standard Model 7
2.2.1 The Higgs Mechanism of the Standard Model 9
2.2.2 Shortcomings of the Standard Model 15
2.3 Supersymmetry as an Extension to the Standard Model 18
2.3.1 General Concept of Supersymmetry 18
2.3.2 The Minimal Supersymmetric Standard Model 22
2.3.3 The Higgs Sector in the MSSM 25
2.3.4 CP violation in the MSSM Higgs Sector 28
2.3.5 Conclusion 31

3 MSSM Higgs Production at e^+e^- Colliders **33**
3.1 MSSM Higgs Boson production 33
3.2 Higgs Boson Decays 36
3.3 MSSM Higgs Boson Searches at LEP 38

4 Accelerators and Detectors **41**
4.1 The LEP Accelerator 41
4.2 The OPAL Detector 44
4.2.1 Standard Model Processes at LEP 2 51
4.2.2 Event Simulation in OPAL 54
4.3 The TESLA Project 56

5 Search for Higgs Bosons in Pair Production at OPAL **63**
5.1 Analysis Tools 63
5.1.1 Energy Flow 64
5.1.2 Jet Finding 65
5.1.3 Kinematic Fit 65
5.1.4 Tagging of B-Hadrons 66
5.2 The Search for Pair Production with heavy $m_{\mathcal{H}_1}$ 69
5.3 The Search for Pair Production with small $m_{\mathcal{H}_1}$ 79
5.4 Systematic Uncertainties 85
5.5 Construction of the Discriminating Variable 88

6 Interpretation of the OPAL Higgs Boson Searches in the MSSM 93
6.1 Statistical Methods . . . 93
6.2 The Search Channels . . . 98
6.2.1 Additional Channels for Higgs Cascade Decays . . . 101
6.2.2 Input Tests . . . 104
6.2.3 External Experimental Constraints . . . 105
6.3 Model Independent Higgs Mass Limits . . . 106
6.4 Limits on Benchmark Scenarios . . . 108
6.4.1 CP-Conserving MSSM Scenarios . . . 111
6.4.2 CP-Violating MSSM Scenarios . . . 122
6.5 Combination of the Results of the LEP Collaborations . . . 129
6.6 Summary . . . 131

7 MSSM Parameter Fits with Fittino 135
7.1 MSSM Signals at e^+e^- Colliders . . . 135
7.2 MSSM Parameter Determination . . . 138
7.3 The Fit Program Fittino . . . 141
7.4 The SPS1a Fit . . . 145
7.4.1 Assumptions and Simplifications . . . 145
7.4.2 Simulated Measurements . . . 146
7.4.3 Fit Results . . . 149
7.4.4 Fits in Subspaces of the Parameter Space . . . 160
7.5 Evolution to the SUSY Breaking Scale . . . 162
7.6 Summary . . . 164

8 Summary and Conclusions 165

Appendix 167

A Fittino Documentation 167
A.1 The MINUIT Fit Methods . . . 167
A.2 The Fittino Steering File . . . 169
A.3 The Fittino Output Files . . . 177

B Fittino Inputs and Results 179
B.1 The Fittino Steering File . . . 179
B.2 The Fittino Output File . . . 182
B.3 Correlation Matrices of Fittino Fits . . . 184

Bibliography 189

Danksagung 201

Chapter 1

Introduction

The experimentally observed fundamental constituents of matter and the interactions among them are described by the Standard Model (SM) of elementary particles. In the Standard Model, there are two different types of particles: fermions and bosons. The former are the constituents of matter, such as electrons and quarks in an atom. The latter are the mediators of the interactions – or forces – between the matter particles. To the group of bosons belongs the photon, which describes the electromagnetic waves, and so also the light. The ordering mechanism in the Standard Model is the principle of local gauge symmetry. This means that the physical theory can only consist of terms whose observable predictions are not subject to change if the basic quantities in the theory are changed under the transformations of a local gauge group. Obeying these rules, imposing certain gauge transformations necessarily requires the existence of the Standard model interactions, the electromagnetic interaction, the weak and the strong interaction.

Unbroken gauge theories, however, can only describe massless boson fields. The gauge theory is destroyed as soon as boson masses are included. In nature, there are massive gauge bosons, namely the Z and $W^{\pm}$ bosons of the weak interaction. The gauge principle can be preserved by the introduction of a mechanism which dynamically creates the particles masses. This mechanism is itself subject to gauge transformation, contrary to direct mass terms of the particles, and therefore preserves the gauge invariance. In such a mechanism, all particles are massless. They acquire self energy and hence mass by the interaction with a background field with non-zero vacuum expectation value: the Higgs field. This mechanism successfully predicts the ratio of the gauge boson masses as predicted by the measurements of the electroweak couplings.

The Higgs mechanism predicts the existence of a spinless particle, the Higgs boson. It is the only particle of the Standard Model which has not yet been experimentally detected. In the context of the Standard Model, all properties of the Higgs boson apart from its mass are predicted. Using precision data [2] and direct Higgs boson searches [3], its mass m_{h} can be constrained to $114.4\,\mathrm{GeV} < m_{\mathrm{h}} \lesssim 251\,\mathrm{GeV}$. The search for this fundamental part of the Standard Model and the precise measurement of its properties is one of the major experimental goals of modern particle physics.

All precision data from physics experiments on earth so far confirm the predictions of the Standard Model with high precision. However, there are measurements of cosmological quantities which are not in agreement with the Standard Model, for example the amount of CP violation needed for baryogenesis and the existence of dark matter, which interacts only weakly but contributes more than 20 % of the total energy in the universe. Additionally, there are theoretical drawbacks of the Standard Model, such as finetuning problems of the Higgs boson mass and the incompatibility with gravity, the only known force which is not described

by quantised local gauge theories. Within the recent years the hope to find an even more fundamental theory than the Standard Model has been fostered by the discovery of neutrino masses.

One of the possible ways to overcome the experimental and theoretical shortcomings of the Standard Model is Supersymmetry (SUSY). This symmetry unifies the bosons and fermions, providing one boson for every fermion of the Standard Model and vice versa. It is required on theoretical grounds by attempts to formulate a possible "Theory of Everything" like string theory, and it solves many of the theoretical and experimental problems of the Standard Model. Most notably it contains candidates for the dark matter in the universe and it stabilises the Higgs boson mass.

Supersymmetry introduces a great wealth of new particles. If Supersymmetry would be unbroken, the Supersymmetry particles would have the same masses as their SM partners with different spin. However, such particles have not yet been observed. Therefore Supersymmetry must be broken. The breaking mechanism of Supersymmetry introduces many new parameters into the theory. Their measurement is important, should Supersymmetry be realized and supersymmetric particles be found. This will be among the most important tasks of future high energy physics experiments such as the Large Hadron Collider (LHC) and the Linear Collider (LC).

Supersymmetry also introduces an enlarged Higgs sector. In the MSSM, three neutral and two charged Higgs bosons exist. While there is no strict direct upper mass bound on the Higgs boson mass in the Standard Model, the MSSM constrains the mass of the lightest Higgs boson to approximately 135 GeV, very close to the presently accessible kinematic region. This is the reason for the fact that searches for Higgs bosons are among the most important searches for Supersymmetry.

A Very Short History of Particle Physics

The notion of particles as the basic building blocks of matter was invented 2500 years ago by the Greek philosophers Leukipp and Demokrit. Even more interesting, this invention was very closely connected to the first abstract subject of western philosophy and cosmology, the dispute about the nature of change. This very dispute shows the first known occurrence of the hypothetical-deductive method, which is the method of science still today.

This first problem of western philosophy has its origin in purely cosmological questions about the nature of space, time and matter. It manifests itself in the concurrent theories of Heraklit and Parmenides. The former realized the logical problem of change, that is, how can things change (as they apparently do, as our senses tell us) and still maintain their own identity? Parmenides found a very elegant rational solution to this problem, which contradicts all empirical approaches. This simple solution is that while our senses tell us falsely that the world is in a state of constant change, that the sun and the stars are moving, that night changes to day and day to night, and that the moon apparently changes its shape, in reality no change happens at all. As far as we know, he was the first to realize that the moon does not change its shape at all, that the *dark* part of it remains constantly the same, only the *illuminated* part of it traits our untrustful senses and makes us falsely belief that the moon would change its shape.

Parmenides complemented this idea, motivated by cosmology and contradicting all empirical impressions, with the philosophical idea that the void does not exist (in this sense he also invented the vacuum state full of particles). Starting from this assumption, he deduces that if the world is full without any voids, nothing can move and therefore he concludes rationally that the sensual impression of change must be an illusion and that our senses are misguided,

that only rationality is a means of acquiring knowledge about the world.

Of course this theory was not regarded as very compelling by most of his fellow philosophers, although they have been impressed by the logic of Parmenides' argumentation. And so Leukipp and Demokrit brought the hypothetical-deductive method of science to its first completion: They concluded that if the logic of Parmenides theory was compelling and if the conclusion was obviously contradicting everything we can sensually realize, the assumption must be wrong. Therefore they discarded the idea that the void does not exist. Instead, Leukipp and Demokrit invented the idea of undividable and unchanging particles, the atoms, which form the matter of the world and which move in space and time. Between these atoms there is space filled with nothing, therefore they can move. This impressive theory is not just a physical theory of the structure of matter, it was also a philosophical theory in the sense that it solves the logical problem of change while not contradicting empirical observations, and it was the first conscious use of the hypothetical-deductive method of science.

In some sense particle physics as we know it today still reflects the basic philosophical problem of Heraklit and Parmenides. The theory of special relativity describes space and time as an fully deterministic unchangeable four-dimensional object, in which the absolute direction of the flow of time might be no objective fact but merely a subjective impression, a notion shared by Einstein himself [4]. On the other hand, quantum mechanics describes a world full of undetermined and individually unpredictable measurements, whose future is completely open and which seems to be in a state of constant change during each measurement. Just as the invention of a particle by Leukipp and Demokrit inherited both the notion of unchangeable objects and the notion of constant movement, the quantum field theories, on which modern particle physics is based, combine the deterministic theory of special relativity with the indeterministic world of quantum fields.

Subject of this Thesis

The subject of this thesis is the measurement of parameters of the Minimal Supersymmetric Standard Model (MSSM), the minimal realistic implementation of Supersymmetry, respectively the exclusion of areas in the parameter space in the absence of a signal of supersymmetric particles. The experimental topological search for Higgs bosons motivated by the MSSM is performed at the OPAL experiment at LEP. Then the interpretation of the search results of all searches for Higgs bosons in the MSSM in the OPAL experiment at LEP is investigated. Finally this thesis describes the measurement of the Lagrangian parameters of the MSSM at future colliders. The results of this thesis are published in [5] and [6].

After this introduction, in the second chapter of this thesis, the theoretical basis of the Standard Model, the Higgs mechanism and the MSSM are described. The mechanism of CP violation in the Higgs sector of the MSSM, first studied experimentally at LEP in the context of this thesis, is introduced. The next chapter presents the production mechanisms of Higgs bosons at LEP. In the fourth chapter, the experimental setups are described. The LEP accelerator is introduced and the OPAL experiment at LEP is presented, on whose data the experimental search in this thesis is based. Its data and precision is compared with the expected performance of a future experiment at the Linear Collider. Finally the data reconstruction and the background processes from known Standard Model interactions are presented.

The fifth chapter describes the topological search for Higgs bosons at LEP in the pair production channel $e^+e^- \to \mathcal{H}_1\mathcal{H}_2 \to b\bar{b}b\bar{b}$, where $\mathcal{H}_1$ and $\mathcal{H}_2$ are two neutral Higgs boson mass eigenstates in the MSSM, decaying each into a pair of b quarks. This production channel is one of the two main Higgs boson production mechanisms in the MSSM. The sixth chapter

concentrates on the interpretation of the results of all topological neutral Higgs boson searches in OPAL in the context of the MSSM. For the first time, CP violating MSSM scenarios and CP conserving scenarios aimed to set the stage for Higgs searches at the Large Hadron Collider are studied experimentally. Limits on Higgs boson masses and the MSSM parameter $\tan\beta$ are set. Then the search results of OPAL and all other LEP experiments together are combined and interpreted in the MSSM.

Since no statistically significant signals of MSSM particles have been found at previous experiments, in principle all possible combinations of values of MSSM parameters ("models") have to be tested by comparing their predictions for the Higgs sector with the observations at OPAL. However, if Supersymmetry is realized, future experiments will deliver a wealth of precise data from various supersymmetric particles, allowing to derive the MSSM parameters directly from the measurements. The global parameter measurements, taking into account the full correlation among the parameters and the most precise available predictions for the MSSM particles are presented in the seventh chapter. Finally a summary and an outlook is presented in the eighth chapter.

Chapter 2

Theoretical Context

This chapter outlines the theoretical foundation of modern particle physics, the Standard Model (SM) [7], and its most acclaimed possible extension, supersymmetry (SUSY) [8]. After a brief historical outline of the experimental and theoretical developments which lead to the establishment of the Standard Model, first the particle content of the SM is explained and the fundamental principles of the interactions between particles are introduced. The Higgs mechanism, allowing particle masses also in the presence of local gauge invariance, is described, followed by an overview of the theoretical shortcomings and experimental problems of the SM. As a possible solution to some of the theoretical and experimental challenges, SUSY is introduced. Since SUSY must be broken, different SUSY breaking mechanisms are shortly reviewed. A suitable phenomenological description of any kind of minimal supersymmetry is the minimal supersymmetric standard model (MSSM), which here is described together with the phenomenological description of a general SUSY breaking mechanism. Finally, the Higgs sector of the MSSM including possible effects of CP-violation in the soft SUSY breaking Lagrangian is investigated.

2.1 Foundations of the Standard Model

The Standard Model is based on the principle of quantised local gauge theories. The foundations of these theories have been laid in the nineteen-thirties and nineteen-forties by Dirac, Schwinger, Feynman, Drell, Yan and many others. By the end of the nineteen-forties, Quantum Electrodynamics (QED) very successfully described the electromagnetic interactions by means of an abelian gauge symmetry. However, the area of the strong and weak interactions remained somewhat mysterious and no unified theoretical description for these fields was found.

The strong interaction was described by discrete SU(3) symmetries. Using these and the hypothesis of three quarks up, down and sstrange, the "zoo" of lots of mesonic and baryonic states with different strangeness, spins and masses was described. However, one of the fermionic states experimentally observed showed an apparent violation of the Pauli principle: the Δ^{++} was described as three up-quarks with their spins aligned in parallel. This was a violation of the Pauli principle, because all three quarks, fermionic particles, were apparently in the same internal state. As a solution, the internal symmetry of colour charges was proposed in 1973, with a local non-abelian SU(3) symmetry to describe the forces among the quarks [9]. This theory also nicely described the ratio of the cross-section of $e^+e^- \rightarrow$ hadrons to $e^+e^- \rightarrow \mu^+\mu^-$. More experiments in the field of deep inelastic scattering, hadron spectroscopy and jet physics later impressively showed the power of $SU(3)_C$ to describe

the great variety of the phenomenons of the strong interaction between asymptotic freedom and confinement.

In the same time, the weak interaction was described by Fermis $V - A$ theory with a variety of theoretical and experimental problems. There the weak interaction is described as a contact interaction between four fermions, consisting of a vector current V and an axial current A. However, it predicted that unitarity was violated at large centre-of-mass energies $\sqrt{s}$, and it was in disagreement with experimental measurements, such as charged and neutral Kaon branching rations.

In the end of the nineteen-sixties a new model of the weak and the electromagnetic interactions was presented by Glashow, Salam and Weinberg [7], the GSW model, avoiding the unitarity violations of the $V - A$ theory. It predicted the existence of charged heavy vector bosons $W^{\pm}$, which transmit the interactions already described by the $V - A$ theory. Additionally, it proposed the existence of weak neutral currents, mediated by a heavy neutral vector boson Z. The masses of these vector bosons, forbidden by the SU(2)×U(1) gauge group of the theory, are dynamically generated by the Higgs mechanism [10]. All lepton and quark generations are treated uniformly in this model. However, it first was not possible to show the renormalisability of the infinities of the model. This was achieved in the beginning of the nineteen-seventies by 't Hooft [11]. However, the model was still not regarded as outstanding.

Still in the beginning of the nineteen-seventies, another approach was made to solve the problem of the description of the Kaon branching ratios $K_L^0 \to \mu^+\mu^-$ and $K^+ \to \mu^+\nu_\mu$, which were different by a factor of 10^8, which could not be explained in the $V - A$ theory. Glashow, Iliopoulos and Maiani proposed the existence of a fourth quark, the charm quark, ordered with the strange quark in an SU(2) doublet as in the GSW model. It lead to the cancellation of all neutral $\Delta s \neq 0$ currents and thus to the cancellation of the undesired $K_L^0 \to \mu^+\mu^-$ branching ratio [12].

Finally the predictions of these impressive theories, which were invented in order to fit already existing experimental measurements, were confirmed in the so-called "November revolution" of particle physics in 1974. In two experiments at the Stanford Linear Accelerator Centre SLAC and at the Brookhaven National Laboratory BNL the predicted charm quark was discovered in the form of the J/ψ resonance [13]. At CERN the neutrino bubble chamber experiment Gargamelle discovered the weak neutral currents as predicted by the GSW model [14]. Basically over night the foundations of the Standard Model were laid by these discoveries.

The vector bosons of the strong interaction were found in form of three-jet events in e^+e^- collisions at the PETRA accelerator at DESY [15] in 1979. Finally the massive vector bosons predicted by the GSW model were directly discovered in 1983 by the UA1 and UA2 experiments at the $Sp\bar{p}S$ collider at CERN [16]. The ratio of their masses was found to be exactly the one predicted by the Higgs mechanism. With these discoveries, the basic principles of the SM were established. In the meantime, all particles but one predicted by the SM are discovered, including also the particles of the third lepton and quark generation [17] and the SM mechanism of the introduction of CP-violation is successfully tested experimentally [18]. However, the Higgs boson remains as the only undetected particle in the SM. The era of the precision measurements of the SM observables [19] began, and searches for new phenomenons like the one presented in this thesis are performed in order to test the limits of the Standard Model.

2.2 The Standard Model

The Standard Model consists of a set of three quantum field theories, based on the principle of local gauge invariance. Gauge invariance means that the physical observations should stay the same, no matter what gauge transformation of a given gauge group is imposed on the quantities of the theory. Local gauge invariance means that these gauges can be chosen independently at each point in space and time.

The abelian electromagnetic gauge theory gives rise to the photon field A_μ. It can be unified with the non-abelian gauge theory of the weak interactions to the electroweak theory or Quantum Flavour Dynamics (QFD). This theory consists of the gauge group $\mathrm{SU}(2)_L \times \mathrm{U}(1)_Y$, which means that a SU(2) gauge transformation, acting on the weak isospin I of left-handed SU(2)-doublets is combined with a U(1) gauge theory acting on the hypercharge Y. Additionally the SM consists of the non-abelian theory of strong interactions, Quantum Chromo Dynamics (QCD). The latter is not described in detail here.

The principles of the electroweak interactions are illustrated in the following, using the first generation of leptons as an example. Neutrino masses are neglected here. The quantum fields manifest themselves under second order quantisations as field quanta, which are associated with particles. They consist of left-handed components

$$L = \begin{pmatrix} \nu \\ e \end{pmatrix}_L = \frac{1}{2}(1-\gamma^5)\begin{pmatrix} \nu \\ e \end{pmatrix}, \begin{array}{l} I_3 = +\frac{1}{2},\, Q = 0,\, Y = -1 \\ I_3 = -\frac{1}{2},\, Q = -1,\, Y = -1 \end{array} \tag{2.1}$$

where the neutrino ν and the electron e form a doublet under $\mathrm{SU}(2)_L$ transformations, and of right-handed components

$$R = e_R = \frac{1}{2}(1+\gamma^5)e,\ I_3 = 0,\, Q = -1,\, Y = -2. \tag{2.2}$$

The electrical charge Q_e is connected to the other quantum numbers by $Q_e = I_3 + \frac{Y}{2}$. Under the gauge transformation $\mathrm{SU}(2)_L$ they transform as follows:

$$L \to L' = e^{ig\alpha^a \frac{\sigma_a}{2}} L, \quad R \to R' = R \tag{2.3}$$

where the σ_a are the Pauli-matrices, and under $\mathrm{U}(1)_Y$ as

$$L \to L' = e^{ig'\beta\frac{Y}{2}} L, \quad R \to R' = e^{ig'\beta\frac{Y}{2}} R. \tag{2.4}$$

The gauge transformations are called *local*, since both α^a $(a = 1, 2, 3)$ and β^a are functions of space and time. The strength of the interaction which is later associated with the gauge transformation is described by the couplings g and g'.

Using only the above particle content and constructing the Lagrangian of the free fields L and R one obtains the massless Lagrangian without interactions:

$$\mathcal{L} = i\overline{L}\gamma^\mu\partial_\mu L + i\overline{R}\gamma^\mu\partial_\mu R, \tag{2.5}$$

which is not locally gauge invariant. No interactions among particles are present and all particles are massless. Using e. g. (2.4) the transformation is

$$\mathcal{L} \to \mathcal{L}' = \mathcal{L} + g'(\overline{L}\gamma^\mu L + \overline{R}\gamma^\mu R)\partial_\mu\beta. \tag{2.6}$$

In order to compensate the additional terms and render $\mathcal{L}$ gauge invariant, the gauge fields W_μ^a for the $\mathrm{SU}(2)_L$ transformation and B_μ for the $\mathrm{U}(1)_Y$ transformation have to be introduced to the covariant derivative

$$\partial_\mu \to D_\mu = i\left(\partial_\mu + ig\frac{\sigma_a}{2}W_\mu^a + ig'\frac{Y}{2}B_\mu\right). \tag{2.7}$$

The gauge fields transmit the interactions between particles, which are a direct consequence of the local gauge invariance. In order to reestablish gauge invariance, they must transform as follows:

$$W_\mu^a \to W_\mu^{a\prime} = W_\mu^a - \frac{1}{g}\partial_\mu \alpha^a - \varepsilon_{bc}^a \alpha^b W_\mu^c. \tag{2.8}$$

$$B_\mu \to B'_\mu = B_\mu + \frac{1}{g'}\partial_\mu \beta. \tag{2.9}$$

Using this, the massless part of the QFD Lagrangian can be formulated:

$$\mathcal{L}_{\mathrm{QFD}} = -\frac{1}{4}W_{\mu\nu}^a W_a^{\mu\nu} - \frac{1}{4}B_{\mu\nu}B^{\mu\nu} + i\overline{L}\not{D}L + i\overline{R}\not{D}R, \tag{2.10}$$

where $\not{D} = D^\mu \gamma_\mu$. It also contains the kinetic field energy of the gauge fields. The field strength tensors $W_{\mu\nu}^a$ and $B_{\mu\nu}$ are defined as

$$W_{\mu\nu}^a = \partial_\mu W_\nu^a - \partial_\nu W_\mu^a - g\varepsilon_{bc}^a W_\mu^b W_\nu^c \tag{2.11}$$

$$B_{\mu\nu} = \partial_\mu B_\nu - \partial_\nu B_\mu. \tag{2.12}$$

In this form the QFD-Lagrangian contains only gauge fields all of which couple to the neutrino. Since the photon field does not couple to the neutrino, the fields B_μ and W_μ^a can not be identified with the physical fields. The physical fields of the photon A_μ and the weak neutral current Z_μ are obtained by the rotation with the Weinberg angle θ_W:

$$\begin{pmatrix} \mathrm{Z}_\mu \\ \mathrm{A}_\mu \end{pmatrix} = \begin{pmatrix} \cos\theta_W & \sin\theta_W \\ -\sin\theta_W & \cos\theta_W \end{pmatrix} \begin{pmatrix} \mathrm{W}_\mu^3 \\ \mathrm{B}_\mu \end{pmatrix}, \qquad \cos\theta_W = \frac{g}{\sqrt{g^2+g'^2}}, \tag{2.13}$$

$$\mathrm{W}_\mu^+ = \mathrm{W}_\mu^1 + i\mathrm{W}_\mu^2, \tag{2.14}$$

$$\mathrm{W}_\mu^- = \mathrm{W}_\mu^1 - i\mathrm{W}_\mu^2 \tag{2.15}$$

As a result the charged currents and their coupling to the $\mathrm{W}^\pm$ are obtained

$$\frac{g}{2\sqrt{2}}(\bar{\nu}_L \gamma^\mu e_L \mathrm{W}_\mu^+ + h.c.) \tag{2.16}$$

as well as the neutral currents and their coupling to the gauge fields

$$\frac{\sqrt{g^2+g'^2}}{4}(\overline{L}\gamma^\mu \sigma_3 L - 2\frac{g'^2}{g^2+g'^2}\bar{e}_R\gamma^\mu e_R)\mathrm{Z}_\mu, \qquad \underbrace{\frac{gg'}{\sqrt{g^2+g'^2}}}_{Q_e}\bar{e}\gamma^\mu e\,\mathrm{A}_\mu \tag{2.17}$$

with the different coupling of the Z to the left- and right-handed fields and the vanishing coupling of the photon field A_μ to the neutrinos.

The predictive power of this theory is enormous, since it predicts the photon, the charged and the neutral currents with the correct couplings to the fermions. All these couplings have been measured with great precision at the experiments at LEP and SLD [19]. All predictions of the SM are in agreement with the precision measurements. Also the full particle spectrum of the SM besides the Higgs boson has been confirmed experimentally. All particles of the theory are shown in Tables 2.1 and 2.2. It is formulated analogously to the above example for all the fermion generations and for both quarks and leptons universally. All particles of the

Table 2.1: *Overview of the SM fermions. Their properties are shown in terms of their charges Q_e, their weak isospin I_W, their hypercharge Y and their mass [18, 20]. The masses of the five lightest quarks are subject to strong corrections from QCD in the bound systems in which they occur. The* u, d *and* s *masses are given in the current quark mass scheme and the* c *and* d *quark masses are given in the* $\overline{\text{MS}}$ *scheme.*

quarks			
$Q_e = +\frac{2}{3}, I_{W,L} = +\frac{1}{2}, I_{W,R} = 0,$ $Y_L = +\frac{1}{3}, Y_R = +\frac{4}{3}$		$Q_e = -\frac{1}{3}, I_{W,L} = -\frac{1}{2}, I_{W,R} = 0,$ $Y_L = +\frac{1}{3}, Y_R = -\frac{2}{3}$	
u	$1.5 \ldots 4\,\text{MeV}$	d	$4 \ldots 8\,\text{MeV}$
c	$1.15 \ldots 1.35\,\text{GeV}$	s	$80 \ldots 130\,\text{MeV}$
t	$178.0 \pm 4.3\,\text{GeV}$	b	$4.1 \ldots 4.4\,\text{GeV}$
leptons			
$Q_e = 0, I_{W,L} = +\frac{1}{2}, I_{W,R} = 0,$ $Y_L = -1, Y_R = 0$		$Q_e = -1, I_{W,L} = -\frac{1}{2}, I_{W,R} = 0,$ $Y_L = -1, Y_R = -2$	
ν_e	$< 3\,\text{eV}$	e^-	$511\,\text{keV}$
ν_μ	$< 19\,\text{keV}$	μ^-	$106\,\text{MeV}$
ν_τ	$< 18.2\,\text{MeV}$	τ^-	$1.78\,\text{GeV}$

first three generations of quarks and leptons and all vector bosons have been experimentally discovered and the measurement of their properties is in agreement with the SM [19].

Unfortunately, the SM in this form predicts that the masses of the fermions as well as the gauge boson are zero. This is due to the fact that mass terms for the fermions $m\,\overline{e}_L e_R$ and the gauge bosons $M^2\,\text{W}^a_\mu W^\mu_a$ are not invariant under $\text{SU}(2)_L \times \text{U}(1)_Y$ transformations. This contradicts the experimental findings that all SM particles besides the photon and the gluon are massive. Therefore a mechanism has to be found which dynamically generates particle masses, without violating the powerful gauge principle which leads to the impressive correct prediction of the particle spectrum and the couplings among the particles.

2.2.1 The Higgs Mechanism of the Standard Model

The most compelling (and most simple) solution to the aforementioned problem of the vanishing particle masses is the Higgs mechanism [10]. It describes particle masses as an effect of the interaction of the particles with a background field, which has a non-vanishing constant vacuum expectation value and therefore is omnipresent. This field manifests itself in the complex SU(2) doublet

$$\Phi = \begin{pmatrix} \phi^+ \\ \phi^0 \end{pmatrix}, Y = +1 \tag{2.18}$$

which in the broken theory is expanded around its vacuum expectation value

$$\Phi = e^{i\frac{\chi_a \alpha^a}{2v}} \frac{1}{\sqrt{2}} \begin{pmatrix} 0 \\ v + h \end{pmatrix}. \tag{2.19}$$

Table 2.2: *Overview of the SM bosons. Their properties are given in terms of their spin and their mass [18]. Gravity is not described by the SM.*

interaction	exchange boson	spin	mass
strong	8 gluons (g)	1	0
electromagnetic	γ	1	0
weak	$W^{\pm}$	1	80.4 GeV
	Z	1	91.2 GeV
gravity	graviton?	2	0
	Higgs	0	?

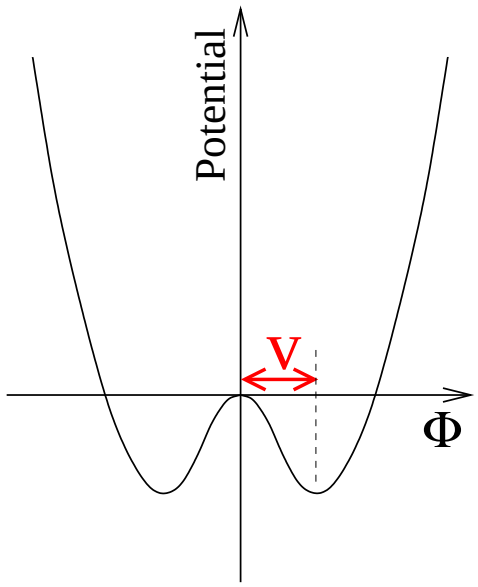

Figure 2.1: *The one-dimensional projection of the potential of the Higgs field. The minimum at $\Phi = v$ obeys a rotational symmetry, which is broken spontaneously.*

$v = \sqrt{-\mu^2/\lambda}$ is the non-vanishing vacuum expectation value (v.e.v.) of the field Φ in the potential

$$V(\Phi) = \frac{\mu^2}{2}\Phi^+\Phi + \frac{\lambda}{4}(\Phi^+\Phi)^2 \tag{2.20}$$

with $\lambda > 0$ and $\mu^2 < 0$. This potential is shown in Fig. 2.1. It ensures the non-vanishing v.e.v. of the field. The charged component ϕ^+ has to be set to 0 in the vacuum, otherwise the charge operator $Q = I_3 + \frac{Y}{2}$ would be broken by the non-zero v.e.v. of a charged field, and the photon could not be massless. The Higgs field has to carry both isospin and hypercharge in order to give mass to the gauge bosons of both $SU(2)_L$ and $U(1)_Y$. Therefore it has to be a doublet field. Finally three degrees of freedom are needed to give mass to the three bosons W^+, W^- and Z, therefore the doublet has to consist of complex fields with four degrees of freedom overall.

Using a global SU(2) transformation the rotational degree of freedom of the Higgs field is gauged away

$$L \to L' = e^{-i\frac{\lambda^a \alpha_a}{2v}} L \Rightarrow \Phi = \frac{1}{\sqrt{2}} \begin{pmatrix} 0 \\ v+h \end{pmatrix}. \tag{2.21}$$

This mechanism is called spontaneous symmetry breaking, since the ground state of one of the fields of the theory does not preserve the initial symmetry of the theory. It spontaneously breaks down the $SU(2)_L \times U(1)_Y$ symmetry to the electromagnetic interaction $U(1)_{EM}$ at low energies, since only the photon remains massless and therefore only the interactions of the particles with the photons are dominant at low energies. The following expression for the mass part of the QFD Lagrangian is obtained:

$$\mathcal{L}_{\text{QFD}}^{\text{mass}} = -\sqrt{2}\lambda_f(\overline{L}\Phi R + \overline{R}\Phi^+ L) + |D_\mu \Phi|^2 - V(\Phi). \tag{2.22}$$

This Lagrangian contains effective mass terms for the gauge bosons

$$\frac{g^2 v^2}{4} W_\mu^a W_a^\mu, \quad \frac{(g^2+g'^2)v^2}{4} Z_\mu Z^\mu$$

with fixed couplings. The predicted masses of the gauge bosons are

$$M_{\text{A}} = 0, \quad M_{\text{W}^\pm} = \frac{gv}{2}, \quad M_{\text{Z}} = \frac{\sqrt{g^2+g'^2}v}{2}. \tag{2.23}$$

The relation $M_{\text{W}^\pm}/M_{\text{Z}}$ is precisely measured by the LEP experiments. It should be mentioned that another sign of the elegance of the theory lies in the fact that exactly the rotation angle θ_W, which leads to vanishing couplings of the photon to the neutrino, also leads to a massless photon. The physical Higgs field itself, described by h, acquires mass, since (2.22) contains a term

$$-\lambda v^2 h^2.$$

The mass of the Higgs boson, described by the coupling parameter λ (from (2.20)), is the only free parameter of the theory which is up to now unmeasured. Bounds on the Higgs boson mass from experiments and theoretical considerations are discussed later. Additionally the Higgs mechanism predicts Higgs self interaction terms proportional to h^3, h^4 and interaction terms with the gauge fields proportional to hWW, hZZ and h^2ZZ, which allow for the production of Higgs bosons from gauge bosons.

The mass terms for the fermions are accompanied by one free parameter per fermion, the Yukawa coupling parameter λ_f. These parameters are used to adjust the fermion masses. The mass term then reads

$$\lambda_{\text{e}} \overline{L}\Phi R.$$

The generation of the boson and fermion masses in the Higgs sector can also be visualised in terms of the interactions of the particle fields with the Higgs background field. This is shown in Fig. 2.2. A massive particle does not have a defined helicity. That means, if a particle has mass there must be a mechanism allowing the particle to change its helicity. This is the interaction with the background field of the Higgs boson with non-zero v.e.v.

Fig. 2.2 shows the propagation of a massless fermion.This fermion couples with a coupling constant λ_f to the scalar field with strength $v/\sqrt{2}$. Each interaction changes the helicity of the fermion. Since a scalar field cannot absorb spin, the fermion has to change its state of motion during the interaction. This can be regarded as the occurrence of an effective mass [21]:

$$\frac{1}{\not p} + \frac{1}{\not p}\frac{\lambda_f v}{\sqrt{2}}\frac{1}{\not p} + \frac{1}{\not p}\frac{\lambda_f v}{\sqrt{2}}\frac{1}{\not p}\frac{\lambda_f v}{\sqrt{2}}\frac{1}{\not p} + \cdots = \frac{1}{\not p + (\lambda_f v)/(2\sqrt{2})} = \frac{1}{\not p + m_f} \tag{2.24}$$

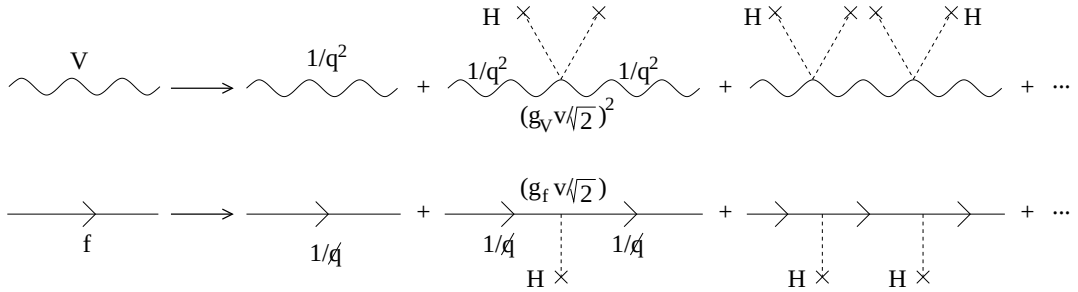

Figure 2.2: *The generation of particle masses through the Higgs mechanism. In the upper diagram, the mass generation for spin-1 bosons is shown. The massless propagator* $1/q^2$ *interacts with the Higgs background field. In the lower diagram, the same mechanism is shown for fermions.*

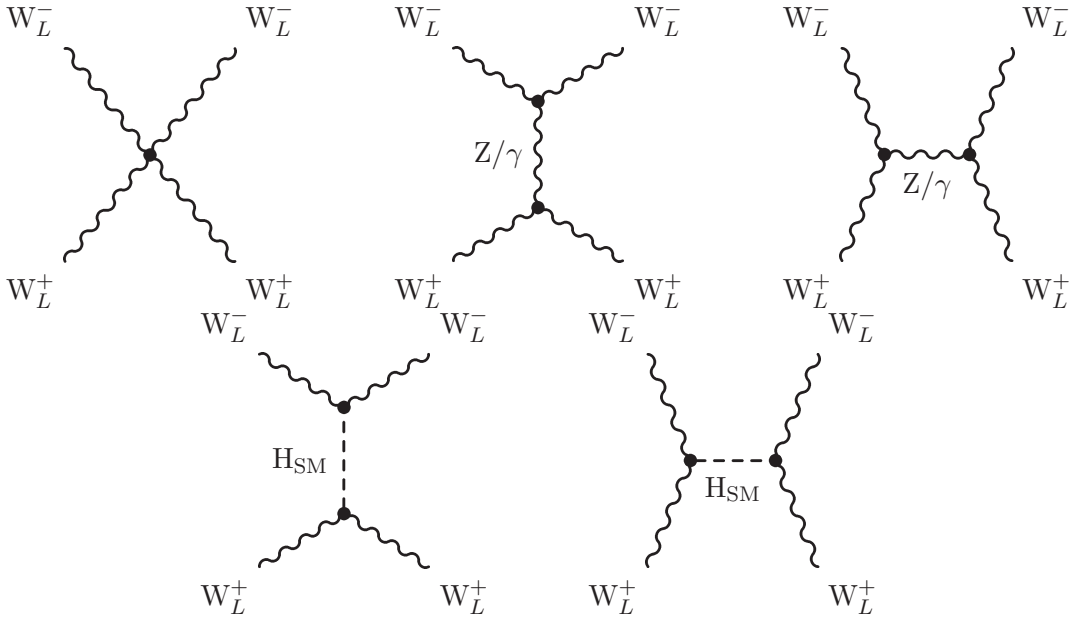

Figure 2.3: *Divergent* WW *cross-section graphs and their cancellation. The upper three diagrams violate unitarity starting from* $\sqrt{s} \approx 1.2\,\mathrm{TeV}$. *These unitarity violations are cancelled by the lower two diagrams involving Higgs boson exchange.*

This mechanism works equivalently for the massive gauge bosons. Since these are massless spin 1 particles, each interaction with the background field has to change the helicity by ± 2, therefore two Higgs field quanta per interaction are necessary.

$$\frac{1}{q^2} + \frac{1}{q^2}\left(\frac{gv}{2}\right)^2 \frac{1}{q^2} + \frac{1}{q^2}\left(\frac{gv}{2}\right)^2 \frac{1}{q^2}\left(\frac{gv}{2}\right)^2 \frac{1}{q^2} + \cdots = \frac{1}{q^2 + (gv/2)^2} = \frac{1}{q^2 + m_W^2} \tag{2.25}$$

The interactions of a massless field with the constant background field therefore generates the impression of massive particles, while the $\mathrm{SU}(2)_L$ and $\mathrm{U}(1)_Y$ symmetries are preserved at high energies since only massless fields are used.

Mass bounds on the SM Higgs boson

The generation of particle masses and the successful prediction of the ratio $M_W/M_Z = \cos\theta_W$ are not the only parts of the SM where the Higgs mechanism provides elegant solutions.

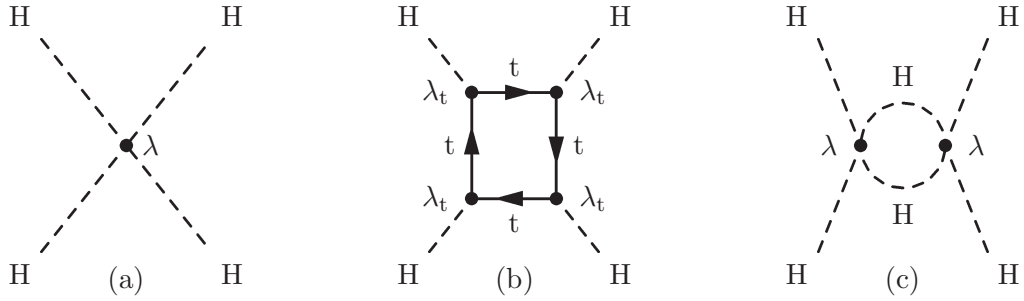

Figure 2.4: *Loop corrections to the quartic Higgs self coupling. For a light Higgs boson, the dominant loop contribution to the Higgs mass arises from top quark loops (b). For heavy Higgs bosons, Higgs loops form the dominant contribution (c).*

Without an additional interaction, the cross-section of longitudinal WW scattering, shown in the first three graphs in Fig. 2.3, would be divergent and violate unitarity bounds from $\sqrt{s} = 1.2$ TeV onwards. The Higgs mechanism cancels the divergencies of the cross-section of the longitudinal degrees of freedom of the W bosons by destructive interference of the last two graphs of Fig. 2.3 with the first three graphs. Thus the cross-section does not diverge and no violation of unitarity occurs.

This mechanism only works if the Higgs boson is not too heavy, otherwise it would not contribute enough to the scattering amplitudes before unitarity is violated. Therefore the Higgs boson mass must be below approximately 850 GeV. If there is no Higgs boson below 850 GeV, an additional strong force acting on the W bosons is needed to cancel the divergencies.

Another bound on the Higgs boson mass stems from loop corrections to the quartic term in the Higgs potential (2.20) itself. The Feynman graph of the Higgs self coupling with strength λ is shown in Fig. 2.4 (a). If the Higgs boson is light, λ is small and the dominant loop contribution to the Higgs potential comes from top loops as in Fig. 2.4 (b), since λ_t is large due to the large mass of the top quark. As an effect of the loop contribution, the effective λ_{eff} after loop corrections is reduced. If the Standard Model is valid as an effective theory up to the scale Λ, then these loop contributions have to be summed up until this scale. For the Higgs mechanism to remain valid, the effective λ_{eff} must not be negative, otherwise no minimum exists in the potential and no stable spontaneous symmetry breaking occurs. This places a lower bound on λ, hence on m_{H}, depending on the cut-off scale Λ.

Additionally to this lower bound on m_{H} also an upper bound exists. If λ is large, then the loop contribution from Higgs loops in Fig. 2.4 (c) dominates over the top loops in Fig. 2.4 (b). Due to their different spin statistics, the Higgs loops have the opposite effect on λ_{eff} with respect to the top loops. For heavy m_{H}, λ_{eff} would grow to infinity (Landau-pole) and no well-defined theory would exist, since the Higgs potential in Fig. 2.1 would be reduced to an infinitesimally thin band with a v.e.v. equal to 0 and infinitely strong interactions.

Fig: 2.5 shows the upper and lower bounds on m_{H} depending on the cutoff scale Λ, until which the divergent loop-contributions are taken into account. It can be seen that for the SM to be valid until the Planck scale ($\Lambda \approx 10^{19}$ GeV), m_{H} must be around 160 GeV.

Additionally to these theoretical bounds on the SM Higgs boson mass, also experimental constraints exist. Direct searches for the Higgs boson have been conducted at the LEP experiments at CERN from 1989 to 2000 in e^+e^- collisions at $\sqrt{s} = 91 - 209$ GeV. Despite a slight excess of candidates in the ALEPH dataset [23] at the kinematical limit of Higgs boson production, no statistically significant signal was found in the combined LEP data. An experimental lower bound of $m_{\text{H}} > 114.4$ GeV at 95 % confidence level was set [3].

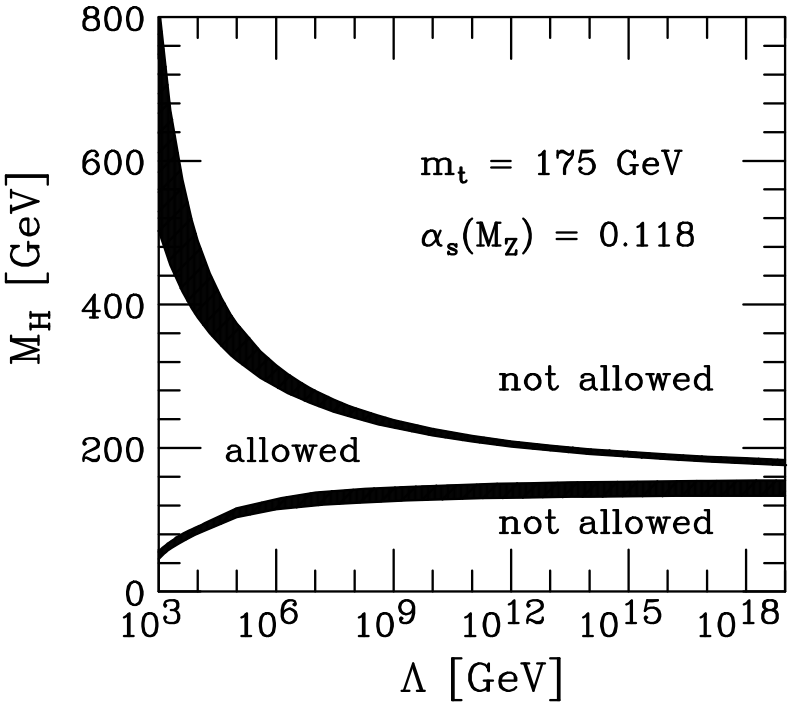

Figure 2.5: *Theoretical bounds on the SM Higgs mass as a function of the cut-off scale. It is assumed that the SM is a valid theory up to the scale* Λ*. Then the upper and lower bound on the Higgs mass, stemming from Higgs-self-energy corrections, are shown by the black line [22].*

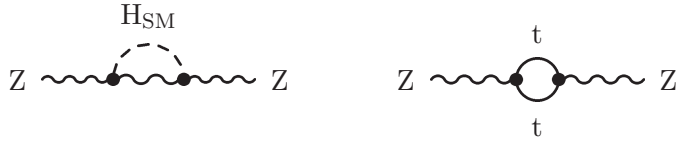

Figure 2.6: *Loop contributions to the* Z *boson mass. These loop corrections allow the indirect measurement of the Higgs mass, if the top quark mass is known.*

An indirect measurement of m_{H} within the SM framework is possible using SM precision measurements of the Z pole, the top quark mass and the W mass and properties. Such measurements have been performed by the LEP experiments from 1989 to 1995 and by SLC at SLAC from 1993 to 1998. A fit of the SM parameters to the precision observables, such as $\sin^2\theta_W$ or m_{Z} is performed [19]. Since Higgs boson loops contribute to the self-energy of the Z (see Fig. 2.6 (a)) and the W, this fit is logarithmically sensitive on m_{H}.

The measurement of m_{H} is correlated with other parameters of the SM, such as hadronical corrections to α_{EM} or, most notably, the top quark mass m_{t}. The self-energy-graph including the top quark loop is shown in Fig. 2.6 (b).

The indirect determination of m_{H} from this fit is shown in Fig. 2.7. It displays the $\Delta\chi^2 = \chi^2 - \chi^2_{\mathrm{min}}$ of the the fit with respect to the hypothetical Higgs boson mass. The dotted line shows the fit result for the new world average of $m_{\mathrm{t}} = 178 \pm 4.3$ GeV [20] and the most precise available low-energy data [24]. Due to its opposite spin statistics the top quark loop and the

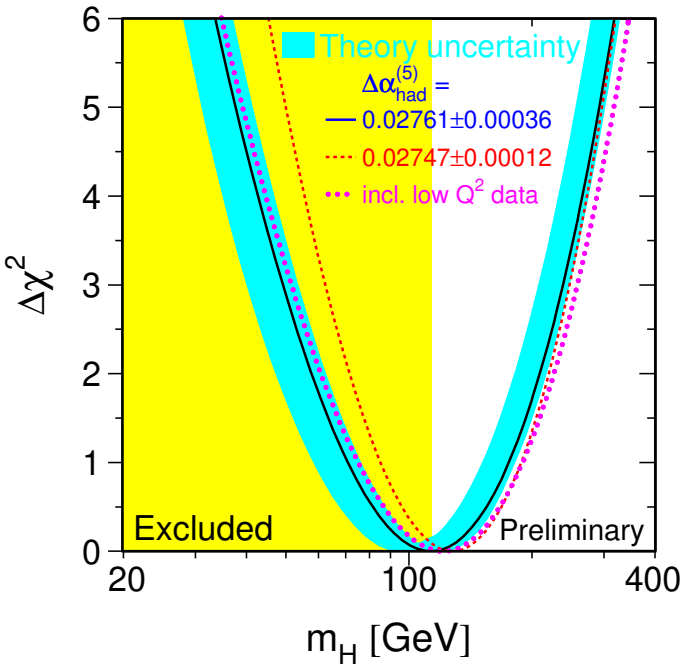

Figure 2.7: *Experimental indirect determination of the Higgs boson mass. The yellow (light grey) area is excluded by direct searches for the SM Higgs boson at LEP. The parabolic lines show the $\Delta\chi^2$ of the best fit to the SM precision observables for different values of the hadronic corrections as a function of $m_{\mathrm{H_{SM}}}$. The thick dotted line represents the $\Delta\chi^2$ for the new world average of $m_{\mathrm{top}} = 178\,\mathrm{GeV}$ and the most precise available low energy data. The minimum is located at $m_{\mathrm{H_{SM}}} = 117\,\mathrm{GeV}$ [24].*

Higgs boson loop influence m_{Z} with opposite sign. Hence the best fit for m_{H} grows with larger m_{t}, since both effects have to shrink with the same magnitude in order to give constant m_{Z}. The best fit lies at $m_{\mathrm{H}} = 117$ GeV, directly above the direct exclusion at $m_{\mathrm{H}} > 114.4$ GeV, displayed as the yellow area.

Due to the logarithmic dependence of m_{Z} on m_{H}, the Higgs mass bound is relatively weak for larger Higgs masses. A upper limit of $m_{\mathrm{H}} < 251$ GeV can be set on the 95 % confidence level.

These considerations show that both from experiment and from high-energy stability of the SM a light Higgs boson below 200 GeV is preferred. Unfortunately, as the next section will show, this is not the natural scale of m_{H} in the SM.

2.2.2 Shortcomings of the Standard Model

Although the SM of elementary particles is a perfectly consistent theory successfully describing the precision measurements, and although in principle all physical laws needed to explain low-energy phenomena such as electromagnetism, nuclear and solid-state-physics phenomena, molecular chemistry and so on can be deduced from the SM interactions (albeit the very calculation of predictions might become virtually impossible in the presence of very many

particles), it fails to explain some experimental facts. Additionally, it shows some theoretical imperfections. Therefore it is sure that the SM is a low-energy approximation to the theory of everything. However, it should be mentioned that it is an extremely good approximation, otherwise it wouldn't have survived more than 20 years of tests without failure in any precision experiment.

Experimental Problems

The strongest experimental challenge to the SM is the creation of the universe and cosmological precision measurements, which have become available during the last years. First, the abundance of antimatter in the visible universe and the measured ratio $n_\gamma/n_{\text{baryons}} \approx 10^9$ [25] places a lower bound on the amount of CP-violation, which is one of the three requirements for the creation of the matter/antimatter asymmetry [26]. The SM incorporates CP-violation only in the CKM mechanism [27], relating the weak eigenstates of the quarks to their mass eigenstates. These effects are currently measured precisely by the B-factory experiments BABAR and BELLE. The measured CP-violation in the SM is estimated to be about a factor of 10^8 too small to account for the cosmological matter/antimatter asymmetry [25]. This means that there must be an additional source of CP-violation beyond the SM. A possible solution for this problem in the context of the MSSM [28] will be outlined in Section 2.3.4.

Next, the measurements of redshift vs. distance of distant galaxies, the rotational velocity distribution of our own galaxy and the precise determination of the microwave background radiation with the WMAP experiment [29] allow the measurement of the curvature of the universe Ω, the amount of dark energy Ω_{Λ_C}, cold dark matter Ω_{DM} and ordinary matter Ω_{M} in the universe. Dark energy is the amount of energy stored in the field of the cosmological constant Λ_C, which accelerates the expansion of the universe. Cold dark matter is only weakly interacting matter consisting of particles, which are by several orders of magnitude more massive than neutrinos, which are the only candidates for this sort of matter in the SM. Due to their small mass, neutrinos could only contribute to the so-called hot dark matter, for which there is little experimental hint. With the above mentioned cosmological measurements it is possible to determine the cosmological parameters to

$$\begin{aligned} \Omega &= 1 \\ \Omega_{\Lambda_C} &\approx 0.7 \\ \Omega_{\text{DM}} &\approx 0.25 \\ \Omega_{\text{M}} &\approx 0.05 \end{aligned}$$

This means that only 5 % of the amount of energy in the universe is stored in ordinary matter as known by the SM. For the remaining 95 % of the energy in the universe there is no explanation in the SM. A compelling extension to the SM should therefore provide a weakly interacting massive particle (WIMP) which serves as a candidate for the dark matter.

During the last years experiments like SuperKamiokande [30], K2K [31], SNO [32] and Kamland [33] have established neutrino oscillations. This is a clear sign of neutrino mass, since only massive particles have a time evolution and therefore can oscillate, if mass differences between neutrino mass eigenstates exist. Together with the non-observation of neutrino masses in direct mass measurements [34], absolute upper limits on neutrino masses can be set (see Tab. 2.1).

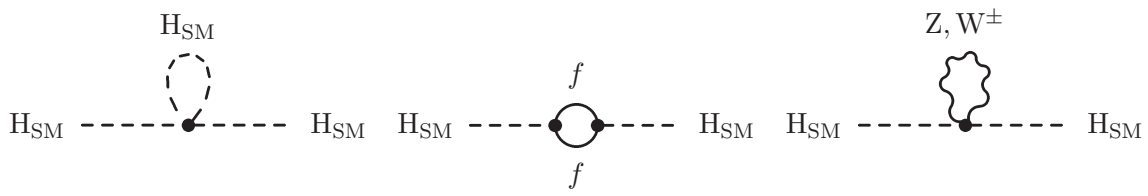

Figure 2.8: *Divergent loop contributions to the Higgs boson mass. The quadratic divergencies from these graphs are not cancelled in the SM.*

Theoretical Shortcomings

The question of the natural mass scale of the SM Higgs boson has already been raised in the previous section. Fig. 2.8 shows the dominant contributions to the self-energy of the Higgs boson from Higgs, fermion and boson loops. If the SM is valid up to an energy scale Λ, then the size of these contributions is

$$\Delta m_{\mathrm{H}}^2 \sim \Lambda^2. \tag{2.26}$$

In contrast to these corrections, the fermion masses are only subject to logarithmic divergencies, so that the overall correction is of the scale of the mass itself and no finetuning problem emerges. For the Higgs boson this means that if the SM is valid up to the Planck scale of $\Lambda_P = 10^{19}$ GeV, then the natural scale of the Higgs boson mass is Λ_P, while all other particles have natural mass scales below v. This is the so-called hierarchy problem, which refers to the extremely large splitting of the weak scale and the natural cut-off scale, the Planck scale. In order to achieve the necessary Higgs mass range of $m_{\mathrm{H}} < 1$ TeV, an unnatural finetuning with the relative precision of $m_{\mathrm{H}}/\Lambda_P > 10^{16}$ has to be applied. This finetuning is not explained in the context of the SM and it is solved by extensions of the SM, as Section 2.3 will show.

Up to now only the weak and the electromagnetic interaction have been discussed in detail. Additionally to these two forces, unified in the electroweak model, the SM contains also the strong interaction or Quantum Chromo Dynamics (QCD). Every interaction possesses its own coupling constant, which is subject to energy-scale dependent loop corrections.

If the three independent forces of the SM are to be contained in one force at very high energy scales in a natural way, which is broken down by some mechanism to the known SM forces (just as $\mathrm{SU}(2)_L \times \mathrm{U}(1)_Y$ is broken spontaneously to $\mathrm{U}(1)_{\mathrm{EM}}$ by the Higgs mechanism below the scale v), then the coupling constants of the SM forces should unify at the unification scale. If the measured running of the coupling constants α_{QED}, α_{QFD} and α_{QCD} is extrapolated, then the scale of the so-called Grand Unified Theory (GUT) is at around $\Lambda_{GUT} = 10^{16}$ GeV.

As Fig. 2.9 shows, the three coupling constants unfortunately do not meet at the same point, which means that without an additional mechanism below Λ_{GUT} the three independent forces of the SM can not be derived from one single interaction at high scales, which then is broken. Section 2.3 will show how such a mechanism could be realized.

The problem of anomaly cancellation is also connected to possible GUTs. In the SM the chiral anomalies in triangular loop graphs of the electroweak interaction and the chiral anomalies of QCD both give rise to unrenormalizable divergencies. Both anomalies cancel however, if the relation

$$N_C(Q_{\mathrm{u}} + Q_{\mathrm{d}}) = -Q_{\mathrm{e}} \tag{2.27}$$

holds [35]. That is, the number of colours in QCD, N_C, is related to the electromagnetic charge of the up- (Q_{u}) and down-type (Q_{d}) quarks and the electron Q_{e}. This relation holds in the SM just by chance, no explanation for it is given, since QCD and QFD are completely

independent theories. A possible GUT could provide the mechanism for the realization of this relation among the independent charges of the theory.

Another shortcoming of the SM is the up to now unsuccessful attempt to integrate gravity into its framework. While gravity is a sort of a non-quantised gauge theory of space and time, the three SM forces are described by gauge theories of fields *in* space and time. Every theory connecting these two different approaches would be helpful to achieve a complete unification of all forces.

Finally the SM could be criticised because of the number of free parameters, which is 18 without neutrino masses and at least 25 if neutrino masses are taken into account. While this seems to be a small number of parameters for a theory of almost everything (compared to the incredible number of observables which are in agreement with the SM), it is a large number compared to the aesthetical optimum of a fundamental theory, where all scales, couplings and masses should emerge naturally and without individual tuning. Unfortunately, as Section 2.3 will show, the most prominent ideas for extensions of the SM are not really capable of reducing the number of free parameters, either.

In summary, the SM is the most successful theory invented to date, which remains successful despite experimentalists efforts for more than 20 years to prove its incompleteness. However, one crucial part of the SM, the Higgs mechanism, has not been confirmed. If the Higgs mechanism is valid, then an even greater miracle emerges in the form of the mechanism behind electroweak symmetry breaking and in the mechanism of its stabilisation. But most of all, the SM fails to describe cosmological measurements and therefore badly needs assistance by a more complete and fundamental theory. The crucial test for the possible solutions of the problems of the SM can be expected from the next generation of high energy experiments, such as the Large Hadron Collider LHC and the Linear Collider LC. The mysteries of present physics, be it spontaneous symmetry breaking or dark matter, will most likely be uncovered at these experiments, combining the presently highest possible energies in the case of the LHC with the presently highest possible precision in the case of the LC.

2.3 Supersymmetry as an Extension to the Standard Model

The precision measurements of the past decades, most notably at LEP and SLD [19] and increasingly at the Tevatron, place tight bounds on possible extensions of the SM. Every new theory must contain the SM as its low-energy limit. This means especially that new, more massive particles do not destroy the successful prediction of precision observables through loop effects. The most prominent extension of the SM which is in complete agreement with the precision measurements [36] is Supersymmetry (SUSY). In this section the concept of SUSY is introduced, followed by a description of the minimal SUSY model, the MSSM. Finally the Higgs sector in the MSSM will be discussed in detail, together with a description of the effects of CP-violating elements in the SUSY soft-breaking Lagrangian on the Higgs sector.

2.3.1 General Concept of Supersymmetry

In order to solve the hierarchy problem, for each particle a partner is introduced which is connected to the SM particles by a symmetry transformation under which the theory is invariant. In order to cancel the quadratic divergencies responsible for the hierarchy problem, SUSY introduces a new boson for each fermion and vice versa. Then for each divergent diagram in Fig. 2.8 there exists a counter-diagram with opposite spin statistics (see Fig. 2.10), cancelling the divergency and stabilising the gap between the GUT scale and the electroweak scale [37]. This new symmetry is called Supersymmetry. It is realized by introducing the operator Q

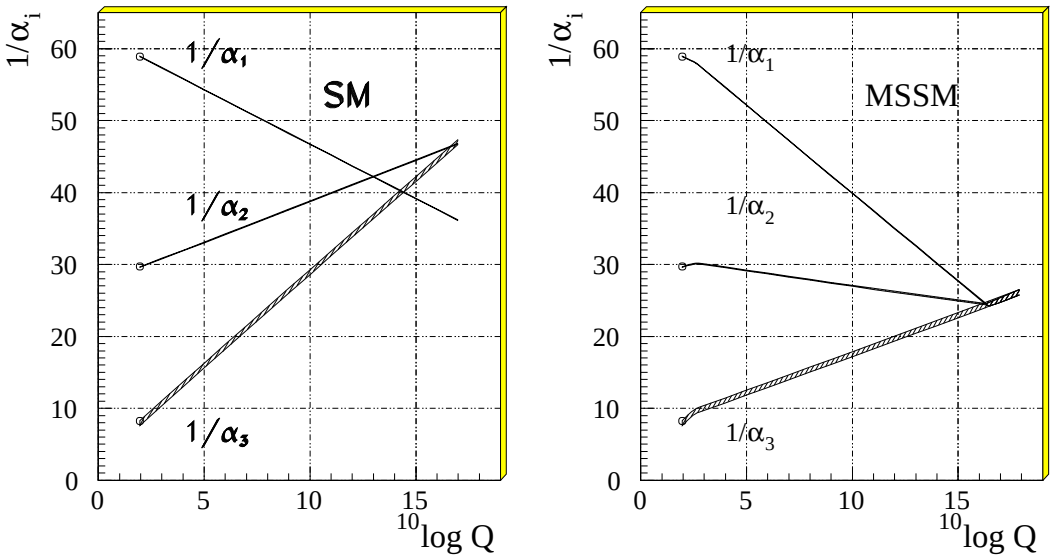

Figure 2.9: *Unification of the forces in supersymmetric models. The three coupling constants α_1, α_2 and α_3 are not unified at any scale in the SM. Additional SUSY particles alter the running of the coupling constants, leading to unification at the GUT scale.*

which translates bosons $|B\rangle$ into fermions $|f_\alpha\rangle$ and vice versa

$$Q_\alpha |f_\alpha\rangle = |B\rangle, \qquad Q_\alpha |B\rangle = |f_\alpha\rangle, \tag{2.28}$$

where α is the spinor index. One can see that Q_α is a fermionic operator. Therefore one could also say that SUSY solves the hierarchy problem by introducing a new fermionic dimension.

Now every SM boson has a fermionic partner, and every SM fermion has a bosonic partner. The partner of a fermionic SM particle is called sparticle, while the partners of the SM bosons are identified by the extension "-ino". All their quantum numbers, apart from their spin, are respectively the same, and they share the same masses. The spectrum of particles is shown in Tab. 2.3. The matter fields, for example L, are connected with their superpartner fields $\tilde{L}$ to the superfields $\hat{L} = (L, \tilde{L})$. Since the number of degrees of freedom (d.o.f.) has to be conserved under Q, for every spin-$\frac{1}{2}$ particle in the SM there exist two SUSY spin-0 particles, called f_L, the partner of the left-handed fermion f, and f_R, the partner of the right-handed fermion f.

Apart from solving the hierarchy problem, SUSY has another advantage since it achieves unification of the forces [38]. This is illustrated in Fig. 2.9. While the running of the coupling constants α_i in the SM does not converge at one point, the running in SUSY does. This is achieved by the introduction of the new particles, which introduce new loop contributions. The convergence of all three coupling constants at one point at the GUT scale of $\Lambda \approx 10^{16}$ GeV can be seen in Fig. 2.9 (b).

Another theoretical advantage of SUSY is the possibility to connect the gauge theories to gravity. This is achieved since the defining commutation relation for the supersymmetry operator Q (the 'new fermionic dimension') is connected to the momentum operator P (the 'traditional dimensions') by

$$\{Q_\alpha, Q_\beta\} = 2\sigma^\mu_{\alpha\beta} P_\mu, \tag{2.29}$$

where $\sigma^\mu = (1, \vec{\sigma})$ are the Pauli matrices. By making SUSY a local symmetry, the so-called mSUGRA model is realized. It also can be shown that a unified theory with spin-2 bosons

Table 2.3: *The MSSM particle spectrum. The quantum numbers of the superpartners are the same as for the SM particles in Tab. 2.1 and 2.2.*

Superfield	Boson field	Fermion Field
Gauge multiplets		
$\hat{G}$	g	$\tilde{g}$
$\hat{W}^{\pm}$	$W^{\pm}$	$\tilde{W}^{\pm}$
$\hat{Z}$	Z	$\tilde{Z}$
$\hat{A}$	A	$\tilde{A}$
Matter multiplets		
$\begin{pmatrix}\hat{L}\\ \hat{E}\end{pmatrix}$	leptons $\begin{cases}\begin{pmatrix}\tilde{L}_j=(\tilde{\nu}_j,\tilde{e}_j^-)_L\\ \tilde{E}_j=\tilde{e}_{j,R}^-\end{pmatrix}\end{cases}$	$\begin{pmatrix}L_j=(\nu_j,e_j^-)_L\\ E_j=e_{j,R}^-\end{pmatrix}$
$\begin{pmatrix}\hat{Q}\\ \hat{U}\\ \hat{D}\end{pmatrix}$	quarks $\begin{cases}\begin{pmatrix}\tilde{Q}_j=(\tilde{u}_j,\tilde{d}_j)_L\\ \tilde{U}_j=\tilde{u}_{j,R}\\ \tilde{D}_j=\tilde{d}_{j,R}\end{pmatrix}\end{cases}$	$\begin{pmatrix}U_j=(u_j,d_j)_L\\ U_j=u_{j,R}\\ D_j=d_{j,R}\end{pmatrix}$
$\begin{pmatrix}\hat{H}_1\\ \hat{H}_2\end{pmatrix}$	Higgs $\begin{cases}\begin{pmatrix}H_1^j\\ H_2^j\end{pmatrix}\end{cases}$	$\begin{pmatrix}(\tilde{H}_1^0,\tilde{H}_1^-)_L\\ (\tilde{H}_2^+,\tilde{H}_2^0)_L\end{pmatrix}$
Gravity		
$\hat{G}r$	gr	$\tilde{g}r$

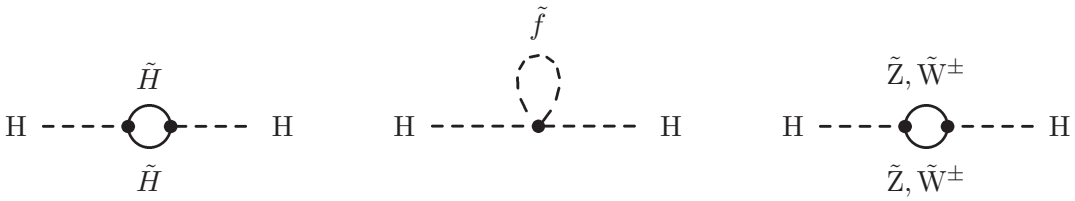

Figure 2.10: *SUSY contributions to the Higgs boson mass. The quadratic divergencies to the Higgs mass introduced by the graphs in Fig. 2.8 are cancelled by the graphs above.*

(the graviton gr) and spin-1 bosons is only possible by introducing a symmetry which creates spin-$\frac{3}{2}$ fermions (the gravitino $\tilde{gr}$) [39].

The definition of Q is not unambiguous, it is possible to use several operators Q^i at the same time. In this thesis only models with one SUSY operator ($N = 1$) will be discussed.

Finally, it can be shown that SUSY is a necessary symmetry if string theory, one of the candidates for a theory of everything, should be realized in nature.

While SUSY has an impressive list of advantages, it suffers from the fact that none of the superpartners have been discovered to date. No bosonic partners to the known fermions exist, which have the same couplings, the same charges and the same masses as their SM partners. Therefore, if SUSY exists, it can not be realized unbroken. A scale Λ_{SUSY} must exist, at which SUSY is broken spontaneously or directly, and which should not be several orders of magnitude away from the scale v, otherwise a new hierarchy problem would emerge, this time

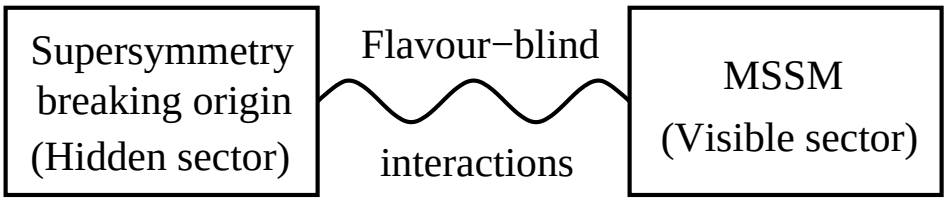

Figure 2.11: *The mediation of SUSY breaking from the hidden sector. Unspecified physics at the GUT scale in a so-called hidden sector leads to SUSY breaking. This breaking is then transferred to the visible sector via a messenger field, which can be a known field like gauge fields of gravity or new physics.*

between v and Λ_{SUSY} instead between v and Λ_{GUT}. Also the unification of the couplings, as shown in Fig. 2.9, is not possible for too large values of Λ_{SUSY}.

SUSY Breaking Mechanisms

The question of SUSY breaking can be addressed in two different ways. Either it is treated in a purely phenomenological way by the introduction of all possible terms which are directly breaking SUSY. This method is described in Section 2.3.2. On the other hand fundamental sources for direct or spontaneous SUSY breaking can be invented, which typically involve a hidden sector (typically at the GUT scale), where SUSY is broken. This SUSY breaking is mediated by a flavour-blind interaction to the visible world. Apart from that, no specific assumptions are made about the hidden sector. This is shown in Fig. 2.11.

The most popular candidate for the flavour-blind messenger field is gravity. These models are called gravity mediated SUSY breaking scenarios. This is the case in mSUGRA, where additionally SUSY is a local symmetry. The scale of the $\Lambda_{\mathrm{Hidden}}$ of the unknown model in the hidden sector can be estimated from (see e.g. [40])

$$\Lambda_{\mathrm{SUSY}} \approx \frac{\Lambda^2_{\mathrm{Hidden}}}{\Lambda_{\mathrm{Planck}}}. \tag{2.30}$$

For a SUSY breaking scale Λ_{SUSY} no higher than 1 TeV, this means that $\Lambda_{\mathrm{Hidden}}$ is of the order of 10^{11} GeV. The Lagrangian terms at the GUT scale which communicate between the two sectors depend on only four free parameters and one sign, which are

$\tan\beta$	the ratio of the Higgs v.e.v. of the two doublets
$m_{1/2}$	the mass scale of the gauginos of SU(3), SU(2) and U(1)
m_0	the mass scale of the sfermions and higgsinos
A	the common trilinear coupling between H and $\tilde{f}\tilde{f}$
$\mathrm{sign}(\mu)$	the sign of the Higgsino mixing parameter

Typically in such a model the neutralino is the lightest supersymmetric particle. Other breaking mechanisms are gauge mediated SUSY breaking (GMSB), where the messenger particles have $\mathrm{SU(3)}_C \times \mathrm{SU(2)}_L \times \mathrm{U(1)}_Y$ interactions, and anomaly mediated SUSY breaking (AMSB). Those models differ from the mSUGRA scenario typically in the fact that other particles such as the gravitino in case of the GMSB play the role of the lightest supersymmetric particle. These scenarios will not be pursued further here.

2.3.2 The Minimal Supersymmetric Standard Model

It seems bold to speculate about SUSY breaking mechanisms near Λ_{GUT} while none of the sparticles have been detected to date. Instead, it is possible to describe the SUSY breaking purely phenomenologically in the form of direct SUSY breaking terms in the soft SUSY breaking Lagrangian $\mathcal{L}_{\mathrm{soft}}$. Soft breaking means that only logarithmically divergent terms are included and no new quadratically divergent terms (as in case of the SM Higgs mass) emerge [41]. Every form of SUSY breaking near the GUT scale can be described in $\mathcal{L}_{\mathrm{soft}}$ using parameters at the scale Λ_{SUSY}.

The minimal supersymmetric model is constructed by adding one operator Q to the SM operators. Thus $N = 1$ supersymmetry is realized. The Higgs sector has to be extended, since the use of the doublet Φ for the generation of the down-type fermion masses and the use of the conjugate doublet Φ^* for the up-type masses is forbidden by SUSY. Also the existence of just one charged fermionic superpartner to the Higgs field $\tilde{H}^-$ would give rise to unrenormalizable chiral anomalies, which have to be cancelled by a second charged Higgsino $\tilde{H}^+$. Therefore a second Higgs doublet Φ_2 is introduced. The doublet Φ_1 (with hypercharge $+1$) is used to give rise to the down-type fermion masses, and Φ_2 (with hypercharge -1) gives mass to the up-type fermion masses. The resulting model is consistent and represents the most minimalistic version of a realistic SUSY theory.

Since both Higgs doublets are coupled to the gauge bosons, the following results are obtained for the boson masses:

$$m_{\mathrm{W}^\pm} = \frac{1}{2} g \sqrt{v_1^2 + v_2^2} \tag{2.31}$$

$$m_{\mathrm{Z}} = \frac{1}{2} \sqrt{(g^2 + g'^2)(v_1^2 + v_2^2)}, \tag{2.32}$$

where v_1 and v_2 are the v.e.v. of the two Higgs doublets. In order to retain the mass predictions from the SM case (2.23), the relation

$$v^2 = v_1^2 + v_2^2$$

must hold. One d.o.f. is removed and the remaining d.o.f. can be described with the parameter

$$\tan\beta = \frac{v_2}{v_1}.$$

The most general Lagrangian $\mathcal{L}_{\mathrm{MSSM}} = \mathcal{L}_{\mathrm{SUSY}} + \mathcal{L}_{\mathrm{soft}}$ that can be constructed using these assumptions has 104 free parameters. Its full form is given e.g. in [42]. In the context of this thesis, the specific minimal model is constructed following the further assumptions

- *R-parity conservation*
  The SUSY Lagrangian $\mathcal{L}_{\mathrm{MSSM}}$ only contains terms respecting the quantum number

  $$R = (-1)^{3(B-L)+s},$$

  which is 1 for SM particles and -1 for the superpartners. B is the baryon number, L the lepton number and s the spin. As a consequence, SUSY particles can only be produced in pairs, and the lightest SUSY particle is stable, since it can not decay into SM particles. This provides the candidate for the cosmic cold dark matter [43].

- *No mixing between generations*
  It is assumed that the mass eigenstates of the squarks and sleptons are formed of same-flavour sparticles only. That means, no CKM-like mixing matrix involving different flavours is introduced.

- *Suppressed mixing in the first two generations*
  The squark and slepton mass eigenstates of the third generation are mixtures of the left- and righthanded sparticles, while this mixing is neglected for the first and second generation. This assumption is justified since the off-diagonal terms in the mixing matrix (2.36) are proportional to the fermion masses, which almost vanish for the first two generations.

In the SUSY studies presented in this thesis, which are not dedicated to Higgs searches at LEP, it will be further assumed that no additional CP-violation exists in $\mathcal{L}_{\text{MSSM}}$. That means that the possible complex phases of μ, $m_{\tilde{g}}$ and $A_{t,b,\tau}$ are set to 0. Using these assumptions, the number of free parameters of $\mathcal{L}_{\text{MSSM}}$ can be reduced from 104 to 24. The remaining parameters are listed and described in Tab. 2.4.

Sparticle properties

From the parameters in Tab. 2.4 the following properties of the sparticles can be deduced on tree-level.

Sleptons The slepton masses are given by their mass matrix, which for the third generation reads:

$$M^2_{\tilde{\nu}} = M^2_{\tau_L} + \frac{1}{2} m_Z^2 \cos 2\beta \tag{2.33}$$

$$M^2_{\tilde{\tau}} = \begin{pmatrix} M^2_{\tau_L} + m_\tau^2 - m_Z^2(\frac{1}{2} - s_W^2)\cos 2\beta & m_\tau(A_\tau - \mu \tan\beta) \\ m_\tau(A_\tau - \mu \tan\beta) & M^2_{\tau_R} + m_\tau^2 - m_Z^2 s_W^2 \cos 2\beta \end{pmatrix} \tag{2.34}$$

with $s_W^2 = \sin^2\theta_W$. The mixing terms $A_\tau - \mu \tan\beta$ are generally only taken into account for the third generation. For the other generations the expressions are equivalent, the only difference being that the off-diagonal elements in the mass matrix are neglected. The diagonalisation of this mass matrix gives the slepton masses.

Squarks Also in the squark sector the squark masses are determined by their mixing matrix, which for the third generation is

$$M^2_{\tilde{t}} = \begin{pmatrix} M^2_{\mathrm{t}_L} + m_t^2 + m_Z^2(\frac{1}{2} - \frac{2}{3}s_W^2)\cos 2\beta & m_t(A_t - \mu \cot\beta) \\ m_t(A_t - \mu \cot\beta) & M^2_{\mathrm{t}_R} + m_t^2 + m_Z^2 \frac{2}{3} s_W^2 \cos 2\beta \end{pmatrix} \tag{2.35}$$

$$M^2_{\tilde{b}} = \begin{pmatrix} M^2_{\mathrm{t}_L} + m_b^2 - m_Z^2(\frac{1}{2} - \frac{1}{3}s_W^2)\cos 2\beta & m_b(A_b - \mu \tan\beta) \\ m_b(A_b - \mu \tan\beta) & M^2_{\mathrm{b}_R} + m_b^2 - m_Z^2 \frac{1}{3} s_W^2 \cos 2\beta \end{pmatrix} \tag{2.36}$$

Again, for the other generations the expressions are equivalent, the only difference being that the off-diagonal elements for all first and second generation quark flavours q are neglected due to the small masses of the SM quarks of these generations. The squark mass parameters can be deduced on tree level from the inverted diagonalised mass matrix.

Charginos The Winos $\tilde{W}^\pm$ and charged Higgsinos $\tilde{H}^\pm$ can mix. Their mass eigenstates are called charginos. The chargino mass matrix is

$$\begin{pmatrix} \chi_1^+ \\ \chi_2^+ \end{pmatrix} = \begin{pmatrix} M_2 & \sqrt{2} m_W \sin\beta \\ \sqrt{2} m_W \cos\beta & \mu \end{pmatrix} \begin{pmatrix} \tilde{W}^+ \\ \tilde{H}^+ \end{pmatrix}. \tag{2.37}$$

Table 2.4: *The MSSM parameters. The parameters listed in this table represent the full set of MSSM parameters for the models studied here. Generally, there are 104 free additional parameters in MSSM models.*

Parameter	Description
$\tan\beta$	Ratio of Higgs vacuum expectation values
M_1	$U(1)_Y$ gaugino (Bino) mass parameter
M_2	$SU(2)_L$ gaugino (Wino) mass parameter
M_3	$SU(3)_C$ gaugino (gluino) mass parameter
A_t	Top trilinear coupling
A_b	Bottom trilinear coupling
A_τ	Tau trilinear coupling
μ	μ parameter, controls Higgsino mixing
m_A	Pseudoscalar Higgs mass
M_{e_L}	Left 1st. gen. scalar lepton mass parameter
M_{μ_L}	Left 2nd. gen. scalar lepton mass parameter
M_{τ_L}	Left 3rd. gen. scalar lepton mass parameter
M_{e_R}	Right scalar electron mass parameter
M_{μ_R}	Right scalar muon mass parameter
M_{τ_R}	Right scalar tau mass parameter
M_{u_L}	Left 1st. gen. scalar quark mass parameter
M_{c_L}	Left 2nd. gen. scalar quark mass parameter
M_{t_L}	Left 3rd. gen. scalar quark mass parameter
M_{u_R}	Right scalar up mass parameter
M_{c_R}	Right scalar charm mass parameter
M_{t_R}	Right scalar top mass parameter
M_{d_R}	Right scalar down mass parameter
M_{s_R}	Right scalar strange mass parameter
M_{b_R}	Right scalar bottom mass parameter

By convention, $m_{\chi_1^+} \leq m_{\chi_2^+}$ is chosen. The mixing matrix elements U_{ij} and V_{ij} determine the chargino couplings.

Neutralinos The neutralinos are the mass eigenstates of $(\tilde{B}, \tilde{W}^3, \tilde{H}_1^0, \tilde{H}_2^0)$, which mix and form mass eigenstates according to their mass matrix (in the basis given above):

$$Y = \begin{pmatrix} M_1 & 0 & -m_Z c_\beta s_W & m_Z s_\beta s_W \\ 0 & M_2 & m_Z c_\beta c_W & -m_Z s_\beta c_W \\ -m_Z c_\beta s_W & m_Z c_\beta c_W & 0 & -\mu \\ m_Z s_\beta s_W & -m_Z s_\beta c_W & -\mu & \end{pmatrix} \tag{2.40}$$

In the limit of heavy masses $m_{\chi_i^0} \gg m_Z$ the following mass eigenstates

$$\chi_i^0 = \left[\tilde{B},\, \tilde{W}_3,\, \sqrt{\frac{1}{2}}(\tilde{H}_1 - \tilde{H}_2),\, \sqrt{\frac{1}{2}}(\tilde{H}_1 + \tilde{H}_2)\right] \tag{2.41}$$

with masses $|M_1|$, $|M_2|$, $|\mu|$, and $|\mu|$ are obtained. Neutralinos are Majorana particles, i.e. they form their own antiparticles. Their mass eigenstates own a phase $\eta_i m_{\chi_i^0}$ with $\eta_i = \pm 1$, which gives the CP-eigenvalue of the particle.

Gluino On tree level, the gluino mass is given by

$$m_{\tilde{g}} = M_3. \tag{2.42}$$

In scenarios inspired by supergravity or gauge mediated SUSY breaking, it usually is much heavier than the lightest charginos and neutralinos.

After this overview of the sparticle properties, the Higgs sector will be studied in more detail in the following sections.

2.3.3 The Higgs Sector in the MSSM

As discussed in the previous section, the MSSM contains two doublet Higgs fields

$$H_1 = (H_1^+, H_1^0), \qquad H_2 = (H_2^0, H_2^-)$$

where H_1 has $Y = +1$ and H_2 has $Y = -1$. The vacuum expectation values are chosen to be $(0, v_1)$ and $(v_2, 0)$, respectively. In this section, the requirements and properties of the neutral MSSM Higgs bosons in a CP-conserving scenario will be introduced, followed by a discussion of the loop induced corrections. Including the soft-supersymmetry-breaking terms, the MSSM Higgs potential of the two Higgs doublets H_1 and H_2 reads

$$\begin{aligned} V_{\text{Higgs}} \;=\; & m_{1H}^2 |H_1|^2 + m_{2H}^2 |H_2|^2 - m_{12}^2 (\epsilon_{ij} H_1^i H_2^j + h.c.) \\ & + \frac{1}{8}(g^2 + g'^2)\left(|H_1|^2 - |H_2|^2\right)^2 + \frac{1}{2} g^2 |H_1^* H_2|^2 \end{aligned} \tag{2.43}$$

where $m_{iH}^2 \equiv |\mu|^2 + m_i^2 \quad (i = 1, 2)$. The parameters m_i^2 $(i = 1, 2)$ are real and can be either positive or negative. The only place where a phase could show up is the term proportional to $H_1^i H_2^j$, where any CP-violating phase of m_{12}^2 can be absorbed in a redefinition of the phases of H_1 and H_2. Thus the MSSM Higgs potential is invariant under CP transformations on tree-level. The parameters m_{1H}^2, m_{2H}^2 and m_{12}^2 can be expressed in terms of the known parameters

of $\mathcal{L}_{\text{MSSM}}$, as explained below. The Higgs potential V_{Higgs} contains both soft-SUSY-breaking terms, namely the three mass terms, and SUSY-conserving terms, namely the last two terms.

The three parameters m_{1H}^2, m_{2H}^2 and m_{12}^2 of the Higgs potential can be re-expressed in terms of the two Higgs vacuum expectation values, v_i and one physical Higgs mass. The parameter m_{12}^2 is fixed by the mass of the CP-odd Higgs boson

$$m_A^2 = \frac{m_{12}^2}{\sin\beta\cos\beta}. \tag{2.44}$$

The parameters m_{1H}^2 and m_{2H}^2 can then be determined from the requirement that spontaneous symmetry breaking of $\text{SU}(2)_L\times\text{U}(1)_Y$ to $\text{U}(1)_{EM}$ exists, which yields

$$m_{1H}^2 = \frac{m_A \tan\beta}{\sqrt{\sin\beta\cos\beta}\mu} - \frac{{m_\text{Z}}^2}{2}\cos 2\beta \tag{2.45}$$

$$m_{2H}^2 = \frac{m_A}{\sqrt{\sin\beta\cos\beta}\tan\beta\mu} + \frac{{m_\text{Z}}^2}{2}\cos 2\beta \tag{2.46}$$

Using these relations, there are only two free parameters, which are chosen to be m_A and $\tan\beta$.

Note that supersymmetry directly creates spontaneous symmetry breaking, i.e. $\mu^2 < 0$. It is generated automatically by the renormalisation group equation (RGE) running of μ, provided that the top quark mass is large. In gravity mediated models the above relations do not even have to be required, instead they are fulfilled automatically at the electroweak scale by radiative symmetry breaking [44]. In this sense SUSY is able to explain the symmetry breaking, which is added 'by hand' to the SM. On the other hand this advantage of SUSY might not be too impressive, given the fact that no known explanation for SUSY breaking exists.

The mass eigenstates of the Higgs fields are obtained as follows. Starting with eight real scalar degrees of freedom, there are three Goldstone modes absorbed by the $W^\pm$ and Z. The remaining five degrees of freedom yield the physical Higgs bosons of the model. First, there is one neutral CP-odd scalar called A. Its mass m_A is one of the free parameters of the model. The two CP-even Higgs boson degrees of freedom do mix. Their mass eigenstates h, H are obtained. Their mass matrix

$$\mathcal{M}^2 = \begin{pmatrix} {m_\text{A}}^2\sin^2\beta + m_Z^2\cos^2\beta & -({m_\text{A}}^2 + m_Z^2)\sin\beta\cos\beta \\ -({m_\text{A}}^2 + m_Z^2)\sin\beta\cos\beta & {m_\text{A}}^2\cos^2\beta + m_Z^2\sin^2\beta \end{pmatrix} \tag{2.47}$$

is diagonalised by a rotation matrix with the angle α

$$\cos 2\alpha = -\cos 2\beta\left(\frac{{m_\text{A}}^2 - {m_\text{Z}}^2}{{m_\text{H}}^2 - {m_\text{h}}^2}\right), \tag{2.48}$$

which together with $\tan\beta$ determines the Higgs boson couplings, as will be discussed later. The mixing matrix of the Higgs mass eigenstates in the basis of the weak eigenstates a (CP-odd) and h_1, h_2 (CP-even) then reads

$$\begin{pmatrix} \text{A} \\ \text{h} \\ \text{H} \end{pmatrix} = \begin{pmatrix} 1 & 0 & 0 \\ 0 & \cos\alpha & -\sin\alpha \\ 0 & \sin\alpha & \cos\alpha \end{pmatrix} \begin{pmatrix} a \\ h_1 \\ h_2 \end{pmatrix}. \tag{2.49}$$

The following masses are obtained on tree-level:

$$m_{\text{H, h}}^2 = \frac{1}{2}\left({m_\text{A}}^2 + m_Z^2 \pm \sqrt{({m_\text{A}}^2 + m_Z^2)^2 - 4m_Z^2{m_\text{A}}^2\cos^2 2\beta}\right) \tag{2.50}$$

with $m_{\mathrm{h}} < m_{\mathrm{H}}$ by definition. Finally two charged degrees of freedom are found, which carry the mass

$$m_{H^{\pm}}^2 = m_W^2 + m_A^2 \,. \tag{2.51}$$

Using (2.50) and (2.51), the following bounds on the Higgs masses are found on tree level:

$$\begin{aligned} m_{\mathrm{h}} &\leq m_{\mathrm{A}} \,, \\ m_{\mathrm{h}} &\leq m|\cos 2\beta| \leq m_{\mathrm{Z}} \,, \qquad \text{with } m \equiv \min(m_{\mathrm{Z}}, m_{\mathrm{A}}) \\ m_{\mathrm{H}} &\geq m_Z \\ m_{\mathrm{H}^{\pm}} &\geq m_W \end{aligned} \tag{2.52}$$

As one can see, the limit on m_{h} is very tight. For most parameter choices of the MSSM, it is accessible by searches at LEP (see Sections 5 and 6). Hence the MSSM would be almost completely ruled out. It is saved by the large radiative corrections to the lightest CP-even Higgs mass [45, 46, 47]. The upper bound on m_{h} in the presence of loop-effects can be parametrised as follows [21]:

$${m_{\mathrm{h}}}^2 \leq {m_{\mathrm{Z}}}^2 \cos^2 2\beta + \delta M_t^2 + \delta M_X^2 . \tag{2.53}$$

The most important correction δM_t^2 stems from top quark loops (due to its high mass and hence very strong coupling to the Higgs boson)

$$\delta M_t^2 = \frac{3G_F}{\sqrt{2}\pi^2} m_{\mathrm{top}}^4 \log \frac{m_{\tilde{\mathrm{t}}_1} m_{\tilde{\mathrm{t}}_2}}{m_{\mathrm{top}}^2}, \tag{2.54}$$

showing that the top quark mass has a very strong effect on the upper bound of the Higgs boson mass. The second contribution δM_X^2 originates from loops involving the scalar tops $\tilde{t}_1$ and $\tilde{t}_2$ and introduces a strong dependence on the squark mixing parameter $X_t = A_t - \mu \cot \beta$. It reads

$$\delta M_X^2 = \frac{3G_F}{2\sqrt{2}\pi^2} X_t \left[2g_1(m_{\tilde{\mathrm{t}}_2}^2, m_{\tilde{\mathrm{t}}_2}^2) + X_t g_2(m_{\tilde{\mathrm{t}}_2}^2, m_{\tilde{\mathrm{t}}_2}^2) \right], \tag{2.55}$$

where the functions

$$g_1(a,b) = \frac{1}{a-b} \log \frac{a}{b} \qquad \text{and} \qquad g_2(a,b) = \frac{1}{(a-b)^2} \left[2 - \frac{a+b}{a-b} \log \frac{a}{b} \right]$$

are used. Including all known corrections, there still is an upper bound on the lightest Higgs mass, which is around 135 GeV [48, 46, 47].

Since the sparticles $\tilde{t}_1$ and $\tilde{t}_2$ are involved in important loop corrections, the Higgs sector can not be described only by $\tan\beta$ and m_{A}, as on tree level. The most important parameters entering on loop-level are

- M_{SUSY}: the common SUSY breaking scale, to which all squark and slepton mass parameters $M_{\tilde{Q}}$ are set.
- μ: the Higgsino mixing parameter.
- M_2: the $SU(2)_L$ gaugino (Wino) mass parameter. The parameter M_1 is then calculated using the GUT-inspired relation $M_1 = 5/3 \tan^2 \theta_W M_2$, which depends on the unification of the gaugino masses M_1, M_2 and M_3 at the GUT scale.
- $m_{\tilde{g}}$: the gluino mass.

Table 2.5: *Couplings of the neutral MSSM Higgs bosons. Given are the correction factors with respect to the SM couplings of the SM Higgs boson [21].*

Fermion	Higgs boson		
	h	A	H
down-type	$-\frac{\sin\alpha}{\cos\beta}$	$\tan\beta$	$\frac{\cos\alpha}{\cos\beta}$
up-type	$\frac{\cos\alpha}{\sin\beta}$	$\cot\beta$	$\frac{\sin\alpha}{\sin\beta}$
Gauge boson	Higgs boson		
	h	A	H
Z,W	$\sin(\beta-\alpha)$	0	$\cos(\beta-\alpha)$

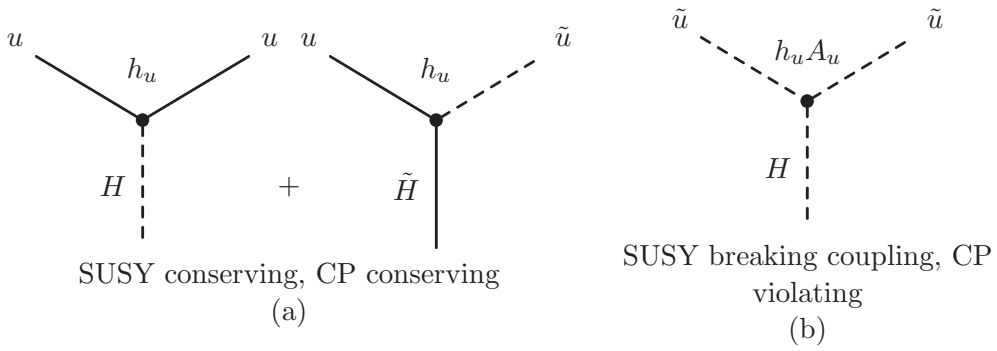

Figure 2.12: *Trilinear couplings in the MSSM. The first two graphs together conserve SUSY and CP symmetries. The third graph represents the trilinear coupling. This coupling violates SUSY symmetry and complex phases of the coupling constant A can be used to introduce CP violation.*

- $X_t = A_t - \mu \cot\beta$: the stop mixing parameter. In most models, $A_b = A_t$ is used.

The SUSY parameter of the first two generations also influence the Higgs sector on a much smaller level than the third generation parameters. Therefore, if just the Higgs sector and its phenomenology shall be described, it is fair to use a unified set of parameters for all generations.

The couplings of the neutral MSSM Higgs bosons to the SM fermions and bosons are given in Tab. 2.5. They depend on $\tan\beta$, since this determines the relative contribution to the mass generation of the two doublets, and on α, which determines the mixing of the two neutral CP-even d.o.f. of the two doublets into the mass eigenstates. The consequences of these couplings on Higgs boson production and decay are presented in Section 3.

2.3.4 CP violation in the MSSM Higgs Sector

In the MSSM, the Higgs potential is invariant under CP transformations at tree level. This manifests itself for example in (2.49), where only the CP-even weak Higgs eigenstates mix among each other, and the CP-odd weak eigenstate is preserved as a mass eigenstate. However, in the MSSM it is possible to explicitly or spontaneously break CP symmetry by radiative

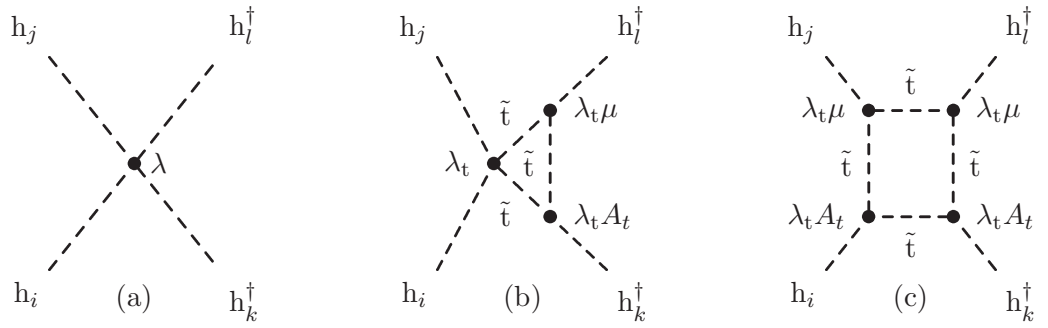

Figure 2.13: *Introduction of CPV effects into the Higgs potential. The non-zero minimum of the Higgs potential is formed by the quartic coupling graph. It is subject to loop corrections from stop loops, which radiatively introduce CP violation into the Higgs potential.*

corrections [49, 50]. This is interesting because the SM fails to provide enough CP-violation to explain the cosmological matter-antimatter asymmetry. CP-violating effects in SUSY can help to reduce this crisis [28]. The CP-breaking manifests itself in complex phases of the parameters of $\mathcal{L}_{\text{MSSM}}$. In particular, the phases of $A_{\text{t,b}}$ and $m_{\tilde{\text{g}}}$ are important for the introduction of CP-violation into the Higgs potential via loop effects. In general there is CP-violation in the Higgs potential on one-loop-level, as soon as the relation

$$\text{Im}(m_{12}^2 \mu A_{t,b}) \neq 0 \tag{2.56}$$

holds. The phases of m_{12}^2 and μ can be absorbed by redefinition of the fields. Hence the phase of $A_{t,b}$ is the only parameter left to introduce the CP-violation. On two-loop-level the phase of $m_{\tilde{\text{g}}}$ enters as an additional parameter, which can provide CP-violation.

The CP-violation in the Higgs thus can be parametrised using the trilinear couplings $A_{t,b}$. The CP-conserving (CPC) and CP-violating (CPV) couplings of the Higgs bosons to sfermions involving this coupling are shown in Fig. 2.12. As opposed to the CPC and SUSY-conserving coupling between a Higgs boson and two fermions and the coupling of a Higgsino, a sfermion and a fermion in (a), it is the coupling of a Higgs boson to two sfermions in (b) which contributes to the soft SUSY breaking Lagrangian and breaks CP invariance.

These trilinear couplings contribute to the loop corrections to the Higgs potential. The CPV one-loop contributions to the Higgs potential are shown in Fig. 2.13. In (a), the tree-level quartic coupling of the Higgs potential between the weak Higgs eigenstates h_i is shown. In (b) and (c), the loop-effects introducing the trilinear couplings $A_{t,b}$ are shown. As a consequence, CP-violation is introduced in the Higgs potential.

If CP is broken in the Higgs sector, then the Higgs boson mass eigenstates do not anymore correspond to CP eigenstates, as in (2.49). As a consequence, the Higgs boson mass matrix is more complex than in (2.49). The weak eigenstates a, h_1, h_2 are connected with the general Higgs mass eigenstates H_1, H_2 and H_3 via the general orthogonal matrix O_{ij}

$$\begin{pmatrix} \text{H}_1 \\ \text{H}_2 \\ \text{H}_3 \end{pmatrix} = O_{i,j} \begin{pmatrix} a \\ h_1 \\ h_2 \end{pmatrix} \tag{2.57}$$

The size of the CPV off-diagonal elements of the Higgs boson mass matrix which mix the CP-odd and the CP-even components, O_{1j}^2 with $j = 2, 3$, and hence the size of CPV effects, scale qualitatively [51] as

$$O_{1j}^2 (j \neq 1) \propto \frac{m_{\text{top}}^4}{v^2} \frac{\text{Im}(\mu A_t)}{32\pi^2 M_{\text{SUSY}}^2}. \tag{2.58}$$

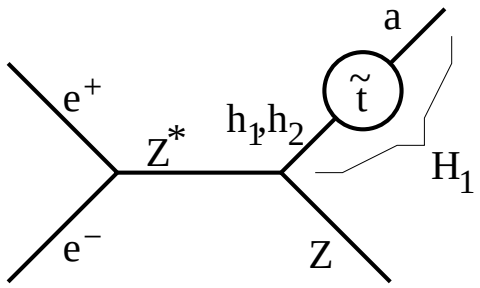

Figure 2.14: *The mixing of weak Higgs boson eigenstates in CPV models. Also in CPV models, only the CP even weak Higgs states h_1 and h_2 couple to the* Z *boson. However, the Higgs mass eigenstate also carries a CP-odd component a that does not couple to the* Z*, reducing the total coupling of the mass state* H_1*.*

Large CPV effects, and thus models dissimilar from the CPC case, are therefore obtained if the SUSY breaking scale m_{SUSY} is small and the imaginary contribution to μA_t large. Also large values of m_{top} increase the CPV effects.

When choosing the parameters, experimental constraints [52] from electric dipole moment (EDM) measurements of the neutron and the electron have to be fulfilled. However, cancellations among different contributions to the EDM may emerge [50]; hence those measurements provide no universal exclusion in the MSSM parameter space, while direct searches at LEP provide a good testing ground for a CPV MSSM. Additionally the EDM sector depends on the choice of the parameters M_1 and M_2, to which the Higgs sector is largely insensitive.

The couplings of the Higgs mass eigenstates to the SM fermions and bosons are obtained from the orthogonal matrix O_{ij} from (2.57). The couplings of the Higgs mass eigenstates to the SM bosons are given by

$$g_{\mathrm{H}_i\mathrm{ZZ}} = \cos\beta\, O_{2i} + \sin\beta\, O_{3i} \tag{2.59}$$

$$g_{\mathrm{H}_i\mathrm{H}_j\mathrm{Z}} = O_{1i}\left(\cos\beta\, O_{3j} - \sin\beta\, O_{2j}\right) - O_{1j}\left(\cos\beta\, O_{3i} - \sin\beta\, O_{2i}\right) \tag{2.60}$$

and obey the sum rules

$$\sum_{i=1}^{3} g^2_{\mathrm{H}_i\mathrm{ZZ}} = 1 \tag{2.61}$$

$$g_{\mathrm{H}_k\mathrm{ZZ}} = \frac{1}{2}\sum_{i,j=1}^{3} \varepsilon_{ijk} g_{\mathrm{H}_i\mathrm{H}_j\mathrm{Z}}. \tag{2.62}$$

As (2.59) shows, only the CP-even weak eigenstates h_1 and h_2 (corresponding to the second and third component of O_{ij}) couple to the Z in Higgsstrahlung, as in the CPC case. Fig. 2.14 shows the coupling of a mixed mass eigenstate H_1 consisting of admixtures from the CP eigenstates h_1, h_2 and a. Since only the CP-even field components h_1 and h_2 couple to the Z boson, the individual coupling of the mass eigenstates are reduced in the CPV case with respect to a CPC case.

This can have consequences if the lightest mass eigenstate H_1 largely consists of a CP-odd admixture, as is shown in the example of Fig. 2.15. The coupling of the lightest Higgs boson in Higgsstrahlung will be strongly reduced, while the other Higgs bosons also have slightly reduced couplings with respect to the SM and can be too heavy to be detected in a collider experiment.

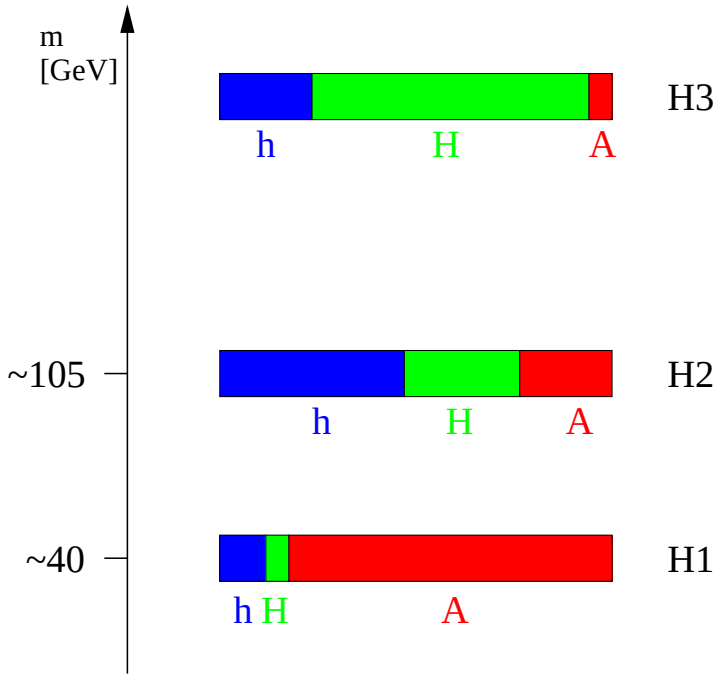

Figure 2.15: *Mass and weak eigenstates of Higgs bosons in CPV models. In this schematic model for a specific parameter set, the Higgs boson mass eigenstate* H_1 *at* $m_{H_1} = 40\,\text{GeV}$ *has a large admixture of the CP-odd weak eigenstate, and therefore has a small coupling to the* Z *boson in Higgsstrahlung.*

2.3.5 Conclusion

While the SM is the most successful theory of elementary physics ever, the idea of supersymmetry is able to solve many of the experimental and theoretical problems of the SM. It provides the cosmic cold dark matter and can contain enough CP-violation to explain the baryon asymmetry. Also it solves some theoretical problems, since electroweak symmetry breaking is explained, unification of the forces is achieved and the hierarchy problem is solved. On the other hand the mechanism of SUSY-breaking remains not directly accessible.

If SUSY is realized, this will manifest itself in an extended Higgs sector. In the MSSM, three neutral Higgs bosons are present, and one of these bosons is predicted to be lighter than 135 GeV, providing an excellent test of the MSSM at future colliders.

Other possible extensions of the SM comprise for example Technicolor, where a new strong force is introduced to give rise to boson masses and cancel the unitarity violation of the longitudinal W-scattering, compositeness, where the spectrum of SM particles is explained as bound states of even more fundamental particles, or little Higgs models, where the quadratic Higgs mass divergencies are not cancelled by particles with the opposite spin statistics but by new particles with the same spin statistics, which contribute with a negative squared coupling [53]. But none of these models contains such a large number of successful solution to SM problems as SUSY models. Since from the theoretical side the question for the extension of the SM is still open, experiments have to test extensions of the SM, which will be discussed in the remaining parts of this thesis.

Chapter 3

MSSM Higgs Production at e^+e^- Colliders

After the previous chapter illustrated general properties of the SM and the MSSM, this chapter will concentrate on specific properties of MSSM Higgs signals at e^+e^- colliders. Apart from the search for pair production of Higgs bosons decaying into $b\bar{b}$ pairs, which is the topic of this thesis (described in Section 5) and which is one of the two main Higgs production mechanisms in the MSSM, other Higgs production mechanisms and decays are studied at the experiments at LEP. In the first part the Higgs boson production mechanisms will be described, followed by a list of decays and final states under study at LEP.

3.1 MSSM Higgs Boson production

In the MSSM, there are several production mechanisms of neutral Higgs bosons. In a CP-conserving (CPC) model, the two main mechanisms are Higgsstrahlung $e^+e^- \to hZ$, as in the SM, and pair production $e^+e^- \to hA$. In a CP-violating (CPV) model, these two main channels are generalised to $e^+e^- \to H_iZ$ and $e^+e^- \to H_iH_j$ (with $i \neq j$ due to Bose symmetry).[1] The Higgs boson production channels in the MSSM have the following properties:

- *Higgsstrahlung* $e^+e^- \to H_iZ$
  This process is the dominant production channel in the SM. In the MSSM, only CP-even Higgs bosons h, H (or mass eigenstate components) can couple in these channels, since only those have a coupling to a pair of SM vector bosons (see Tab. 2.5). This production channel is displayed in Fig. 3.1 (a). Additionally to Higgsstrahlung, The processes of the weak boson fusion $e^+e^- \to W^+W^-\nu\bar{\nu} \to H_i\nu\bar{\nu}$ and $e^+e^- \to ZZe^+e^- \to H_ie^+e^-$ exist. They are displayed in (b) and (c) and at LEP energies tend to be only relevant at the kinematical limit of the Higgsstrahlung process. The Z fusion channel in (c) is additionally suppressed with respect to the W fusion channel in (b) by a factor of ≈ 10 due to the smaller coupling of the Z to the leptons and the Higgs boson. Therefore the production of a single Higgs boson will mainly depend on the Higgsstrahlung process. In the so-called decoupling regime, when m_A and m_H are much larger than m_Z (and thus m_h), the Higgs sector of the MSSM resembles the SM Higgs sector. In this case, Higgsstrahlung will be the main Higgs production process.

[1] The notation is as follows. hH (CP-even) and A (CP-odd) denote the Higgs mass- and CP-eigenstates in the CP-conserving (CPC) models. H_1, H_2 and H_3 denote the mass eigenstates (with mixed CP content) in CPV models. General Higgs eigenstates, either in CPC or CP-violating (CPV) models, are denoted by $\mathcal{H}_1, \mathcal{H}_2$ and $\mathcal{H}_3$ or generally by $\mathcal{H}$.

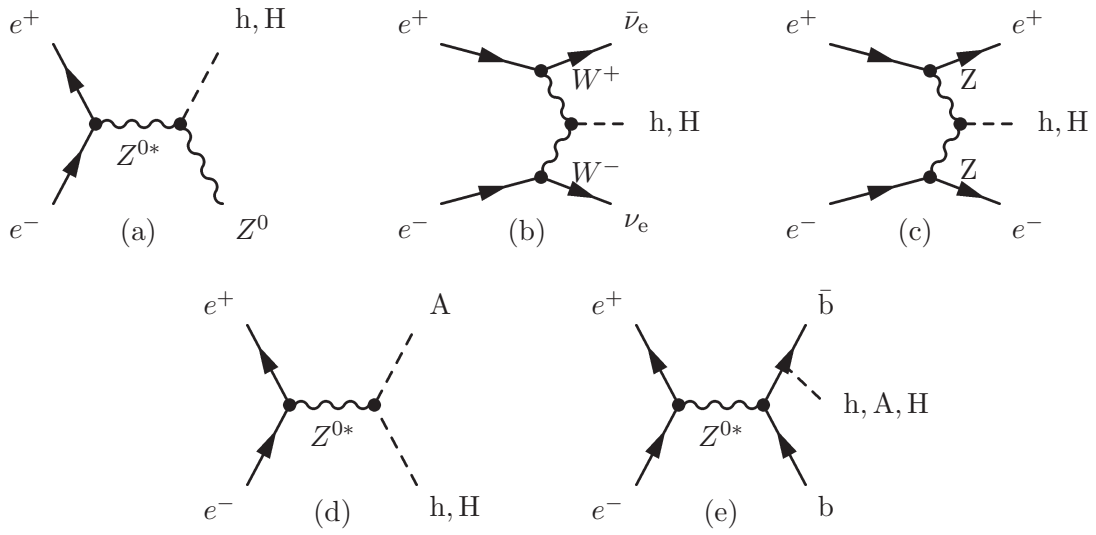

Figure 3.1: *Higgs boson production mechanisms in the MSSM at* e^+e^- *colliders. Mechanism (a) is the Higgsstrahlung process, mechanisms (b) and (c) represent the boson fusion channels. These three channels are the dominant production channels in the SM. Pair production, shown in (d), is added in the MSSM. Finally, (e) shows the Yukawa production channel, which can be dominant in some regions of the MSSM parameter space and which plays a minor role in the SM.*

- *Pair Production* $e^+e^- \to H_iH_j$
  The other main production channel in the MSSM besides Higgsstrahlung is pair production. In CPC models, its final state always contains a CP-even Higgs boson h or H and the CP-odd Higgs boson A. The production Feynman graph is shown in Fig. 3.1 (d). As is described below, its cross-section is complementary to the cross-section of the Higgsstrahlung channel. It is dominant for $\tan\beta \gtrsim 10$ and $m_A < 100$ GeV.

- *Yukawa Production* $e^+e^- \to b\bar{b} \to H_ib\bar{b}$
  For very small parts of the parameter space, typically for very large $\tan\beta$ and very small masses m_h, the Yukawa production channel can also contribute. Its Feynman graph is shown in Fig. 3.1 (e).

The direct resonant production $e^+e^- \to \mathcal{H}_i$ of Higgs bosons is strongly suppressed due to the small electron-Higgs coupling, which is proportional to the electron mass. Therefore the dominant production mechanisms are those where the Higgs bosons can couple to a heavy fermion or boson, as described above.

In the MSSM, the Higgsstrahlung and pair production processes have complementary cross-sections. Their relative rate is regulated by sum rules which are different in the CPC and CPV scenarios. In the CPC scenario, the cross-sections for the processes $e^+e^- \to hZ$, $e^+e^- \to HZ$, $e^+e^- \to hA$ and $e^+e^- \to HA$ are given by

$$e^+e^- \to hZ : \quad \sigma_{hZ} = \sin^2(\beta-\alpha)\ \sigma_{HZ}^{SM}(m_h), \tag{3.1}$$
$$e^+e^- \to HZ : \quad \sigma_{HZ} = \cos^2(\beta-\alpha)\ \sigma_{HZ}^{SM}(m_H), \tag{3.2}$$
$$e^+e^- \to hA : \quad \sigma_{hA} = \cos^2(\beta-\alpha)\ \bar{\lambda}\ \sigma_{HZ}^{SM}(m_h), \tag{3.3}$$
$$e^+e^- \to HA : \quad \sigma_{HA} = \sin^2(\beta-\alpha)\ \bar{\lambda}\ \sigma_{HZ}^{SM}(m_H), \tag{3.4}$$

where $\sigma_{\mathrm{HZ}}^{\mathrm{SM}}$ is the cross-section for the SM Higgsstrahlung process $\mathrm{e^+e^-} \to \mathrm{H_{SM}Z}$, which is at tree-level given by [21]

$$\sigma_{\mathrm{HZ}}^{\mathrm{SM}}(m) = \frac{{m_{\mathrm{Z}}}^4}{2v^4} \frac{(4\sin^2\theta_W - 1)^2 + 1}{96\pi s} \sqrt{\lambda(m, m_{\mathrm{Z}})} \frac{\lambda(m, m_{\mathrm{Z}}) + 12{m_{\mathrm{Z}}}^2/s}{(1 - {m_{\mathrm{Z}}}^2/s)^2}, \tag{3.5}$$

where $\sqrt{s}$ is the centre-of-mass energy. The symbol $\bar{\lambda}$ denotes the kinematic phase-space factor

$$\bar{\lambda} = \frac{\lambda_{\mathrm{Ah}}^{3/2}}{\lambda_{\mathrm{Zh}}^{1/2}(12M_{\mathrm{Z}}^2/s + \lambda_{\mathrm{Zh}})} \tag{3.6}$$

with

$$\lambda(m_i, m_j) = \frac{1 - (m_i + m_j)^2/s}{1 - (m_i - m_j)^2/s}.$$

All cross-sections are given without radiative corrections. At LEP energies, the most important corrections are the radiation of a photon from the initial state and the Z width. The effect of the radiative return can reduce the cross-section by more than 20 % of the total cross-section. Electroweak corrections and the width of the Higgs boson have a much smaller effect [55]. The typical cross-sections (without radiative corrections) for the two main channels of MSSM Higgs boson production in the "$m_{\mathrm{h}}-$max" MSSM model (see Section 6) at $\mathrm{e^+e^-}$ colliders are given in Fig. 3.2. In (a) and (b), the cross-section is given as a function of m_{A} for different $\tan\beta$ at $\sqrt{s} = 200$ GeV. At low $\tan\beta$, the Higgsstrahlung channel dominates and the lightest Higgs boson is accessible up to the highest masses of m_{A}. At large $\tan\beta$, the pair production channel is dominating over the Higgsstrahlung channel, as long as it is kinematically accessible. For large values of m_{A}, no Higgs boson is accessible. In (c), the same cross-sections are shown for fixed $m_{\mathrm{A}} = 80$ GeV and variable $\tan\beta$.

The highest accessible Higgs boson masses at around $m_{\mathrm{h}} = 114$ GeV yield cross-sections more than three orders of magnitude lower than the dominant background processes $\mathrm{e^+e^-} \to \mathrm{WW, ZZ, q\bar{q}}$ [56].

Due to the complementarity of the Higgsstrahlung and pair production processes, expressed in Equations (3.1) and (3.3), the searches have to include both of them in order to maintain a high sensitivity over the whole MSSM parameter space.

Similar, but more complex, sum rules regulate the relative rates in the CPV scenario. Using the couplings from (2.59) and (2.60), the cross-sections for the processes $\mathrm{e^+e^-} \to \mathrm{H}_i\mathrm{Z}$ and $\mathrm{e^+e^-} \to \mathrm{H}_i\mathrm{H}_j$ are given by [51]

$$\mathrm{e^+e^-} \to \mathrm{H}_i\mathrm{Z} \ : \qquad \sigma_{\mathrm{H}_i\mathrm{Z}} = g^2_{\mathrm{H}_i\mathrm{ZZ}}\ \sigma_{\mathrm{HZ}}^{\mathrm{SM}}(m_{\mathrm{H}_i}), \tag{3.7}$$

$$\mathrm{e^+e^-} \to \mathrm{H}_i\mathrm{H}_j \ : \qquad \sigma_{\mathrm{H}_i\mathrm{H}_j} = g^2_{\mathrm{H}_i\mathrm{H}_j\mathrm{Z}}\ \bar{\lambda}\ \sigma_{\mathrm{HZ}}^{\mathrm{SM}}(m_{\mathrm{H}_i}), \tag{3.8}$$

In Higgsstrahlung and pair production in $\mathrm{e^+e^-}$ collisions the kinematic properties of the CPC and CPV signal processes are expected to be very similar. In both CPC and CPV models, the production process in Higgsstrahlung only contains couplings between the Z boson and a CP-even Higgs state, and the pair production always involves a CP-even and a CP-odd state. The production angle distributions are therefore expected to be the same. The Higgs decay angle distributions are also the same for CPC and CPV since both the CP-odd and the CP-even states are spin 0 bosons. Small differences not measurable at LEP arise from different spin correlations in the decay products of the Higgs boson.

The situation is different for the Yukawa channel, where either the CP-even or the CP-odd Higgs boson can be produced directly, resulting in different angular distributions. Therefore in this channel also CPV Higgs bosons with mixed CP-content will have angular distributions different from purely CP-even or CP-odd Higgs bosons.

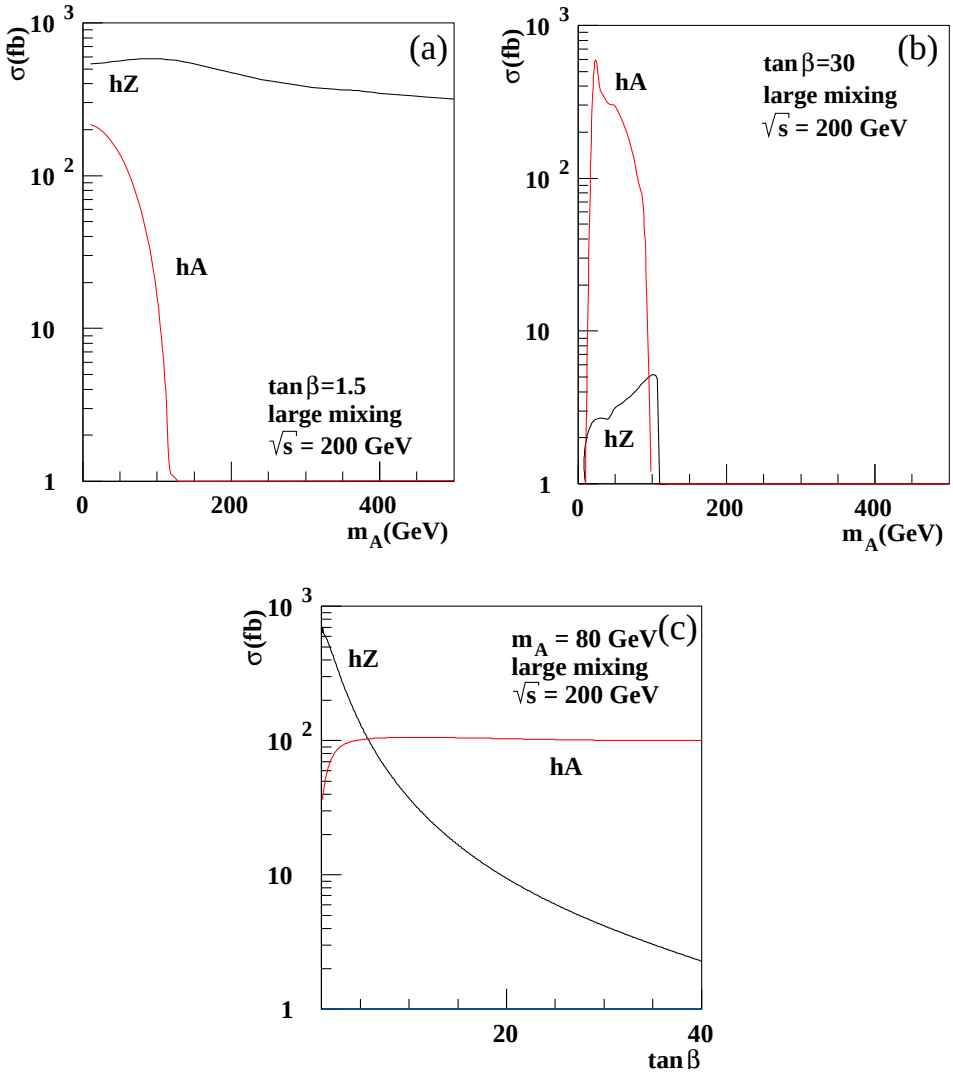

Figure 3.2: *Production cross-sections of the MSSM Higgs production processes at* e^+e^- *colliders, calculated with FEYNHIGGS(XS) [54]. In (a) and (b), the cross-section of Higgsstrahlung* hZ *and pair production* hA *as a function of* m_A *in the "*m_h*−*max*" benchmark scenario for different values of* $\tan\beta$ *are displayed. In (b), the cross-sections are shown as a function of* $\tan\beta$*. The centre-of-mass energy is* $\sqrt{s} = 200$ *GeV for all plots.*

3.2 Higgs Boson Decays

Generally Higgs bosons decay predominantly into the heaviest particles which are kinematically allowed. The decay of Higgs bosons can be classified as follows [21].

- *Higgs decay to SM fermions* $\mathcal{H} \to f\bar{f}$
  For Higgs masses below 130 GeV this usually is the dominant decay. Since the Higgs boson couples proportionally to the fermion mass $g^2_{\mathcal{H}ff} \sim m_f^2$, the decay $\mathcal{H} \to b\bar{b}$ dominates, followed by $\mathcal{H} \to \tau^+\tau^-$.

- *Higgs cascade decay* $\mathcal{H}_2 \to \mathcal{H}_1\mathcal{H}_1$
  In some regions of the parameter space the cascade decay is dominant when kinematically

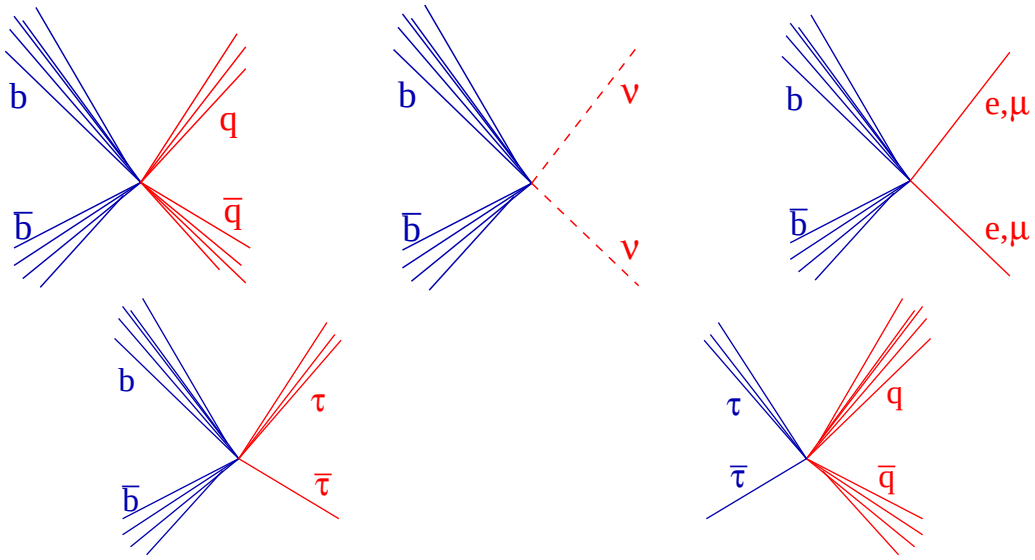

Figure 3.3: *The signatures of SM-like Production channels of Higgs bosons at* e^+e^- *colliders. The Higgs boson decay products are shown in blue (dark, left side), the* Z *decay products in red (light, right side).*

accessible, i.e. if $2m_{\mathcal{H}_1} < m_{\mathcal{H}_2}$.

- *Higgs decay into SM bosons* $\mathcal{H} \to ZZ, W^+W^-, gg$
  For $m_{\mathcal{H}} > 130$ GeV, the decay $\mathcal{H} \to WW^*$ becomes accessible and generally dominates over the other kinematically possible decays. Since $m_{\mathcal{H}} = 130$ GeV is out of the direct kinematical reach of LEP, this decay will not be discussed further. Another possibility is the decay into gluons via top loops. This decay plays a role in some MSSM models and is briefly discussed in Chapter 6.

- *Higgs decay into sparticles*
  The decays $\mathcal{H} \to \chi_i^+\chi_j^-$ or $\mathcal{H} \to \chi_i^0\chi_j^0$ are possible and can be strong due to the large mass of the sparticles. However, it is kinematically not allowed in the scenarios under study here (see Section 6), which yield $m_{\chi_i^{0,\pm}} > m_h/2$, due to the value of $M_1 = 5/3 \tan^2\theta_W M_2 \gtrsim 100$ GeV. Small values of $m_{\chi_1^{0,\pm}} < m_h/2$ are experimentally depreciated [57], however if no GUT relation among M_1 and M_2 is assumed no strict experimental lower limit on $m_{\chi_1^0}$ exists. Therefore there are also independent searches for Higgs decays into invisible particles [58].

The Higgs boson decays in the MSSM do not just depend on the Higgs boson mass, as in the SM, but on the MSSM parameter choice. For two of the MSSM benchmark sets used in Section 6, the Higgs branching ratios of the h boson are displayed in Fig. 3.4. In the upper two plots, the dominating branching ratios for the no mixing scenario at $\tan\beta = 1.5$ and $\tan\beta = 30$ are shown. In the lower plots, the same information for the m_h−max scenario is given. Typically, the decay $h \to b\bar{b}$ dominates if it is kinematically accessible, otherwise $e^+e^- \to \tau^+\tau^-$ takes over. Where kinematically allowed, the cascade decay $h \to AA$ contributes.

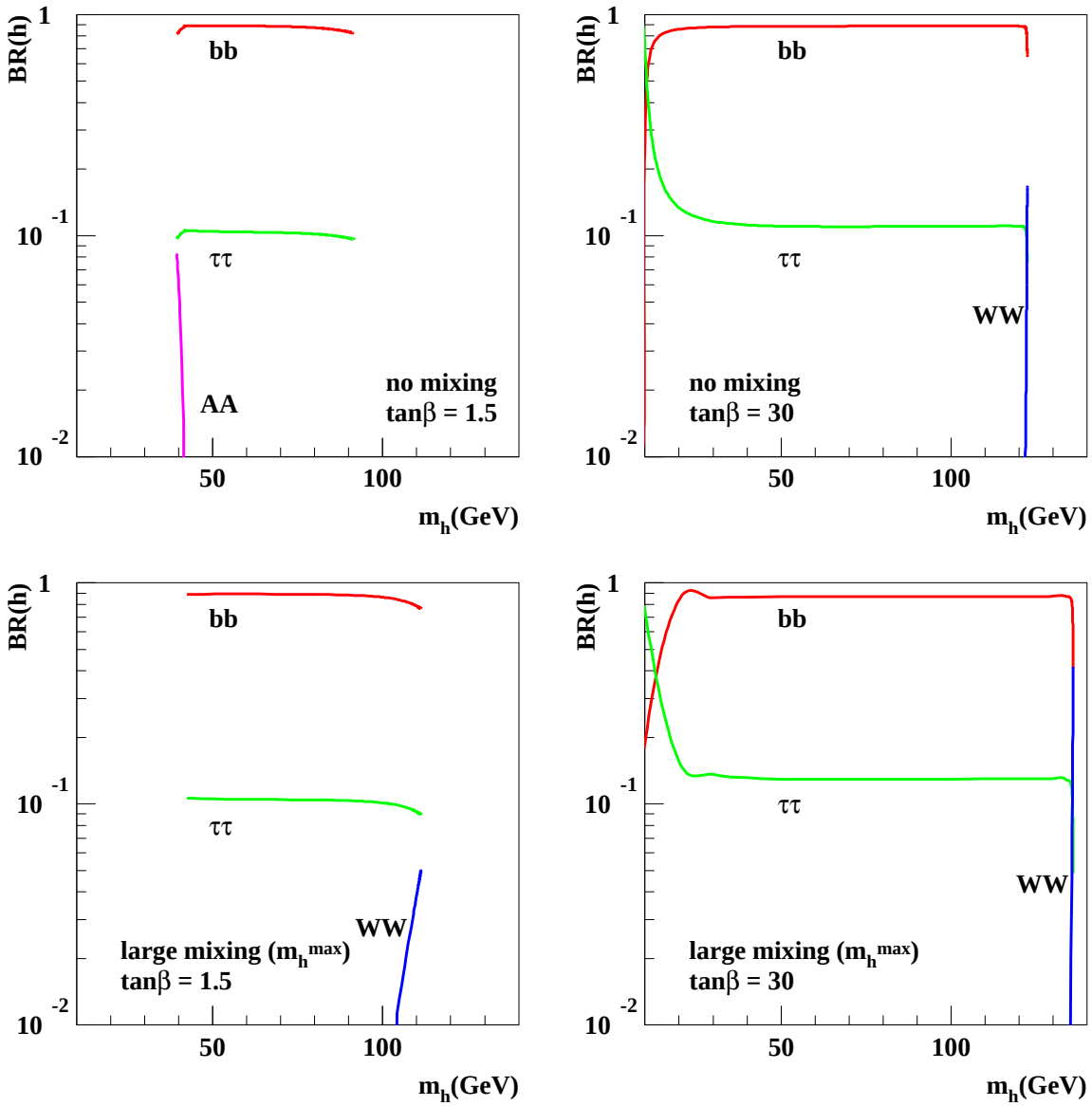

Figure 3.4: *Typical Higgs boson branching ratios for two of the MSSM scenarios described in Section 6 for different values of* $\tan\beta$. *The predictions are calculated using FEYNHIGGS(DECAY) [54].*

3.3 MSSM Higgs Boson Searches at LEP

Following the dominant patterns in production and decay of Higgs bosons, the searches at LEP are performed for the two dominant production mechanisms Higgsstrahlung and pair production and for the three dominant decays at LEP, $\mathcal{H} \to b\bar{b}, \tau^+\tau^-$ and $\mathcal{H}_2 \to \mathcal{H}_1\mathcal{H}_1 \to b\bar{b}b\bar{b}$. For Higgsstrahlung production, the Higgs signatures can further be classified according to the decay of the Z boson. This is shown in Fig. 3.3, showing the Higgsstrahlung search channels at the OPAL experiment at LEP. The name 'channel' refers to a self-contained search for an independent signature at a given centre-of-mass energy of the accelerator. The decay $\mathcal{H} \to b\bar{b}$ is studied for $Z \to q\bar{q}, \ell^+\ell^-$ (ℓ =e,μ) and $\nu\bar{\nu}$ (the latter containing also

Figure 3.5: *The signatures of pair production channels of Higgs bosons at* e^+e^- *colliders, for Higgs bosons decaying in the dominant modes* $b\bar{b}$ *and* $\tau^+\tau^-$.

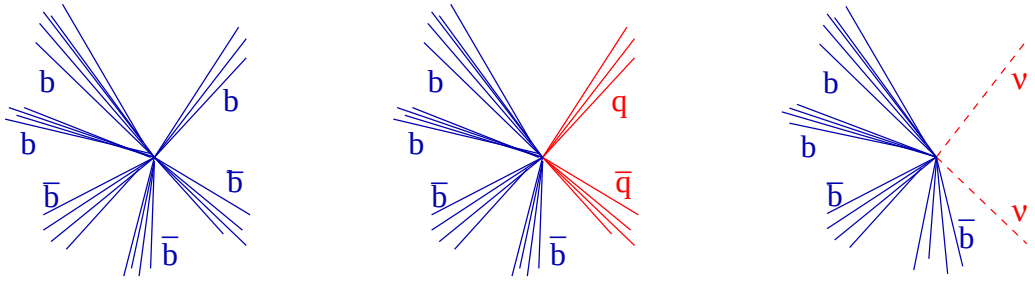

Figure 3.6: *The signatures of cascade-decay channels of Higgs bosons at* e^+e^- *colliders. In the MSSM, the decay* $\mathcal{H}_2 \to \mathcal{H}_1\mathcal{H}_1 \to b\bar{b}b\bar{b}$ *can be dominant in some regions of the parameter space.*

the contribution from boson fusion). Additionally, the decays ($\mathcal{H} \to b\bar{b}, Z \to \tau^+\tau^-$) and ($\mathcal{H} \to \tau^+\tau^-, Z \to q\bar{q}$) are combined in one channel.

For the MSSM, additionally the pair production channels in Fig. 3.5 are searched for. Only $\mathcal{H}_1\mathcal{H}_2 \to b\bar{b}b\bar{b}$ and $\mathcal{H}_1\mathcal{H}_2 \to b\bar{b}\tau^+\tau^-$ are used. The branching ratio $BR(\mathcal{H} \to \tau^+\tau^-)$ is generally below 15 % and thus too low to justify a search for $\mathcal{H}_1\mathcal{H}_2 \to \tau^+\tau^-\tau^+\tau^-$.

Finally, the branching ratio of the cascade decay $\mathcal{H}_2 \to \mathcal{H}_1\mathcal{H}_1$ can be close to 100 % where it is kinematically possible, due to the strong self-coupling of the Higgs bosons. At OPAL it is studied in the decay channels shown in Fig. 3.6. They are $e^+e^- \to \mathcal{H}_1\mathcal{H}_2 \to \mathcal{H}_1\mathcal{H}_1\mathcal{H}_1$, $e^+e^- \to \mathcal{H}_2Z \to \mathcal{H}_1\mathcal{H}_1q\bar{q}$ and $e^+e^- \to \mathcal{H}_2\nu\bar{\nu} \to \mathcal{H}_1\mathcal{H}_1\nu\bar{\nu}$.

In the context of this thesis, the signal processes $e^+e^- \to \mathcal{H}_1\mathcal{H}_2 \to b\bar{b}b\bar{b}$ and $e^+e^- \to \mathcal{H}_1\mathcal{H}_2 \to \mathcal{H}_1\mathcal{H}_1\mathcal{H}_1 \to b\bar{b}b\bar{b}b\bar{b}$ are sought. These are the most important extensions of the SM Higgs searches for the MSSM. This search is described in Section 5.

Chapter 4

Accelerators and Detectors

In this chapter the accelerators and detectors are described, on which the measurements and studies in this thesis are based. This is the accelerator LEP at CERN, probably the largest and highest energetic e^+e^- storage ring ever. One of its experiments is OPAL, on whose data the measurements presented in Chapters 5 and 6 are based. General concepts of accelerators and the LEP ring are described, followed by an introduction of the OPAL experiment. The precision experiments at LEP will probably be succeeded by a future linear collider (LC) in the 0.5 to 1 TeV range. The proposed LC project TESLA and its detector concept is described.

4.1 The LEP Accelerator

General Concepts of Accelerators

Particle Accelerators were invented in 1929 by Ernest Lawrence in Berkeley [59]. He used the concept of a Cyclotron, were particles move on variable radii in a constant magnetic field, to accelerate electrons to energies up to around 80 keV. Modern Accelerators are built either as Synchrotrons, were particles move on constant radii in variable magnetic fields, or as linear accelerators. High-energy experiments are mostly performed using colliders, were two beams of particles, organised in bunches and moving in opposite directions at high energies, do collide in an experimental setup.

Two basic quantities govern the performance of the accelerator, the centre-of-mass energy $\sqrt{s}$ and the luminosity $\mathcal{L}$. The former can either be adjusted precisely to produce a particle resonantly, or it can be set as high as possible in order to test new and previously unexplored scales and the most fundamental phenomena. The latter should be as high as possible, in order to produce as much events as possible. The luminosity is defined as

$$\mathcal{L} = \frac{1}{\sigma}\frac{\mathrm{d}N}{\mathrm{d}t}, \tag{4.1}$$

where σ is the cross-section of a given process and $\mathrm{d}N/\mathrm{d}t$ is its event rate. It can be calculated from the machine parameters

$$\mathcal{L} = \frac{N_{p_1} N_{p_2} f_b}{4\pi\sigma_x\sigma_y}.$$

Here N_{p_1} and N_{p_2} are the number of particles in the two colliding beams, f_b is the rate of bunch crossings and σ_x and σ_y are the transversal beam spot sizes at the interaction point (IP). In order to achieve high luminosity, the numbers of bunches and the number of particles per bunch should be as high as possible, while the beam spot sizes should be as small as possible. However, there are limitations to the frequency of the bunches and numbers of particles from

Table 4.1: *Machine parameters of the LEP accelerator. Luminosity, accelerating gradient and bending field are given for the data taking at* $\sqrt{s} \approx 206$ *GeV [60].*

centre-of-mass energy	$\sqrt{s}$	$91 - 209$ GeV
beam spot size	$\sigma_x \times \sigma_y$	$200\,\mu\text{m} \times 2.5\,\mu\text{m}$
collision frequency	f_b	$22\,\mu\text{s}$
No. particles per bunch	N	3×10^{11}
Luminosity	$\mathcal{L}$	10^{31} cm^{-2}s^{-1}
accelerating gradient		up to 7 MV/m

the energy consumption of the accelerator. An advantage of a circular collider is that bunches can be reused until the beam quality or charge is not sufficient anymore. On the other hand, the beam energy is limited by synchrotron radiation, and the beam spot sizes are limited by the requirement that the bunches should not be disrupted during collisions. Finally one important design parameter is the type of particles that should be accelerated. This depends on the physics goals. Highest energy can be achieved if heavy particles such are protons are used, since there the energy loss from synchrotron radiation is limited. Highest precision on the other hand is achieved if pointlike particles, such as electrons are used.

The LEP Collider

The Large Electron Positron Collider (LEP) was operated at CERN[1] from 1989 to 2000. It collided electron and positron bunches at highest energies in the experiments ALEPH, DELPHI, L3 and OPAL, as shown in Fig 4.1. The LEP ring had a circumfence of 26.7 km and was located below the French and Swiss surface near Geneva in Switzerland. The machine parameters of LEP are given in Tab. 4.1.

In the phase of LEP 1 from 1989 to 1995 the accelerator was operated at and around $\sqrt{s} = 91.2$ GeV. This is the mass of the Z boson, which is produced as a real particle in resonance. The properties of the Z, its production and decay, the gauge structure $\text{SU}(3)_C \times \text{SU}(2)_L \times \text{U}(1)_Y$ and the electroweak coupling constants were measure with high precision. At a rate of around 1 Z boson per second around 6 million Z per experiments were recorded.

In the phase of LEP 2 from 1996 to 2000 the maximum beam energy was increased by the instalation of superconduction accelerating cavities. It grew from 161 GeV to 183 GeV in 1996 and 1997. In 1998, the beam energy was 189 GeV. In 1999 and 2000, it was increased from 192 to 209 GeV. In the year 2000, it was increased up to the largest possible value during each run step-by-step. In the phase of LEP 2, the focus of the LEP measurements were the $\text{W}^\pm$ mass and couplings and the search for new particles, most notably the Higgs boson of the SM, extended Higgs models and SUSY searches. More than 10 000 W^+W^- pairs and more than 400 Z pairs per experiment were recorded.

In the year 2000 the LEP operation stopped and the accelerator and the experiments were dismantled. The LEP tunnel is now used to host the LHC, which will collide proton bunches at $\sqrt{s} = 14$ TeV starting in 2007. Two experiments, ATLAS [61] and CMS [62] will search for new phenomena at the highest energies, and most notably try to find the mechanism behind electroweak symmetry breaking.

[1] European Laboratory for Particle Physics, abbreviation from the former name Centre Européen pour la Recherche Nucléaire

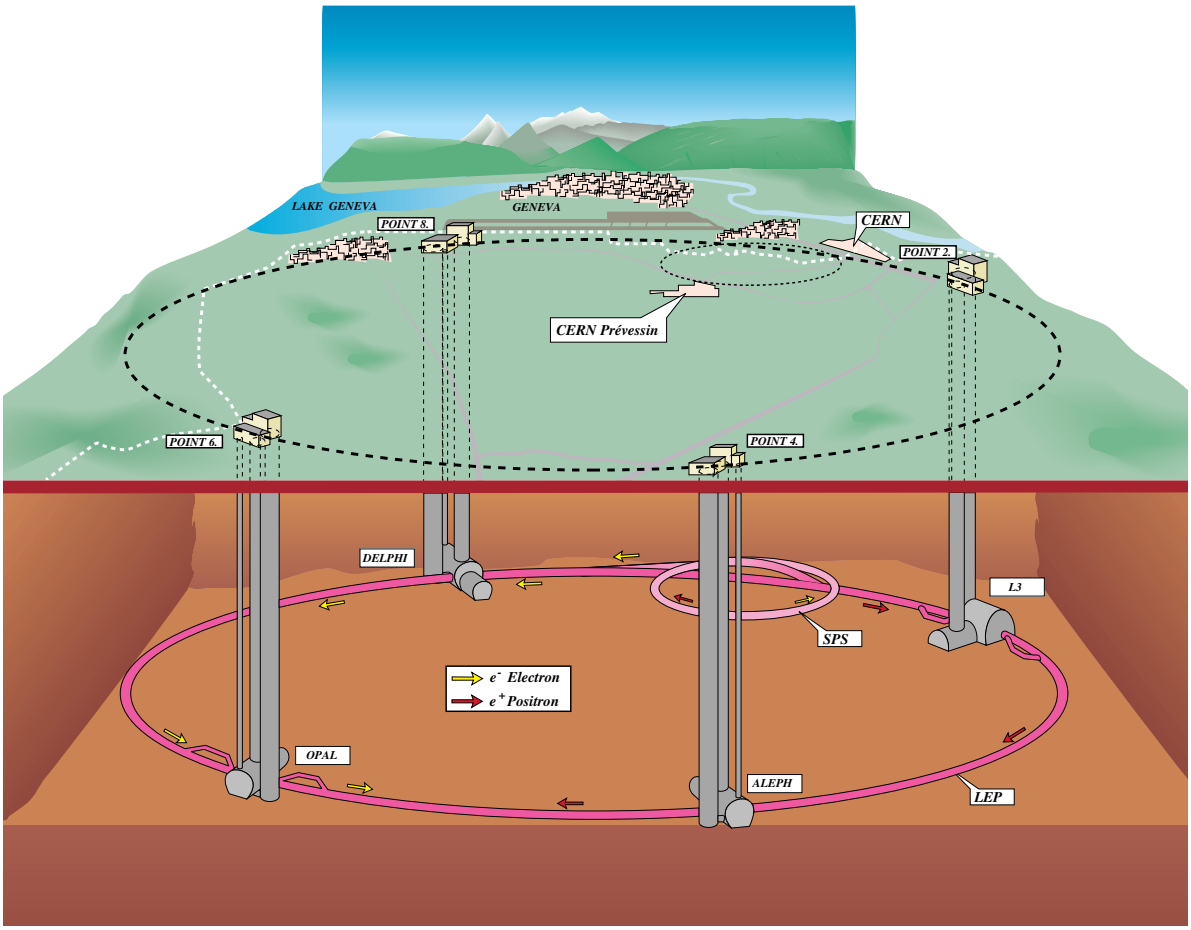

Figure 4.1: *The LEP collider at CERN. It is located 50 to 150 m below the surface near Geneva.*

Beam Parameter Measurements

The most important beam parameters for the experiments are the luminosity $\mathcal{L}$, the beam energy E_b and the bunch cross rate f_b. While the latter is clearly determined by the synchrotron circumfence and the number of bunches, the luminosity has to be measured in each experiment. Forward detectors like the silicon-tungsten luminometer in OPAL (see Section4.2) measure the rate N_B of well-known interactions like Bhabha-scattering $e^+e^- \rightarrow e^+e^-$. The Bhabha cross-section σ_B can be precisely calculated, and therefore relation (4.1) can be used to determine $\mathcal{L}$. In OPAL the luminosity is determined up to a precision of 0.15 %.

The measurement of the beam energy is performed at dedicated positions in the accelerator in front of the experiments. During the operation of LEP, two different techniques were used to measure the beam energy. At $E_b < 60$ GeV, the beams aquire a measurable transverse polarisation through the Sokolov-Ternov-mechanism [63]. It can be measured using the angular distribution of Compton-backscattered laser light. The spin precession frequency of the electrons depends on their boost, thus the resonant depolarisation using a transversely oscillating magnetic field can be deduced from the resonant frequency of the magnetic field [64]. The precision of the beam energy measurement achieved at LEP 1 is of the order of 200 keV.

At $E_b > 60$ GeV, no transverse polarisation is built up in LEP. Therefore the beam energy

is measured using dedicated bending magnets, whose magnetic field is precisely measured with NMR probes. The bending angle of the beam in the magnet is then measured using beam position monitors. The NMR beam energy measurement was cross-calibrated with the polarisation measurement at $E_b < 60$ GeV. A precision of 15 MeV on E_b was achieved [65].

Limitations of LEP

During its last year of operation the LEP beam energy was increased during each fill until the beams were lost due to a failure in the accelerating cavities due to overload. This border was at around $\sqrt{s} = 209$ GeV. It was not possible to increase the beam energy further because of the energy loss due to synchrotron radiation, which is

$$E_{\text{loss}} \sim \frac{1}{r} \left(\frac{E_b}{m} \right)^4 .$$

Since E_{loss} grows with the beam energy E_b to the fourth power, no further increase of E_b was possible. At $E_b = 100$ GeV, the lost energy is $E_{\text{loss}} = 2$ GeV, which has to be restored at each revolution of the bunches to keep the beam energy at a constant level. Therefore, around 100 MW of electrical power are needed to run LEP at highest energies.

Not only the beam energy is limited, also the beam spot size at the IP and thus the luminosity $\mathcal{L}$ is limited for circular colliders. A radical shrinking of the beam spot size would increase the luminosity, but on the other hand the beams would disrupt themselves during the collision due to inter-bunch interactions and thus could not be stored in the accelerator for a long time.

In order to increase the beam energy, the mass of the accelerated particle m can be increased. For protons, 2000 times heavier than electrons, only negligible energy is lost due to synchrotron radiation. This has the drawback that protons are no elementary particles but are composed of quarks and gluons. Therefore the primary interaction is always accompanied by strong hadronic backgrounds, and the interacting partons do not carry a defined energy close to the full beam energy. This way is chosen for the LHC. On the other hand, the radius r can be increased. Since an electron synchrotron with $\sqrt{s} = 500$ GeV using LEP technology would require a circumfence of around 1000 km to have the same radiation loss, it is more economical to use a LC than a synchrotron. This has the disadvantage that each accelerating cavity is used only once per particle, that the particles cannot be reused in subsequent collisions and that multiple experiments at the same collider have to share the luminosity which is available. On the other hand no energy is lost due to synchrotron radiation.

4.2 The OPAL Detector

The Onmi Purpose Apparatus at LEP (OPAL) was operated at LEP from 1989 to 2000. It was a complex experimental setup in the typical onion-type form. Obeying a cylindrical symmetry subdetectors were placed around the interaction point, each measuring different properties if the particles in the final state of the e^+e^- reaction. It covered 97 % of the solid angle in order to detect as much outgoing particles as possible. The only uncovered region was the incoming and outgoing beamline. The total detector was 10 m in diameter and 12 m in length. A cut-away view of the OPAL detector is presented in Fig. 4.2. Starting from the innermost layer, the subdetectors had the following purposes:

- *Impact parameter measurement*
  The innermost detector layer measured the impact parameter of the trajectories of

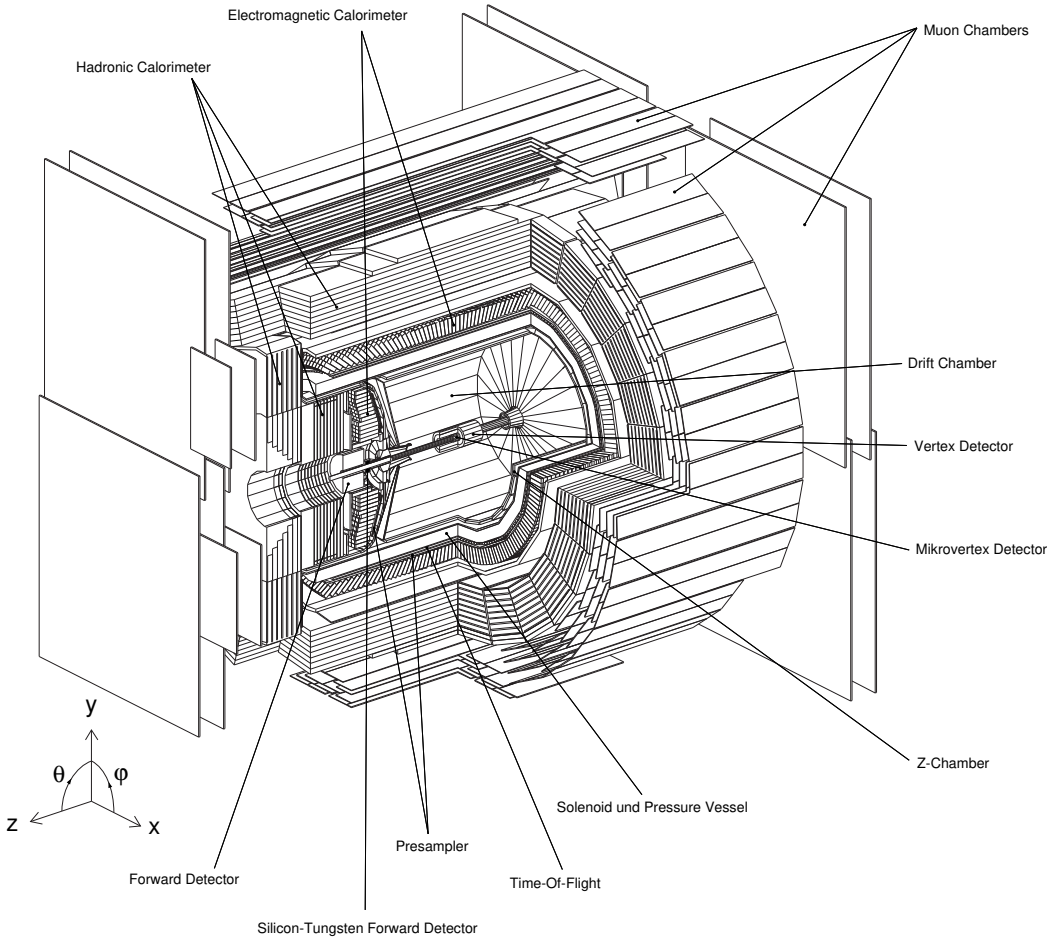

Figure 4.2: *The OPAL detector. It is a collider detector with almost complete coverage of the solid angle, located at the LEP* e^+e^- *collider at CERN. It has a diameter of 10 m and a length of 12 m.*

charged particles with respect to the nominal IP. This allows the tagging of decaying particles with lifetime.

- *Momentum measurement*
  The next detector layers measured the trajectories of charged particles in a magnetic field in order to determine the particle momentum and the particle charge.

- *Particle identification*
  The energy loss per flight length $\mathrm{d}E/\mathrm{d}x$ of a charged particle can be used, together with the momentum information, to identify the particle mass and hence the particle identity.

- *Energy measurement*
  After the information about the impact parameter, the momentum and the particle identity have been inferred in the most non-destructive way, the particles are collected in instrumented dense material, the calorimeter, to measure their energy.

- *Muon identification*
  The outermost detector layer has the purpose to detect muons, the only interacting particles which are able to cross the calorimeter.

OPAL uses a right-handed coordinate system where the $+z$ direction is along the electron beam and where $+x$ points to the centre of the LEP ring. The polar angle θ is defined with respect to the $+z$ direction and the azimuthal angle ϕ with respect to the $+x$ direction. The centre of the e^+e^- collision region defines the origin of the coordinate system.

A detailed description of the OPAL detector is given in [66]. In the following, the OPAL detector and its components will be introduced. A detailed view of the detector in the $r-\phi$ and in the $r-z$ plane is given in Fig. 4.3.

The Silicon-Microvertex detector (SI) The interaction point is surrounded by a beryllium beampipe with 53.5 mm radius and only 1.1 mm thickness. Inside the OPAL pressure tube the vertex detector [67] is located, which was installed in 1991. It consists of two layers of double-sided silicon microstrip detectors of 18.3 cm length, surrounding the beampipe at a radius of 61 and 75 mm. The inner layer covers $|\cos\theta| < 0.93$, the outer layer covers $|\cos\theta| < 0.89$. In ϕ the inner layer consists of 12 modules, while the out layer consists of 15 modules, each 33 mm wide.

On both sides the microvertex detector is covered with strips with 25 μm pitch. On the front side they are oriented in the z direction and measure a space point in $r-\phi$. Every second strip is read out and a track point resolution in $r-\phi$ of 5 μm is reached. On the backside, with strips oriented perpendicular to the z direction, only every fourth strip is read out, thus the spacial track point resolution in $r-z$ is only 12 μm.

The Silicon-Microvertex detector is most important to measure the secondary vertices produced by short-lived particles with measurable lifetime. B hadrons with a lifetime of around 10^{-12} s travel around 400 μm from the primary vertex, until they decay and form a secondary vertex. Using the Silicon-Microvertex detector, an impact parameter resolution of tracks from secondary vertices of 18 μm in the $r-\phi$ plane and 85 μm in the z direction is achieved.

The Vertex Chamber (CV) The vertex chamber is a cylindrical drift chamber of 1.1 m length, an inner radius of 8.8 cm and an outer radius of 23.5 cm. It surrounds the silicon-microvertex detector and is located inside the OPAL pressure tube in a pressure of 4 bar. A gas mixture of argon (88.2 %), methane (9.8 %) and isobutane (2.0 %) is used. It consists of two layers with 36 sectors each. In the inner layer each sector had 12 signal wires parallel to the z direction. The 6 signal wires of the outer layer are mounted at a stereo angle of 4° with respect to the z axis, allowing a determination of the tracks z coordinate of 300 μm. The resolution in the $r-\phi$ plane is 50 μm.

Before the installation of the silicon-microvertex detector, the vertex chamber was the only device to measure impact parameters. After the upgrade, it still was important to connect the tracks in the jet chamber to the hits in the silicon-microvertex detector.

The Central Jet Chamber (CJ) The most prominent part of the OPAL detector is the huge central jet chamber [68] operates with the same gas mixture as the vertex chamber. It is used to measure the trajectories of charged particles, from which the particle charge and the momentum can be determined, and the $\mathrm{d}E/\mathrm{d}x$ of the charged particle tracks. The chamber had a length of 4 m and an outer diameter of 3.7 m. It is located inside the pressure vessel and inside a solenoid coil with a magnetic field of 0.435 T. It consists of 24 identical sectors in

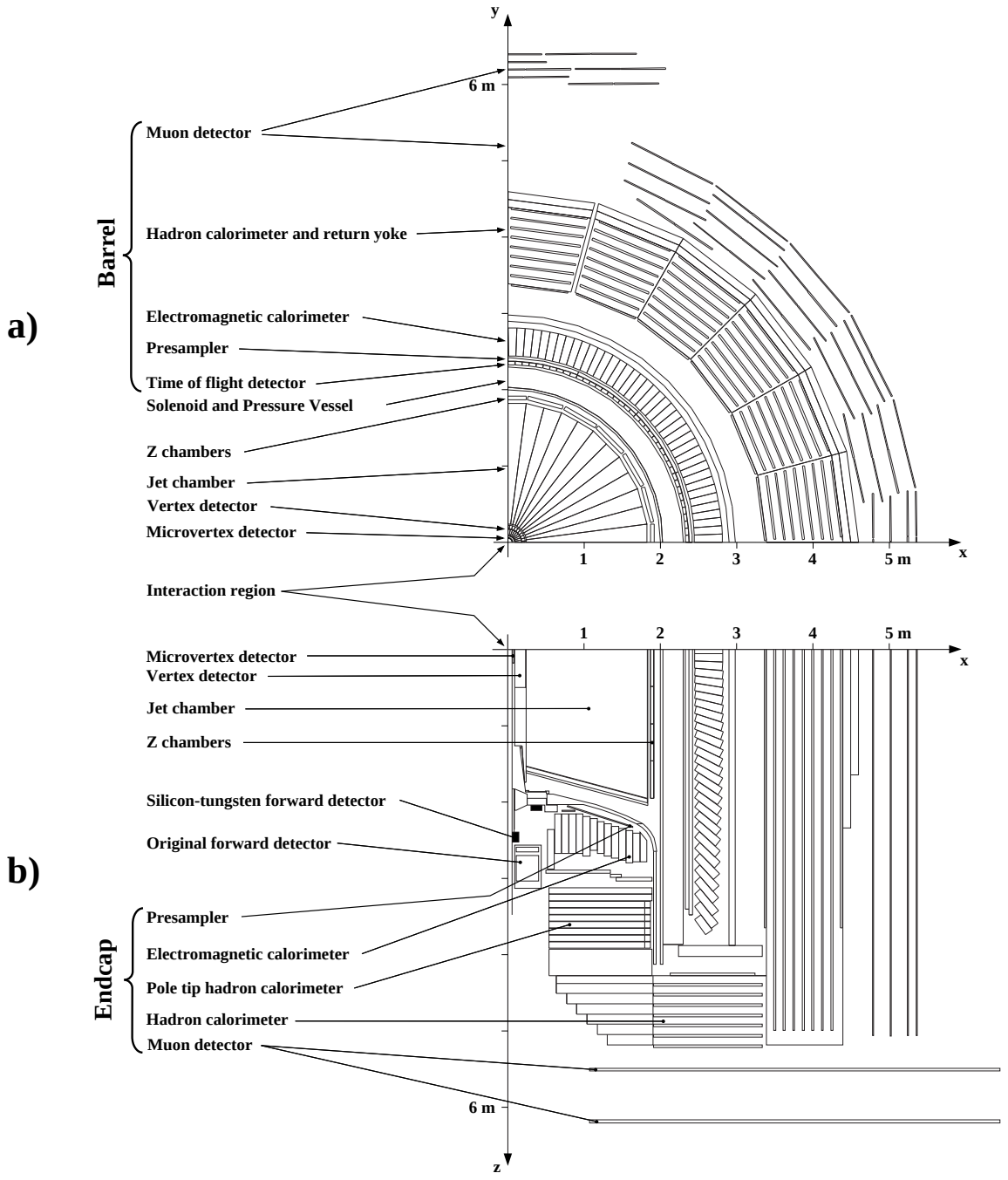

Figure 4.3: *Cut-away view of the OPAL detector. In (a), the x, y view of the detector is shown, in (b) the x, z view.*

ϕ with 159 anode wires each, separated by cathode planes. The wires are spanned along the z axis with a spacing of 1 cm. Consecutive anode wires are shifted by $\pm 100\,\mu$m in the $r-\phi$ plane to avoid ambiguities in the track reconstruction.

Charged particles leave a trajectory of ionised argon atoms and free electrons along their path. In a constant electric field of 1 kV/cm the electrons drift up to 25 cm to the anode wire plane, where the electrons are amplified with a gain of 10^4. The drift time of the electrons with respect to the nominal bunch crossing time allows the reconstruction of the trajectory in the $r-\phi$ plane, orthogonal to the wires.

The resolution for single tracks with an average drift distance of 7 cm is 130 μm in the $r-\phi$ plane. For dense jets the resolution is worse. The double track resolution in $r-\phi$ is around 2 mm. The z position of the track is determined using charge sharing at the $+z$ and $-z$ end of the wires. The resolution in z is around 6 mm for single tracks [69].

Design goals of the jet chamber are good space resolution and good double hit resolution (for optimal event reconstruction and momentum measurement) combined with very good particle identification using the $\mathrm{d}E/\mathrm{d}x$ of the tracks. These goals are achieved by placing the chamber into a pressure vessel with a pressure of 4 bar. This minimises the diffusion. A high pressure p means that the drift field E_{drift} has to be large in order to reach the same drift velocity

$$v_{\mathrm{drift}} \sim \frac{E_{\mathrm{drift}}}{p}.$$

The maximal drift velocity v_{max} is basically independent of p, i. e. the chosen value of E_{drift} is proportional to the value of p. Since the diffusion is proportional to $1/\sqrt{E_{\mathrm{drift}}}$, it decreases for large $p \sim E_{\mathrm{drift}}$. Additionally the high pressure leads to high $\mathrm{d}E/\mathrm{d}x$ and thus to good energy loss resolution.

Using the bending of the tracks in the magnetic field, the momentum of the charged particles and their charge can be measured. The momentum resolution for isolated tracks is

$$\frac{\sigma_{p_t}}{p_t} = \sqrt{0.02^2 + (0.0015 p_t)^2} \tag{4.2}$$

for the momentum p_t (in GeV) transversal to the beam axis. The specific energy loss $\mathrm{d}E/\mathrm{d}x$ is measured to a precision of

$$\frac{\sigma_{\mathrm{d}E/\mathrm{d}x}}{\mathrm{d}E/\mathrm{d}x} = 3.8\,\% \tag{4.3}$$

for tracks in the central region of $43^\circ < \theta < 137^\circ$, where all 159 signal wires can be used [70].

The z-Chamber (CZ) The z-chamber is located outside the barrel part of the jet chamber at $|\cos\theta| < 0.72$, but still inside the pressure vessel. It improves the measurement of the z coordinate, which is not very precisely determined in the jet chamber. This is needed for good angular distribution resolution and improves the invariant mass resolution. It consists of 24 drift chambers, divided each into 8 cells of 6 anode wires, which are spanned in the $r-\phi$ plane perpendicular to the jet chamber wires. The z coordinate is measured with a precision of 300 μm.

The Time-of-Flight measurement (TOF) Outside the pressure vessel and the solenoid coil the time-of-flight detector is located. It consists of plastic scintillator strips, read out at both sides of the barrel using photo multipliers. It achieves a time resolution of 300 ps [71]. It is mainly used for triggering and cosmic rejection.

The Presampler (PB and PE) The pressure vessel and the coil provides approximately two radiation lengths of material in front of the electromagnetic calorimeter. That means that most particles start to shower before the calorimeter. In order to correct for the energy loss in the vessel and the coil the presampler measures the shower size and particle multiplicity in front of the calorimeters, which is proportional to the energy already lost. In the barrel, two layers of streamer tubes (PB) are installed. In the endcap, multiwire proportional chambers are used (PE).

The electromagnetic calorimeter (EB and EE) The electromagnetic calorimeter (ECAL) measures the energy of light electromagnetically interacting particles. In the barrel part (EB) it consists of 9940 lead glass blocks. Each block is $10 \times 10\,\mathrm{cm}^2$ wide and 24.6 electromagnetic interaction lengths deep. The blocks are oriented towards a point near the interaction point, which is 56 to 158 mm off from the IP. Thus the resolution is optimised, since most particles hit mostly one block, while no photons can escape undetected along the block borders. The spatial resolution is around 1 cm, using the centre-of-gravity of the energy deposited in adjacent blocks. The depth of the blocks ensures that all the energy is lost in the calorimeter.

The energy is measured from the Čerenkov light emitted in the crystal from the secondary electrons in the cluster. The light is collected and measured using photon multipliers. The energy resolution is measured to be

$$\frac{\sigma_E}{E} = \sqrt{0.015^2 + \frac{0.16^2}{E(GeV)}}. \tag{4.4}$$

In the endcap (EE) the ECAL consists of 1132 blocks on each side, $9.2 \times 9.2\,\mathrm{cm}^2$ wide and at least 20.5 electromagnetic interaction lengths deep. Each block is oriented parallel to the z axis. Since the calorimeter in this partly is in the inhomogeneous region of the solenoidal magnetic field, phototriods are used as light detectors. The energy resolution is

$$\frac{\sigma_E}{E} = \sqrt{0.018^2 + \frac{0.218^2}{E(GeV)}}. \tag{4.5}$$

With this resolution, the energies of electrons, photons and pions can be precisely determined in a range of 100 MeV to 100 GeV. Additionally, π^0 and γ can be separated. The total angular coverage of the ECAL is $|\cos\theta| < 0.98$.

The Hadronic Calorimeter (HB, HE and HP) The hadron calorimeter (HCAL) measures the energy of strongly interacting particles and assists in muon identification. It is a sampling calorimeter, consisting consecutively of 8 layers of steel plates as absorber material and of 9 layers of proportional streamer tubes as active component. It covers 97 % of the solid angle and is approximately 1 m thick. The spatial resolution is limited by the segmentation of 7.5° in ϕ and 5° in θ. The energy resolution in the barrel (HB) and endcap (HE) is

$$\frac{\sigma_E}{E} = \frac{1.2}{\sqrt{E(GeV)}} \tag{4.6}$$

for isolated particles. The total hadronic energy is calculated as a weighted sum from the energy deposit in the ECAL and the HCAL. The calorimeter has a depth of around 7 hadronic interaction lengths, thus the probability of a pion to punch through all layers without interaction is just 0.001. It also serves as return yoke for the magnetic field. In the pole tips (HP) up to $|\cos\theta| < 0.99$ multiwire proportional chambers are used as active components.

Table 4.2: *Integrated luminosities recorded by the OPAL detector at different energies during the LEP data taking. The bulk of the luminosity has been taken at* $\sqrt{s} = 189 - 209$ *GeV.*

Year	Energies (GeV)	Luminosity (pb^{-1})
LEP 1		
1989 – 1995	91.2	46.3
LEP 2		
1996	130–136	5.2
1996	161	10.4
1996	172	10.0
1997	183	54.1
1998	189	172.1
1999	192	28.9
1999	196	74.8
1999	200	77.2
1999	202	36.1
2000	199 – 204	8.9
2000	204 – 206	72.9
2000	206 – 207	117.4
2000	207 – 209	8.1

The Muon Chambers (MB and ME) The outermost detector layer are the muon chambers. In the barrel (MB) part 110 flat drift chambers of 1.20 m length and 9 cm deepness are mounted in four layers. The wires are spanned parallel to the z direction. The endcap region (ME) is instrumented with four layers of streamer. The total angular coverage of the detector is $|\cos\theta| < 0.98$. The spatial resolution in both regions is a few millimetres.

Due to the fact that more than 7 hadronic interaction lengths are located in front of the muon system, the probability for a 5 GeV pion to fake a muon is just 1 %. The muon identification efficiency for muons in $|\cos\theta| < 0.98$ and more than 3 GeV energy is basically 100 %.

The Luminosity Detectors The luminosity delivered by the accelerator is measured by two dedicated detectors very close to the beampipe in the forward region. They also assist in the tagging of photons from initial state radiation and electrons from $\gamma\gamma$ events. The *Forward Detector* (FD) consists of several single detectors covering the angular range of 47 mrad to 120 mrad. The main component is a sandwich lead-scintillator with a presampler and 20 interaction lengths. Drift chambers and proportional chambers are also used as active components. Outside the main detector, at a distance of 7.85 m from the IP, a lead scintillator calorimeter is installed covering the extreme angular range of 5 mrad to 10 mrad. Using the complete system, a precision of the luminosity measurement of 0.4 % is achieved.

In 1993 the *Silicon-Tungsten Luminometer* (SW) was additionally installed to cover the angular range of 25 (later 33) mrad to 59 mrad [72]. It consists of 19 layers of silicon detectors and 18 layers of tungsten absorbers, adding up to a total thickness of 22 electromagnetic interaction lengths. Its main purpose is the measurement of low angle electrons from Bhabha scattering for the luminosity determination, where an uncertainty of 0.15 % is achieved using the high spatial resolution and the coverage of low angles.

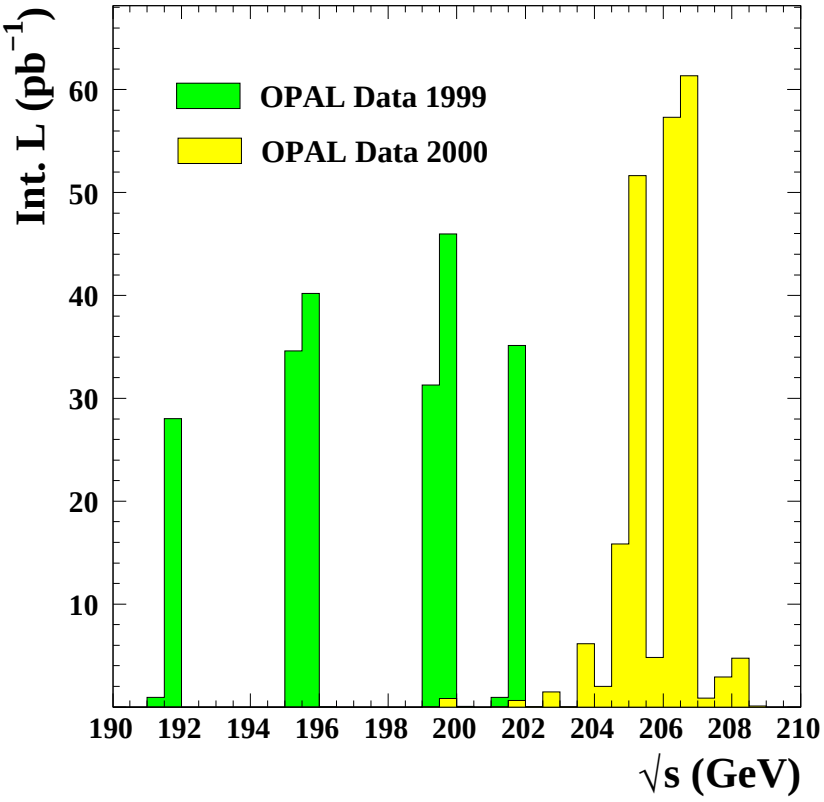

Figure 4.4: *The integrated luminosity taken with OPAL at different centre-of-mass energies in the years 1999 (green, dark grey) and 2000 (yellow, light grey). In 2000, the energy has been increased step-by-step during each fill. Therefore a smeared spectrum with the bulk of the luminosity at* $\sqrt{s}$ *=205 and 207 GeV appears.*

Another forward detectors is the *MIP plug*, which was installed in 1996 and serves as a tool for the unambiguous determination of the collision time. It is located below the barrel part of the poletip HCAL and is build of scintillators with 3 ns time resolution. Finally the *Gamma Catcher* is a lead-scintillator closing the hole between the ECAL and the forward detector and thus improving the hermeticity of the detector for electromagnetically interacting particles.

The data taking of the OPAL detector was divided in the LEP 1 phase around $\sqrt{s} = 91.2$ GeV and the LEP 2 phase at $130\,\text{GeV} < \sqrt{s} < 209$ GeV. The luminosities collected at the different energies in the different years are shown in Tab 4.2. The luminosity distribution in the data of the years 1999 and 2000, on which the analysis presented in Section 5 is based, is shown in detail in Fig. 4.4. It can be seen that in 2000 in order to achieve highest possible energies, the accelerator did not run at one sharp energy but was operated up to the highest achievable energy during each run, which was reached in several steps.

4.2.1 Standard Model Processes at LEP 2

The precise measurement of physical quantities at high energy physics experiments requires a very good knowledge of the possible signal and background processes. For the analysis presented in this thesis, all SM processes without a Higgs boson are treated as background.

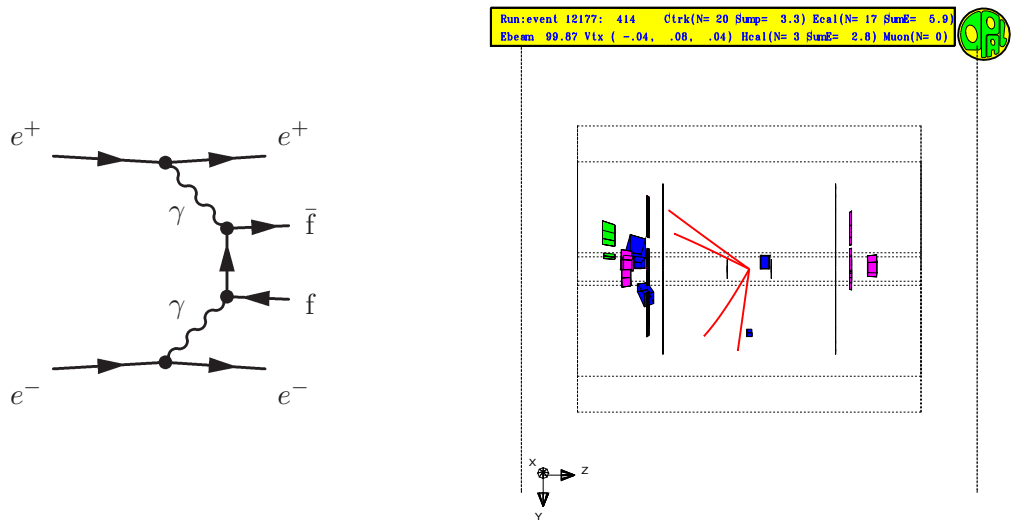

Figure 4.5: *The $\gamma\gamma$ process at LEP. Two photons are radiated from the incoming beams. They can create hadronic final states in their collision, which appears in the detector with small energy and unbalanced momentum.*

The understanding of this background is crucial, since its rates at LEP 2 energies are up to 7 orders of magnitude larger than the rate of the signal process. The relevant SM background processes are described in the following. The focus lies on hadronic decays, since also the signal process described in Section 5 decays into hadronic final states.

2-Photon Processes The 2-photon processes or $\gamma\gamma$ processes have the largest cross-section of all SM processes at LEP 2. The cross-section is around 10 nb, 6 to 7 orders of magnitude higher than a signal process. A typical $\gamma\gamma$ event and its resulting signature in the OPAL detector for a hadronic final state is shown in Fig. 4.5. The incoming electrons and positrons both radiate a photon, the Weizsäcker-Williams photon. The photons interact and create fermion pairs. Mostly the transverse momentum of the photons is very low, thus the electrons are not recorded in the detector but disappear in the beampipe. Also usually only one of the photons is high-energetic, since the energy of the photons is inversely proportional to their production probability. Therefore the reconstructed event tends to be unbalanced in the z direction. Since the electron and positron mostly escape undetected, the measured Energy is mostly much below the centre-of-mass energy.

2-Fermion Processes The 2-fermion processes have the next highest cross-section after the $\gamma\gamma$ events. The incoming electrons and positrons form a Z* or γ^*, which then decays into two fermions. The cross-section of this process is around 100 pb. The closer the centre-of-mass energy is to the Z mass, the higher is the cross-section. In most of the events the Z (BR(Z $\rightarrow$hadrons = 70 %)) or γ^* (BR(γ^* $\rightarrow$hadrons = 56 %)) decays hadronically.

Two different types of 2-fermion events can be distinguished. Since the cross-section for Z production at the Z pole is around 2 orders of magnitude larger at $\sqrt{s} = 91.2$ GeV than at $\sqrt{s} = 200$ GeV, it is very probable that the incoming electrons and positrons reduce their effective centre-of-mass energy by photon radiation from the initial state (Initial State Radiation, ISR). A hadronic radiative return event is shown in Fig. 4.6. The new effective centre-of-mass energy is called $\sqrt{s'}$. At LEP 2 energies, the distribution of the effective centre-of-mass energy peaks around $\sqrt{s'} \approx m_Z$. As Fig. 4.6 shows, a large amount of energy is

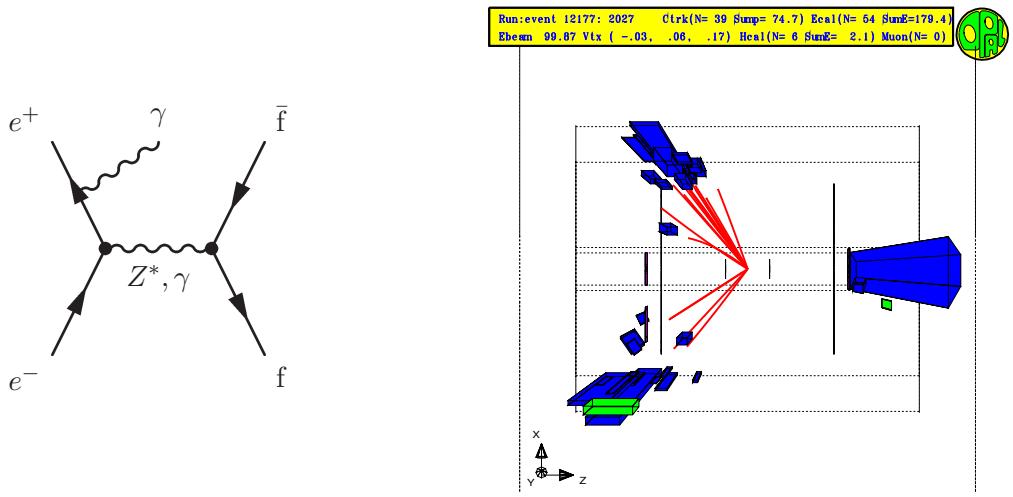

Figure 4.6: *A radiative return event at LEP 2. In this event, the radiated photon is visible in the detector, which is not generally the case.*

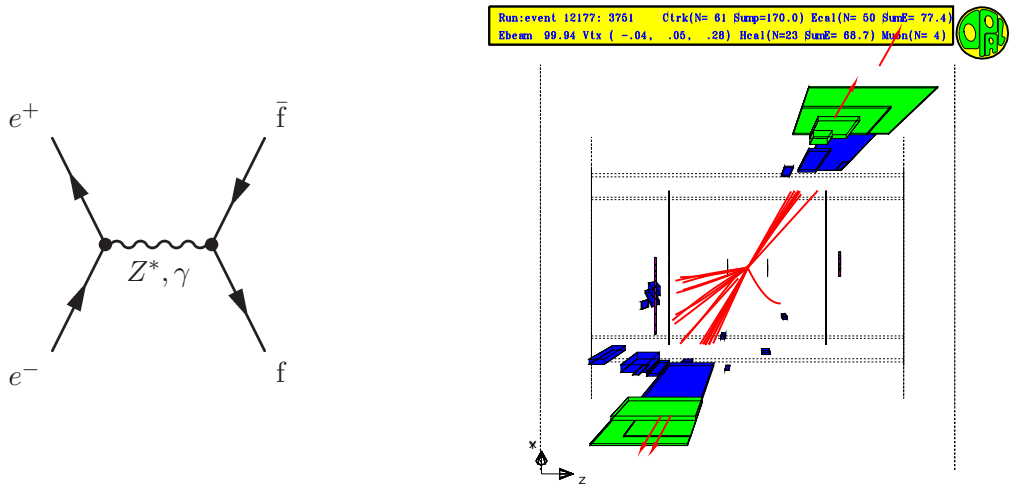

Figure 4.7: *The* $e^+e^- \rightarrow q\bar{q}$ *process at LEP. The events have a clear two-jet structure and have a balanced momentum sum.*

carried by one photon, detected in the forward region of the detector or (more often) escaping undetected through the beam pipe. The rest of the event is unbalanced in the z direction and carries significantly less energy than $\sqrt{s}$.

The other type of the 2-fermion events does not radiate a hard ISR photon. The full energy is visible in the detector. A hadronic 2-fermion event is shown in Fig. 4.7. Two primary quarks in the initial state mostly lead to a clear 2-jet structure. However, gluon radiation from the outgoing quarks in the hadronic events can lead to more jets. As in the case of the Weizsäcker-Williams photons, the radiation probability is inversely proportional to the gluon energy, therefore most of the jets are soft and their direction tends to be close to the direction of the primary quark.

4-Fermion Processes The most complex SM backgrounds for the analysis presented in Section 5 are the 4-fermion processes. They contain different types of processes, of which the Z pair and the W pair production are dominant. The production diagrams are shown in Fig. 4.8. W pairs are produced in triple gauge coupling processes with ZWW coupling or in t

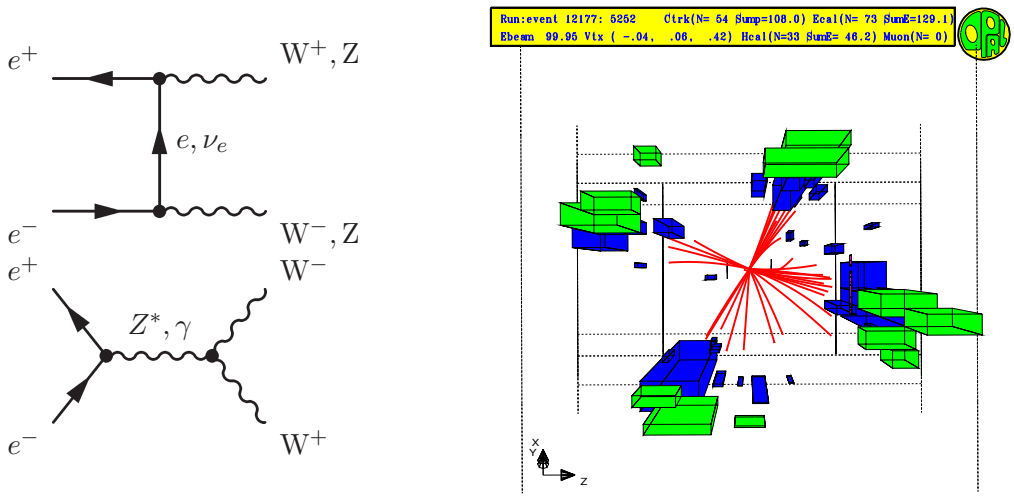

Figure 4.8: *The four-fermion process at LEP. Clear four-jet events with balanced energy and momentum are visible in the detector.*

channel production. The Z pairs are produced in the t channel exchange process.

The probability that two W's decay hadronically is 49 %. The hadronic production cross section is around 10 pb for $\sqrt{s} \approx 200$ GeV, one or two orders of magnitude larger than the signal cross section. The resulting event consists of four jets from four primary quarks. The events can be identified from two criteria. First, the mass of the di-jets with correct pairings is each 80.3 GeV, and the jets do not contain b-quarks but consist of ud and cs combination. This is due to the fact that tb production is kinematically forbidden and that cb production is Cabbibo-suppressed.

The cross-section of Z pair production is a factor of ≈ 20 smaller than W pair production, due to the smaller amount of diagrams and due to the larger coupling of the W to leptons. The total hadronic branching ratio is also 49 %. The decay of the Z's produces four jets in the detector, of which the correct di-jet pairing has a mass of 91.2 GeV. The events can be further separated from the W pair events with larger amount of b quarks produced in Z decays.

The measurement of the W and Z pair production, their cross-section at various centre-of-mass energies and their couplings was an important part of the LEP 2 measurements. It allows to measure the SM gauge structure with great precision [73].

4.2.2 Event Simulation in OPAL

In order to understand the detector response to particles, the physics process as well as the detector must be understood in great detail. This is achieved in two steps. First the fundamental physics process itself is simulated using a Monte Carlo generator. The output of this is a set of simulated events with the full four-vectors of all intermediate and final state particles. Next a full detector simulation with the `GEANT3` package [74] based on Monte Carlo techniques is performed for all the simulated particles, which is implemented in the `GOPAL` package [75].

Depending on the physics process, different generators are used to simulate the fundamental interaction and the decay and hadronisation of the final state particles. On the basis of the SM and MSSM models the matrix elements are calculated and the differential cross-sections are derived. On this basis e^+e^- physics events are simulated using Monte Carlo techniques. The following generators are used:

Table 4.3: *Cross-section of background SM processes. Generally, cross-sections decrease with raising energy. The Monte Carlo statistics for all processes other than $\gamma\gamma$ exceeds the data statistics by a factor of more than 15. The number of events is given per Monte Carlo energy.*

Process	Generator	No. events per energy	Cross-section in pb						
			192	196	200	202	205	206	207
qq	KK2F	250000	94.84	90.09	85.56	83.37	81.31	79.46	79.38
qqqq	grc4f 2.1	≈ 44000	8.657	8.816	8.909	8.944	8.967	8.974	8.970
$\ell\ell$qq	grcf4 2.1	≈ 44000	8.947	9.140	9.277	9.319	9.390	9.403	9.417
$\gamma\gamma$	PHOJET	4000000	10890	11424	11560	11424		11170	

- **Signal Events:** The generator HZHA [76] is used to generate signal events in the channels $e^+e^- \to \mathcal{H}_1\mathcal{H}_2 \to b\bar{b}b\bar{b}$ and $e^+e^- \to \mathcal{H}_1\mathcal{H}_2 \to \mathcal{H}_1\mathcal{H}_1\mathcal{H}_1 \to b\bar{b}b\bar{b}b\bar{b}$.

- **2-Fermion Events:** The generator KK2F [77] is used for the generation of 2-fermion events. It is based on matrix elements and incorporates an good description of photon initial and final state radiation and of gluon radiation.

- **4-Fermion Events:** The $W^{\pm}$ and Z pair production events are generated with GRC4F [78]. The full set of all 4-fermion diagrams on tree level and their interference is calculated.

- **2-Photon Events:** The generator PHOJET [79] is used to generate $\gamma\gamma$ events.

Hadronisation for all processes involving hadronic final states is performed with the string hadronisation model of JETSET in PYTHIA6.125 [80]. A perturbative calculation of QCD processes, such as gluon radiation, is performed as long as the energy of the partons is high enough to yield a small α_s. For non-perturbative processes a string-hadronisation model is used. Also the decay of short-lived resonances is performed in this step.

The Monte Carlo Datasets used in the analysis described in Section 5 are described in Tab. 4.3. The statistics of the Monte Carlo samples exceeds the statistics of the data typically by a factor of 10 to 20.

After the generation of the fundamental physics process and after the hadronisation has been performed, the detector response to the final state particles is determined. For this purpose, the program GOPAL [75] is used. It is based on GEANT3 [74]. In this step the interactions of the final state particles with every detector component is calculated. From these interactions, the detector signals are determined. The decay of particles with intermediate lifetime is performed and the creation of secondary particles is taken care of. The signals generated with this simulation are stored in the same format as the real detector signals.

The reconstruction of the data and the simulated signal and background events is performed with the same reconstruction tool, ROPE [81]. The output of the reconstruction are the physical observables of the e^+e^- reaction, namely the tracks and calorimeter clusters with all their physical quantities: impact parameter d_0, momentum p, specific energy loss $\mathrm{d}E/\mathrm{d}x$, and energy E. On the basis of this information, the search for hadronic jets, b quarks and finally Higgs bosons is performed.

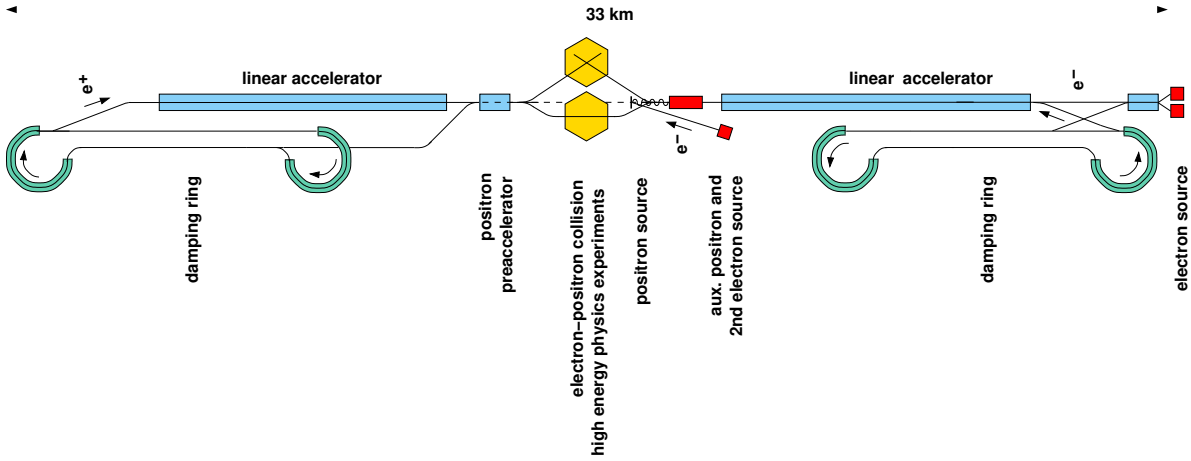

Figure 4.9: *The TESLA linear accelerator. Particles are accelerated in two separate machine arms with 16.5 km length each and brought to collision at one or two central inter action regions with* $\sqrt{s} = 91.2$ *to* $\sqrt{s} = 800\,\mathrm{GeV}$.

4.3 The TESLA Project

As outlined in Section 4.1, the design of circular accelerators for e^+e^- collisions has reached its physical limitations. Therefore a linear e^+e^- collider with a centre-of-mass energy of 0.5 to 1 TeV is proposed as the next step. It has been agreed on in a worldwide consensus within the high energy physics community that this machine should be the next global high energy physics project [82].

The linear collider has a rich physics case, starting from SM physics such as top quark and W physics, covering the precise determination of all properties of the SM Higgs boson, and reaching to precise measurements of the structure of possible extensions of the SM, such as Supersymmetry, compositeness or large extra dimensions. As a precision measurement facility it is complementary in its physics case to the discovery facility LHC. According to the current plans, such an accelerator could come into operation around 2015. However, intense studies and design efforts are underway already now.

The TESLA Linear Accelerator

The TESLA[2] [83] project, proposed by an international collaboration based at DESY, is one of three international proposals for the next linear collider in the range of $\sqrt{s} = 0.5 - 1$ TeV. It is based on superconducting accelerator cavity technology, while the other two proposals NLC[3] [84] in the USA and GLC[4] [85] in Japan are based on normal conducting cavities.

The advantage of such a design is that no synchrotron radiation is lost. On the other hand, each bunch can only be used once, and the accelerator tends to be expensive since the cost-intensive accelerating cavities can act on each bunch only once, therefore basically the whole length of the collider has to be filled with cavities. These disadvantages are slightly compensated by the fact that the repetition rate can be high and that the bunch size at the IP can be reduced to a very small value, thus high luminosities can be reached.

[2] Tera Electronvolt Superconducting Linear Accelerator
[3] Next Linear Collider
[4] Global Linear Collider

The basic design of the TESLA accelerator is shown in Fig. 4.9. It is 33 km in length and consists of two half-arms. In one side, polarised electrons are produced in an laser driven electron source. These are pre-accelerated to an energy of 5 GeV and then cooled in a damping ring system. Then they are extracted and accelerated. The main linac is 15 km in length on each side. An accelerating gradient of 23.4 MV/m is needed to reach $\sqrt{s} = 500$ GeV. The gradient for $\sqrt{s} = 800$ GeV is 35 MV/m, which has been exceeded in realistic test setups and reached in the fully functional accelerator of the TESLA Test Facility TTF [86].

After the main linac, the source for polarised positrons is located, followed by the final focus system. Two interaction regions are foreseen. Unlike at circular accelerators, the available luminosity has to be shared between the two interaction regions. It is foreseen that the main interaction region has zero (or almost 0) crossing angle, in order to achieve highest luminosity and best hermeticity of the detector. The other interaction region is planned with a crossing angle of around 34 mrad, in order to allow eγ or $\gamma\gamma$ collisions, for which no electromagnetic separation of the ingoing and outgoing beams is possible.

The TESLA accelerating structures consist of 9-cell cavities made of pure niobium. Their relatively low RF frequency of 1.3 GHz allows for large apertures and thus tolerant alignment with respect to the warm technology accelerators, where the RF frequency is 11.3 GHz and the cavities are around 10 times smaller than at TESLA. Always 12 of the 9-cell cavities are stored in one 18 m long cryostatic vessel. Each of the cavities has its own RF supply. The cavities are cooled in a bath of liquid helium at 2 K. A total number of 21024 cavities is needed for the accelerator.

The cavities are not operated continuously, but in pulses with a repetition rate of 5 Hz. The pulse length of up to 1 ms allows to place up to 2820 bunches with a bunch spacing of 337 ns into one pulse. The bunches within one pulse are called bunch train. The required luminosity is determined by the cross-section of anticipated physics processes. Given a cross-section of SM Higgs boson production in Higgsstrahlung at $m_{\mathrm{H_{SM}}} = 120$ GeV and $\sqrt{s} = 350$ GeV of $\sigma_{\mathrm{H_{SM}}} = 139$ fb, an integrated luminosity of around 500 fb^{-1} is aimed for in order to precisely measure the Higgs mass and the Higgs production and decay properties. This means that $\mathcal{L} \approx 3 \times 10^{34}$ cm^{-2}s^{-1} has to be achieved if in total 80 000 Higgs bosons shall be produced in approximately one year of data taking.

Since the repetition rate of the bunch crossings is limited by beam power, the beam size at the IP has to be decreased by several orders of magnitude with respect to LEP. This however is constrained by beamstrahlung: For very dense beams the space charge and thus the electromagnetic fields inside the bunch are so strong that the particles in one bunch are scattered in the electromagnetic field of the other bunch. This is called beamstrahlung. As a result, photons and e$^+$e$^-$ pairs are generated in the forward direction, eventually leading to severe backgrounds due to backscattering. Additionally, the effective energy spectrum of the beams is widened. The average energy loss due to beamstrahlung is proportional to

$$\Delta_{E_b} \sim \frac{1}{\sigma_z(\sigma_x + \sigma_y)^2}.$$

Thus the beamstrahlung is independent of σ_y as long as $\sigma_y \ll \sigma_x$ is satisfied. Since anyhow the final focus quadrupoles focus the beam primarily in one direction, an extremely elliptical beam spot with $\sigma_x \times \sigma_y = 553\,\mathrm{nm} \times 5\,\mathrm{nm}$ is chosen.

Using these settings, a luminosity of $\mathcal{L} = 3.4 \times 10^{34}$ cm^{-2}s^{-1} is achieved. The machine parameters for TESLA 500 and TESLA 800 are summarised in Tab. 4.4. The number of beamstrahlung photons per bunch crossing at $\theta > 4.6$ mrad amounts to 120 000 photons, depositing more than 20 TeV per bunch cross in the forward detectors.

Table 4.4: *TESLA machine parameters for $\sqrt{s} = 500 - 800$ GeV, compared with the LEP 2 machine parameters at $\sqrt{s} \approx 206$ GeV.*

Parameter	LEP 2	TESLA	
$\sqrt{s}$	209 GeV	500 GeV	800 GeV
$\sigma_x \times \sigma_y$	$200\,\mu\text{m} \times 2.5\,\mu\text{m}$	$553\,\text{nm} \times 5\,\text{nm}$	$391\,\text{nm} \times 2.8\,\text{nm}$
f_b	$22\,\mu\text{s}$	337 ns	176 ns
N	3×10^{11}	2×10^{10}	1.4×10^{10}
$\mathcal{L}$	10^{31} cm^{-2}s^{-1}	3.4×10^{34} cm^{-2}s^{-1}	5.8×10^{34} cm^{-2}s^{-1}
accelerating gradient	7 MV/m	23.4 MV/m	35 MV/m

The measurement of beam parameters is performed in an analogous way as at LEP 2. However, the situation is more challenging at TESLA since a higher precision is required and since the beamstrahlung will distort the polarisation and the beam energy spectrum directly at the IP.

The injection and main linac components of the proposed TESLA linear collider have been tested at the TTF at DESY and will be used on a large scale basis in the XFEL[5] light source at DESY.

The Detector for TESLA

The large luminosity at TESLA, statistically allowing very high precision measurements, and the relatively low background and radiation damage to the detectors allows a detector design purely driven by physics requirements.

The requested performance of the detector can be deduced from the expected production and decay of particles like the Higgs boson or supersymmetric particles. This sets the following benchmarks on the individual detector performances:

- **Vertexing:** In order to distinguish a SM Higgs boson from any other spin 0 boson, the couplings of the Higgs boson to the SM fermions have to be measured precisely. In the SM they are predicted to be proportional to the particle masses. This requires excellent vertexing to be able to distinguish b-quark, c-quark and uds-quark and gluon jets. Since the average impact parameter of charmed particles in the TESLA detector is around 100 μm, an impact parameter resolution of the microvertex detector of

  $$\delta_{d_0} \approx 5\,\mu\text{m}$$

  is required to efficiently tag c quark decays.

- **Tracking:** The most model independent way to discover any spin 0 boson coupling to the Z boson is an analysis of the recoil mass spectrum of the $\text{Z} \to \ell^+\ell^-$ decay products and their angular distribution. In order to be limited by the natural width of the Z, a momentum resolution of

  $$\delta_{p_t} < 5 \times 10^{-5}(1/GeV)$$

  for single leptons has to be achieved. Thus the width of the recoil spectrum of the di-lepton mass alone of around 1.5 GeV will not be limited by the detector resolution.

[5] X-ray Free Electron Laser

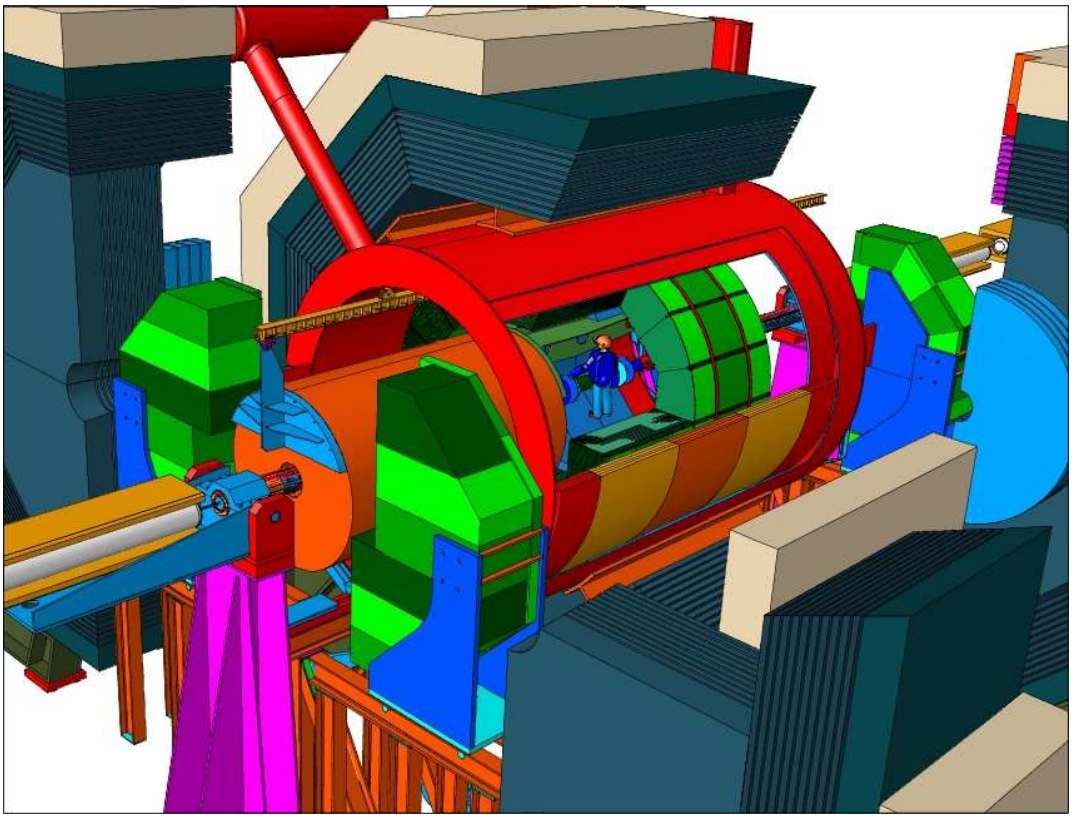

Figure 4.10: *Three dimensional sketch of the TESLA detector. A coil with 8 m length and 6 m inner diameter contains the complete vertexing, tracking and calorimetry. The muon system is installed outside the coil.*

The Higgs boson mass can then be measured to a precision of around 200 MeV. For multi-partonic final states the tracking system should also be capable of high efficiency in dense track environments.

- **Calorimetry:** The most demanding precision test of the SM Higgs boson is the determination of the Higgs self coupling λ. This can be deduced from events of the type $e^+e^- \to H^*_{SM}Z \to H_{SM}H_{SM}Z$, yielding six-fermion final states with four b-jets. In order to separate this final state from top decays, an excellent jet reconstruction and a good jet energy resolution of
$$\frac{\sigma_E}{E} \approx \frac{0.3}{\sqrt{E(GeV)}}$$
is required. Very little material in front of the calorimeter is required for that. This also is needed to separate WW from ZZ final states in Higgs or triple gauge coupling studies.

- **Hermeticity:** Most of the final states emerging in supersymmetric particle production show a considerable amount of missing energy, carried away by heavy particles interacting only weakly (see Section 7.1). In order to discriminate these events from SM background, excellent hermeticity and a coverage of the forward calorimeters down to $\theta \approx 5$ mrad is required.

One possible detector concept meeting these requirements is shown in Fig. 4.10 and 4.11. It consists of a 5 layer silicon pixel vertex detector, a large TPC as tracker and the full calorimetry

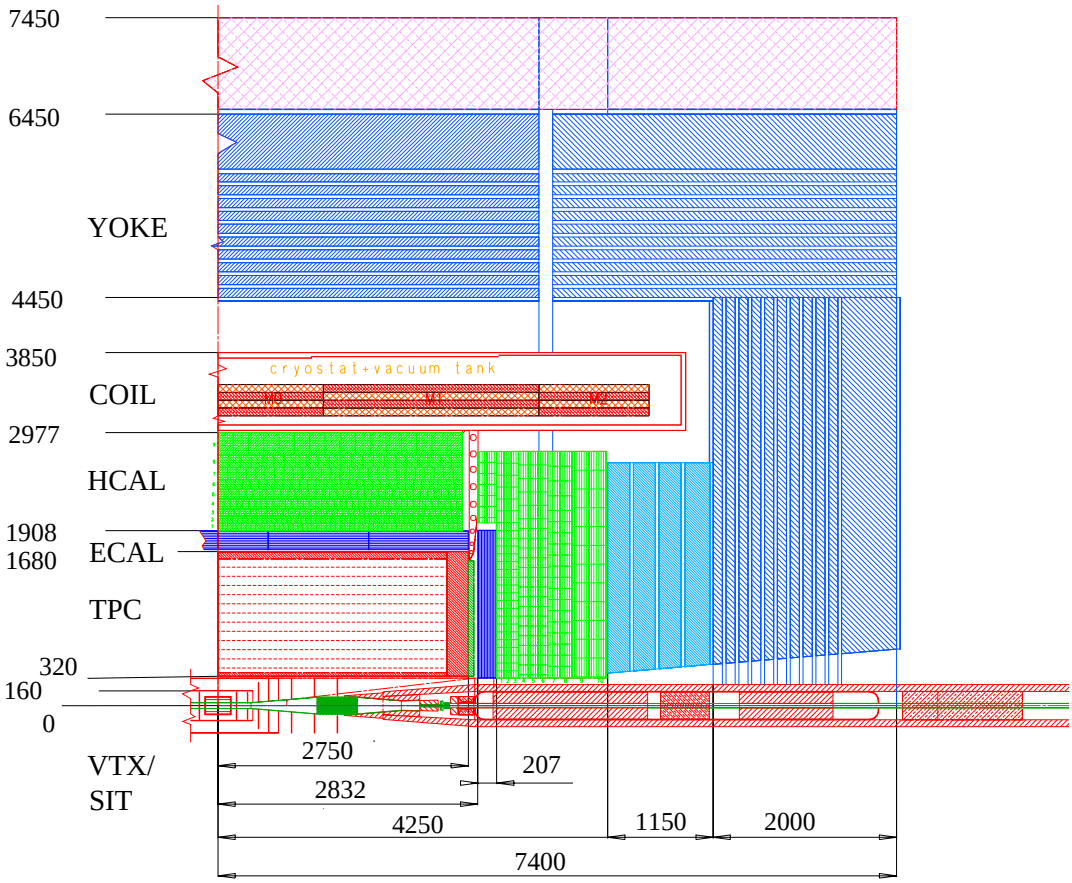

Figure 4.11: *One quarter of the TESLA detector. The tracking system extends up to* $r = 1.68$ *m. The complete calorimetry is inside the 4 T coil, the muon system outside.*

inside the solenoidal coil of 6 m inner radius and 4 T field. The properties of the proposed components are described in detail in [87]. The design is not yet final and R&D for several options of each detector component is underway. In the following an outline of the proposed setup is given, without covering all technologies which are presently discussed.

Vertex Detector The proposed vertex detector (VTX) is a silicon pixel detector with 5 layers, starting at a radius of $r = 1.6$ cm from the IP and extending up to $r = 6$ cm. It is shown close to the IP in Fig. 4.11. Up to 800 million pixels of $20 \times 20\,\mu\text{m}^2$ size are planned. Four different technologies (CCD [88], CMOS [89], DEPFET [90] and hybrid pixels [91]) are under study. The material budget of the vertex detector is extremely small, since the sensors are only 50 μm thick, adding up to only 0.3 % of a radiation length. A point resolution of $1.5\,\mu$m is achieved, translating into an impact parameter resolution of $\approx 5\,\mu$m.

Tracking System The tracking system consists of the vertex detector described above, the Silicon Intermediate Tracker SIT [92], the Forward Tracker Disks (FTD), the large Time Projection Chamber (TPC) [93] and the Forward Chambers (FCH). The SIT and the FTD close the gap between the vertex detector and the TPC, while the TPC performs the main tracking with around 200 measured 3D points per track. The FCH determine the endpoint of forward-going tracks precisely, for which there are not many track points in the TPC.

The SIT and FTD consists of silicon microstrip detectors. The main tracker is a TPC because it has minimal material budget, has excellent 3D resolution and measures many space points. This allows the very efficient unambiguous reconstruction of tracks in dense environments. Additionally the measurement of the specific energy loss $\mathrm{d}E/\mathrm{d}x$ is possible. The TPC is foreseen to be 5 m long, to have an inner radius of 36.2 cm and to have an outer radius of 161.8 cm. For the readout of the TPC, an electron gas amplification system based on micro pattern gaseous detectors is forseen, such as Gas Electron Multipliers (GEM) [94] as amplification device and pads for the two-dimensional readout at the endplate. Other possibilities include the Micromegas [95] technique for the gas amplification or silicon pixel detectors for the readout [96]. Using these techniques, the undesired ion feedback can be naturally reduced and a x, y point resolution of $100\,\mu$m can be achieved. The resolution of the TPC alone is $\delta_{p_t} < 1.5 \times 10^{-4}(1/GeV)$ and $\delta_{\mathrm{d}E/\mathrm{d}x} = 5\%$. The TPC operates continuously during one bunch train of 1 ms length. The information of approximately 160 bunch crossings is contained simultaneously in the TPC volume. Due to the time resolution of around 200 ns of the TPC alone (at a drift velocity of the electrons in the gas of around 4.7 cm/μs), an unambiguous tagging of the bunch crossing (at a distance of 337 ns) of each track is possible.

In the region of $0.87 < |\cos\theta| < 0.99$, the FCH adds resolution and compensates the precision loss due to a low number of space points in the TPC and the multiple scattering in the endplates. They consist of three stereo layers of straw tubes.

The overall resolution of the vertex and the tracking system is $\delta_{p_t} < 5 \times 10^{-5}(1/GeV)$, as shown in many detailed simulations [97]. The total material budget in front of the calorimeters adds up to only 3 % of a radiation length.

Calorimeters The calorimeters of the TESLA detector are designed to make optimal use of the particle flow concept. This concept uses the fact that for charged particles the excellent tracking of high-energetic particles allows the precise determination of the particle energy from the particle momentum, using the pion mass hypothesis. In order to use the tracking information on the momentum p for charged particles inside a dense jet, the energy clusters belonging to the charged particles have to be identified precisely and separated from the clusters from neutral particles. The clusters from charged particles are then removed from the reconstruction of the event, their energy is replaced by the energy measured from the momentum, and the remaining energy in the calorimeter is assigned to the neutral particles.

In order to make this algorithm most efficient, a very high granularity and a large inner radius of the calorimeter has to be chosen, in order to separate clusters and assign them unambiguously to tracks in the tracking system. This means that the calorimeter can also be used as tracking device for minimum ionising particles.

For the electromagnetic calorimeter, a silicon-tungsten calorimeter with 1 cm^2 cell size and 32 million channels is foreseen [98]. Additionally to the precise cluster reconstruction, it achieves an energy resolution of

$$\frac{\sigma_E}{E} \leq 1\,\% + \frac{10\,\%}{\sqrt{E(GeV)}}.$$

One of the options for the hadronic calorimeter is a sampling calorimeter made of stainless steel and scintillating tiles of 3×3 cm^2 to 5×5 cm^2 cell size [99]. It would reach an energy resolution of

$$\frac{\sigma_E}{E} \leq 3\,\% + \frac{35\,\%}{\sqrt{E(GeV)}}$$

for single hadrons. The high granularity is also needed for efficient software weighting of

electromagnetic and hadronic clusters, which can be separated using information on their shape.

Magnet and Muon System In order to achieve the momentum resolution of $\delta_{p_t} < 5 \times 10^{-5}(1/GeV)$, a very high and uniform magnetic field is needed. In the current proposal, the CMS[6] coil design [100] is adopted. The uniform field of 4 T extends 6 m in diameter and 8 m in length. The complete calorimetry can be placed inside the coil. The steel return yoke of the magnet is instrumented with resistive plate chambers [101] and acts as muon system. It also serves as tail-catcher for hadronic showers leaking out of the hadron calorimeter.

Forward Detectors A very good desired hermeticity and the need for precise and fast luminosity measurements place strong requirements on the forward detector. The detector described so far has already a coverage down to $\theta > 120$ mrad. In the TESLA TDR proposal, the Low Angle Tagger LAT extends down to $\theta = 27.5$ mrad. It is a silicon tungsten sandwich calorimeter and is mounted on the front side of the masks shielding the final focus quadrupoles. Inside the mask, covering $4.6 < \theta < 28$ mrad, the Low angle Calorimeter LCAL [102] is located. It is a sampling calorimeter with either radiation hard silicon or diamond as active material, since doses up to 1 MGy per year from beamstrahlung are expected close to the beam.

The purpose of the forward detectors is to ensure optimal hermeticity, tag electrons from $\gamma\gamma$ events down to very small angles and perform a very fast luminosity measurement using Bhabha events. With a sampling time of around 30-50 ns, the bunch position can be adjusted from bunch to bunch in order to achieve highest possible luminosity.

[6] Compact Muon Solenoid

Chapter 5

Search for Higgs Bosons in Pair Production at OPAL

The search for the extended Higgs sector of the MSSM is one of the main efforts of the test of the existence of SUSY. If Higgs boson pair production is found, it does not only prove the existence of two new particles, but also is a direct test of the structure of the new theory.

This chapter first describes the analysis tools used for the search for pair produced Higgs bosons. The techniques of jet-finding, kinematic reconstruction and the tagging of B-hadrons is explained. The topological search for the pair production process $e^+e^- \to \mathcal{H}_1\mathcal{H}_2 \to b\bar{b}b\bar{b}$ is divided into two parts, depending on the kinematical regime of the Higgs boson masses. After the description of the search, the determination of the systematic uncertainties and the format providing the search results for the calculation of cross-section and SUSY parameter limits is introduced.

The search presented in this chapter is a topological search for the decay of a virtual Z boson into a CP odd and a CP even spin 0 particle, which then both decay into a pair of b quarks. This search can be interpreted both in CPC and CPV models, since in both cases a CP odd and a CP even Higgs boson eigenstate is produced. In the CPC case, these CP eigenstates are also mass eigenstates, in the CPV models the mass eigenstates are mixtures of the produced CP eigenstates. In Section 6, a re-interpretation of this search for the $e^+e^- \to \mathcal{H}_1\mathcal{H}_2 \to \mathcal{H}_1\mathcal{H}_1\mathcal{H}_1 \to b\bar{b}b\bar{b}b\bar{b}$ final state is described.

5.1 Analysis Tools

The output of the reconstruction of the events recorded with the OPAL detector (described in Section 4) are the tracks and clusters of the event, their impact parameter, momentum and $\mathrm{d}E/\mathrm{d}x$ or energy. This information is used to calculate the energy and momentum of the fundamental partons produced in the interaction, taking kinematical constraints into account. Finally the probability of B-hadrons in the reconstructed event is calculated. The individual steps of this analysis are the following.

- The selection for multihadronic events at LEP 2 is applied [103]. It is required that more than 4 tracks and more than 6 clusters in the ECAL exist. The visible energy in the event E_{vis} should exceed 14 % of the centre-of-mass energy and less than 75 % of the visible energy should be deposited in one hemisphere. This removes the largest part of the $\gamma\gamma$ events.

- Only tracks and clusters reconstructed with a high quality are accepted. Therefore,

a minimal number of hits in the individual tracker systems and a minimal number of ECAL blocks per cluster is required [104].

- The energy correction of the tracks and clusters is applied, the so-called "energy flow" technique. It is described in Section 5.1.1.

- Bundles of tracks and clusters are identified which most probably stem from one common parton of the fundamental process. These bundles of objects are called jets. Their momentum and energy is used to calculate the kinematical properties of the fundamental process. The jet finding is explained in Section 5.1.2.

- The beam energy and the total momentum of the initial reaction is known with great precision. This knowledge is exploited in the kinematical fit, where the jet momentum and energy is corrected. This improves the mass resolution strongly. The fit procedure is explained in Section 5.1.3.

- Finally B-hadrons inside the jets are identified, using information from displaced vertices, leptonic B-decays and the jet shape. The calculation of the probability of a B-hadron inside a jet is described in Section 5.1.4.

5.1.1 Energy Flow

Charged particles are detected both in the tracking systems and in the calorimeter, whereas photons and strongly interacting neutral particles are only detected in the calorimeter. Generally the momentum reconstruction has a much smaller uncertainty than the energy reconstruction (see Section 4.2). Therefore the energy of charged particles with several GeV is best estimated from their momentum, using a pion mass hypothesis. Then the energy information in the cluster matching the track is removed. The calorimeter information is used to measure the momentum and energy of neutral particles. After the energy flow calculation so called energy flow objects contain the best possible information of both the momentum and the energy measurement. This technique is called energy flow or particle flow. Depending on the position of tracks and clusters, the algorithm works as follows [105, 106]:

- *Isolated tracks or clusters*
  For tracks not pointing to a cluster the corresponding energy is calculated from the track momentum, using the hypothesis that the particle is a pion, which is true in 70 % of the cases. For an isolated cluster with no track pointing to it, the corresponding momentum is calculated using a photon hypothesis.

- *Matching tracks and clusters*
  For tracks pointing to a cluster, the energy is calculated using a pion hypothesis. The calculated energy is then subtracted from the cluster. If significant additional energy is left over, a new neutral object is introduced, to which the additional energy is assigned.

- *Electrons*
  For particles identified as electrons, using a neural net with $\mathrm{d}E/\mathrm{d}x$, p/E, time of flight and cluster shape information [107], the energy is determined most precisely by the electromagnetic calorimeter, therefore the momentum and energy for electrons is taken from the calorimeter.

5.1.2 Jet Finding

In order to estimate the momentum and energy of the fundamental partons, neighbouring energy flow objects in an hadronic event are sorted into bundles of objects, the jets. The OPAL jet reconstruction algorithm [108, 109] is based on the Durham algorithm [110] with some elements of the Jade jet finder [111]. The algorithm uses the following steps:

- All energy flow objects are regarded as pseudo-jets.
- For all combinations of two pseudo-jets i and j the quantity y_{ij} is calculated:

$$y_{ij} = \frac{2\min(E_i^2, E_j^2)\,(1-\cos\theta_{ij})}{E_{\text{vis}^2}},$$

  where E_i^2 and E_j^2 are the energies of the two pseudo-jets, $\cos\theta_{ij}$ is the angle between them and E_{vis^2} is the visible energy in the detector.
- The pseudo-jet pairing with the smallest y_{ij} is combined into one new pseudo-jet with $p = p_i + p_j$.
- The procedure is repeated until either a given number of pseudo-jets or until a given size of the smallest y_{ij} is reached. The pseudo-jets at this step are then interpreted as the real jets.

For the search for pair production the fixed number of four jets is required, i. e. all events with at least four energy flow objects are forced into four jets. The quantity y_{ij} then gives a measure of how four-jet like an event is. The Durham flip value y_{54} is defined as the smallest y_{ij} when the event flips from five to four jets. If it is small, then the event is likely not to be 5-jet like. The quantity y_{43} is analogously defined as the smallest y_{ij} when the event flips from four to three jets. If this quantity is large, then the event has large spacing between the four jets and therefore is likely to be a four (or more) jet event.

After the Durham jet finding, a correction of the assignment of the individual objects to the tracks is made using the Jade scheme. The energy and momenta of the jets are calculated and kept fixed for this step. The momentum direction of the jet is also called jet axis. Next each object i is reassigned to the jet whose most energetic particle α is closest using the Jade-measure

$$y_{\alpha i} = \frac{E_\alpha E_i (1-\cos\theta_{\alpha i})}{E_{\text{vis}}^2}.$$

The object i is re-assigned to the jet with most energetic particle α with respect to which it has the smallest $y_{\alpha i}$. After this step, the jet energy and momenta are calculated again. Using this re-assignment, the particle association to the correct jets, and thus the di-jet mass resolution, is improved. This is proved using the mass reconstruction of WW four-jet events as a reference [109].

5.1.3 Kinematic Fit

Due to energy and momentum conservation the total energy of the event E_{tot} has to equal the centre-of-mass energy $E_{\text{tot}} = \sqrt{s}$. Since e^+ and e^- collide head-on with the same momentum, the total momentum has to be $\vec{p}_{\text{tot}} = 0$. This fact can be used in the reconstruction of the event. In hadronic events, some energy is lost due to undetected neutrinos which are emitted in leptonic decays of heavy quarks. Additionally, some particles may be lost along the beampipe (which is probable for example for photons from initial state radiation) or due to inefficiencies

of the detector. Therefore generally the measured event has a visible energy $E_{\text{vis}} \neq E_{\text{tot}}$ and a visible momentum $\vec{p}_{\text{vis}} \neq \vec{p}_{\text{tot}}$.

A kinematical fit can be used to correct the measured jet momenta p_i such that the total energy matches the centre-of-mass energy and that the total momentum is 0. By doing so, the precision of the mass determination is increased.

The fitted four-momenta p' of the jets are determined such that the following conditions are fulfilled:

- Energy-momentum conservation: $\sum_i \vec{p}_i' = 0$, $\sum_i E_i' = \sqrt{s}$
- Constant jet masses: $E_i'^2 - \vec{p}_i'^2 = m_i$

Since energy and momentum conservation (four constraints) is required, the fit is also called 4C fit. A formula $f(\vec{p}_i')$ is constructed from the above conditions such that $f(\vec{p}_i') = 0$ if they are fulfilled. The χ^2 of the fit is then constructed as

$$\chi^2(\vec{p}_i', \lambda) = \sum_i (\vec{p}_i - \vec{p}_i')\,(V_i)^{-1}(\vec{p}_i)\,(\vec{p}_i - \vec{p}_i') + 2\lambda\, f(\vec{p}_i'), \tag{5.1}$$

where the V_i are the 3×3 covariance matrices of the measured momenta $\vec{p}_i$ and λ are the Lagrange multipliers, which go to infinity during the process of the fit, in order to ensure $f(\vec{p}_i') = 0$. In this way the fitted momenta $\vec{p}_i'$ (and energies E_i') are found which are closest to the measured momenta $\vec{p}_i$, but fulfil energy and momentum conservation. The jet momenta are not varied in Cartesian coordinates, but in $\log(|\vec{p}|)$, ϕ and θ, where the uncertainties are approximately distributed according to normal distributions.

This kinematic fit is used for two purposes. First, the momentum and mass resolution is improved using the above explained 4C fit. Second, the effective centre-of-mass energy of the event is determined. Initial state radiation of photons from the initial electron or positron modify the effective beam energies in the reaction. The amount of ISR radiation can be determined by measuring high energetic photons in the forward detectors and by a 3C kinematic fit of the event under the hypothesis that one or several photons are lost along the beam pipe. From a combination of both methods, the effective centre-of-mass energy $\sqrt{s'}$ is determined.

5.1.4 Tagging of B-Hadrons

For a final state of the Higgs boson signal with four b quarks, the identification of B-hadrons in jets is the most important analysis tool in order to discriminate the signal from the background. The following three properties of jets from b quarks can be identified:

- *Lifetime*
  Due to the relatively long lifetime of the B hadrons of $\tau = 1.6 \times 10^{-12}$ s, the average decay length in the detector is around 0.5 mm. Due to the large mass of the B hadrons of 5.3 GeV or higher the multiplicity at the B hadron decay vertex is sufficient to identify this secondary vertex inside the jet.

- *Leptonic Decays*
  About 30 % of the B hadrons decay semileptonically. In these cases, due to the large mass of the B hadron, a lepton with large transversal momentum with respect to the jet axis emerges in the jet.

- *Jet Shape*
  The average topology of a jet with B hadrons is different from other jets. Again due to the large mass of the B hadron, the average transverse momentum with respect to the jet axis of the decay products is large and the average multiplicity of the jet is high.

The OPAL b tagging [112, 113, 114] uses all three properties to calculate the likelihood of a jet to be produced from a primary b quark. It consists of three individual components, each exploiting one of the above properties. The individual components are each based on multivariate analyses, namely likelihoods and artificial neural nets (ANN) [115]. Their outcome is combined using a likelihood. In the following, the three components of the b tag and their combination and test with data is explained.

B lifetime The largest sensitivity for b quarks in jets is obtained with the search for secondary vertices. A typical jet from a b quark has a primary vertex, which stems from the fragmentation process around the b quark. In this fragmentation process, the B hadron and several other hadronic particles are formed. Within the beampipe, around 0.5 mm from the primary vertex, the B hadron decays and forms a secondary vertex. If a D hadron is created from the B, a tertiary vertex occurs at the decay of the D hadron.

The algorithm searching for secondary vertices consists of two parts. Either a decay vertex of a possible B hadron decay is found, which is separated from the primary vertex, where the tracks originate from the fragmentation process of the b quark. If no secondary vertex is found the distribution of the impact parameters of the tracks in the jet is used.

For the search for secondary vertices, sub-jets are formed within the jet. Using a CONE algorithm [116], a cone of the typical radial size of the B hadron decay products is formed. Tracks within the jet are sorted into the sub-jet if they have a large probability not to come from the primary vertex. To calculate this probability, the impact parameter significance $|d_0/\sigma_{d_0}|$ in $r-\phi$ and $|z_0/\sigma_{z_0}|$ in the z direction, the track momentum, the transverse momentum with respect to the cone axis and the track direction are used. Up to 6 tracks within the sub-jet with the highest probability to come from the secondary vertex are selected for the calculation of the significance of the secondary vertex.

The likelihood $\mathcal{L}_{SV}$ of a B hadron inside the jet, calculated from the search for secondary vertices, is then calculated using a 'tear down' algorithm from the 6 selected tracks in the sub-jet. Only tracks with a contribution to the χ^2 of a fit to the secondary vertex of less than 5 are used. After the secondary vertex is formed in this way, other tracks are attached to it if they can be fitted to the secondary vertex. Additionally the reduced vertex significance is calculated by removing the most significant track from the vertex and fitting the vertex again. This reduces background from K^0 mesons and single falsely measured tracks. If more than one sub-jet with a secondary vertex are found within the jet, the sub-jet with the highest significance is used for the calculation of $\mathcal{L}_{SV}$.

Not in all jets with B hadrons secondary vertices can be found. Therefore an additional likelihood $\mathcal{L}_{IP}$ is formed which calculates the likelihood of a B hadron in the jet from the distribution of the impact parameters s_0 in 3 dimensions.

The two likelihoods $\mathcal{L}_{SV}$ and $\mathcal{L}_{IP}$ are strongly correlated, therefore an ANN is used to combine then into one likelihood $\mathcal{L}_{\mathrm{Decay}}$. This variable is used in the combined B probability calculation.

Leptonic B Decays The second most significant method to find B hadrons is the search for leptons with large transverse momentum with respect to the jet axis, since about 30 % of the b quarks decay semileptonically $\mathrm{b} \to \ell\bar{\nu}\mathrm{c}$. 20 % decay into electrons or muons, which are

most useful here. The large mass of the B hadron of 5.3 GeV or more leads to the large p_T of the lepton track with respect to the jet.

The search for leptons in jets [117] requires a lepton momentum of at least 3 GeV. The production angle of the primary b quark and the jet axis approximately coincide due to the large momentum fraction which the primary b quark transfers to the B hadron. From the transverse momentum p_T of the lepton with respect to the jet momentum a likelihood $\mathcal{L}_L$ is formed, which is used in the combined B probability calculation. In only 5.9 % of all jets a lepton with high p_T is found, in which case the lepton tag adds a lot of sensitivity to the identification of B hadrons.

Jet Shape Due to the cascade decay of the b quark $\mathrm{b} \to \mathrm{W}^{*-}\mathrm{c} \to \mathrm{f}\bar{\mathrm{f}}\,\mathrm{W}^{*+}\mathrm{s} \to \ldots$ the decay multiplicity is large, therefore the b jets tend to consist of many objects. Also the jet width is large due to the large mass of the B hadron, which translates into large transverse momenta of the decay products. An ANN uses the number of objects in the jet and the sphericity (in the rest-frame of the jet) of sub-jets inside the jet in order to calculate the likelihood $\mathcal{L}_{JS}$, which is used in the combined B probability calculation. This method has the smallest significance among the three independent b-tagging methods used here.

Combination of the B Tagging Variables The individual parts of the search for B hadrons are combined using a likelihood. The combined probability of a B hadron in a given jet is

$$\mathcal{B} = \frac{R_b(\mathcal{L}^b_{\mathrm{Decay}}\mathcal{L}^b_L\mathcal{L}^b_{JS})}{\prod_{i=b,c,uds} R_i(\mathcal{L}^i_{\mathrm{Decay}}\mathcal{L}^i_L\mathcal{L}^i_{JS})} \tag{5.2}$$

The weights R_b, R_c and R_{uds} give the relative probability to find a jet coming from a given quark flavour. The probabilities are set to $R_b = R_c = 0.2$ and $R_{uds} = 0.6$.

In order to be free of any biases from the data of possible signal processes, and in order to maximise the available number of b quarks in the data, the b tagging has been trained and optimised using data of the calibration run at $\sqrt{s} = m_{\mathrm{Z}}$ in the year 1999. There primarily 2-fermion events are produced. The hadronic events are forced into two jets. The kinematics of the jets of 2-fermion events at $\sqrt{s} = m_{\mathrm{Z}}$ is comparable with the kinematics of 4-fermion events at $\sqrt{s} = 192 - 209$ GeV. The distribution of $\mathcal{B}$ for 2-jet events at $\sqrt{s} = m_{\mathrm{Z}}$ is shown in Fig. 5.1 (a). The data has been taken in the year 1999. The data and the simulation is in good agreement. The jets from primary b quarks are accumulated at high $\mathcal{B}$, while jets from light quarks are found to have low $\mathcal{B}$.

The upper plot in Fig. 5.1 (b) shows the relative difference of $\mathcal{B}$ between data and background for jets opposite to anti-b-tagged jets. There a very low $\mathcal{B}$ is expected. The fluctuation of the data is in good agreement with the expected fluctuation, determined from Monte Carlo simulation and shown in the yellow band. The same systematical test is shown for jets opposite to b-tagged jets in the lower plot of Fig. 5.1 (b). The Plot in Fig. 5.1 (c) shows $\mathcal{B}$ for jets opposite to b-tagged jets. As expected, the data is perfectly described by simulated b quark jets only.

Additional tests of the b tagging have been performed using high-energy data at $\sqrt{s} = 192-209$ GeV. Radiative return events to the Z pole have been used. Also $\mathrm{W}^+\mathrm{W}^-$ events have been studied, for which very few primary b quarks are expected due to the very small CKM matrix elements V_{ub} and V_{cb}. The distribution of $\mathcal{B}$ for those events is shown in Fig. 5.1 (d). Also in this case a very good agreement between data and simulation is achieved.

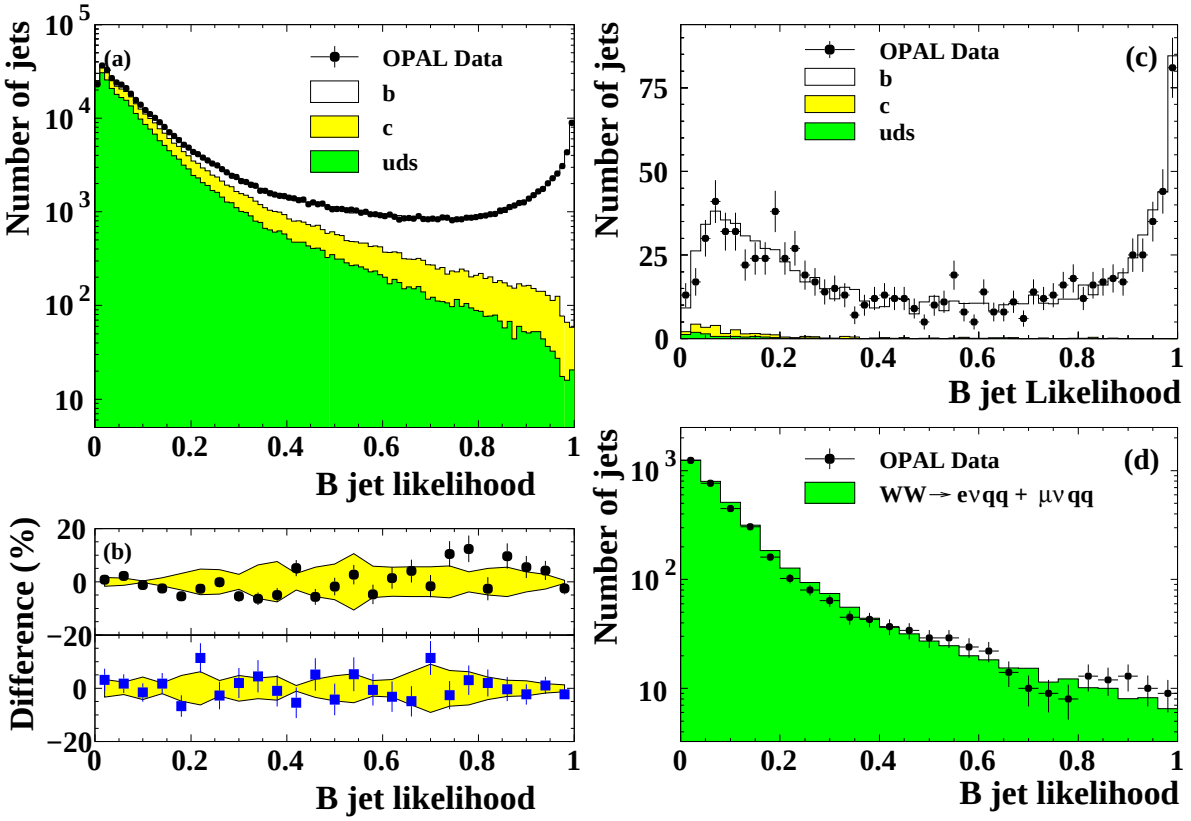

Figure 5.1: *The OPAL b-tag calibration distributions. In (a) the B probability of jets in the calibration data at $\sqrt{s} = m_Z$ in th year 1999 is shown. The simulation of b jets (open), c jets (yellow, light grey) and uds jets (green, dark grey) shows a very good agreement with the data. Jets from b quarks tend to have a large B probability. In (b), the relative difference between the data and the Monte Carlo is tested (see text). In (c), the B probability of jets opposite to b-tagged jets is given, and in (d) the B probability in W^+W^- events is shown [114].*

5.2 The Search for Pair Production with heavy $m_{\mathcal{H}_1}$

The pair production process $e^+e^- \to \mathcal{H}_1\mathcal{H}_2$ is one of the two main Higgs boson production channels in the MSSM. It occurs for large $\cos^2(\beta-\alpha)$, which in most MSSM models is realized in the range of $\tan\beta > 10$ and $m_{\mathcal{H}_1} \leq m_{\mathcal{H}_2}$ not much larger than m_Z. In CPC models, $\cos^2(\beta-\alpha)$ is typically large in regions of the parameter space where $m_{\mathcal{H}_1} \approx m_{\mathcal{H}_2}$. For CPV models, also $m_{\mathcal{H}_1} \ll m_{\mathcal{H}_2}$ occurs. In such a case, the large boost of the light $\mathcal{H}_1$, recoiling against the heavy $\mathcal{H}_2$, leads to a more three-jet-like structure of the event than in the case $m_{\mathcal{H}_1} \approx m_{\mathcal{H}_2}$. Therefore the selection is divided into two parts, depending on the kinematical range of $m_{\mathcal{H}_1}$. For $m_{\mathcal{H}_1} > 30$ GeV, the selection is described in this section.

Events from the process $\mathcal{H}_1\mathcal{H}_2 \to b\bar{b}b\bar{b}$ with high $m_{\mathcal{H}_1}$ have four energetic b-jets and a total visible energy close to the centre-of-mass energy. The dominant background arises from the four-fermion processes, mainly $e^+e^- \to ZZ$ and $e^+e^- \to W^+W^-$, and from two-fermion processes $e^+e^- \to q\bar{q}(\gamma)$. Irreducible background amounts from $e^+e^- \to ZZ$ processes with one or two Z bosons decaying into $b\bar{b}$.

Due to the complexity of the events and due to the fact that there is background from 4-fermion processes, which is very similar to the signal, a multivariate analysis technique is

used to combine the information from several observables into one discriminating variable. The individual steps of the selection are:

- *Preselection*
  A cut-based preselection is used to reduce the background from processes which are strongly different from the signal process, such as $\gamma\gamma$ events. This step also enhances the performance of the following multivariate analysis. If the multivariate analysis had to disentangle the signal process from a background process with large cross-section like the $\gamma\gamma$ process, which is very different from the signal, it would tend to sort the 4-fermion background, which is very similar to the signal and has a much smaller cross-section than the $\gamma\gamma$ process, into the same category as the signal. Thus separation power for the difficult separation of the 4-fermion background from the signal would be lost.

- *Likelihood Selection*
  As a multivariate selection the likelihood technique is chosen. It is very efficient for several input variables with not too strong correlation among each other. It is a good choice if many uncorrelated variables exist, which each have only a limited separation power if they are used without other variables.

The data taken with the OPAL detector in the years 1999 and 2000 have been studied. The centre-of-mass energies range from $\sqrt{s} = 192$ GeV to 209 GeV. The luminosity taken at the different energies is shown in Fig. 4.4 and Tab. 4.2. Monte Carlo Samples for the signal are produced at 192, 196, 200, 202 and 206 GeV. For each Higgs boson mass combination $(m_{\mathcal{H}_1}, m_{\mathcal{H}_2})$ in the Monte Carlo 2000 events are produced, using the generators introduced in Section 4.2. For the background processes (as listed in Tab. 4.3), Monte Carlo samples are produced at $\sqrt{s} = 192, 196, 200, 202, 205, 206$ and 207 GeV.

In the production of the signal Monte Carlo samples it is assumed that the physical width of the Higgs bosons is negligible with respect to the detector resolution. In the models studied in Section 6 this is generally true for $\tan\beta < 40$, where $\Gamma_{\mathcal{H}}$ is smaller than 1 GeV.

Previous searches for the process $e^+e^- \to \mathcal{H}_1\mathcal{H}_2$ at OPAL have been performed at $\sqrt{s} = 91.2 - 189$ GeV[118, 108]. For typical MSSM scenarios studied in Section 6, these searches exclude Higgs bosons produced in pair production with $m_{\mathcal{H}_1} \approx m_{\mathcal{H}_2} < 75$ GeV [108]. Therefore this search is optimised for Higgs boson masses $m_{\mathcal{H}_1} \approx m_{\mathcal{H}_2} = 80 - 90$ GeV.

Preselection

The preselection is designed to reduce background which is not four-jet like and does not include many hadrons. All $\gamma\gamma$ events and all leptonic 2-fermion events are removed. The following cut-based selection is applied:

1. The event must qualify as a multi-hadronic final state as described in Section 5.1. All events with a low number of tracks or unbalanced total momentum are removed. This cut excludes most of the $\gamma\gamma$ background, leptonic 2-fermion events and radiative return events where the ISR photon escapes in the beampipe.

2. The effective centre-of-mass energy $\sqrt{s'}$ [103] after ISR is required to be higher than $0.794\sqrt{s}$. All radiative return events surviving the previous cut are removed. Two different methods are used to calculate $\sqrt{s'}$. Either the ISR photon is radiated with large p_T and visible in the detector. For those events, the largest energy deposition in the electromagnetic calorimeter E_γ without associated track is removed from the event. The effective centre-of-mass energy is then $\sqrt{s'} = \sqrt{(s - E_\gamma)^2 - |\vec{p}_\gamma|^2}$. In the case that

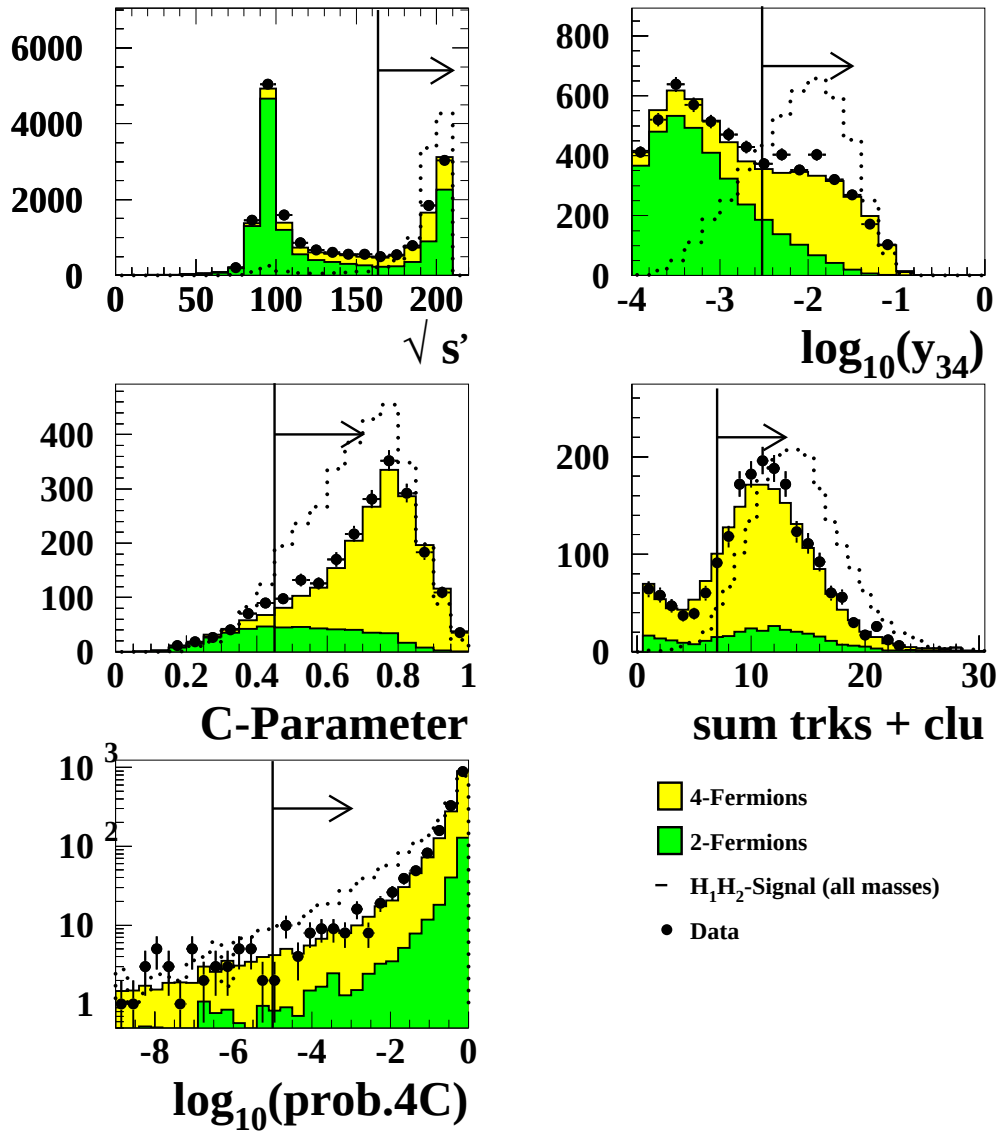

Figure 5.2: *Distribution of the preselection variables in the search for* $e^+e^- \to \mathcal{H}_1\mathcal{H}_2$ *for heavy* $m_{\mathcal{H}_1}$ *and for the data at* $\sqrt{s} = 199 - 209$ *GeV recorded in the year 2000.*

the ISR photon escapes along the beam pipe, the effective centre-of-mass energy is determined using the 3C kinematical fit ($\sqrt{s'}$ fit) introduced in Section 5.1.3. For each measured event, $\sqrt{s'}$ is calculated with both techniques. The smaller of the two values of $\sqrt{s'}$ is used.

3. All events are forced into four jets as described in Section 5.1.2. The 3-to-4 jet resolution parameter y_{43} [110] is required to be larger than 0.003. This cut reduces the largest part of the hadronic 2-fermion background, which is mostly two-jet like. Only 2-fermion events with one or two hard gluons radiated from the outgoing quarks are left after this cut.

4. The C-Parameter [119], which is a measure of the spherical shape of the event, is required

Table 5.1: *Cut flow in the $\mathcal{H}_1\mathcal{H}_2$ channel for high $m_{\mathcal{H}_1}$ and for all data taken at $\sqrt{s}$ = 192 to 209 GeV: effect of the cuts on the data and the background, normalised to the integrated luminosity of the data. The two-photon background, not shown separately, is included in the total background. The signal efficiencies are given in the last column for $m_{\mathcal{H}_1}$=$m_{\mathcal{H}_2}$=90 GeV.*

Cut	Data	Total bkg.	$q\bar{q}(\gamma)$	4-fermi.	Efficiency (%) $m_{\mathcal{H}_1} = m_{\mathcal{H}_2} = 90$ GeV
$\mathcal{H}_2\mathcal{H}_1 \rightarrow$4b Channel					
(1)	39367	39375.6	30958.7	8325.6	99.8
(2)	13792	13895.2	8914.4	4976.0	98.4
(3)	4682	4509.6	1110.5	3397.9	88.3
(4)	3997	3994.5	707.7	3285.7	86.4
(5)	3474	3431.0	566.3	2863.6	85.6
(6)	3331	3271.5	520.4	2749.9	83.7
$\mathcal{L}^{\mathcal{H}_1\mathcal{H}_2} > 0.95$	22	19.9 ± 0.3	6.5	13.4	49.4

to be larger than 0.45. The C-Parameter is calculated from the momentum-tensor θ_{ij} of the event in the following way. The normalised tensor θ_{ij} is defined as

$$\theta_{ij} = \frac{\sum_{a=1}^{N} p_i^a p_j^a / |\vec{p}^a|}{\sum_{a=1}^{N} |\vec{p}^a|}, \tag{5.3}$$

where $i, j = 1, 2, 3$ are the three space directions and a is the number of the particle with momentum $\vec{p}^a$. The sphericity axis (or thrust axis) of the event is the direction of the eigenvector belonging to the largest eigenvalue e_3 of the energy-momentum-tensor matrix. The eigenvalues are $e_1 < e_2 < e_3$. Using these eigenvalues, the C-Parameter is defined as

$$C = 3(e_1e_2 + e_2e_3 + e_1e_3). \tag{5.4}$$

For events which are oriented along one axis (e. g. 2-fermion events), this parameter is small since one or two of the eigenvalues (orthogonal to the thrust axis of the event) are small. Geometrically events with small C-Parameter look cigar- or disk-shaped, whereas the signal events (and 4-fermion events) with high C-Parameter look more like a ball.

5. The sum of the number of reconstructed tracks and electromagnetic clusters not associated to tracks [105, 106] belonging to each jet has to be larger than six. This reduces semileptonic decays of W bosons and events where individual highly energetic photons, for example from ISR, form one of the jets.

6. To discriminate against poorly reconstructed events, a 4-constraint kinematic fit is applied, using energy and momentum conservation; this fit is required to converge and the χ^2 probability is required to be larger than 10^{-5}. The small value of the cut is explained by the fact that also the events surviving the previous five cuts still can have some amount of ISR, which degrades the kinematic fit quality.

The distribution of the preselection variables is shown in Fig. 5.2. Each distribution is shown for the events of all centre-of-mass energies and after all previous cuts. The large amount of radiative return events in the background is clearly visible in the $\sqrt{s'}$ distribution. The y_{43}

distribution shows the large amount of 2-fermion events with $y_{43} < 0.003$. The C-Parameter distribution further reduces the two-jet like background, while the last two cuts clean up badly measured events and events with large amounts of energy in leptons or photons. In all distributions the data is well described by the simulated background.

The cut-flow of the preselection is shown in Tab. 5.1. Already after cut (1) the total background consists almost entirely of 2-fermion and 4-fermion events. There is good agreement between data and background. The signal efficiency for a signal with $m_{\mathcal{H}_1} = m_{\mathcal{H}_2} = 90$ GeV after all preselection cuts is 83.7 %. The remaining 3331 events in the data of the years 1999 and 2000 is further studied using a likelihood selection.

Likelihood Selection

The purpose of the likelihood selection is the separation of the signal from background which is so similar in its properties to the signal, that there exists no single variable which clearly distinguishes the two classes. In such a situation, multivariate analyses can be used to find the most optimal combination of variables to discriminate signal and background.

If infinite statistics were available and systematic effects were precisely known, the most optimal discriminating variable would be

$$\mathcal{L} = \frac{P_s(\vec{O})}{P_s(\vec{O}) + P_b(\vec{O})},$$

where $\vec{O}$ is the vector of observables of a given event, $P_s(\vec{O})$ is the probability to find the multidimensional combination of variables $\vec{O}$ in the signal and $P_b(\vec{O})$ is the probability to find this combination of observables in the background. All distributions of variables and all correlations are taken into account and the optimal separation power of signal from background is achieved. Unfortunately, for several observables O_i and several bins in each observable, the Monte Carlo statistics needed for a precise determination of P_s and P_b becomes impossible, and the selection is very sensitive to mismodelling.

For these reasons, an obvious simplification is to factorise the probability distributions of the individual variables. The likelihood function for i observables O_i used here is

$$\mathcal{L} = \frac{\prod_i P_{s^i}(O_i)}{\prod_i P_{s^i}(O_i) + \prod_i P^{4f}_{b^i}(O_i) + \prod_i P^{2f}_{b^i}(O_i)},$$

where $P^{4f}_{b^i}$ is the probability in the ith variable of an event to stem from the 4-fermion background, and $P^{2f}_{b^i}$ is the probability to belong to the 2-fermion background. By separating the two background classes, the sensitivity is enlarged where the sum of the background has the same probability distribution as the signal, but the individual backgrounds have shapes differing from the signal. In this way, still the optimal sensitivity is obtained for uncorrelated O_i. The larger the correlation, the more the sensitivity degrades, since the likelihood overestimates the separation power of the correlated variables. But still in the presence of correlations the above likelihood is an unbiased estimator of the probability of an event to belong to the signal.

The selection of the variables for the likelihood has been done such that those variables are selected, which have the largest sensitivity for the separation of signal and background, the smallest correlations and little dependence on the Monte Carlo Higgs boson masses. In this way the same selection can be used for a large variety of Higgs boson masses. The information on the mass is used only after the selection in the construction of the discriminating variable for the limit calculation (see Section 5.5). The seven likelihood variables chosen in this selection are

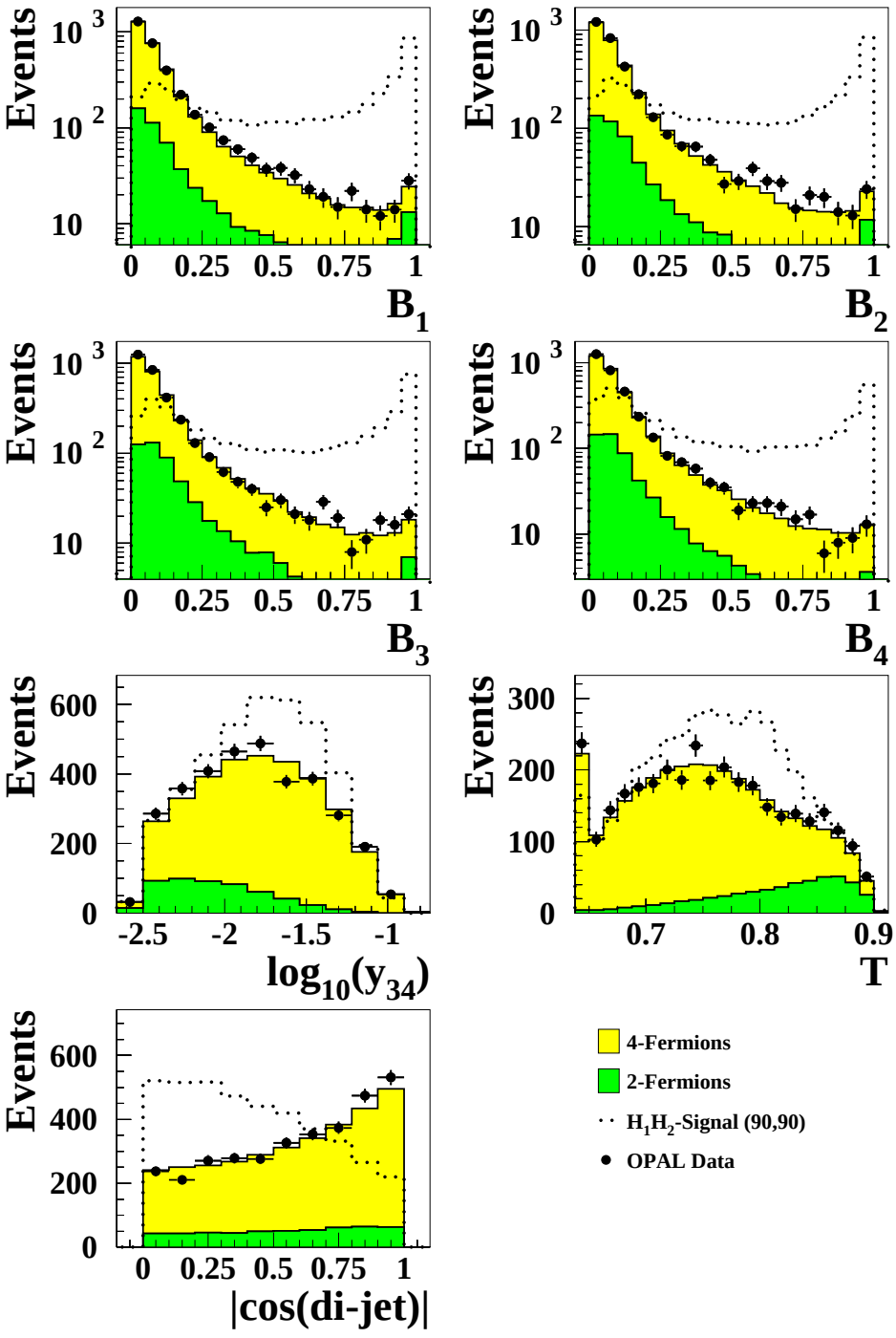

Figure 5.3: *Likelihood input distributions for heavy $m_{\mathcal{H}_1}$ in the search for* $e^+e^- \to m_{\mathcal{H}_1} m_{\mathcal{H}_2} \to b\bar{b}b\bar{b}$. *There is good agreement between data and background simulation.*

1. The four b-tagging discriminants $\mathcal{B}_i$ [108] for each of the four jets, ordered by energy. The b tagging probabilities are ordered by jet energy in order to avoid correlations among them. If an ANN would be used, it could be better to order the $\mathcal{B}_i$ from the best b tag to the worst b tag. This is not beneficial here since it introduces correlations, because events with low best b tag $\mathcal{B}_1$ have very low other b tags, too. The b tags are large for the signal and rather low for the background, which in most cases does not contain four primary b quarks.

2. The logarithm of the jet resolution parameter y_{43}. It is low for 2-fermion events with no four-jet like structure and higher for the signal and the 4-fermion events.

3. The event thrust value T. The thrust value is identical to the largest eigenvalue of the momentum tensor θ_{ij}. It is large for events which are oriented along a longitudinal axis, such as two-jet like events.

4. The estimate of the $\mathcal{H}_1\mathcal{H}_2$ production angle, $|\cos\theta_{\mathrm{dijet}}|$, which is defined as follows. For the jet pairing that yields the smallest difference between the two di-jet-masses, $|\cos\theta_{\mathrm{dijet}}|$ is the absolute value of the cosine of the di-jet polar angle. The four-jet background from WW and ZZ events is dominated by t channel processes, which dominantly have an angular distribution of $\mathrm{d}\sigma/\mathrm{d}\cos\theta \sim (1+\cos^2\theta)/(\sin^4\theta)+\cdots$ [120]. This means that the dominant background is produced in the direction of the beam axis. The pair production signal, on the other hand, is produced according to $\mathrm{d}\sigma/\mathrm{d}\cos\theta = \sin^2\theta$ [56], i. e. more towards the central region. Since the background processes of WW and ZZ production have an equal mass of both bosons, this variable is still sensitive for Higgs boson mass signals with unequal mass, where the angle $\cos\theta_{\mathrm{dijet}}$ is unlikely to yield the correct Higgs boson production angle.

The signal reference histograms are obtained using all Monte Carlo samples with a mass combination of $m_{\mathcal{H}_1} \geq 60$ GeV and $m_{\mathcal{H}_2} \geq 60$ GeV. This ensures sensitivity to a wide range of Higgs boson mass combinations. The reference histograms and the likelihood selection are performed independently for each energy in the data of the year 1999. One common selection is used for the data in the year 2000, which mainly is recorded at$\sqrt{s} = 205 - 207$ GeV. The Monte Carlo Higgs mass combinations produced are shown in Tab. 5.2. For the background, reference histograms are formed from $\mathrm{e^+e^-} \to \mathrm{q\bar{q}}(\gamma)$ and $\mathrm{e^+e^-} \to \mathrm{q\bar{q}q\bar{q}}$ events. All other background processes are suppressed by the preselection (see Tab. 5.1) and need not be taken into account in the reference histogram generation. The distributions of the input variables to the likelihood are shown in Fig. 5.4. Good agreement between data and Monte Carlo simulation is observed.

The distribution of the likelihood output is shown in Figure 5.4. Also here a very good agreement of data and background simulation is observed. The signal is clearly centred at high values of $\mathcal{L}$. Events are selected if they satisfy $\mathcal{L} > 0.95$, which provides the best sensitivity measured in terms of $s/\sqrt{b+2}$ for $m_{\mathcal{H}_1} = m_{\mathcal{H}_2} = 90$ GeV for s signal events and b background events. The significance in terms of $s/\sqrt{b+2}$ is the best estimate of the sensitivity of Poisson-distributed variables [121]. This is used as an estimate for the optimisation of the likelihood cut. The final calculation of the significance is described in detail in Section 6.

The numbers of observed and expected background events after each preselection cut and the final likelihood cut are shown in Table 5.1 for data taken at $\sqrt{s} = 192$ to 209 GeV. In the data at $\sqrt{s} = 192 - 209$ GeV, taken in the years 1999 and 2000, the following number of

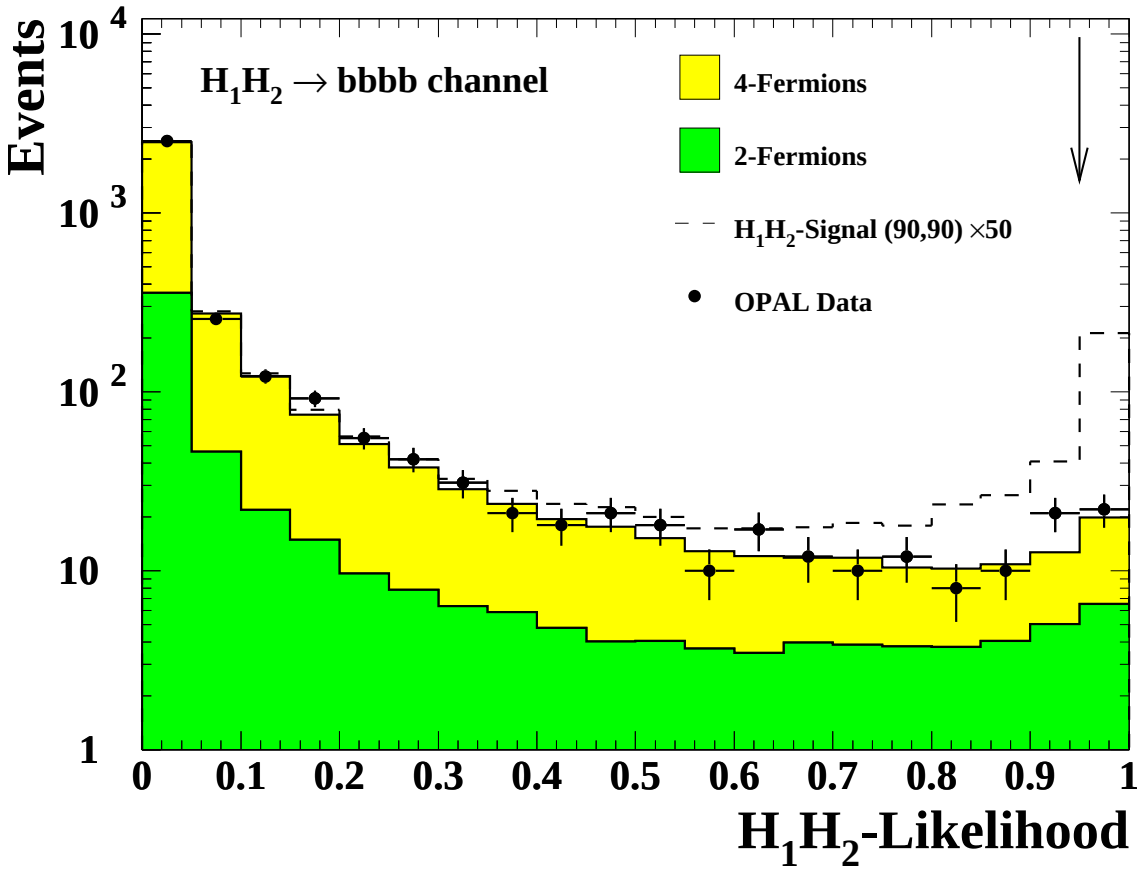

Figure 5.4: *Likelihood distribution in the* $e^+e^- \rightarrow H_1H_2 \rightarrow b\bar{b}b\bar{b}$ *channel for heavy* $m_{\mathcal{H}_1}$. *There is good agreement between data and background simulation.*

events is observed:

Expected background:	19.9 ± 0.3 events
Observed data:	22 events

These numbers are in agreement with each other, since the statistical uncertainty of 22 events is ±4.7 events. No clear sign of Higgs bosons has been found.

The efficiencies for various combinations of $(m_{\mathcal{H}_1}, m_{\mathcal{H}_2})$ are shown in Tab. 5.2. It can be seen that the search is optimised for mass combinations with heavy $m_{\mathcal{H}_1}$ and $m_{\mathcal{H}_2}$ and small $m_{\mathcal{H}_2} - m_{\mathcal{H}_1}$. The efficiency for a signal with $m_{\mathcal{H}_1} = m_{\mathcal{H}_2} = 90$ GeV is $\varepsilon = 47.9\,\%$. The efficiency degrades for low masses, which in the scenarios studied in Section 6 are already excluded from the data taken at lower energies.

The mass of the Higgs boson candidates is reconstructed using the 4C fit requiring energy and momentum conservation. The mass of the Higgs bosons can be reconstructed each from the mass of a pair of jets. This is illustrated in Fig. 5.5. For four jets, three different possible pairings of the jets exist which can be used to calculate the Higgs mass according to $m_{\mathcal{H}} = (E_i + E_j)^2 - (\vec{p}_i + \vec{p}_j)^2$ for the pair ij of jets. For illustration, the three mass combinations of

Table 5.2: *Signal efficiencies of the* $\mathcal{H}_1\mathcal{H}_2 \to \mathrm{b\bar{b}b\bar{b}}$ *analysis for high* $m_{\mathcal{H}_1}$*. The uncertainty from Monte Carlo statistics is typically of the order of* ± 0.015*. The table summarises the Monte Carlo points produced.*

	Efficiency for the process $\mathcal{H}_2\mathcal{H}_1 \to \mathrm{b\bar{b}b\bar{b}}$ (high $m_{\mathcal{H}_1}$) at $\sqrt{s} = 206$ GeV						
$m_{\mathcal{H}_1}$ (GeV)	30.0	40.0	50.0	60.0	70.0	80.0	90.0
$m_{\mathcal{H}_2}$ (GeV)							
30.0	0.001						
40.0	0.0008	0.004					
50.0		0.110	0.215				
60.0	0.103		0.274	0.364			
70.0		0.254		0.381	0.388		
80.0	0.200		0.384		0.425	0.470	
90.0		0.319		0.388		0.472	0.479
100.0			0.374		0.432		0.435
110.0		0.341		0.371			
120.0	0.261		0.349		0.399		
130.0		0.253		0.368			
140.0	0.231		0.290				
150.0		0.177					
160.0	0.116						

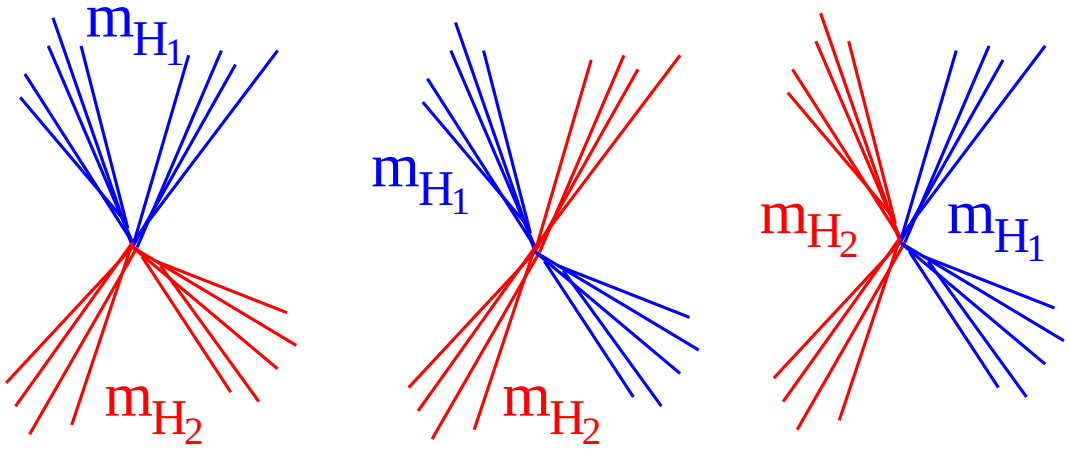

Figure 5.5: *The 3 different di-jet mass combinations. The jets of each four-jet event can be grouped to two pairs of jets (di-jets) such that three different mass combinations occur.*

the two Higgs boson masses are ordered according to their mass difference $\Delta m = m_{\mathcal{H}_2} - m_{\mathcal{H}_1}$. Figures 5.6(a)–(c) show the distributions of the sum of the reconstructed Higgs boson masses, $M_{\mathrm{sum}} = m^{\mathrm{rec}}_{\mathcal{H}_1} + m^{\mathrm{rec}}_{\mathcal{H}_2}$, for the jet combination with the largest, second largest and smallest value for $|m^{\mathrm{rec}}_{\mathcal{H}_1} - m^{\mathrm{rec}}_{\mathcal{H}_2}|$. No significant excess over the expected background is observed. It can be seen that the dominant background emerges from Z pair production, which creates a peak in the mass distribution of Fig. 5.6(a) at $m_{\mathcal{H}_1} + m_{\mathcal{H}_2} = 2m_{\mathrm{Z}}$. The signal shown in Fig. 5.6 has $m_{\mathcal{H}_1} = m_{\mathcal{H}_2} = 80$ GeV. It is normalised to the expected number of selected signal events

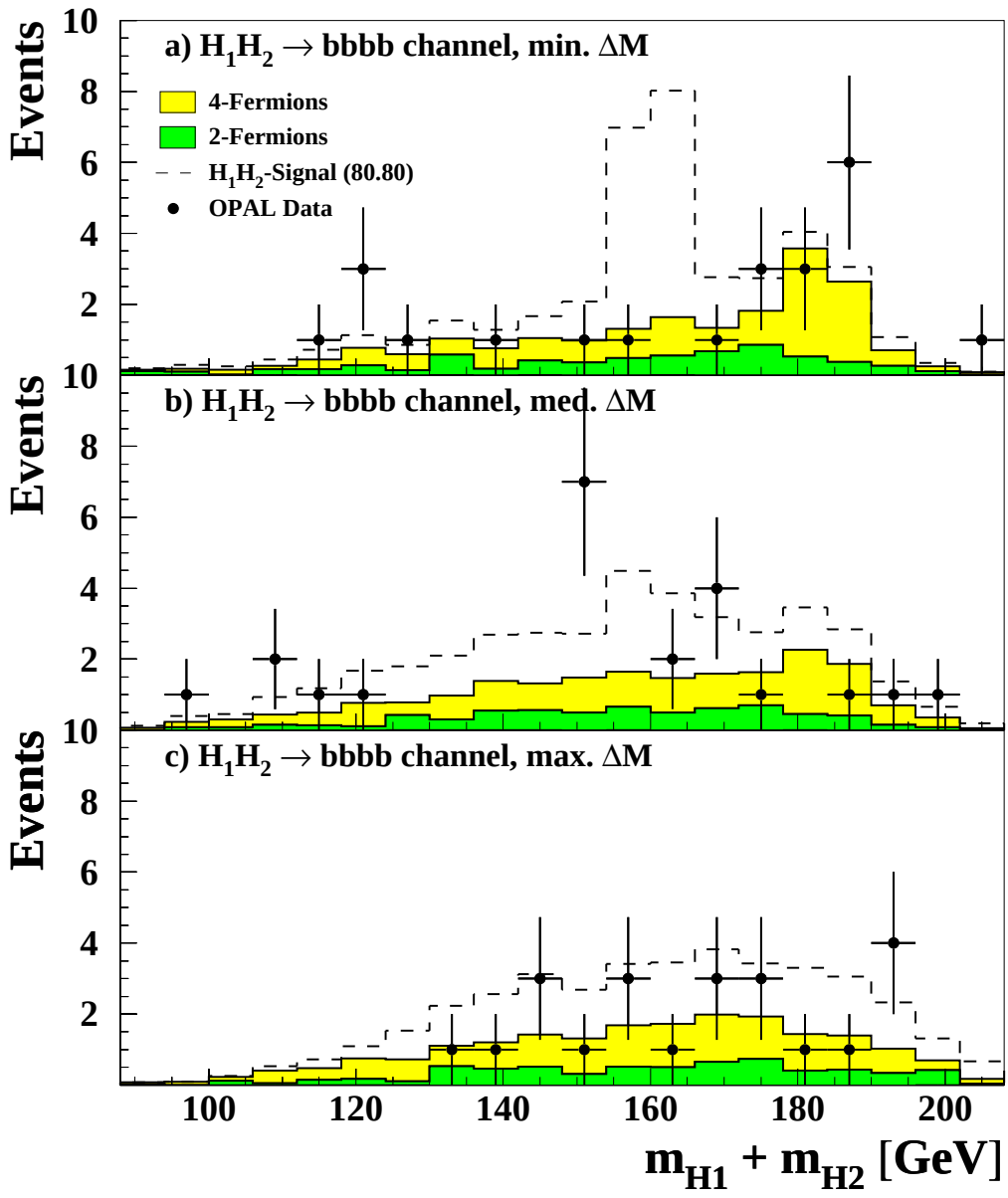

Figure 5.6: *Mass distributions for heavy $m_{\mathcal{H}_1}$. In (a), the sum of the reconstructed Higgs boson masses $m_{\mathcal{H}_1} + m_{\mathcal{H}_2}$ is shown for the jet mass combination with the lowest $\Delta m = m_{\mathcal{H}_2} - m_{\mathcal{H}_1}$. Plot (b) shows $m_{\mathcal{H}_1} + m_{\mathcal{H}_2}$ for the di-jet combination with intermediate Δm, and (c) shows the di-jet combination with largest Δm.*

for $\cos^2(\beta - \alpha) = 1$. It shows a clear peak in the mass combination with minimal Δm. For the other mass combinations it has a flat distribution, since in these wrong combination cases the mass information is coming from a random combination of jet momenta.

The discriminating variable $\mathcal{D}$, which is used in the derivation of limits on cross-sections and MSSM parameters (see Section 6), is a two-dimensional array of reconstructed masses $m^{\text{rec}}_{\mathcal{H}_2} + m^{\text{rec}}_{\mathcal{H}_1}$ and $m^{\text{rec}}_{\mathcal{H}_2} - m^{\text{rec}}_{\mathcal{H}_1}$. Its construction is explained in Section 5.5. The systematic uncertainties are listed in Table 5.5 and are derived as described in Section 5.4. They amount to 3.1% for the signal and 10.3% for the background expectation.

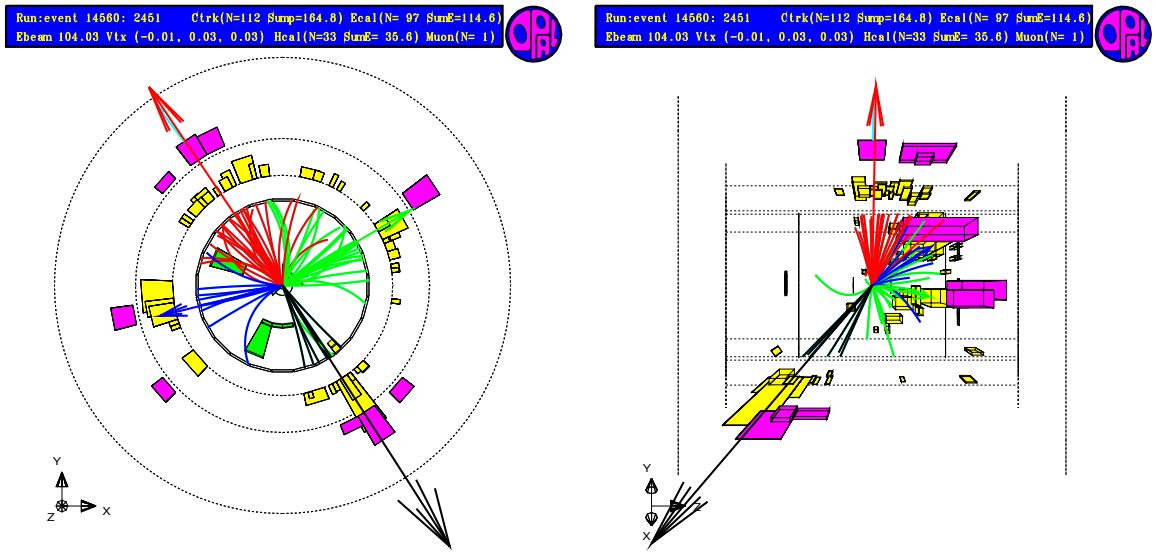

Figure 5.7: *An event selected by the search for pair production with heavy $m_{\mathcal{H}_1}$. The $r\phi$ view is shown on the left and the rz view is shown on the right. The four-jet structure is clearly visible.*

A typical data event selected by the search for $e^+e^- \to \mathcal{H}_1\mathcal{H}_2 \to b\bar{b}b\bar{b}$ with heavy $m_{\mathcal{H}_1}$ is shown in Fig. 5.7. The event was recorded in the year 2000 at $\sqrt{s} = 207$ GeV. It has full visible energy in the detector, a large number of tracks and clusters per jet and a lot of activity in the hadronic calorimeter. It shows a clear four-jet structure, which is best visible in the xy view. In the rz view, it can be seen that it is clearly centred at $\cos\theta \approx 0$ and not going into the forward direction as most of the WW and ZZ background events. It has mostly good b-tags of $\mathcal{B} = 0.98$, 0.93, 0.77 and 0.14.

5.3 The Search for Pair Production with small $m_{\mathcal{H}_1}$

The selection presented above is not sensitive for small $m_{\mathcal{H}_1}$ and large mass differences Δm. For $m_{\mathcal{H}_1} < 30$ GeV and $m_{\mathcal{H}_2} > 90$ GeV, the recoil of the light Higgs boson with respect to the heavier one leads to a strong boost of the decay products of the light Higgs boson $\mathcal{H}_1$. Additionally, due to its low mass, the transverse momentum of the decay products with respect to the $\mathcal{H}_1$ flight direction is small. Therefore the two jets of the $\mathcal{H}_1 \to b\bar{b}$ system are very close together. On the other hand, the $\mathcal{H}_2$ has a small boost and the transverse momentum of its decay products with respect to its flight direction is large, therefore two distinct jets appear from the $\mathcal{H}_2 \to b\bar{b}$ system.

This different kinematic region is covered with a separate selection, introduced in this section. It is applied solely for data taken at $\sqrt{s} = 199 - 209$ GeV in the year 2000. Only one likelihood selection for all energies in the data of the year 2000 is used. The region 12 GeV $< m_{\mathcal{H}_1} < 30$ GeV and $m_{\mathcal{H}_2} > 90$ GeV is of particular interest in the CPV scenario. The following selection is optimised for that kinematic region. The same analysis framework as for large $m_{\mathcal{H}_1}$ is used, but the preselection is modified and the reference histograms of the likelihood selection are changed in order to be most sensitive to events with small $m_{\mathcal{H}_1}$ and large Δm.

Table 5.3: *Cut flow in the $\mathcal{H}_1\mathcal{H}_2$ channel for low $m_{\mathcal{H}_1}$ (see Section 5.3) and for all data taken at $\sqrt{s}$ = 199 to 209 GeV. Shown is the effect of the cuts on the data and the background, normalised to the integrated luminosity of the data. The two-photon background, not shown separately, is included in the total background. The signal efficiencies are given in the last column for $m_{\mathcal{H}_1}$=30 GeV and $m_{\mathcal{H}_2}$=100 GeV in the $\mathcal{H}_1\mathcal{H}_2 \to \mathrm{b\bar{b}b\bar{b}}$ channel.*

Cut	Data	Total bkg.	$\mathrm{q\bar{q}}(\gamma)$	4-fermi.	Efficiency (%) $m_{\mathcal{H}_1} = 30$, $m_{\mathcal{H}_2} = 100$ GeV
$\mathcal{H}_1\mathcal{H}_2 \to$4b Channel for low $m_{\mathcal{H}_1}$					
(1)	18519	17802.0	13705.2	4096.9	99.6
(2)	6538	6427.8	3971.6	2456.3	96.2
(3)	4215	4048.0	2082.4	1965.6	94.2
(4)	3618	3497.5	1546.8	1950.6	93.6
(5)	2712	2625.9	1188.5	1437.4	90.5
(6)	2477	2389.4	1060.0	1329.5	83.5
$\mathcal{L}^{\mathcal{H}_1\mathcal{H}_2} > 0.98$	8	10.4 ± 0.1	6.1	4.3	36.9

Preselection

The distribution of the variables used for the preselection is shown in Fig. 5.8. The preselection is identical to the one of Section 5.2 except for cuts (3) and (4). In (3) the cut on y_{43} is relaxed to 0.0003. As visible in Fig. 5.8, due to the more three-jet like structure of the signal events, the signal distribution of y_{43} peaks at much smaller values than in Fig. 5.2.

In order to compensate for the increased $\mathrm{q\bar{q}}\gamma$-background passing the cut on y_{43}, an additional requirement is introduced in cut (3): the sum of the two smallest angles between any jets, J_2, has to satisfy the requirement $30^\circ < J_2 < 175^\circ$ and the sum of the four smallest angles between jets, J_4, has to satisfy $220^\circ < J_4 < 400^\circ$. These variables are shown in Fig. 5.8. The cut on the C-Parameter in (4) is relaxed to $C > 0.2$. This increases the acceptance for asymmetric three-jet-like events, since the sphericity of the event can be smaller. The number of selected events after each cut, along with the expected background, is shown in Table 5.3. Compared with the selection shown in Tab. 5.1, it can be seen that more 2-fermion background passes the preselection, since less four-jet like events are allowed. The signal efficiency after preselection is 83.5 %.

Likelihood Selection

After the preselection, a likelihood function is constructed from the same seven variables as described in Section 5.2. However, the signal reference histograms are formed from Monte Carlo samples with $12 < m_{\mathcal{H}_1} < 30$ GeV and $90 < m_{\mathcal{H}_2} < 110$ GeV. The distributions of the input variables are shown in Fig. 5.9. While the distribution of the b-tag variables $\mathcal{B}_i$ is similar to those of Fig. 5.3, the signal peaks at lower y_{43}. The variable $|\cos\theta_{\mathrm{dijet}}|$ looses some of its sensitivity due to the fact that the signal does not come from the di-jet mass combination with the smallest mass difference Δm.

The resulting likelihood distribution is shown in Fig. 5.10. An excess of the data over the expected background can be seen around $0.6 < \mathcal{L} < 0.8$. In order to test the significance of this excess the background and data have been integrated starting from $\mathcal{L} = 1$. The strongest statistical significance of the excess is $2.52\,\sigma$, which is reached at $\mathcal{L} = 0.6$. Given the fact

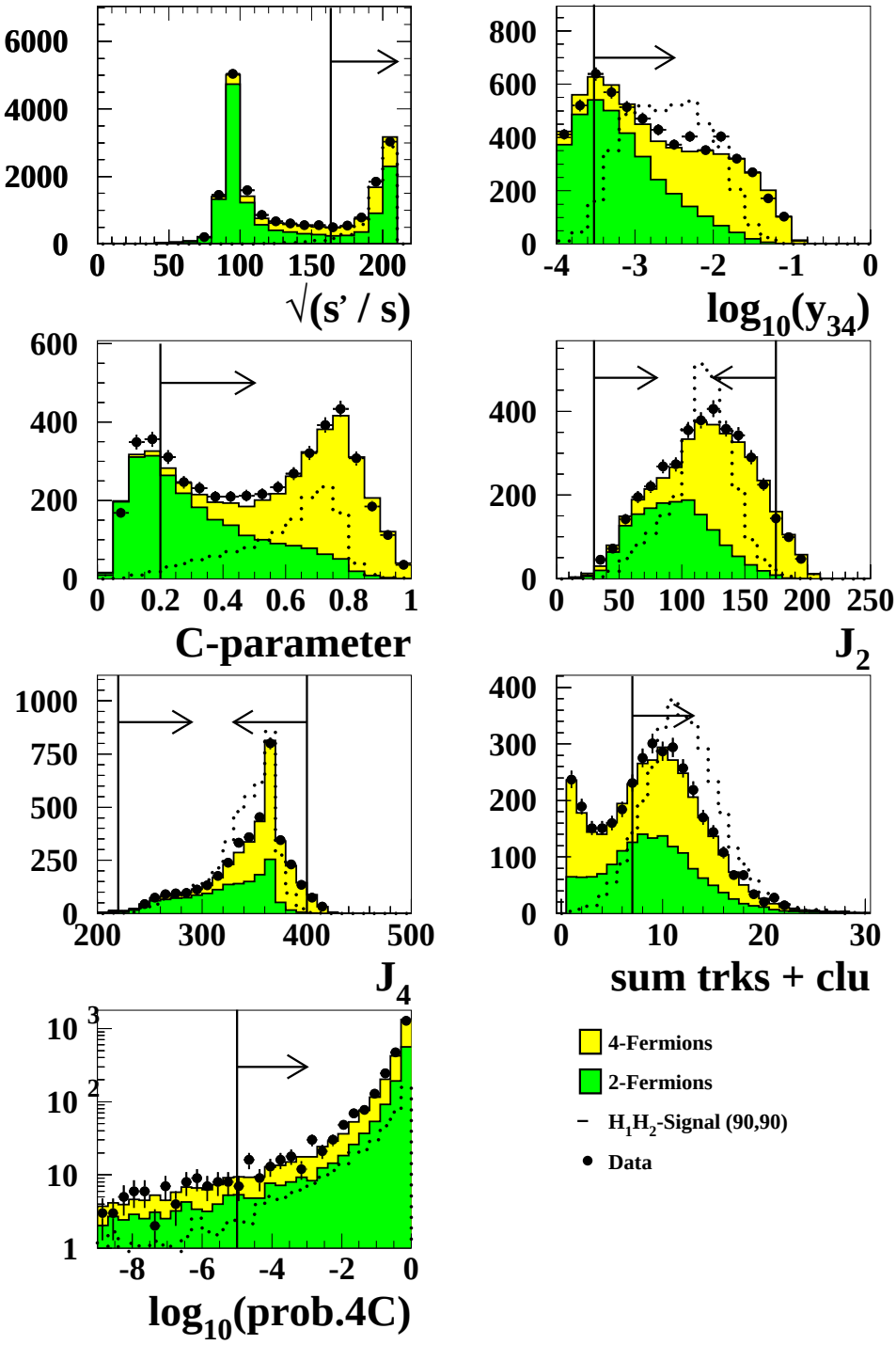

Figure 5.8: *Distribution of the preselection variables in the search for* $e^+e^- \to \mathcal{H}_1\mathcal{H}_2$ *for light* $m_{\mathcal{H}_1}$.

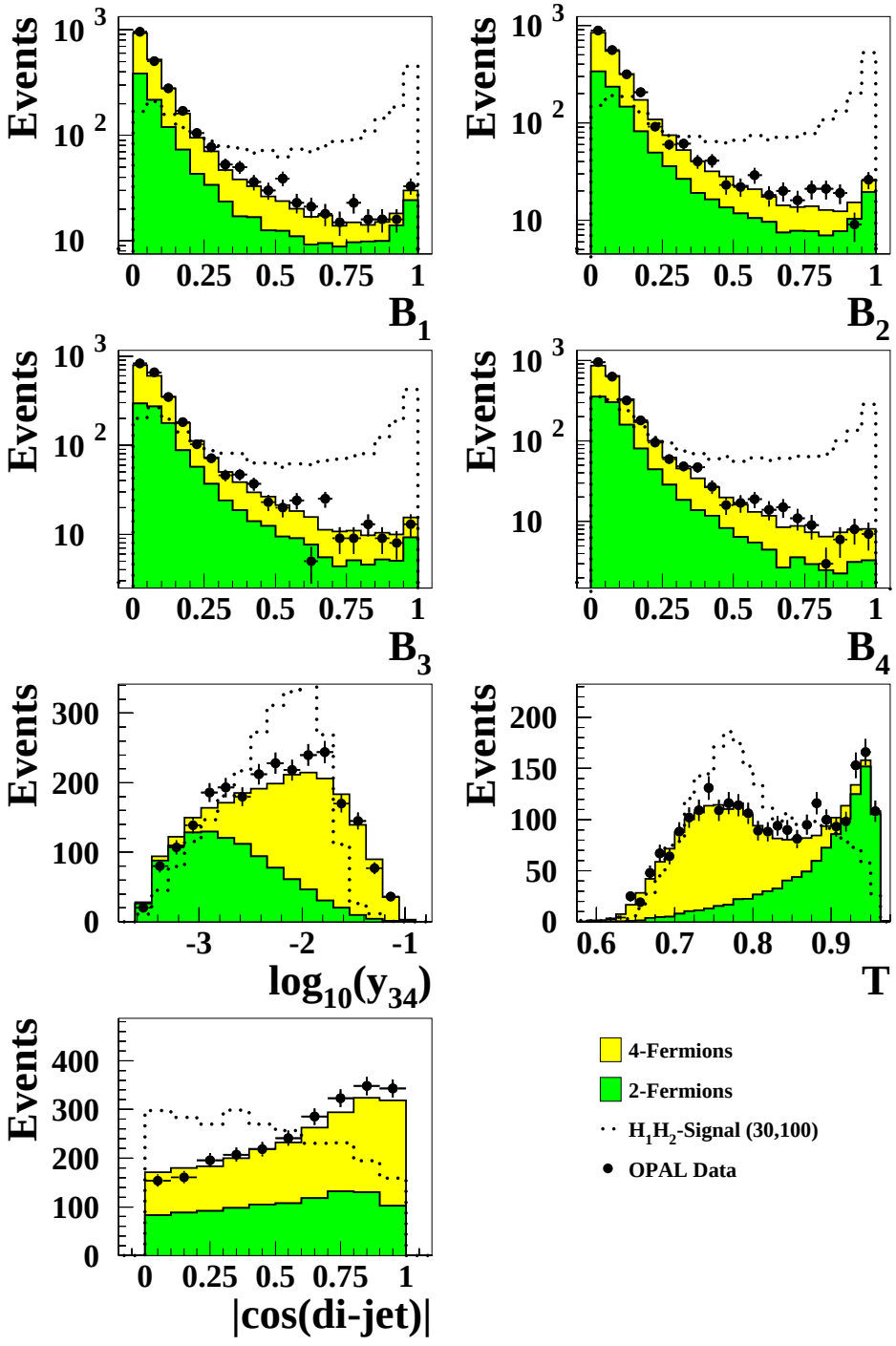

Figure 5.9: *Likelihood input distributions for light* $m_{\mathcal{H}_1}$.

that it is not in the signal region, the excess of this significance is regarded as acceptable. Most probably it is due to the modelling of hard gluon radiation from 2-fermion events, which represents a more significant background in this search compared with the search in Section 5.2.

The cut $\mathcal{L} > 0.98$ is applied, which is optimal for $m_{\mathcal{H}_1} = 30$ GeV and $m_{\mathcal{H}_2} = 100$ GeV. Due to the larger amount of 2-fermion background after the preselection, the likelihood cut has to

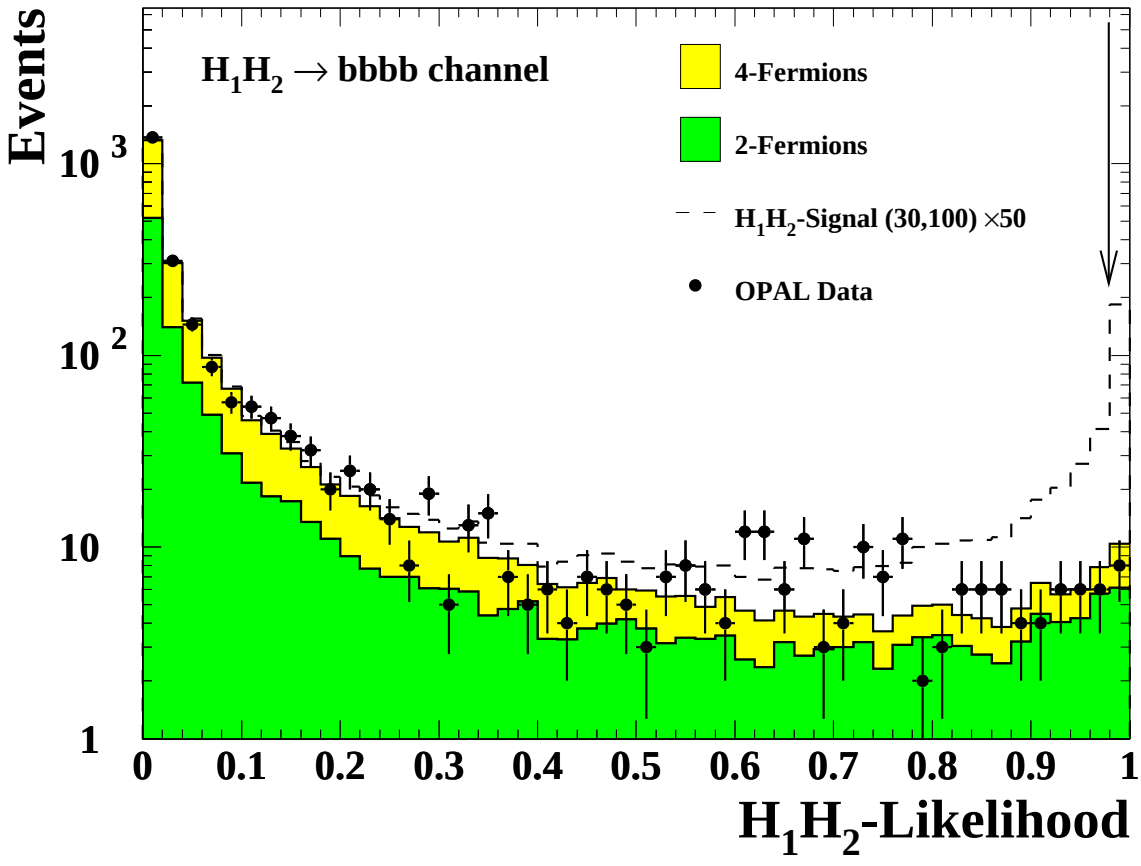

Figure 5.10: *Likelihood distribution in the* $e^+e^- \rightarrow H_1H_2 \rightarrow b\bar{b}b\bar{b}$ *channel for light* $m_{\mathcal{H}_1}$.

be tightened with respect to the selection in Section 5.2. The observed number of events in data and the expected number of events in the background is

Expected background:	10.4 ± 0.1 events
Observed data:	8 events

which is statistically in agreement with each other. No sign of Higgs boson pair production in this kinematic region has been found. The efficiencies for various combinations of $(m_{\mathcal{H}_1}, m_{\mathcal{H}_2})$ are shown in Table 5.4. The selection has an almost uniform efficiency over the mass range under study. The efficiency for $m_{\mathcal{H}_1} = 30$ GeV and $m_{\mathcal{H}_2} = 100$ GeV is 36.9 %.

The distribution of the reconstructed mass sum M_{sum} is shown in Fig. 5.11. No significant excess over the background is observed. The dominance of the Z pair background is slightly reduced compared to the mass distribution in Fig. 5.6, but still a peak is visible at $m_{\mathcal{H}_1} + m_{\mathcal{H}_2} = 2m_Z$ in the background distribution for small Δm. The signal for $m_{\mathcal{H}_1} = 30$ GeV and $m_{\mathcal{H}_2} = 100$ GeV emerges in the distributions for intermediate and large Δm at $m_{\mathcal{H}_1} + m_{\mathcal{H}_2} = 130$ GeV over a continuous background of 2-fermion and 4-fermion events.

As in Section 5.2, the discriminating variable $\mathcal{D}$ is a two-dimensional array of reconstructed masses $m_{\mathcal{H}_2} + m_{\mathcal{H}_1}$ and $m_{\mathcal{H}_2} - m_{\mathcal{H}_1}$. The systematic uncertainties are listed in Table 5.5 and

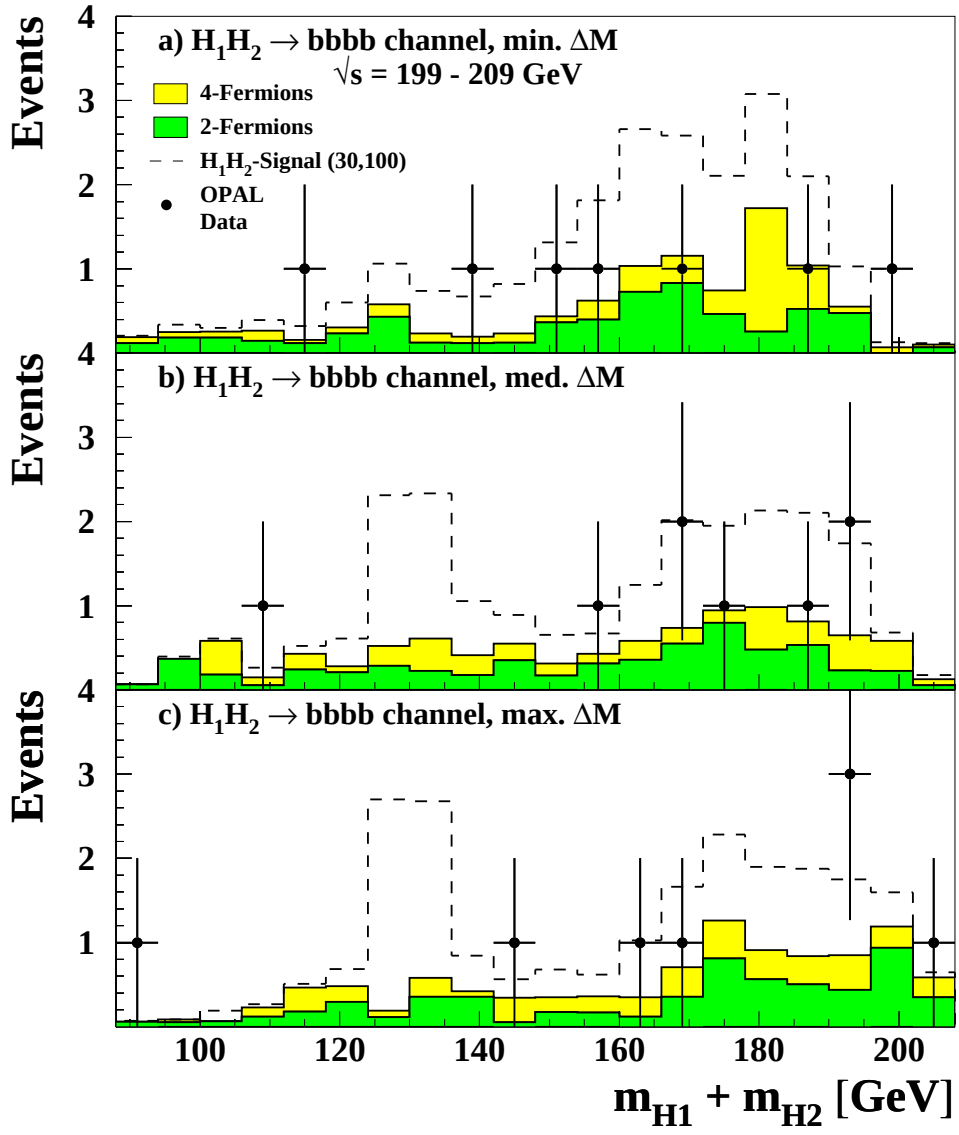

Figure 5.11: *Mass distributions for light $m_{\mathcal{H}_1}$. In the uppermost plot, the sum of the reconstructed Higgs boson masses $m_{\mathcal{H}_1} + m_{\mathcal{H}_2}$ is shown for the jet mass combination with the lowest $\Delta m = m_{\mathcal{H}_2} - m_{\mathcal{H}_1}$. The plot in the middle shows $m_{\mathcal{H}_1} + m_{\mathcal{H}_2}$ for the di-jet combination with intermediate Δm, the lowest plot shows the di-jet combination with largest Δm.*

are derived in the same way as for the search described in Section 5.2. They amount to 4.7% for the signal and 10.5% for the background expectation.

A typical event selected by the search for $e^+e^- \rightarrow \mathcal{H}_1\mathcal{H}_2$ with light $m_{\mathcal{H}_1}$ is shown in Fig. 5.12. It has been recorded in the year 2000 at an energy of $\sqrt{s} = 207$ GeV. With respect to the event shown in Fig. 5.7, it clearly has a more three-jet like shape. Also this event is relatively central in the detector and it has full energy. It has mostly good b-tags of $\mathcal{B} = 0.99$, 0.96, 0.52 and 0.44.

Table 5.4: *Signal efficiencies of the* $\mathcal{H}_1\mathcal{H}_2 \to \mathrm{b\bar{b}b\bar{b}}$ *analysis for low* $m_{\mathcal{H}_1}$ *(see Section 5.3). The uncertainty from Monte Carlo statistics is of the order of* ± 0.011.

Efficiency for the process $\mathcal{H}_2\mathcal{H}_1 \to \mathrm{b\bar{b}b\bar{b}}$ (low $\mathcal{H}_1$) at $\sqrt{s} = 206$ GeV			
$m_{\mathcal{H}_1}$ (GeV)	12.0	20.0	30.0
$m_{\mathcal{H}_2}$ (GeV)			
90.	0.269	0.330	0.370
95.	0.286	0.341	0.384
100.	0.305	0.366	0.369
105.	0.310	0.358	0.369
110.	0.298	0.351	0.366

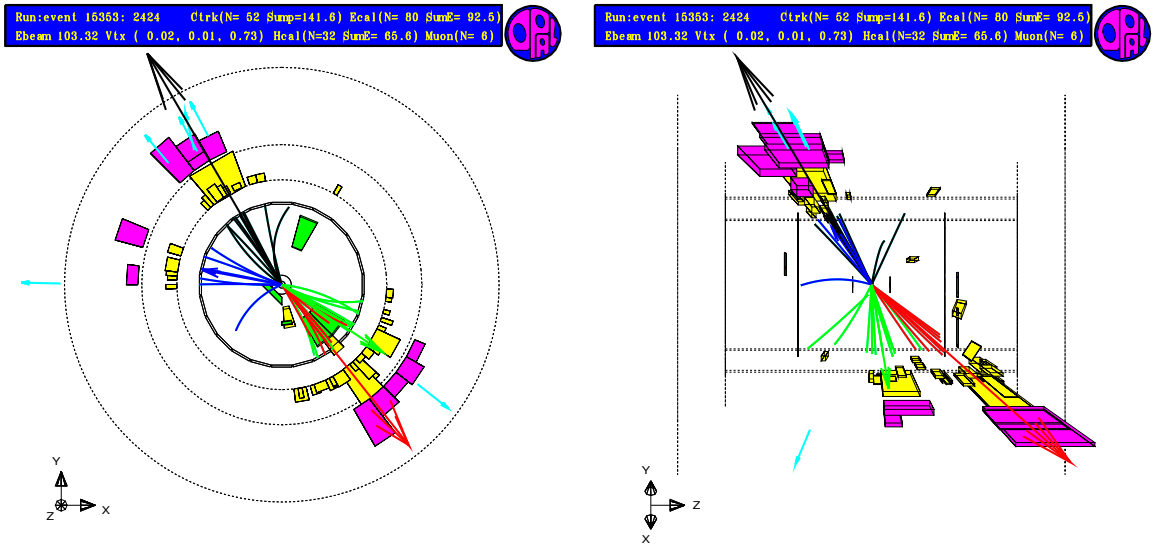

Figure 5.12: *An event selected by the search for pair production with light* $m_{\mathcal{H}_1}$*. The more three-jet like shape with respect to the selected event shown in Section 5.2 is clearly visible.*

5.4 Systematic Uncertainties

The knowledge of the physics processes involved in signal and background is not complete and perfectly precise, e. g. there are uncertainties in the modelling of fragmentation and hadronisation processes, which are important for the efficiency of the search for the signal, and for the number of background events selected. Additionally, the knowledge of the precision and efficiency of the OPAL detector is not perfect. The detector simulation might use slightly different precision as the real detector achieves. These uncertainties are studied in this section.

For each uncertainty, the selection is repeated with varied assumptions on the source of uncertainty. The relative difference of the number of selected signal and background events is then quoted as systematic uncertainty.

The systematic uncertainties on the signal efficiencies and background expectation for the $\mathcal{H}_1\mathcal{H}_2 \to \mathrm{b\bar{b}b\bar{b}}$ search are given in Table 5.5. They are evaluated as for the SM Higgs boson searches in [114] and include the sources listed in the following. Together with the sources of uncertainty the assumption on the correlation of the uncertainty among different search

Table 5.5: *Systematic uncertainties on the signal efficiency and background at $\sqrt{s}$= 206 GeV for the processes $\mathcal{H}_1\mathcal{H}_2 \to \mathrm{b\bar{b}b\bar{b}}$ with high $m_{\mathcal{H}_1}$, low $m_{\mathcal{H}_1}$ and for $\mathcal{H}_2\mathcal{H}_1 \to \mathrm{b\bar{b}}\tau^+\tau^-, \tau^+\tau^-\mathrm{b\bar{b}}$.*

Systematic uncertainties at $\sqrt{s}$= 206 GeV				
	$\mathcal{H}_2\mathcal{H}_1 \to \mathrm{b\bar{b}b\bar{b}}$ (high $m_{\mathcal{H}_1}$)		$\mathcal{H}_2\mathcal{H}_1 \to \mathrm{b\bar{b}b\bar{b}}$ (low $m_{\mathcal{H}_1}$)	
Source	Signal eff.	Background	Signal eff.	Background
MC statistics	2.0%	5.0%	3.0%	5.2%
Detector modelling	0.9%	8.0%	1.1%	8.6%
B-had. Decay Mult.	0.9%	1.2%	2.1%	1.9%
B-had. Fragment.	1.8%	1.5%	2.7%	1.5%
C-had. Fragment.	0.0%	0.5%	0.0%	0.0%
4f-cross-section	0.0%	1.6%	0.0%	1.0%
MC-Generators	0.0%	2.6%	0.0%	2.6%
variable modelling	0.9%	2.3%	1.0%	2.1%
Combined	3.1%	10.3%	4.7%	10.9%

channels is given. For example, the uncertainty of the tracking resolution affects all searches in the same way, therefore in the calculation of limits on masses, model parameters or cross-sections in Section 6 such an uncertainty has to be handled correlated in all channels. The following sources of systematic uncertainties are investigated:

- *Monte Carlo statistics*:
  The Monte Carlo event samples used for the determination of signal and background rates have only limited statistics, therefore a statistical uncertainty of the number of expected events exists. This uncertainty affects the signal and background rate and is uncorrelated between channels, energies, and signal and background, since the number of selected Monte Carlo events is independent in each selection. It is determined from the statistical error of the selected Monte Carlo events.

The following uncertainties are correlated between all channels and centre-of-mass energies. The first part of them describe the uncertainty of the detector precision and uncertainty.

- *Tracking resolution in $r\phi$*:
  This uncertainty is evaluated with the Monte Carlo simulation by multiplying the discrepancy between the true and reconstructed values of the track's impact parameter in the $r\phi$ plane, azimuthal angle ϕ and curvature by smearing factors of 1.05 and comparing efficiencies to the simulation without extra smearing. The smearing factor 1.05 adequately covers the uncertainties seen in Figure 5.1(b). The factor of 1.05 is determined from tracking and alignment studies. In order to calculate the effect of this uncertainty, the signal and background Monte Carlo samples are reconstructed with varying track resolution.

- *Tracking resolution in z*:
  This uncertainty is evaluated by treating the track impact parameter in z and $\tan\lambda = \cot\theta$ in the same way as described above, again using smearing factors of 1.05.

- *Hit-matching efficiency for $r\phi$-hits in the silicon microvertex detector*:
  One percent of the hits on the $r\phi$ strips of the silicon microvertex detector, which are associated to tracks, are randomly dropped and the tracks are refitted. The hit dropping

fractions were obtained from studies of the Z calibration data. Also here the effect of this uncertainty on the selected number of events is evaluated using a reconstruction of the Monte Carlo samples with varying hit-matching efficiency.

- *Hit-matching efficiency for z-hits in the silicon microvertex detector*:
  This uncertainty is evaluated in the same way as for the $r\phi$ hits, except that 3% of the z-hits are dropped.

For the presentation in Tab. 5.5, all the above errors are combined into one error one detector modelling. For the limit calculation in Section 6 all errors are studied separately. The following errors describe the uncertainty of the hadronisation and fragmentation physics processes involved in signal and background events.

- *B hadron charged decay multiplicity*:
  The average number of charged tracks in B hadron decay is varied within the range measured by the LEP Electroweak Heavy Flavour Working Group [122], $n_{\mathrm{B}} = 4.955 \pm 0.062$. The uncertainty is given a positive sign if the selection efficiency increases with the average decay multiplicity. The uncertainty is evaluated using event reweighting.

- *B hadron momentum spectrum*:
  The b fragmentation function has been varied so that the mean fraction of the beam energy carried by B hadrons, $\langle x_E(\mathrm{b})\rangle$, is varied in the range 0.702 ± 0.008 [122] using a reweighting technique. The uncertainty is given a positive sign if the selection efficiency rises with increasing average momentum.

- *Charm hadron momentum spectrum*:
  As for the B hadron momentum spectrum, $\langle x_E(\mathrm{c})\rangle$ has been varied in the range 0.484 ± 0.008 [122].

- *Comparison of different SM background Monte Carlo generators*:
  Besides the main generators used (see Section 4), the background simulations are cross-checked with alternative generators and fragmentation models such as KORALW [123] and HERWIG [124] with multiplicities reweighted to match the JETSET [80] multiplicities. The fragmentation of the hadronic particles is described in empirical models, therefore an estimate of the uncertainty of the model can only be made by comparisons between different models.

- *Four-Fermion production cross-section*:
  This is taken to have a 2% relative uncertainty, arising from the uncertainty in the ZZ and $\mathrm{W^+W^-}$ cross-sections [125].

The remaining uncertainties are channel dependent and assumed uncorrelated between the channels, but correlated between centre-of-mass energies for the same channel:

- *Modelling of variables*:
  The distribution in the data of the variables used in the preselection and in the likelihood selection are not necessarily modelled perfectly in the background Monte Carlo samples. Therefore an uncertainty exists stemming from the potential mismodelling of the variables. These uncertainties are evaluated by rescaling each input variable in the Monte Carlo individually so as to reproduce the mean of the distribution of this variable in the data. This scaling is done at the level of the preselection cuts and the contributions evaluated for each of the variables are then summed in quadrature.

In case of the search for pair production with heavy $m_{\mathcal{H}_1}$, the systematic uncertainty amounts to 3.1% for the signal and 10.3% for the background expectation. In case of the selection for light $m_{\mathcal{H}_1}$, they amount to similar numbers, namely 4.7% for the signal and 10.5% for the background expectation.

5.5 Construction of the Discriminating Variable

In Sections 5.2 and 5.3, the searches for Higgs bosons produced in pair production have been described. The result of these searches is a set of the reconstructed masses of the selected data events, a set of reconstructed masses of the selected simulated background events and the reconstructed masses of the simulated signal events. For each event, three different possibilities exist to for two masses of each a pair of jets, the di-jet masses. That means, three different sets of two Higgs boson masses can be reconstructed from each event.

This section describes how the information of the masses of a given set of Higgs bosons are used in order to construct the distribution of the discriminating variable $\mathcal{D}$, which is used in the limit calculation in Section 6. For this search, a two-dimensional distribution of $\mathcal{D}$ is used. One dimension is the sum of the reconstructed Higgs boson masses $\Sigma m = m^{\text{rec}}_{\mathcal{H}_1} + m^{\text{rec}}_{\mathcal{H}_2}$, the other dimension is the mass difference $\Delta m = m^{\text{rec}}_{\mathcal{H}_2} - m^{\text{rec}}_{\mathcal{H}_1}$.

The discriminating variable is chosen in order to maximise the use of information from the known Higgs boson masses of a given MSSM model. In the searches of Sections 5.2 and 5.3, no direct use of the Higgs boson masses was made in order to keep high sensitivity for all mass combinations. In case the mass information would not be used at all, a given Higgs boson signal, e. g. at $m_{\mathcal{H}_1} = 40$ GeV and $m_{\mathcal{H}_2} = 100$ GeV, would be mixed with the background peak stemming from Z pairs at $\Sigma m = 2m_{\text{Z}}$. This would degrade the sensitivity of the search, since the signal would be located on top of a strong background. In case the mass information is used, the signal is located in a region with low background at $\Sigma m = 140$ GeV and $\Delta m = 60$ GeV (see Fig. 5.6), clearly separated from the background at $\Sigma m = 2m_{\text{Z}}$ and $\Delta m = 0$ GeV.

In order to maximise the sensitivity, the signal, background and data distributions of $\mathcal{D}$ are constructed independently for each energy in the data of the year 1999 and independently in each 1 GeV energy bin in the data of the year 2000.

Signal Shape Fit

In order to use the mass information in the discriminating variable $\mathcal{D}$, the shape of the reconstructed masses have to be modelled. Since in a given model any combination of masses $m_{\mathcal{H}_1}$ and $m_{\mathcal{H}_2}$ can occur, the modelling of the shape of the reconstructed masses is factorised in Σm and Δm. For any Σm and Δm in the signal Monte Carlo sample the shape is determined. For a given Higgs boson mass combination in the MSSM model, these shapes are then centred on the nominal values of Σm and Δm of the model and interpolated between neighbouring distributions. Finally the integral over the distribution in Σm and Δm is normalised to the expected signal, taking the integrated luminosity, the efficiency, the cross-section and the branching ratios into account. Using the two shapes for Σm and Δm, two-dimensional distributions of the reconstructed masses for any given Higgs boson model are obtained.

Since three combinations of Higgs boson masses can be extracted from each event, the combination which is closest to the nominal signal mass combination is chosen in case of the signal mass distribution. Then distributions in the reconstructed mass sum Σm_{rec} are formed for each nominal mass sum Σm_{nom} in the signal Monte Carlo sample.

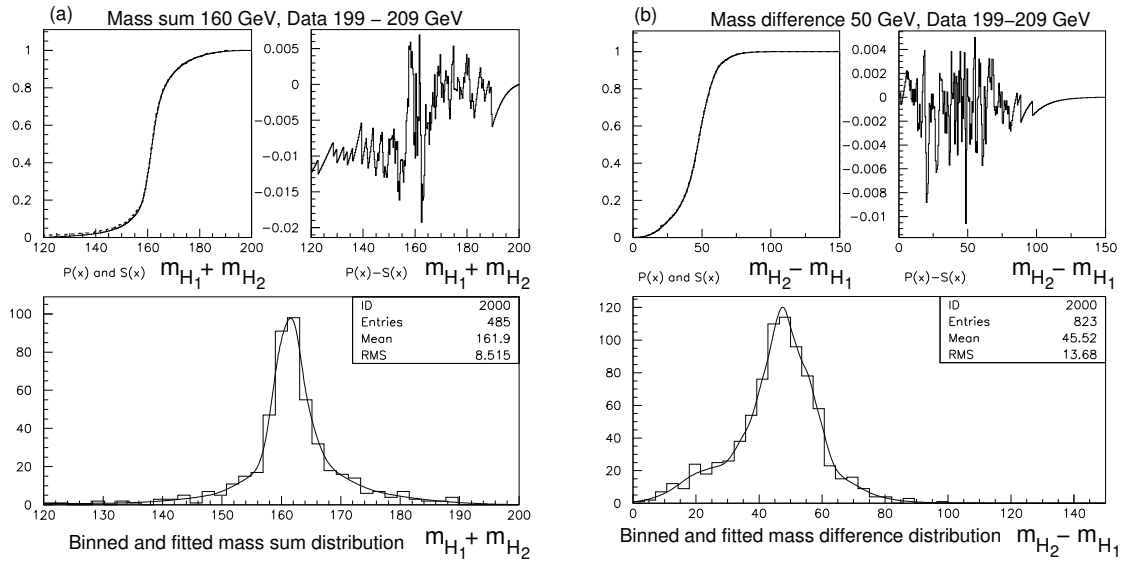

Figure 5.13: *Fit of the* $e^+e^- \to \mathcal{H}_1\mathcal{H}_2 \to b\bar{b}b\bar{b}$ *signal mass sum shape (a) and the mass difference shape (b). The sum of the Higgs boson masses* $m_{\mathcal{H}_1} + m_{\mathcal{H}_2}$ *is 160 GeV, the difference is 50 GeV. The plots are explained in the text.*

In order to avoid fluctuation in the limit on MSSM parameters stemming from statistical fluctuations in the reconstructed signal mass shape, the distributions are smoothed. Since in general the reconstructed mass does not follow a clear analytical function, a kernel based fit method is used for smoothing [126]. In this method, each single event of the unbinned signal shape distribution is replaced by a Gaussian kernel of an adjusted width.

The smoothing is achieved by replacing the original distribution of n events at the positions t_i with the smoothed kernel function

$$f(x) = \frac{1}{nh} \sum_{i=1}^{n} K\left(\frac{x - t_i}{h}\right),$$

where h is the smoothing parameter, also called band width, and K is the function chosen for the kernel. It is natural to choose the normalised Gaussian

$$K(x') = \frac{1}{\sqrt{2\pi}} e^{-x'^2/2}$$

as kernel function. A better adjustment is achieved if the band width h can be adjusted locally. This allow smaller bandwidths in areas of narrow, high structures and large bandwidths is areas with large, flat structures. In this case, the smoothed function is

$$f(x) = \frac{1}{n} \sum_{i=1}^{n} \frac{1}{h_i} K\left(\frac{x - t_i}{h_i}\right),$$

where the h_i are the local band widths, adjusted in an iterative procedure with

$$h_i \approx \frac{h}{\sqrt{f(t_i)}}.$$

Fig. 5.13 shows the distributions of Σm_{rec} and Δm_{rec} and the kernel functions fitted to it. In the lower plot of Fig. 5.13 (a), the experimental distribution $S(\Delta m_{\mathrm{rec}})$ of Σm_{rec} and the fitted

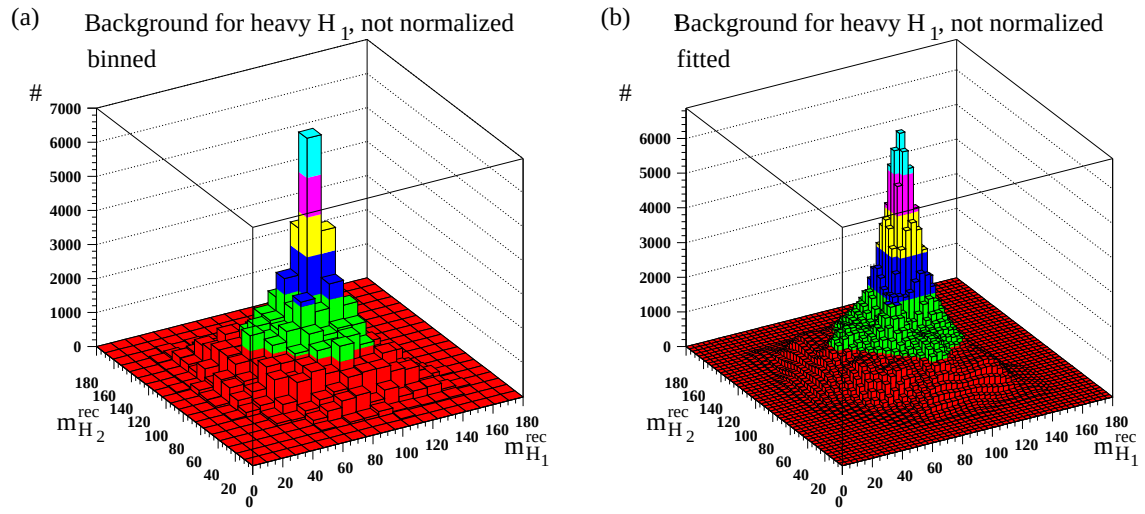

Figure 5.14: *Fit of the two-dimensional background mass distribution for heavy $m_{\mathcal{H}_1}$. In (a), the unfitted binned background distribution is shown. In (b), the fitted distribution for $\sqrt{s} = 199 - 209$ GeV is given.*

kernel function $P(\Delta m_{\text{rec}})$ is shown for $\Sigma m_{\text{nom}} = 160$ GeV. It is perfectly fitted with the kernel function $P(\Delta m_{\text{rec}})$. In the upper left plot the integral over the two functions is shown, and in the upper right plot the Kolmogorov-Smirnov-test values [127] of the fit is presented, which shows almost perfect agreement. The same distributions are shown for Δm_{rec} in Fig. 5.13 (b) for a nominal value of $\Delta m_{\text{nom}} = 50$ GeV. The mass resolution of Σm_{rec} is around 7 to 10 GeV, depending on Σm_{nom}. The resolution in Δm_{rec} with 10 to 15 GeV is slightly broader.

Background Shape Fit

In the case of the background, no clear use can be made of the expected mass combination. Therefore all three mass combinations of each background event are added and summed in one two-dimensional distribution in Σm and Δm. Consequently, each data event is also entered three times at all three different mass combinations. This procedure is conservative for the calculation of an exclusion limit, because more background is entered in the distribution of the discriminating variable $\mathcal{D}$. Since no clear sign of Higgs bosons has been found in this search, it is justified to treat the data conservatively in this sense.

However, this method can be aggressive if $\mathcal{D}$ is tested for a discovery, because accidentally different mass combinations of the same data event may coincide and therefore create an artificial data excess. This is called double counting. Tests for the possible effect of this double counting are presented in Section 6.

For the background distribution, the handling of the smoothed distribution is simpler as for the signal. This is due to the fact that the background distribution and normalisation is the same for all Higgs boson masses in any MSSM model. Still the background distribution has to be smoothed, since due to the strong separation power of the selections only few MC background events contribute to the background distribution, which therefore are subject to statistical fluctuations.

The two-dimensional background distribution is fitted in the projection $m_{\mathcal{H}_1}$ and $m_{\mathcal{H}_2}$. In the distributions in Figs. 5.14 and 5.15, the clear peak from the Z pair background can be seen. The background distribution is then smoothed using a two-dimensional spline fit [128].

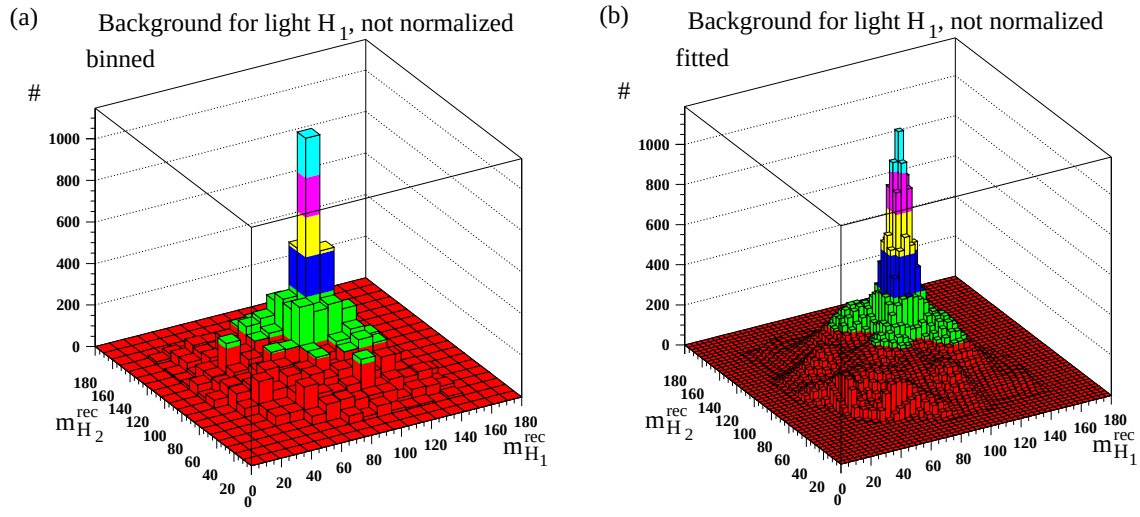

Figure 5.15: *Fit of the two-dimensional background mass distribution for light $m_{\mathcal{H}_1}$. In (a), the unfitted binned background distribution is shown. In (b), the fitted distribution for $\sqrt{s} = 199 - 209$ GeV is given.*

The original distribution and the fitted distribution for the selection in Section 5.2 and the data taken in the year 2000 is shown in Fig. 5.14. There is good agreement between the two functions. The same information is shown in Fig. 5.15 for the selection of Section 5.3. The fitted distributions are then transformed into the projection of Σm and Δm and normalised to the expected background rate.

The Two-Dimensional Input Histogram

For each Higgs boson signal expectation, as predicted by the MSSM model under study, and for each energy bin the distributions of $\mathcal{D}$ for background, signal and data are individually constructed. Fig. 5.16 shows the overlaid distributions in Σm and Δm. In Fig. 5.16 (a), a signal of $m_{\mathcal{H}_1} = m_{\mathcal{H}_2} = 80$ GeV is chosen. The coloured histogram in Fig. 5.16 (a) shows the signal mass peak, scaled for the expected cross-section at $\sqrt{s} = 207$ GeV and $\cos(\beta - \alpha) = 1$. It is located at $\Sigma m = 160$ GeV and $\Delta m = 0$ GeV. The opaque green histogram shows the background distribution with its peak at $\Sigma m = 2m_{\mathrm{Z}}$ and $\Delta m = 0$ GeV. Every background event is conservatively entered with all three mass combinations. The three towers in the histogram are the three mass combinations of the one data event in this energy bin. One can see that one of the mass combinations of the data event is located under the background peak. The other two mass combinations are randomly located in the mass plane.

The same information is shown for the selection of Section 5.3. The signal is chosen to be $m_{\mathcal{H}_1} = 25$ GeV and $m_{\mathcal{H}_2} = 100$ GeV. A clear separation of the signal peak from the background peak can be seen. Two data events with three mass combinations each can be found at $\sqrt{s} = 207$ GeV. This procedure of the individual construction of the data peak for each signal hypothesis ensures maximal sensitivity and accurateness for each signal in the mass range under study in these selections.

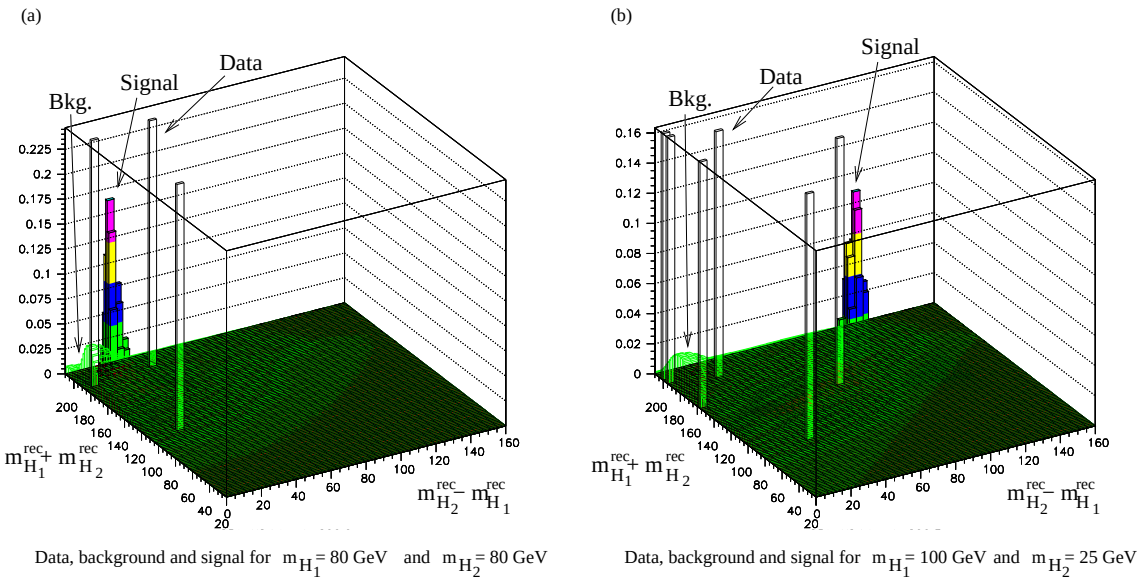

Figure 5.16: *Data, signal and background distributions. The distributions given above are used in the limit calculation of Section 6 as discriminating variable. The reconstructed masses are given in terms of* $m_{\mathcal{H}_1} + m_{\mathcal{H}_2}$ *and* $m_{\mathcal{H}_2} - m_{\mathcal{H}_1}$*. The opaque green (light grey) distribution is the background, the coloured peak is the signal and the data is given in the opaque black peaks. In (a), the search for heavy* $m_{\mathcal{H}_1}$ *is shown, while (b) shows the search for light* $m_{\mathcal{H}_1}$*.*

Chapter 6

Interpretation of the OPAL Higgs Boson Searches in the MSSM

In the searches described in the previous section, no evidence of Higgs boson production has been found. Neither has any statistically significant signal been found in the other search channels for Higgs bosons in the MSSM at OPAL [5]. This leaves two possibilities: Either a Higgs boson signal only is visible in the combination of many of these searches, or no Higgs boson signal is visible at OPAL, in which case limits on the production of Higgs bosons or MSSM parameters can be set. In both cases, an efficient technique for the combination of all search channels has to be used.

In this section, first the statistical methods for the combination of the search channels and the statistical interpretation of the results is described. This is followed by an overview of the search channels used in the OPAL experiment and a description of the channels which have been created in the context of this thesis for signal topologies of the CP violating MSSM scenarios. Then the results are interpreted in a model independent way, placing limits on the product of $\sigma\times$BR for a given combination of Higgs masses $m_{\mathcal{H}_1}, m_{\mathcal{H}_2}$. Next, the CP conserving and CP violating MSSM benchmark sets under study are introduced and limits on their parameters are presented. Finally, the full information from the Higgs boson searches of all four LEP experiments is combined to achieve the maximum sensitivity.

6.1 Statistical Methods

The sensitivity of the searches for hypothetical Higgs bosons is increased by combining the results of the various topological searches. This is done following the statistical method described in the following.

The outcome of searches for new particles is the number of observed events, together with the expected signal and background. The simplest possibility to determine the probability to find a certain number of data events d in the presence of the expectation of s signal events and b background events is the following. The method described in the following is a test of the probabilities of the two hypotheses that d events are observed when b background events are expected, and of the second hypothesis that the number of expected events is $s+b$. Therefore it should be noted that not the "most likely" signal s' is determined in the course of the limit calculation, but the probabilities of the a priori given hypotheses b and $s+b$ are calculated.

Each purely statistically determined observable is distributed according to the Poisson distribution [129], if it is only possible to count the occurrence of an event and not the absence of an event. Therefore the probability P to find the given number of events in the data in the

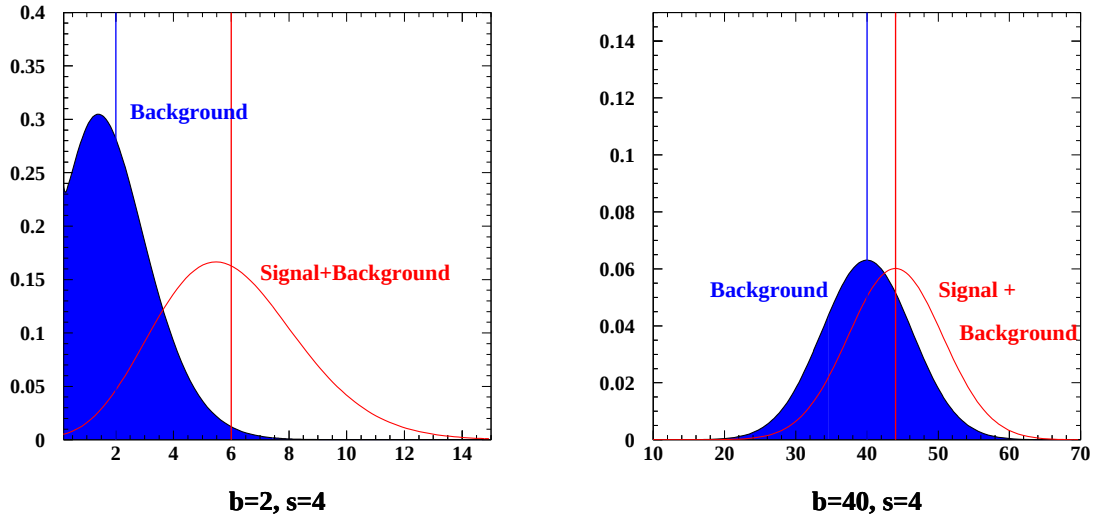

Figure 6.1: *Test statistic of a counting experiment. Each observed event in data, background and signal has the same weight.*

presence of signal and background is

$$P(s+b,d) = \frac{e^{-(s+b)}(s+b)^d}{d!}. \tag{6.1}$$

Such a treatment of the search results is called 'counting experiment', since only the information on the observed number of events and no other information is used. The probability distributions are displayed in Fig. 6.1 (a) for $b = 2$ and $s = 4$. If d data events are observed, then the compatibility $\mathcal{P}_b$ of the data with the background only and $\mathcal{P}_{s+b}$ with signal and background can be calculated as the integral over the probability distributions P:

$$1 - \mathcal{P}_b(b,d) = \sum_{i=0}^{d} \frac{e^{-(b)}(b)^i}{i!}, \qquad 1 - \mathcal{P}_{s+b}(s+b,d) = \sum_{i=0}^{d} \frac{e^{-(s+b)}(s+b)^i}{i!}. \tag{6.2}$$

For large $\mathcal{P}_b$ and small $\mathcal{P}_{s+b}$, the signal hypothesis is unlikely. On the other hand, for very small $\mathcal{P}_b$ the probability of a signal is large.

However, in the presence of different search channels with different sensitivities to the signal this procedure is not optimal. This is shown in Fig. 6.1 (b), where a second search channel with no sensitivity to the signal ($b_2 = 38$ and $s_2 = 0$) is added to the previous channel ($b_1 = 2$ and $s_1 = 4$). The overlap of the probability distribution P_b of the background and the probability distribution P_{s+b} of the signal plus background hypothesis is much larger than in the case of just one channel, therefore the sensitivity is degraded as $\mathcal{P}_b$ and $\mathcal{P}_{s+b}$ will almost coincide in most cases and no means to discriminate the background from the signal plus background hypothesis is given. In this context "channel" denotes the input from one self-contained search for one or several final states.

In order to achieve optimal sensitivity, the likelihood ratio technique [130] can be used to assign weights to each of the individual data events, according to their individual expectation of signal and background. Therefore the results of the searches (as in Section 5.5) are expressed in fine bins of a discriminating variable $\mathcal{D}$. In most cases, $\mathcal{D}$ is a one- or two-dimensional mass distribution. It also can be the output of a likelihood or ANN or a combination of all such information. For each bin i of each search, the individual weights are calculated.

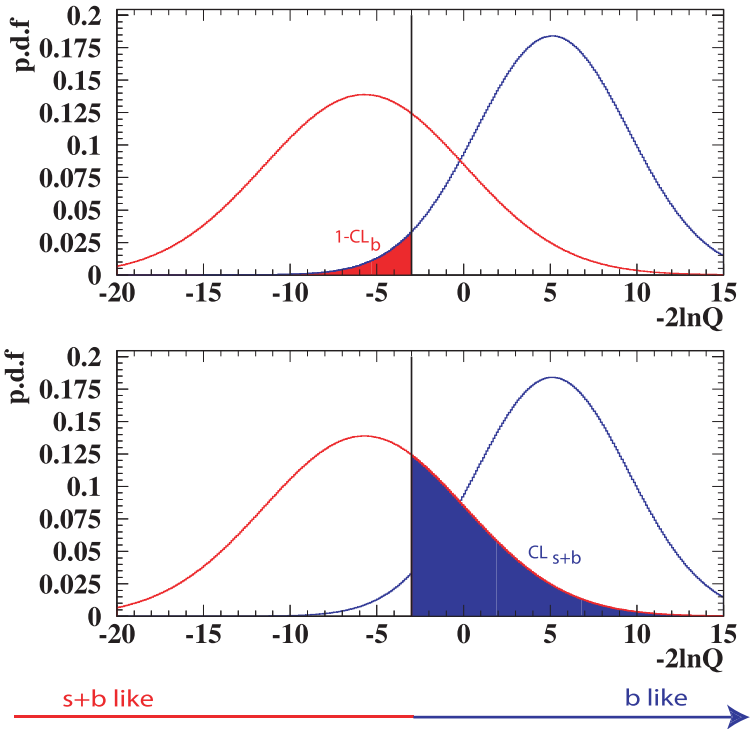

Figure 6.2: *Test statistic of the confidence level calculation. The weight of each event is calculated according to its expected signal and background.*

The compatibility of the data with a certain hypothesis is then calculated from the probability distribution of a certain statistical quantity Q, called 'test statistic', which orders the expected outcomes of test experiments according to their "signal-likeness". Several different choices for Q are possible in principle. In case of the likelihood ratio, the statistically optimal choice of Q for j bins is

$$Q = \prod_{i=1}^{j} \frac{e^{-(s_i+b_i)}(s_i+b_i)^{d_i}}{d_i!} \Bigg/ \frac{e^{-(b_i)}(b_i)^{d_i}}{d_i!}\,, \tag{6.3}$$

i. e. the test statistic Q is the product of the ratio of $\mathcal{P}^i_{s+b}$ over $\mathcal{P}^i_b$ in each bin i. This equation can be re-expressed as

$$-2\ln Q = 2\sum_i s_i - 2\sum_i d_i \ln(1 + s_i/b_i),$$

which expresses that the individual weight ω_i given to each event in bin i with signal s_i and background b_i is $w_i = \ln(1 + s_i/b_i)$. As one can easily see, this weight is zero for any bin with $s_i = 0$. This ensures maximal sensitivity, since bins with no sensitivity to the signal (as in the above example) do not contribute at all to Q, therefore have no impact on the resulting probability distribution and can not degrade the result. The logarithm of Q is chosen for the above equation since then the individual bins add up. It is multiplied by a factor of -2, because then the $1\,\sigma$ difference between observed and expected distributions differ by $\Delta(-2\ln Q) = 1$ in the limit of a large number of events.

The disadvantage of this method is that no signal hypothesis independent test of the compatibility of the data with the background can be made. The reason for this is the fact

that the weights ω_i depend on the signal hypothesis. If s_i/b_i is very small in a bin i with large excess of the data d_i over the background b_i, the excess will not be taken into account since $w_i = \ln(1+s_i/b_i)$ is close to zero. On the other hand, this method ensures maximal sensitivity at any point where there is a signal expectation, therefore it is chosen here for the purpose of setting limits on general Higgs sector properties and MSSM model parameters.

The probability distributions of $-2\ln Q$ are shown in Fig. 6.2. The probability distribution of the expected outcome for many experiments with background only is shown at the right, the probability distribution for signal plus background is to the left.

The confidence level for the background hypothesis, CL_b, is defined as the probability to obtain values of Q no larger than the observed value Q_{obs}, given a large number of hypothetical experiments with background processes only,

$$\mathrm{CL}_b = P(Q \leq Q_{\mathrm{obs}}|\mathrm{background}).$$

Similarly, the confidence level for the signal+background hypothesis, CL_{s+b}, is defined as the probability to obtain values of Q smaller than observed, given a large number of hypothetical experiments with signal and background processes,

$$\mathrm{CL}_{s+b} = P(Q \leq Q_{\mathrm{obs}}|\mathrm{signal} + \mathrm{background}).$$

In principle, CL_{s+b} can be used to exclude the signal+background hypothesis, given a model for Higgs boson production. However, this procedure may lead to the undesired possibility that a downward fluctuation of the background would allow hypotheses to be excluded for which the experiment has no sensitivity due to the small expected signal rate. This problem is avoided by introducing the ratio

$$\mathrm{CL}_s = \mathrm{CL}_{s+b}/\mathrm{CL}_b.$$

Since CL_b is a positive number less than one, CL_s will always be greater than CL_{s+b} and the limit obtained in this way will therefore be conservative. This quantity is adopted for setting exclusion limits and a hypothesis is considered to be excluded at the 95 % confidence level if the corresponding value of CL_s is less than 0.05. This method is also called "modified frequentist approach", since not the frequentistically determined confidence levels CL_b and CL_{s+b} but their ratio is used.

The expected confidence levels are obtained by replacing the observed data configuration by a large number of simulated event configurations for the two hypotheses background only or signal+background. These can be used to estimate the expected sensitivity of a search and to compare the observed exclusion with the one expected with no signal present.

The effect of systematic uncertainties of the individual channels is calculated using a Monte Carlo technique. The signal and background estimations are varied within the bounds of the systematic uncertainties, assuming Gaussian distributions of the uncertainties. Correlations are taken into account. These variations are convoluted with the Poisson statistical variations of the assumed signal and background rates in the confidence level calculation. The effect of systematic uncertainties on the exclusion limits turns out to be generally small for the size of the statistical and systematical errors present in the searches under study.

Two different methods have been used to calculate the confidence levels CL_s, CL_{s+b} and CL_b numerically. A Monte Carlo based method [130] generates the probability distributions of $-2\ln Q$ from 20 000 Monte Carlo toy experiments, where in each bin i the data expectations $\tilde{d}_i$ (with $\tilde{d}_i = s_i + b_i$ for the signal plus background hypothesis and $\tilde{d}_i = b_i$ for the background hypothesis) are varied by the individual Poisson probability plus Gaussian variations from the systematic errors on signal and background. From the observed probability distributions, the

observed confidence levels are obtained by the integration over the distributions starting from the observed value of $-2\ln Q$. This method is accurate, however, for large number of bins (up to $> 10\,000$ in the interpretations used in this thesis), the calculation of the confidence levels is very slow and can take several minutes per model point, which would translate into several weeks for a complete benchmark set. Therefore this method is used only for cross-checks at individual scan points.

Instead, an analytical approximation technique is used [131], based on the probability $\mathcal{P}_n(\omega)$ that d observed events in j bins sum up to a weight sum $\omega = \sum_{i=1}^{j} d_i \ln(1 + s_i/b_i)$. If the probability $\mathcal{P}_1(\omega)$ is known, then the successive probabilities for more observed events can be obtained by folding integrals, which can be analytically calculated. For given $\mathcal{P}_1(\omega)$, the probability to observe the weight sum ω in the presence of 2 events $\mathcal{P}_2(\omega)$ can be calculated from the combined probability of all possible combinations ω_1 and ω_2 adding up to ω. The folding integral for n events is then

$$\mathcal{P}_n(\omega) = \int \mathcal{P}_{n-1}(\omega - \tilde{\omega}) \cdot \mathcal{P}(\tilde{\omega})\,\mathrm{d}\tilde{\omega}.$$

Since the analytical folding is much faster than the Monte Carlo method, and since for large number of events $n > 50$ the folding can be omitted and the final distribution of $\mathcal{P}_n(\omega)$ can be safely replaced by a Gaussian distribution. Its width is calculated from the Poisson statistics

$$\sigma_b^2 = \sum_{i=1}^{n} \omega_i^2 b_i, \qquad \sigma_{s+b}^2 = \sum_{i=1}^{n} \omega_i^2 (s_i + b_i)$$

and the mean is given by the sum of the weights

$$< \omega >_b = \sum_{i=1}^{n} \omega_i b_i, \qquad < \omega >_{s+b} = \sum_{i=1}^{n} \omega_i (s_i + b_i).$$

This method is capable of calculating the confidence levels

$$\mathrm{CL}_b = \int_0^{\omega_{\mathrm{tot}}} \mathcal{P}_b(\omega)\mathrm{d}\omega, \qquad \mathcal{P}_b(\omega) = \frac{1}{\sqrt{2\pi}\sigma_b} e^{-\frac{(\omega - <\omega>_b)^2}{2\sigma_b^2}}$$

even for large numbers of bins j in a reasonable time. It has been tested to be in agreement with the Monte Carlo method for all relevant ranges of d_i, s_i and b_i.

In case of overlapping channels, i.e. channels sharing a fraction of events, the approach described above has to be modified. Such a situation occurs for example for the Higgsstrahlung searches with and without b-tagging [114, 132] or in the case of the Higgsstrahlung four-jet channel and the pair production four-b channel. The expected CL_s including only one of the overlapping channels are calculated in turn, and only the channel that yields the smaller expected CL_s is retained. This procedure is repeated for each signal hypothesis. For different Higgs boson masses therefore different search channels contribute to the exclusion.

The same procedure is applied if two signal processes, for example $\mathcal{H}_1\mathrm{Z}$ and $\mathcal{H}_2\mathrm{Z}$, can contribute to the same event topology, but at different mass values. In the case of the four-jet channel the selection procedure and discriminant variable $\mathcal{D}$ depend on the Higgs mass hypothesis (test mass). Two different test masses have not only different signal distributions s_i but also different background and data distributions b_i and n_i. The selected events in searches for $\mathcal{H}_1\mathrm{Z}$ and for $\mathcal{H}_2\mathrm{Z}$ cannot be combined since the inconsistent background and data distributions for the two hypotheses in general contain an overlapping sample of data events. Therefore only the hypothesis that yields the lower expected CL_s is retained.

6.2 The Search Channels

The searches for Higgs bosons at OPAL follow the signal topologies outlined in Section 3. The following selections for the SM-like Higgsstrahlung production channel are used:

1. The most efficient search for the Higgsstrahlung processes is the one which is designed to search for the Standard Model Higgs boson. This search [114] is interpreted here as a generic search for the corresponding MSSM process $e^+e^- \to \mathcal{H}Z$. It takes advantage of the preferential decay of Higgs bosons into $b\bar{b}$ and $\tau^+\tau^-$ pairs and addresses the following Z boson decays: $Z \to q\bar{q}, \nu\bar{\nu}, e^+e^-, \mu^+\mu^-, \tau^+\tau^-$. Moreover, this search is also sensitive to contributions to the signal from the W^+W^- and ZZ fusion processes $e^+e^- \to \mathcal{H}\nu\bar{\nu}$ and $\mathcal{H}e^+e^-$, which may become important at the kinematic limit of the Higgsstrahlung process.

2. The Higgs cascade decay $\mathcal{H}_2 \to \mathcal{H}_1\mathcal{H}_1$ may play an important role in regions of the MSSM parameter space where it is kinematically possible. In order to increase the sensitivity to cascade decays, the search described in [114] is adapted, in those parts which deal with the "four-jet" final state $e^+e^- \to (\mathcal{H} \to b\bar{b})(Z \to q\bar{q})$ and the "missing energy" final state $e^+e^- \to (\mathcal{H} \to b\bar{b})(Z \to \nu\bar{\nu})$. These searches modified for $e^+e^- \to (\mathcal{H}_2 \to \mathcal{H}_1\mathcal{H}_1)Z$ are described below in Sections 6.2.1 and 6.2.1.

3. The search for Higgs cascade decays is complemented by a search for $e^+e^- \to (\mathcal{H}_2 \to \mathcal{H}_1\mathcal{H}_1)Z$ [135], which is specifically designed to be efficient in the domain $m_{\mathcal{H}_1} < 10$ GeV.

4. For Higgs bosons produced in Higgsstrahlung $e^+e^- \to \mathcal{H}Z$ and decaying into particles other than b-quarks or τ leptons, a flavour-independent search for $e^+e^- \to (\mathcal{H} \to$ hadrons$)\,Z$ [136, 132] is used.

All Higgsstrahlung searches used in the combination of search channels in this thesis are listed in Tab. 6.1. They range from LEP 1 searches up to data taken at the highest energies. The most important channels for the Higgs boson mass limits are the searches in the data at $\sqrt{s} = 192 - 209$ GeV, which have the highest mass reach. Nevertheless, searches at lower energies are important to cover kinematical domains where the high energy searches are inefficient or which are not included in the high energy searches.

As outlined in Section 3, the searches for Higgsstrahlung are complementary to the searches for pair production processes $e^+e^- \to \mathcal{H}_1\mathcal{H}_2$. The following searches for pair production are used:

1. The search for the four-b final state $e^+e^- \to (\mathcal{H}_1 \to b\bar{b})(\mathcal{H}_2 \to b\bar{b})$ provides the highest sensitivity. While in the CPC scenarios under study the pair production process is dominant only for $m_{\mathcal{H}_1} \approx m_{\mathcal{H}_2}$, this is not the case in the CPV scenario. The search in this channel is therefore optimized separately for small $m_{\mathcal{H}_1}$ and large $m_{\mathcal{H}_1}$. These are described below in Sections 5.2 and 5.3.

2. For the Higgs cascade decay $e^+e^- \to (\mathcal{H}_1 \to b\bar{b})(\mathcal{H}_2 \to \mathcal{H}_1\mathcal{H}_1 \to b\bar{b}b\bar{b})$ with 6 b-quarks in the final state, the search in the four-b final state for similar masses described in Section 5.2 is used because it has a reasonably good efficiency. Even for large mass differences and thus small $m_{\mathcal{H}_1}$ this search is more efficient than the one described in Section 5.3, due to the highly spherical shape of the six-b events. This search is described in Section 6.2.1

Table 6.1: *List of the searches for the Higgsstrahlung process. The last column gives the reference or section where the search is described.*

Luminosity table for $e^+e^- \to \mathcal{H}Z$ production				
Channel Name $\mathcal{H}Z \to$	Energies (GeV)	Luminosity (pb^{-1})	Mass range (GeV)	Described in
LEP 1 Channels				
qq$\tau\tau$/$\tau\tau$qq	91.2	46.3	$m_{\mathcal{H}} = 0 - 70$	[133]
$(\mathcal{H}_1\mathcal{H}_1 \to q\bar{q}q\bar{q})\nu\nu$	91.2	46.3	$m_{\mathcal{H}_2} = 10 - 75, m_{\mathcal{H}_1} = 0 - 35$	[133]
qq$\nu\nu$	91.2	46.3	$m_{\mathcal{H}} = 0 - 70$	[133]
qqll	91.2	46.3	$m_{\mathcal{H}} = 20 - 70$	[133]
LEP 2 Channels				
bbqq	161–172	20.4	$m_{\mathcal{H}} = 40 - 80$	[105, 134]
bb$\nu\nu$	161–172	20.4	$m_{\mathcal{H}} = 50 - 70$	[105, 134]
$\tau\tau$qq, bb$\tau\tau$	161–172	20.4	$m_{\mathcal{H}} = 30 - 95$	[105, 134]
Xee	161–172	20.4	$m_{\mathcal{H}} = 35 - 80$	[105, 134]
X$\mu\mu$	161–172	20.4	$m_{\mathcal{H}} = 35 - 80$	[105, 134]
bbqq	183	54.1	$m_{\mathcal{H}} = 40 - 95$	[113]
$(\mathcal{H}_1\mathcal{H}_1 \to$4b)qq	183	54.1	$m_{\mathcal{H}} = 40 - 80$	[113]
bb$\nu\nu$/$(\mathcal{H}_1\mathcal{H}_1 \to$4b)$\nu\nu$	183	53.9	$m_{\mathcal{H}} = 50 - 95$	[113]
bb$\tau\tau$/ $\tau\tau$qq/$\tau\tau(\mathcal{H}_1\mathcal{H}_1 \to$4b)	183	53.7	$m_{\mathcal{H}} = 30 - 100$	[113]
bbee, bb$\mu\mu$	183	55.9	$m_{\mathcal{H}} = 60 - 100$	[113]
bb(bb)qq	189	172.1	$m_{\mathcal{H}} = 40 - 100$	[108]
bb$\nu\nu$/$(\mathcal{H}_1\mathcal{H}_1 \to$4q)$\nu\nu$	189	171.4	$m_{\mathcal{H}} = 50 - 100$	[108]
bb$\tau\tau$/ $\tau\tau$qq/$\tau\tau(\mathcal{H}_1\mathcal{H}_1 \to$4b)	189	168.7	$m_{\mathcal{H}} = 30 - 100$	[108]
bbee, bb$\mu\mu$	189	170.0	$m_{\mathcal{H}} = 70 - 100$	[108]
low $m_A(\mathcal{H}_1\mathcal{H}_1)(\nu\bar{\nu}$,ee,$\mu\mu)$	189–192	201.7	$m_{\mathcal{H}_2} = 45 - 90, m_{\mathcal{H}_1} = 2 - 10.5$	[135]
bbqq	192–209	421.2	$m_{\mathcal{H}} = 80 - 120$	[114]
$(\mathcal{H}_1\mathcal{H}_1 \to$4b)qq	192–209	421.2	$m_{\mathcal{H}_2} = 80 - 120, m_{\mathcal{H}_1} = 12 - m_{\mathcal{H}_2}/2$	6.2.1
bb$\nu\nu$	192–209	419.9	$m_{\mathcal{H}} = 30 - 120$	[114]
bbbb$\nu\nu$	199–209	207.2	$m_{\mathcal{H}_2} = 100 - 110, m_{\mathcal{H}_1} = 12 - m_{\mathcal{H}_2}/2$	6.2.1
bb$\tau\tau$ / $\tau\tau$qq	192–209	417.4	$m_{\mathcal{H}} = 80 - 120$	[114]
bbee, bb$\mu\mu$	192–209	418.3	$m_{\mathcal{H}} = 40 - 120$	[114]
low $m_A(\mathcal{H}_1\mathcal{H}_1)(\nu\bar{\nu}$,ee,$\mu\mu)$	196–209	396.9	$m_{\mathcal{H}_2} = 45 - 90, m_{\mathcal{H}_1} = 2 - 10.5$	[135]
LEP 2 Flavour-Independent Channels				
qqqq	189	174.1	$m_{\mathcal{H}} = 60 - 100$	[136]
qq$\nu\nu$	189	171.8	$m_{\mathcal{H}} = 30 - 100$	[136]
qq$\tau\tau$, $\tau\tau$qq	189	168.7	$m_{\mathcal{H}} = 30 - 100$	[136]
qqee, qq$\mu\mu$	189	170.0	$m_{\mathcal{H}} = 70 - 100$	[136]
qqqq	192–209	424.2	$m_{\mathcal{H}} = 60 - 120$	[132]
qq$\nu\nu$	192–209	414.5	$m_{\mathcal{H}} = 30 - 110$	[132]
qq$\tau\tau$, $\tau\tau$qq	192–209	418.9	$m_{\mathcal{H}} = 60 - 115$	[132]
qqee, qq$\mu\mu$	192–209	422.0	$m_{\mathcal{H}} = 60 - 120$	[132]

Table 6.2: *List of the searches for pair production. The last column gives the reference or section where the search is described. The symbols* $\Sigma = m_{\mathcal{H}_1} + m_{\mathcal{H}_2}$ *and* $\Delta = m_{\mathcal{H}_2} - m_{\mathcal{H}_1}$ *denote the Higgs mass sum and difference.*

Luminosity table for $e^+e^- \to \mathcal{H}_1\mathcal{H}_2$ production				
Channel Name $\mathcal{H}_1\mathcal{H}_2 \to$	Energies (GeV)	Luminosity (pb^{-1})	Mass range (GeV)	Described in
LEP 1 Channels				
6b	91.2	27.6	$m_{\mathcal{H}_2} = 40-70, m_{\mathcal{H}_1} = 5-35$	[133]
qq$\tau\tau$, $\tau\tau$qq	91.2	46.3	$m_{\mathcal{H}_2} = 12-75, m_{\mathcal{H}_1} = 10-78$	[133]
6τ, 4τ2q, 2τ4q	91.2	46.3	$m_{\mathcal{H}_2} = 30-75, m_{\mathcal{H}_1} = 4-30$	[133]
LEP 1.5 Channels				
4b	130–136	5.2	$\Sigma = 80-130, \Delta = 0-50$	[134]
6b	130–136	5.2	$m_{\mathcal{H}_2} = 55-65, m_{\mathcal{H}_1} > 27.5$	[134]
LEP 2 Channels				
4b	161	10.0	$\Sigma = 80-130, \Delta = 0-60$	[105, 134]
6b	161	10.0	$m_{\mathcal{H}_2} = 55-65, m_{\mathcal{H}_1} > 20.0$	[105, 134]
bb$\tau\tau$, $\tau\tau$bb	161	10.0	$m_{\mathcal{H}_2} = 40-160, m_{\mathcal{H}_1} = 52-160$	[105, 134]
4b	172	10.4	$\Sigma = 80-130, \Delta = 0-60$	[105, 134]
6b	172	10.4	$m_{\mathcal{H}_2} = 55-65, m_{\mathcal{H}_1} = 25-35$	[105, 134]
bb$\tau\tau$, $\tau\tau$bb	172	10.4	$m_{\mathcal{H}_2} = 37-160, m_{\mathcal{H}_1} = 28-160$	[105, 134]
4b	183	54.1	$\Sigma = 80-150, \Delta = 0-60$	[113]
6b	183	54.1	$m_{\mathcal{H}_2} = 30-80, m_{\mathcal{H}_1} = 12-40$	[113]
bb$\tau\tau$, $\tau\tau$bb	183	53.7	$\Sigma = 70-170, \Delta = 0-70$	[113]
4b	189	172.1	$\Sigma = 80-180, \Delta = 0-70$	[108]
6b	189	172.1	$m_{\mathcal{H}_2} = 24-80, m_{\mathcal{H}_1} = 12-40$	[108]
bb$\tau\tau$, $\tau\tau$bb	189	168.7	$\Sigma = 70-190, \Delta = 0-90$	[108]
4b	192	28.9	$\Sigma = 83-183, \Delta = 0-70$	5.2
4b	196	74.8	$\Sigma = 80-187, \Delta = 0-70$	5.2
4b	200	77.2	$\Sigma = 80-191, \Delta = 0-70$	5.2
4b	202	36.1	$\Sigma = 80-193, \Delta = 0-70$	5.2
high $m_{\mathcal{H}_1}$ 4b	199–209	207.3	$\Sigma = 120-190, \Delta = 0-70$	5.2
low $m_{\mathcal{H}_1}$ 4b	199–209	207.3	$\Sigma = 100-140, \Delta = 60-100$	5.3
6b	199–209	207.3	$\Sigma = 90-200, \Delta = 40-160$	6.2.1
bb$\tau\tau$, $\tau\tau$bb	192	28.7	$\Sigma = 10-174, \Delta = 0-182$	[5]
bb$\tau\tau$, $\tau\tau$bb	196	74.7	$\Sigma = 10-182, \Delta = 0-191$	[5]
bb$\tau\tau$, $\tau\tau$bb	200	74.8	$\Sigma = 10-182, \Delta = 0-191$	[5]
bb$\tau\tau$, $\tau\tau$bb	202	35.4	$\Sigma = 10-174, \Delta = 0-182$	[5]
bb$\tau\tau$, $\tau\tau$bb	199–209	203.6	$\Sigma = 70-190, \Delta = 0-90$	[5]

Table 6.3: *Efficiencies of the standard* $e^+e^- \to ZH \to q\bar{q}\,b\bar{b}$ *analysis [114] for the* $e^+e^- \to Z\mathcal{H}_2 \to Z\mathcal{H}_1\mathcal{H}_1 \to q\bar{q}\,b\bar{b}\,b\bar{b}$ *final state (see Section 6.2.1). The uncertainties from Monte Carlo statistics are of the order of* ± 0.015.

$m_{\mathcal{H}_2}$	$m_{\mathcal{H}_1}$	Efficiency for the process $\mathcal{H}_2Z \to b\bar{b}b\bar{b}q\bar{q}$ at $\sqrt{s}$				
(GeV)	(GeV)	192 GeV	196 GeV	200 GeV	202 GeV	206 GeV
100.	12.	0.689	0.684	0.717	0.733	0.693
100.	20.	0.651	0.639	0.653	0.659	0.586
100.	30.	0.460	0.461	0.461	0.470	0.480
100.	40.	0.270	0.260	0.283	0.315	0.323
100.	48.	0.328	0.325	0.361	0.392	0.400
105.	12.	0.538	0.658	0.702	0.709	0.701
105.	20.	0.562	0.618	0.697	0.658	0.681
105.	30.	0.490	0.525	0.509	0.536	0.497
105.	40.	0.407	0.306	0.309	0.316	0.319
105.	50.	0.433	0.368	0.355	0.359	0.370
110.	12.			0.637	0.682	0.720
110.	20.			0.625	0.646	0.532
110.	30.			0.556	0.549	0.565
110.	40.			0.380	0.328	0.343
110.	53.			0.395	0.341	0.358

3. The search for the final states $e^+e^- \to (\mathcal{H}_1 \to b\bar{b})(\mathcal{H}_2 \to \tau^+\tau^-)$ and $e^+e^- \to (\mathcal{H}_1 \to \tau^+\tau^-)(\mathcal{H}_2 \to b\bar{b})$ follow the technique described in [114] for the corresponding Standard Model channels. The final likelihood selection and its optimization for the MSSM case is described in Section [5].

The searches for pair production performed at OPAL and used in this combination are listed in Tab. 6.2. For most of the scenarios under study in Section 6.4, the searches at the highest energies would suffice, however for model independent limits also the low energy searches are needed. All the searches listed above are combined in the statistical analysis introduced in Section 6.1. The last of the Higgs production mechanisms, the Yukawa production process, is not included in the combination. Since it occurs only in an otherwise uncovered region of the parameter space of the benchmark sets of Section 6.4, no additional sensitivity would be gained by combining it with other channels. It is used as an additional experimental constraint together with other external constraints, as listed in Section 6.2.3.

6.2.1 Additional Channels for Higgs Cascade Decays

For the first time the CPV scenarios of Section 6.4.2 have been experimentally studied in the context of this thesis. New kinematical domains emerge in these scenarios, in which the cascade decay production channels $e^+e^- \to \mathcal{H}_2Z \to \mathcal{H}_1\mathcal{H}_1Z \to b\bar{b}b\bar{b}Z$ and $e^+e^- \to \mathcal{H}_1\mathcal{H}_2 \to \mathcal{H}_1\mathcal{H}_1\mathcal{H}_1 \to b\bar{b}b\bar{b}b\bar{b}$ occur. The searches for these signatures are explained in the following.

Modification of the search in the four-jet channel

The search for the SM Higgs boson in the channel $e^+e^- \to H_{SM}Z \to b\bar{b}q\bar{q}$ [114] is modified to be sensitive to the cascade decay $\mathcal{H}_2 \to \mathcal{H}_1\mathcal{H}_1$. The event selection is identical to the SM

search, and thus the same candidate events are observed with the same expected background. The whole event is forced into four jets using the Durham jet finder [109, 110]. If $\mathcal{H}_1$ is not too heavy, the two jets from $\mathcal{H}_1 \to b\bar{b}$ are often joined into one jet. The SM four-jet search is therefore also efficient for this decay and the expected signal rates from $e^+e^- \to (\mathcal{H}_2 \to b\bar{b})Z$ and $e^+e^- \to (\mathcal{H}_2 \to \mathcal{H}_1\mathcal{H}_1 \to b\bar{b}b\bar{b})Z$ can simply be added. The efficiencies for various combinations of $(m_{\mathcal{H}_1}, m_{\mathcal{H}_2})$ are given in Table 6.3. The shape of the distribution of the discriminating variable $\mathcal{D}$ [114], however, differs for the two decay modes. $\mathcal{D}$ is a product of a mass independent and a mass dependent likelihood. Depending on $m_{\mathcal{H}_1}$, the mass reconstruction is diluted by wrong jet pairings inside one jet, and thus the likelihood distributions are broadened. The signal distribution of $\mathcal{D}$ is therefore constructed at each point of the MSSM parameter space, taking into account the changing relative contributions from the two decays by first adding the relative contributions of $\mathcal{H}_2 \to b\bar{b}$ and $\mathcal{H}_2 \to b\bar{b}b\bar{b}$ in the two likelihoods and then calculating the product. The systematic uncertainties are essentially the same as for the SM channel $e^+e^- \to H_{SM}Z \to b\bar{b}q\bar{q}$ [114].

Modification of the search in the missing energy channel

For the data taken at $\sqrt{s} = 199$ to 209 GeV, the Artificial Neural Network (ANN) analysis for $e^+e^- \to H_{SM}Z \to b\bar{b}\nu\bar{\nu}$ [114] is reoptimized for $100 < m_{\mathcal{H}_2} < 110$ GeV and modified to be sensitive to $\mathcal{H}_2 \to b\bar{b}$ and $\mathcal{H}_2 \to \mathcal{H}_1\mathcal{H}_1 \to b\bar{b}b\bar{b}$ decays simultaneously. In this mass range, the $\mathcal{H}_2 \to \mathcal{H}_1\mathcal{H}_1$ decay is crucial especially in the CPV scenario. The selection for this simultaneous search channel for $e^+e^- \to \mathcal{H}Z \to b\bar{b}\nu\bar{\nu}$ and $e^+e^- \to \mathcal{H}_2Z \to \mathcal{H}_1\mathcal{H}_1\nu\bar{\nu} \to b\bar{b}b\bar{b}\nu\bar{\nu}$ is described in [5]. A dedicated search and not just a reinterpretation of an existing search is used since for the missing energy channel with typically two visible jets the relative difference to a four-jet event is much larger as for the four-jet channel, where the topological difference to six jets in the detector is not so large.

The input scheme for this search has been developed in the context of this thesis. Two search channels A and B are introduced. Each event is either sorted into selection A or B, depending on its value of y_{32}. Events with a two-jet like structure are sorted into selection A, and all events with a more three- or four-jet like structure are sorted in selection B. This means, that signal events of the four-jet signal topology can also be sorted in the two-jet selection, depending on their response in the detector. This is schematically shown in Fig. 6.3 (a).

For the limit calculation, the discriminating variable $\mathcal{D}$ is constructed for each selection separately as a likelihood formed of the ANN output distribution and the reconstructed mass, which is reconstructed using the di-jet invariant mass after the 1-constraint kinematic fit. The likelihood is formed after adding the two different signals in each subsample according to their relative weight at each model point, using the efficiencies for signal events for both $\mathcal{H}_2 \to b\bar{b}$ and $\mathcal{H}_2 \to \mathcal{H}_1\mathcal{H}_1 \to b\bar{b}b\bar{b}$, which are determined for both selections. The distribution of the reconstructed variable for a signal with $m_{\mathcal{H}_1} = 40$ GeV and $m_{\mathcal{H}_2} = 105$ GeV is shown in Fig. 6.3 (b). Most events obey a four-jet-like structure, therefore almost the complete signal is located in the right part, representing the four-jet selection. The number of candidate events in selection A(B) is 11(8) with 10.0 (7.2) events expected from background.

Search for $e^+e^- \to \mathcal{H}_1\mathcal{H}_2 \to \mathcal{H}_1\mathcal{H}_1\mathcal{H}_1 \to b\bar{b}b\bar{b}b\bar{b}$

The search channel for $\mathcal{H}_1\mathcal{H}_2 \to b\bar{b}b\bar{b}$ optimized for high $m_{\mathcal{H}_1}$ is also used to search for events of the type $e^+e^- \to \mathcal{H}_1\mathcal{H}_2 \to \mathcal{H}_1\mathcal{H}_1\mathcal{H}_1 \to b\bar{b}b\bar{b}b\bar{b}$. Despite the large mass difference $m_{\mathcal{H}_2} - m_{\mathcal{H}_1}$ and generally relatively low $m_{\mathcal{H}_1}$, the selection for high $m_{\mathcal{H}_1}$ (Section 5.2) is more efficient than the selection for low $m_{\mathcal{H}_1}$ (Section 5.3) due to the spherical shape of the $b\bar{b}b\bar{b}b\bar{b}$ events.

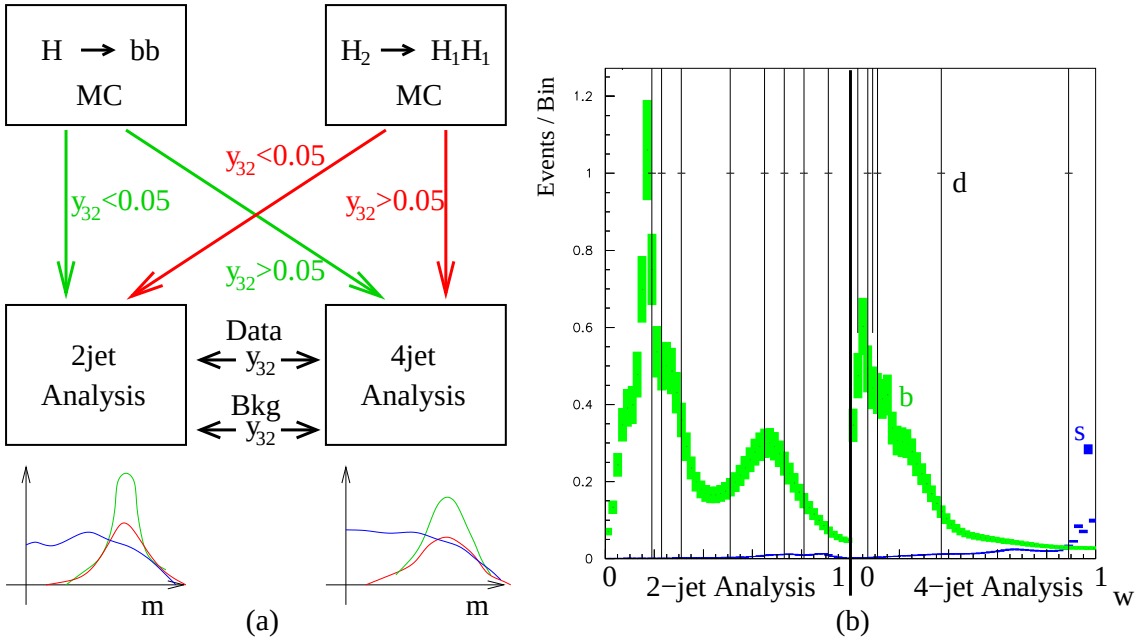

Figure 6.3: *Input method of the missing energy channel for the similataneous search for* $e^+e^- \to \mathcal{H}Z \to b\bar{b}\nu\bar{\nu}$ *and* $e^+e^- \to \mathcal{H}_2Z \to \mathcal{H}_1\mathcal{H}_1\nu\bar{\nu} \to b\bar{b}b\bar{b}\nu\bar{\nu}$. *In (a) the scheme of the two selections is schown. In (b) the input distributions of the two selections are presented. The background is displayed in green (grey), the signal in blue (dark) and the data is shown in the form of the vertical lines.*

Table 6.4: *Efficiencies of the* $\mathcal{H}_1\mathcal{H}_2 \to \mathcal{H}_1\mathcal{H}_1\mathcal{H}_1 \to b\bar{b}b\bar{b}b\bar{b}$ *analysis. The uncertainty from Monte Carlo statistics is* ± 0.010.

	Efficiency for $\mathcal{H}_2\mathcal{H}_1 \to b\bar{b}b\bar{b}b\bar{b}$ at $\sqrt{s} = 206$ GeV							
$m_{\mathcal{H}_1}$ (GeV)	12.0	20.0	30.0	40.0	45.0	50.0	60.0	70.0
$m_{\mathcal{H}_2}$ (GeV)								
80.	0.002	0.188	0.390	0.465				
90.	0.002	0.263	0.447	0.595	0.569			
100.	0.001	0.283	0.486	0.594	0.639	0.629		
110.	0.001	0.300	0.552	0.627	0.662	0.659		
120.	0.002	0.214	0.512	0.671	0.664	0.650	0.695	
130.	0.002	0.292	0.519	0.635	0.680	0.670	0.657	
140.	0.000	0.255	0.536	0.636	0.646	0.670	0.649	0.382

The expected signal distribution is added to the one from the 4b-channel in the same way as described above for the $\mathcal{H}_2Z \to \mathcal{H}_1\mathcal{H}_1Z \to b\bar{b}b\bar{b}q\bar{q}$ cahnnel. The efficiency of this search is shown in Table 6.4 for various $(m_{\mathcal{H}_1}, m_{\mathcal{H}_2})$. The systematic error of the signal of this channel is taken to be the same as for the search optimized for high $m_{\mathcal{H}_1}$.

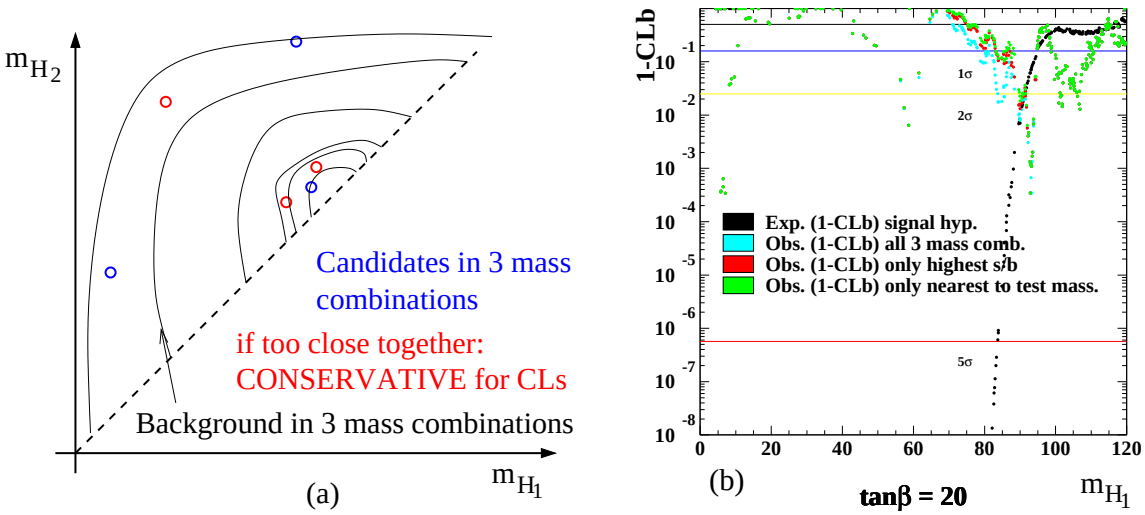

Figure 6.4: *Input test of the inputs of the* $e^+e^- \to \mathcal{H}_2\mathcal{H}_1 \to b\bar{b}b\bar{b}$ *pair production channel. In (a) the general problem of doublecounting is shown schematically. In (b) observed and expected* $(1 - CL_b)$ *for different input schemes are presented.*

6.2.2 Input Tests

The inputs of all channels are tested using a large number of tools. For specific model points, the data and calculated expected background and signal are compared with the output of the combination. The distributions of $\mathcal{D}$ for data, background and signal are displayed and compared with the nominal distributions.

Additionally, specific tests are made to test the inputs of the pair production channels of Sections 5.2 and 5.3. The reason for this sprecial treatment is the fact that signal on the one hand and data and background on the other hand are treated in a different way in these channels only.

As outlined in Section 5.5, three different possibilities exist to form two pairs of jets from four jets. Hence three different mass combinations $(m_{\mathcal{H}_1}, m_{\mathcal{H}_2})$ can be reconstructed from each event. The signal peak is reconstructed from the di-jet combinations only which are closest to the signal mass combination. This ensures optimal resolution and sensitivity. The data and background events are entered three times each at each of the possible reconstructed mass combinations.

This procedure is conservative for an exclusion, since there can be only more background than in any other case where each event is only used once. However, due to the small statistics of the data events, there is the possibility that accidentially some of the data mass combinations of the same event lie very close together and hence create an artificial excess (double-counting). This would be aggressively creating the potential of a false discovery. This possibility is illustrated in Fig. 6.4 (a). For the background such an artificial peak is unlikely due to the fact that the background statistics is about a factor of 25 larger than the data statistics.

In order to estimate the order of magnitude of the artificial excess due to double-counting, two other input schemes have been used which are conservative in terms of a discovery but aggressive in terms of an exclusion. The optimal situation hence must lie in between the original method and these two new methods. The additional methods are

1. Each background event is entered three times, while each of the data events is entered only once, namely at the position with the highest s/b at the given model point.

2. Each background event is entered three times, while each of the data events is entered only once, namely at the position which is closest to the $(m_{\mathcal{H}_1}, m_{\mathcal{H}_2})$ of the model point under study.

The result is presented in Fig. 6.4 (b), where the $(1 - \mathrm{CL}_b)$ is shown as a function of m_h. The smaller $(1 - \mathrm{CL}_b)$, the less background-like the data are. If there would be a signal, the $5\,\sigma$ discovery potential would go up to $m_\mathrm{h} = 83$ GeV, as the black line of dots shows. The largest excess in the data of around $3\,\sigma$ occurs at $m_\mathrm{h} = 93$ GeV. The standard method with three mass combinations per data event is shown in green. This excess is only very slightly altered for methods 1 and 2. Therefore it is concluded that the standard method does not artificially create strong excesses which are not in the data. With the same comparison it has been checked that the loss of sensitivity of the conservative standard method for the exclusion, measured in terms of CL_s, is only marginal. This is due to the fact that most background mass combinations of the same event are far enough apart from each other so that only one of the mass combination is seen by an average signal peak.

6.2.3 External Experimental Constraints

If a given model for Higgs production is not excluded by using the search channels described above, the following additional constraints are considered:

(a) The constraint from the measured Z boson decay width Γ_Z: a model is regarded as excluded if the condition

$$\sum_i \sigma_{\mathcal{H}_i\mathrm{Z}}(91.4\,\mathrm{GeV}) + \sum_{i,j} \sigma_{\mathcal{H}_i\mathcal{H}_j}(91.4\,\mathrm{GeV}) > \sigma_\mathrm{Z}(91.4\,\mathrm{GeV})\,\frac{\Delta\Gamma_\mathrm{Z}}{\Gamma_\mathrm{Z}}$$

is satisfied using results from [19]. The nominal LEP1 centre-of-mass energy of $\sqrt{s} = 91.4$ GeV is used. Γ_Z is the total measured Z width, σ_Z is the total measured Z cross-section and $\Delta\Gamma_\mathrm{Z} = 6.5$ MeV is the maximum additional width that is compatible with the measured width, given the SM hypothesis (obtained from ZFITTER [137]) at the 95% CL. This constraint uses the precisely measured Z width to set a limit on the maximal additional contribution of the Higgs boson production to the total SM cross-section ate LEP 1.

(b) The constraint from the decay mode independent search for $\mathrm{e^+e^-} \to \mathrm{HZ}$ [138]: a model is regarded as excluded if

$$\sigma_{\mathcal{H}_i\mathrm{Z}} > k(m_{\mathcal{H}_i})\,\sigma_{\mathrm{HZ,SM}} \qquad \text{with} \qquad m_{\mathcal{H}_i} = m_\mathrm{H}$$

is fulfilled, where $k(m_{\mathcal{H}_i})$ is the smallest scale factor for the SM Higgs production cross-section that is excluded at the 95% CL by this search. This criterion is used for $\mathcal{H}_i = \mathcal{H}_1$ and $\mathcal{H}_i = \mathcal{H}_2$ and at $\sqrt{s} = 91.4$, 183 and 206 GeV. The use of Z width constraints and decay mode independent analyses is especially helpful for the range $m_{\mathcal{H}_1} < 6$ GeV. This constraint uses a search for $\mathrm{e^+e^-} \to \mathrm{Z}X \to \ell^+\ell^- X$ at LEP 1 and LEP 2. The recoil spectrum of the two leptons from the Z decay is analysed and tested for the presence of a spin-0 boson. The remaining reconstructed particles apart from the two leptons assigned to the Z are not used in the analysis, therefore it is independent of the Higgs boson decay.

(c) The constraint from a search for Yukawa production of a light Higgs boson [139]: a model is regarded as excluded if the predicted value of the Yukawa enhancement factor ξ for $\mathcal{H}_1$, multiplied with the branching fraction $\mathrm{BR}(\mathcal{H}_1 \to \tau^+\tau^-)$, is larger than the smallest value excluded in [139]. In the case of the CPV scan, where $\mathcal{H}_1$ is composed of CP-odd and CP-even parts, the weaker of the two limits calculated for the Yukawa production of a CP-even or a CP-odd Higgs boson is used in the comparison. For CP-even Higgs bosons, $\xi = -\sin\alpha/\cos\beta$, while for CP-odd Higgs bosons $\xi = \tan\beta$ holds. This constraint is helpful in excluding models with large $\tan\beta$, $2\,m_\tau < m_{\mathcal{H}_1} < 2\,m_\mathrm{b}$, and vanishing $\mathrm{e^+e^-} \to \mathcal{H}_1\mathrm{Z}$ cross-section.

(d) Additionally to the exclusion from other sources, the constraint from measurements of inclusive decays of a b quark into an s quark and a photon $\mathrm{BR}(\mathrm{b} \to \mathrm{s}\gamma)$ is shown. A model is shown as excluded by this constraint if the corresponding branching ratio, calculated using [140], falls outside the bounds $2.33 \times 10^{-4} < \mathrm{BR}(\mathrm{b} \to \mathrm{s}\gamma) < 4.15 \times 10^{-4}$ (95 % CL) [141]. This limit is used to constrain the CPC scenarios. This constraint is only shown as an overlay and not strictly as excluded area, because the experimental constraint is independent of the Higgs sector. Therefore, in general, a specific topology in the Higgs sector of a general MSSM model need not be excluded from the $\mathrm{BR}(\mathrm{b} \to \mathrm{s}\gamma)$ constraint. On the other hand this constraint is relatively closely connected to the Higgs sector, since the same MSSM parameters influence the decay $\mathrm{b} \to \mathrm{s}\gamma$ as the MSSM Higgs sector topologies.

These additional constraints are not included in the statistical combination and used independently of the standard search channels Higgsstrahlung and pair production.

6.3 Model Independent Higgs Mass Limits

For the model-independent interpretation of the OPAL Higgs searches the scaling factor

$$s_{95} = \frac{\sigma_{\max}}{\sigma_{\mathrm{ref}}}$$

is computed, where $\sigma_{\max}$ is the largest signal production cross-section consistent with the data at 95 % CL and σ_{ref} is a reference cross-section. For Higgsstrahlung the SM cross-section σ_{SM} is used as σ_{ref}; for pair production the cross-section of equation (3.3) with $\cos^2(\beta-\alpha) = 1$ is used. Initial-state radiation is included according to [142]. This means that a model which predicts a signal cross-section which is larger than $s_{95} \cdot \sigma_{\mathrm{ref}}$ is excluded.

Cross-section limits on the SM-like production and decay can be found in [114] and for flavour independent $\mathcal{H} \to \mathrm{q\bar{q}}$ decays in [132].

Fig. 6.5 (a) shows s_{95} for the production process $\mathrm{e^+e^-} \to \mathcal{H}_2\mathrm{Z} \to \mathcal{H}_1\mathcal{H}_1\mathrm{Z} \to \mathrm{b\bar{b}b\bar{b}Z}$. $\mathrm{BR}(\mathcal{H}_2 \to \mathcal{H}_1\mathcal{H}_1) = 1$ and $\mathrm{BR}(\mathcal{H}_1 \to \mathrm{b\bar{b}}) = 1$ is assumed. The observed borders and discontinuities are due to a number of different searches contributing and being sensitive in different mass ranges. For $m_{\mathcal{H}_2} < 80$ GeV, specific searches for this final state at 183 GeV provide a strong exclusion. For $80 < m_{\mathcal{H}_2} < 100$ GeV, only the $\mathrm{Z} \to \mathrm{q\bar{q}}$ final state is used, giving a weaker exclusion. For $100 < m_{\mathcal{H}_2} < 110$ GeV, the $\mathrm{Z} \to \nu\bar{\nu}$ final state is also employed. The limits are calculated for $m_{\mathcal{H}_1} > 10.5$ GeV only where the decay $\mathcal{H}_1 \to \mathrm{b\bar{b}}$ becomes kinematically possible.

Fig. 6.5 (b) shows s_{95} for the process $\mathrm{e^+e^-} \to \mathcal{H}_1\mathcal{H}_2 \to \mathrm{b\bar{b}b\bar{b}}$. $\mathrm{BR}(\mathcal{H}_1 \to \mathrm{b\bar{b}}) = \mathrm{BR}(\mathcal{H}_2 \to \mathrm{b\bar{b}}) = 1$ is assumed. The kinematic limit for $\sqrt{s} = 206$ GeV is indicated as a dashed line. Most searches apply only for $m_{\mathcal{H}_1} > 30$ GeV. Below $m_{\mathcal{H}_1} = 30$ GeV, only searches for pair

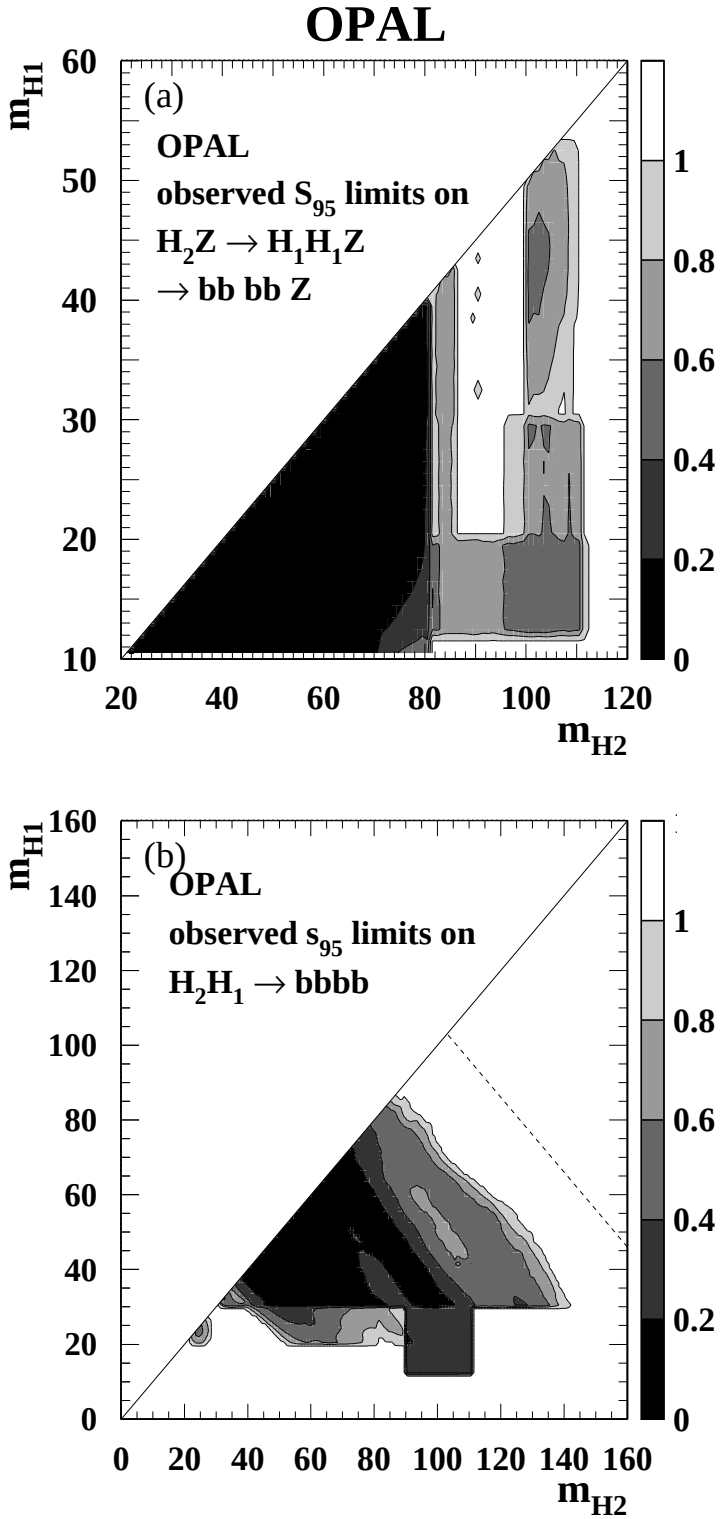

Figure 6.5: *Model-independent upper bounds on* $\sigma \times \mathrm{BR}$ *for (a) the* $\mathrm{e^+e^-} \to \mathcal{H}_2\mathrm{Z} \to \mathcal{H}_1\mathcal{H}_1\mathrm{Z} \to \mathrm{b\bar{b}b\bar{b}Z}$ *channel and (b) the* $\mathrm{e^+e^-} \to \mathcal{H}_1\mathcal{H}_2 \to \mathrm{b\bar{b}b\bar{b}}$ *channel. For (a), the SM cross-section for* $\mathrm{H_{SM}Z}$ *production is taken as normalization. For (b), The MSSM cross-section for* $\mathcal{H}_1\mathcal{H}_2$ *production with* $\cos^2(\beta - \alpha) = 1$ *is taken as normalization. The dashed line indicates the kinematic limit for* $\sqrt{s} = 206$ *GeV.*

production at $\sqrt{s} = 183$ GeV or lower contribute. Additionally, the area of $m_{\mathcal{H}_1} > 12$ GeV and $90 < m_{\mathcal{H}_2} < 110$ GeV is studied in the data at $\sqrt{s} = 199$ to 209 GeV.

In Fig. 6.6 (a) s_{95} for the process $e^+e^- \to \mathcal{H}_1\mathcal{H}_2 \to b\bar{b}\tau^+\tau^-$ is shown. The branching ratios are set to $BR(\mathcal{H}_1 \to b\bar{b}) = BR(\mathcal{H}_2 \to b\bar{b}) = 0.5$ and $BR(\mathcal{H}_1 \to \tau^+\tau^-) = BR(\mathcal{H}_2 \to \tau^+\tau^-) = 0.5$. The kinematic limit for $\sqrt{s} = 206$ GeV is indicated as a dashed line. The domain below $m_{\mathcal{H}_1} = 30$ GeV is covered only by data collected at $\sqrt{s} = 183$ GeV or lower.

Fig. 6.6 (b) shows the exclusion region for the process $e^+e^- \to \mathcal{H}_1\mathcal{H}_2 \to \mathcal{H}_1\mathcal{H}_1\mathcal{H}_1 \to b\bar{b}b\bar{b}b\bar{b}$. $BR(\mathcal{H}_2 \to \mathcal{H}_1\mathcal{H}_1) = 1$ and $BR(\mathcal{H}_1 \to b\bar{b}) = 1$ are assumed. At $m_{\mathcal{H}_2} < 80$ GeV the exclusion is stronger than for higher $m_{\mathcal{H}_2}$ due to dedicated searches at $\sqrt{s}$ up to 189 GeV. Above $m_{\mathcal{H}_2} = 80$ GeV, only searches using data recorded with $\sqrt{s}$ of 199 to 209 GeV are available.

6.4 Limits on Benchmark Scenarios

The presence of neutral Higgs bosons is tested in a constrained MSSM with seven parameters (see Section 2.3.3). Two of these parameters are sufficient to describe the Higgs sector at tree level. A convenient choice is $\tan\beta$ (the ratio of the vacuum expectation values of the Higgs fields) and one Higgs mass; m_A is chosen in the case of the CPC scenario and $m_{H^\pm}$ in the CPV scenario. Additional parameters appear at the level of radiative corrections; these are: m_{SUSY}, M_2, μ, A, and $m_{\tilde{g}}$. All soft SUSY-breaking parameters in the sfermion sector are set to m_{SUSY} at the electroweak scale. M_2 is the SU(2) gaugino mass parameter at the electroweak scale and M_1, the U(1) gaugino mass parameter, is derived from M_2 using the GUT relation $M_1 = M_2(5\sin^2\theta_W/3\cos^2\theta_W)$, where θ_W is the weak mixing angle. The supersymmetric Higgs mass parameter is denoted μ. The parameter $A = A_t = A_b$ is the common trilinear Higgs-squark coupling for up-type and down-type squarks. The stop and sbottom mixing parameters are defined as $X_t = A_t - \mu\cot\beta$ and $X_b = A_b - \mu\tan\beta$. The parameter $m_{\tilde{g}}$ is the gluino mass. For the CPV scenario the complex phases related to $A_{t,b}$ and $m_{\tilde{g}}$ are additional parameters. The phase related to $A_{t,b}$ enters at one-loop level while the one related to $m_{\tilde{g}}$ enters as a second-order correction to stop and sbottom loops. Large radiative corrections to the predicted mass $m_{\mathcal{H}_1}$ arise from top quark and scalar top loops, while the contributions from scalar bottom loops are smaller.

The precise mass of the top quark has a strong impact on $m_{\mathcal{H}_1}$; it is taken to be $m_{top} = 174.3$ GeV, the current average of the Tevatron measurements [143]. To account for the experimental uncertainty, all MSSM interpretations are also done for $m_{top} = 169$ GeV and $m_{top} = 179$ GeV. After the completion of these results, the top qark mass has been updated to $m_{top} = 178 \pm 4.3$ GeV [20].

Rather than varying all of the above MSSM parameters independently, we consider only a certain number of "benchmark sets" where the tree level parameters $\tan\beta$ and m_A (CPC scenario) or $m_{H^\pm}$ (CPV scenario) are scanned while all other parameters are fixed. Results are presented for eight benchmark sets [144] in the CPC scenario and nine in the CPV scenario[51]. Each scan point within a given benchmark set defines an independent realization of the MSSM (a model), which is tested by comparing its predicted observables (masses, cross-sections and decay branching ratios) with the experimental data. The aims of the construction of the individual benchmark sets are the following:

1. "no mixing"
   This scenario assumes no mixing in the stop and sbottom sectors ($X_{t,b} = 0$). It is kinematically accessible in large parts of its parameters space.

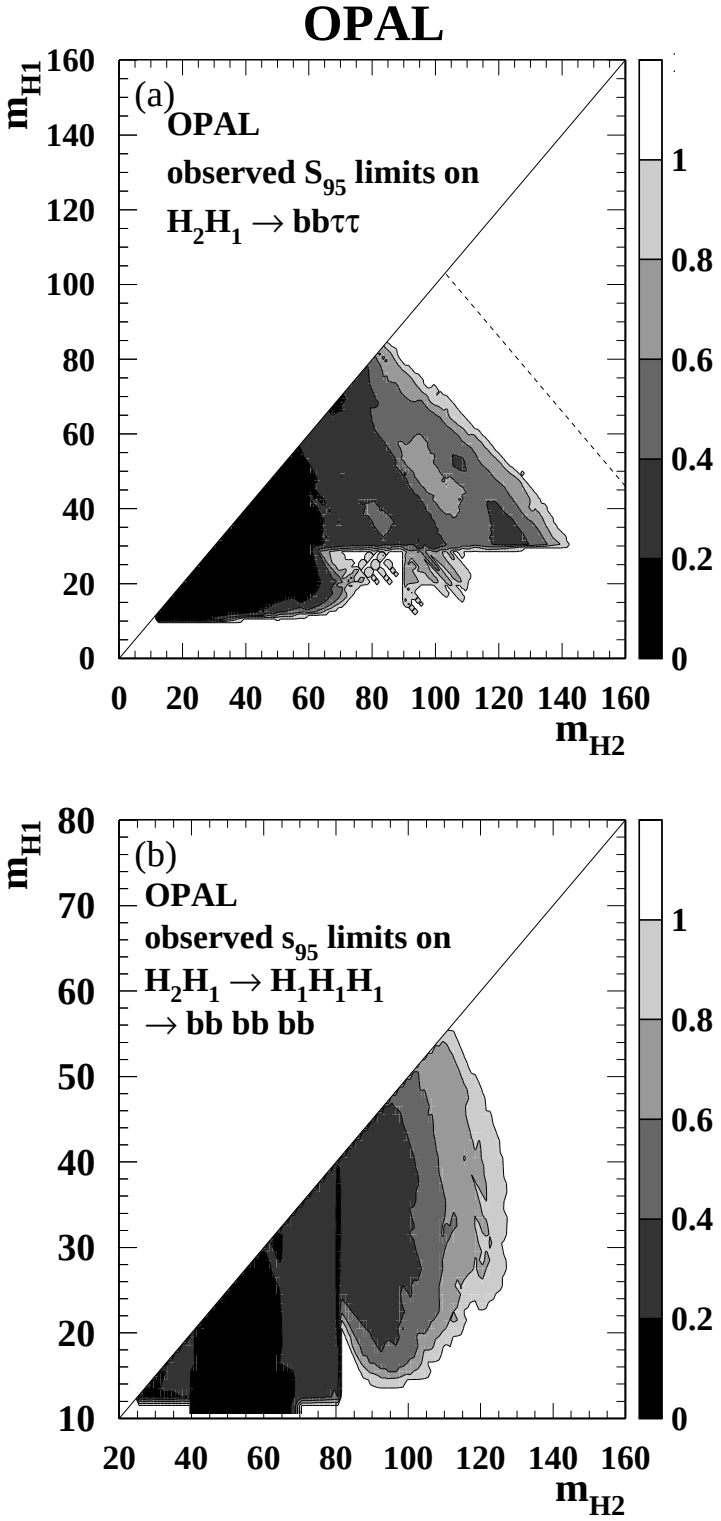

Figure 6.6: *Model-independent upper bounds on* $\sigma \times \mathrm{BR}$ *for (a) the* $\mathrm{e^+e^-} \to \mathcal{H}_1\mathcal{H}_2 \to \mathrm{b\bar{b}}\tau^+\tau^-$ *channel and (b) the* $\mathrm{e^+e^-} \to \mathcal{H}_1\mathcal{H}_2 \to \mathcal{H}_1\mathcal{H}_1\mathcal{H}_1 \to \mathrm{b\bar{b}b\bar{b}b\bar{b}}$ *channel. The MSSM cross-section for* $\mathcal{H}_1\mathcal{H}_2$ *production with* $\cos^2(\beta-\alpha) = 1$ *is taken as normalisation. The dashed line indicates the kinematic limit for* $\sqrt{s} = 206$ *GeV.*

2. "no mixing (2 TeV)"
   A derivate of the "no mixing" scenario, designed in the light of the upcoming Higgs searches at the LHC. It reduces the bounds from LEP by a larger value of M_{SUSY}, increasing the maximal value of m_{h} by about 5 GeV.

3. "$m_{\mathrm{h}}-$max"
   This scenario is designed to yield the most conservative exclusion in terms of $\tan\beta$ in the CPC case. The missing in the stop and sbottom sectors is adjusted such that for each $\tan\beta$ the maximum range of m_{h} is realized. That means, that the highest masses of m_{h} are expected in this scenario for $m_{\mathrm{A}} \gg m_{\mathrm{Z}}$.

4. "$m_{\mathrm{h}}-\mathrm{max}^{+}$"
   This scenario is very close to the "$m_{\mathrm{h}}-$max" concerning the predictions for the Higgs sector. It has a different sign of μ, which is favored by the presently available results on $(g-2)_{\mu}$ [145].

5. "constrained $m_{\mathrm{h}}-$max"
   This scenario is very similar to "$m_{\mathrm{h}}-\mathrm{max}^{+}$" and differs in the sign of X_{t}. It yields slightly smaller maximal values of m_{h} and therefore is not as conservative in the Higgs sector as "$m_{\mathrm{h}}-$max". It is designed to yield better agreement with $\mathrm{BR}(\mathrm{b} \to \mathrm{s}\gamma)$ constraints.

6. "large μ"
   This scenario differs from the other scenarios in the fact that one of the Higgs bosons is kinematically accessible in the complete parameter space. Nevertheless the scenario is difficult because for certain parameter combination the Higgs decays into $\mathrm{b\bar{b}}$ and $\tau^{+}\tau^{-}$ pairs are suppressed.

7. "gluophobic"
   This benchmark set is designed for the upcoming Higgs searches at the LHC. In this scenario the production cross-section is suppressed by a small coupling of the Higgs boson to gluons, otherwise one of the favourite production channels at the LHC.

8. "small α_{eff}"
   This scenario is designed to work as the "large μ" benchmark set. The coupling of the Higgs boson h to $\mathrm{b\bar{b}}$ and $\tau^{+}\tau^{-}$ pairs is suppressed. However, this only happens at $m_{\mathrm{h}} > 120$ GeV, inaccessible for LEP.

9. "CPX"
   This is the first benchmark set in a CP-violating scenario. It is designed to maximise the mixing of the CP-odd and CP-even terms in the mass eigenstates. Since its parameter space is already as well tested as in the CPC case, several derivatives of the "CPX" scenario are tested, too:

   - Different phases from 0° to 180°.
   - Different values of μ from 500 GeV to 4 TeV.
   - Different values of the SUSY breaking scale M_{SUSY} of 500 GeV and 1 TeV.

The parameters of the benchmark scans are summarized in Table 6.5.

For a given scan point the observables in the Higgs sector are calculated using two theoretical approaches. The FEYNHIGGS program [54, 146] is based on a two-loop diagrammatic approach [48, 147] and uses the on-shell (OS) renormalization scheme, while SUBHPOLE and

its CPV variant CPH [51] are based on a one-loop renormalization group improved calculation [148, 149, 150, 151] and uses the $\overline{\text{MS}}$ scheme. Both calculations give consistent results although small differences naturally exist. Numerical values for parameters in this thesis are given in the modified minimal substraction ($\overline{\text{MS}}$) scheme.

In the CPC case, the FEYNHIGGS calculation is retained for the presentation of the results since it yields slightly more conservative results (the theoretically allowed parameter space is wider) than SUBHPOLE. Also, FEYNHIGGS is preferred on theoretical grounds since its radiative corrections are more detailed than those of SUBHPOLE.

For this thesis, the existing calculations for the CPC benchmark sets 1, 3 and 6 have been repeated and all other scenarios have been calculated for the first time with the newest version of the calculation programs at the time of completion of the scans, FEYNHIGGS2.0 and CPH.

In the CPV case, neither of the two existing calculations is preferred a priori on theoretical grounds. While FEYNHIGGS contains more advanced one-loop corrections, CPH is more precise at the two-loop level. Therefore a solution is chosen where, in each scan point, the calculation yielding the more conservative result (less significant exclusion) is retained. For illustration, the results from FEYNHIGGS and CPH are also shown separately for the main CPV scenario "CPX" (see Section 6.4.2).

The exclusions obtained for the different benchmark sets are summarized in Table 6.6.

6.4.1 CP-Conserving MSSM Scenarios

Traditionally, CPC models have been used to test the Higgs sector of the MSSM. Only for this case theoretical predictions of Higgs boson masses and couplings have been available before the year 2000. Still, the CPC models are very important benchmark sets. While they do not represent the full generality of the model, they avoid other experimental constraints like the measurement of electric dipole moments of electrons and neutrons, which strongly constrain CP violation in the MSSM. Each of the models used here is in good agreement with the electroweak precision data. That mmeans that the ρ parameter is predicted to be

$$\rho = \frac{m_{\mathrm{W}}}{m_{\mathrm{Z}} \cos\theta_W} = 1.$$

For the CPC scenarios, almost all searches from Tab. 6.1 and 6.2 are needed to cover the complete parameter space. Depending on the values of $\tan\beta$, m_{h} and m_{A} different production and decay channels are dominant. The coverage of the parameter plane of a typical CPC scenario is shown in Fig. 6.7. The theoretically inaccessible reagionis shown in yellow (light grey). There, typically tachionic particles are predicted and therefore the model point is regarded as unphysical.

The areas of the dominance of different channels is shown in the boxes in Fig. 6.7. For large $\tan\beta$ and $m_{\mathrm{h}} < 10$ GeV, typically the production cross-section if $\mathrm{e^+e^-} \to \mathrm{hA}$ at the Z pole would be too large to be compatible with the LEP 1 Z shape measurements. For large $\tan\beta$ and $m_{\mathrm{h}} > 10$ GeV, the pair production channels $\mathrm{e^+e^-} \to \mathrm{hA} \to \tau^+\tau^-\mathrm{b\bar{b}}$ and $\mathrm{e^+e^-} \to \mathrm{hA} \to \mathrm{b\bar{b}b\bar{b}}$ are used. For $\tan\beta < 6$, the Higgsstrahlungschannel dominates over the pair production. All SM Higgs searches can be used. Finally, for very low $\tan\beta$ and large m_{h}, the decay channel $\mathrm{h} \to \mathrm{AA}$ is kinematiccally allowed.

Calculation of the Model Predictions

Out of the eight CPC benchmark sets examined in this thesis, sets 1, 3 and 6 have been used in the past [152]. All other scenarios are experimentally studied for the first time. Scenarios 4 and 5 are motivated by experimental constraints on the branching ratio of the inclusive

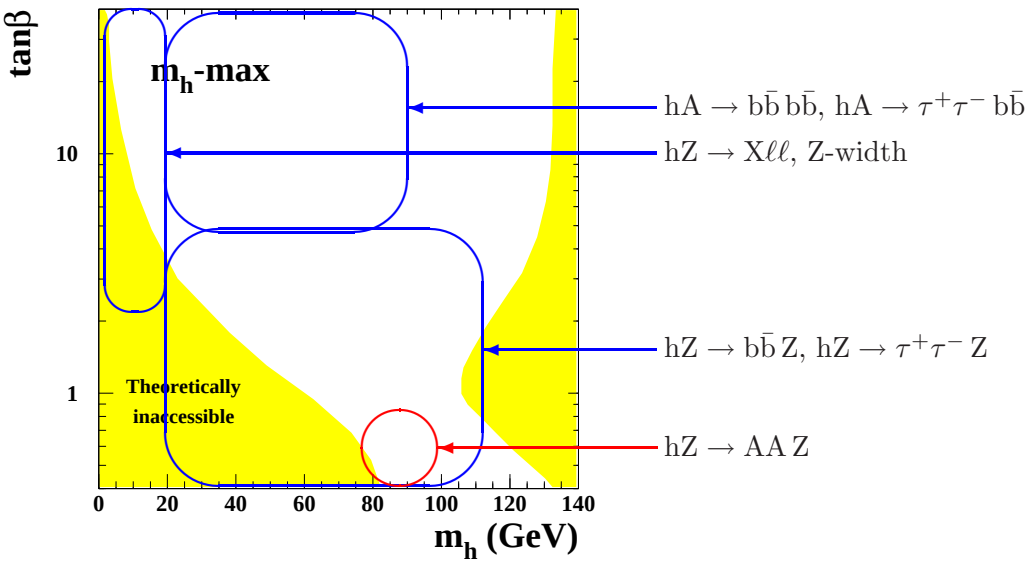

Figure 6.7: *The use of the individual searches in the "$m_{\mathrm{h}}-$max" scenario. In red, the areas are shown were the exclusion is difficult, although the Higgs boson is kinematically accessible.*

decay b→sγ and recent measurements of the muon anomalous magnetic moment $(g-2)_\mu$. Benchmark sets 2, 7 and 8 are motivated by the fact that the Higgs searches at the LHC may have low sensitivity to detect Higgs bosons in these situations. The choice of parameters is summarized in Table 6.5. In general, a full coverage of the MSSM Higgs phenomenology is achieved by these models, apart from the invisible decay of Higgs bosons, which is studied separately [58].

In most cases, $\tan\beta$ is scanned between 0.4 and 40. For values below 0.4 the theoretical predictions become unreliable; for $\tan\beta$ larger than 40 the decay width of the Higgs bosons may become comparable to or larger than the experimental mass resolution, and the modelling of the signal efficiencies may loose precision. Additionally, for large $\tan\beta$ a very strong b-quark yukawa coupling results, yielding theoretical inaccuracies of the predictions. Also, the observed exclusion regions (see below) do generally not anymore vary for $\tan\beta \gtrsim 30$. The value of m_{A} is scanned between 0 and 1000 GeV. For values of $m_{\mathrm{A}} < 2$ GeV, the branching ratios of the A become dominated by resonances and their calculation is unstable. However this area can be probed using direct searches for the heavier h boson, decay independent searches and Γ_{Z} constraints.

All other parameters are kept fixed inside each scenario. Out of the complete set of CP conserving MSSM parameters as listed in Tab. 2.4, only the parameters listed in Tab. 6.5 have a dominant impact on the observables of the Higgs sector. All other parameters can be safely ignored without loosing any interesting phenomena in the Higgs sector of the model.

Generally there is good agreement between the data and the background estimation, therefore limits on the MSSM parameters can be derived. In the CPC scenarios, the largest observed excess of the data over the background appears at $m_{\mathrm{h}} = 95$ GeV in the "$m_{\mathrm{h}}-$max" benchmark set. It has a significance of $2.8\,\sigma$. It should be noted, however, that there is a strong statistical probability of such an excess to appear somewhere in the parameter space under study. This is due to the fact that for each region in the parameter space of the model with different combinations of $(m_{\mathrm{h}}, m_{\mathrm{A}})$ a statistically independent experiment is tested, if in the model points differ by more than the mass resolution of the searches. Since the mass resolution is generally

Table 6.5: *Parameters of benchmark scenarios considered. Note that the values for X_t and $A_{t,b}$ are given for the $\overline{\text{MS}}$-renormalization scheme. Columns 2 to 6 refer to the CPC benchmark sets and the last column refers to the basic CPV benchmark set "CPX".*

Parameter	no mixing /(no-mixing (2 TeV))	m_h-max /(m_h-max$^+$) /(C m_h-max)	large-μ	gluophobic	small α_{eff}	CPX
Parameters varied in the scan						
$\tan\beta$	0.4–40 /(0.7–40)	0.4–40	0.7–40	0.4–40	0.4–40	0.6–40
m_A (GeV)	0–1000	0–1000	0–400	0–1000	0–1000	–
$m_{H^\pm}$ (GeV)	–	–	–	–	–	4–1000
Fixed parameters						
m_t (GeV)	174.3	174.3	174.3	174.3	174.3	174.3
m_{SUSY} (GeV)	1000 /(2000)	1000	400	350	800	500
M_2 (GeV)	200	200	400	300	500	200
μ (GeV)	-200 /(200)	-200 /(200) /(200)	1000	300	2000	2000
$m_{\tilde{g}}$ (GeV)	800	800	200	500	500	1000
X_t (GeV)	0	$\sqrt{6}\,m_{\text{SUSY}}$ /($\sqrt{6}\,m_{\text{SUSY}}$) /($-\sqrt{6}\,m_{\text{SUSY}}$)	-300	-750	-1100	$A_t - \mu\cot\beta$
$A_{t,b}$ (GeV)	$X_t + \mu\cot\beta$	$X_t + \mu\cot\beta$	$X_t + \mu\cot\beta$	$X_t + \mu\cot\beta$	$X_t + \mu\cot\beta$	1000
$\arg(A_{t,b})$	0	0	0	0	0	90°
$\arg(m_{\tilde{g}})$	0	0	0	0	0	90°

in the order of 10 GeV, up to around 100 statistically independent different experiments are performed for each scenario. The probability of a $2.8\,\sigma$ excess to show up somewhere in 100 statistically independent experiments is 26 %. Therefore, on the basis of the given significance of the excess, no claim of a discovery is possible.

Exclusions on CP Conserving MSSM models

In the following, each of the eight CPC scenarios is introduced and the exclusion on its parameter space is explained.

1. In the "no mixing" benchmark set the stop mixing parameter X_{t} is put at zero. The other parameters are fixed at the following values: $m_{\mathrm{SUSY}} = 1$ TeV, $M_2 = 200$ GeV, $\mu = -200$ GeV. The gluino mass $m_{\tilde{\mathrm{g}}}$ has little effect on the phenomenology of this scenario; its value is set to 800 GeV.

   The corresponding exclusion plots are shown in Fig. 6.8. The small unexcluded region with $64 < m_{\mathrm{h}} < 88$ GeV and $m_{\mathrm{A}} < 43$ GeV is due to the dominance of the cascade decay $\mathrm{h} \rightarrow \mathrm{AA}$ for which the search sensitivity is lower than for the $\mathrm{h} \rightarrow \mathrm{b\bar{b}}$ and $\tau^+\tau^-$ channels. One should note, however, that in this domain the charged Higgs boson mass $m_{\mathrm{H}^\pm}$ is predicted to smaller than 81 GeV. This area is probed by charged Higgs boson searches [153], which will be further extended in the future (see Fig. 6.8 (d)).

   The region with $m_{\mathrm{h}} > 83$ GeV and $m_{\mathrm{A}} > 82$ GeV is still unexcluded. In this domain, either the cross-section for Higgsstrahlung $\mathrm{e^+e^-} \rightarrow \mathrm{hZ}$ is small ($\sin^2(\beta-\alpha)$ is close to 0, see Eq. 3.1 in Section 3.1) or the pair production process $\mathrm{e^+e^-} \rightarrow \mathrm{hA}$ is kinematically forbidden.

   If one disregards the unexcluded domain at low $\tan\beta$, the following lower bounds are obtained at the 95% confidence level: $m_{\mathrm{h}} > 83$ GeV and $m_{\mathrm{A}} > 82$ GeV. Including all unexcluded regions, values of $\tan\beta$ are excluded from 0.8 to 6.2. However, the $\tan\beta$ limit is strongly dependent on the top quark mass which was taken to be $m_{\mathrm{top}} = 174.3$ GeV. For $m_{\mathrm{top}} = 179$ GeV, the $\tan\beta$ exclusion is reduced to $0.8 < \tan\beta < 4.7$.

   The constraint from the measured value of BR(b→sγ) (see Section 6.2.3) is indicated in Fig. 6.8 (b).

2. The "no mixing (2 TeV)" benchmark set differs from the no mixing scenario in the flipped sign of μ (which is preferred by the current results on $(g-2)_\mu$) and by a larger SUSY mass scale $M_{SUSY} = 2$ TeV. The value of $\tan\beta$ is scanned only from 0.7 to 40 due to numerical instabilities in the diagonalisation of the mass matrix for very low $\tan\beta$. Therefore the largest part of the unexcluded region of the "no mixing" case at low $\tan\beta$ is not probed in this scenario.

   The corresponding exclusion region is shown in Fig. 6.9. For $m_{\mathrm{A}} > 2$ GeV, i.e. above the region of resonant Higgs boson decays, absolute limits can be set for the Higgs boson masses and on $\tan\beta$, which are $m_{\mathrm{h}} > 83.3$ GeV, $m_{\mathrm{A}} > 84.3$ GeV and $\tan\beta > 4.2$. If the unexcluded area at $m_{\mathrm{A}} < 2$ GeV is also regarded, the exclusion in $\tan\beta$ is $0.9 < \tan\beta < 4.2$. The reduced $\tan\beta$ exclusion with respect to the "no mixing" case reflects the increased value of M_{SUSY}. This limit is further weakened to $\tan\beta > 3.2$ for $m_{\mathrm{top}} = 179$ GeV.

   The measurements of BR(b→sγ) exclude the no mixing (2 TeV) scenario for $m_{\mathrm{A}} < 450$ GeV, as can be seen in Fig. 6.9 (b).

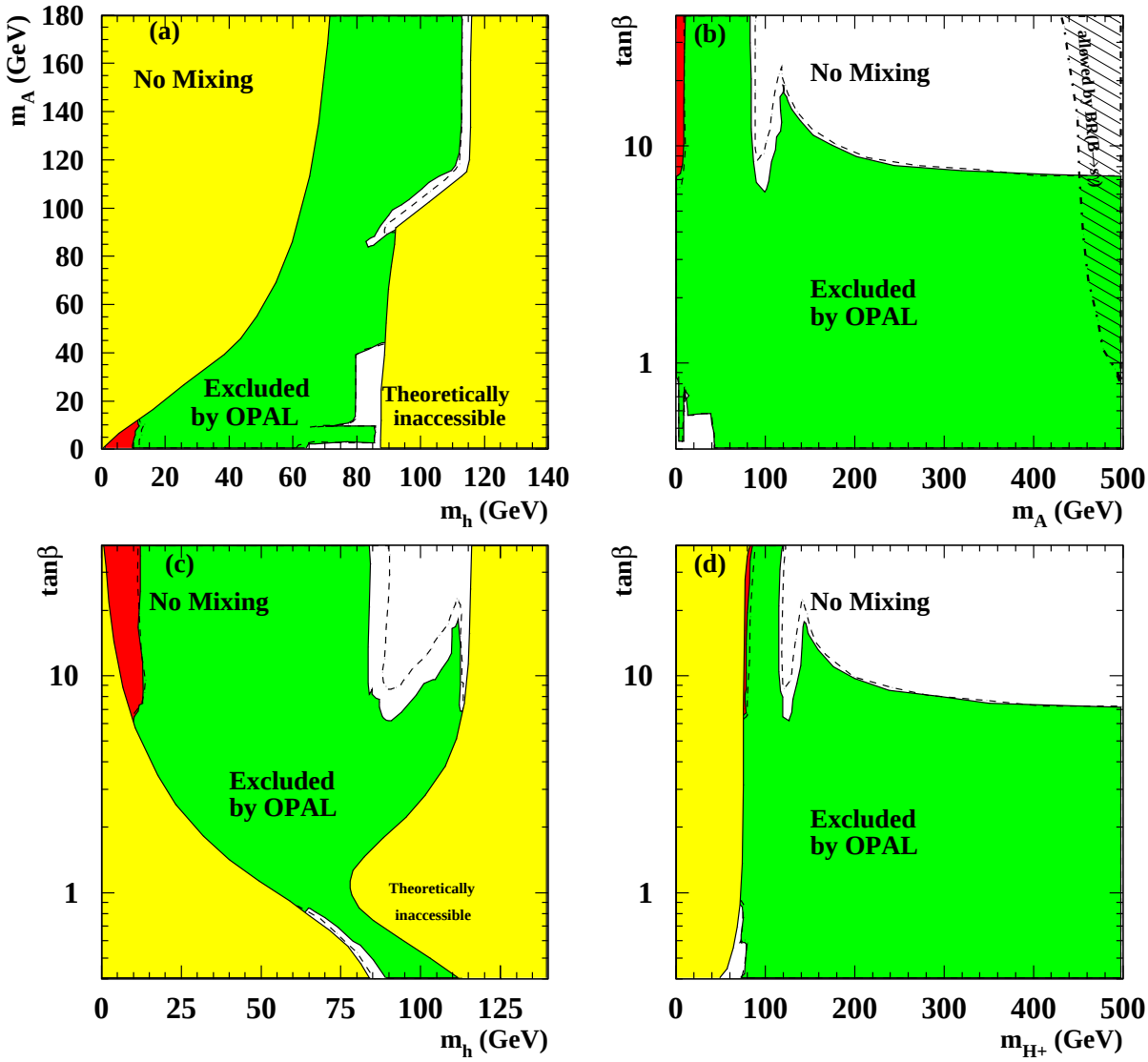

Figure 6.8: *Results for the "no mixing" benchmark scenario. The figure shows the excluded regions in darker grey (green) and theoretically inaccessible regions in light grey (yellow) as functions of the MSSM parameters in four projections: (a) the (m_{h}, m_{A}) plane, (b) the (m_{A}, $\tan\beta$) plane, (c) the (m_{h}, $\tan\beta$) plane and (d) the ($m_{\mathrm{H}^{\pm}}$, $\tan\beta$) plane. The dashed lines indicate the boundaries of the regions expected to be excluded at the 95% CL if only SM background processes are present. The region excluded by Yukawa searches, Z-width constraints or decay independent searches is shown in dark grey (red). In (b) the hatched area is still allowed by* $\mathrm{BR}(\mathrm{b} \to \mathrm{s}\gamma)$ *searches.*

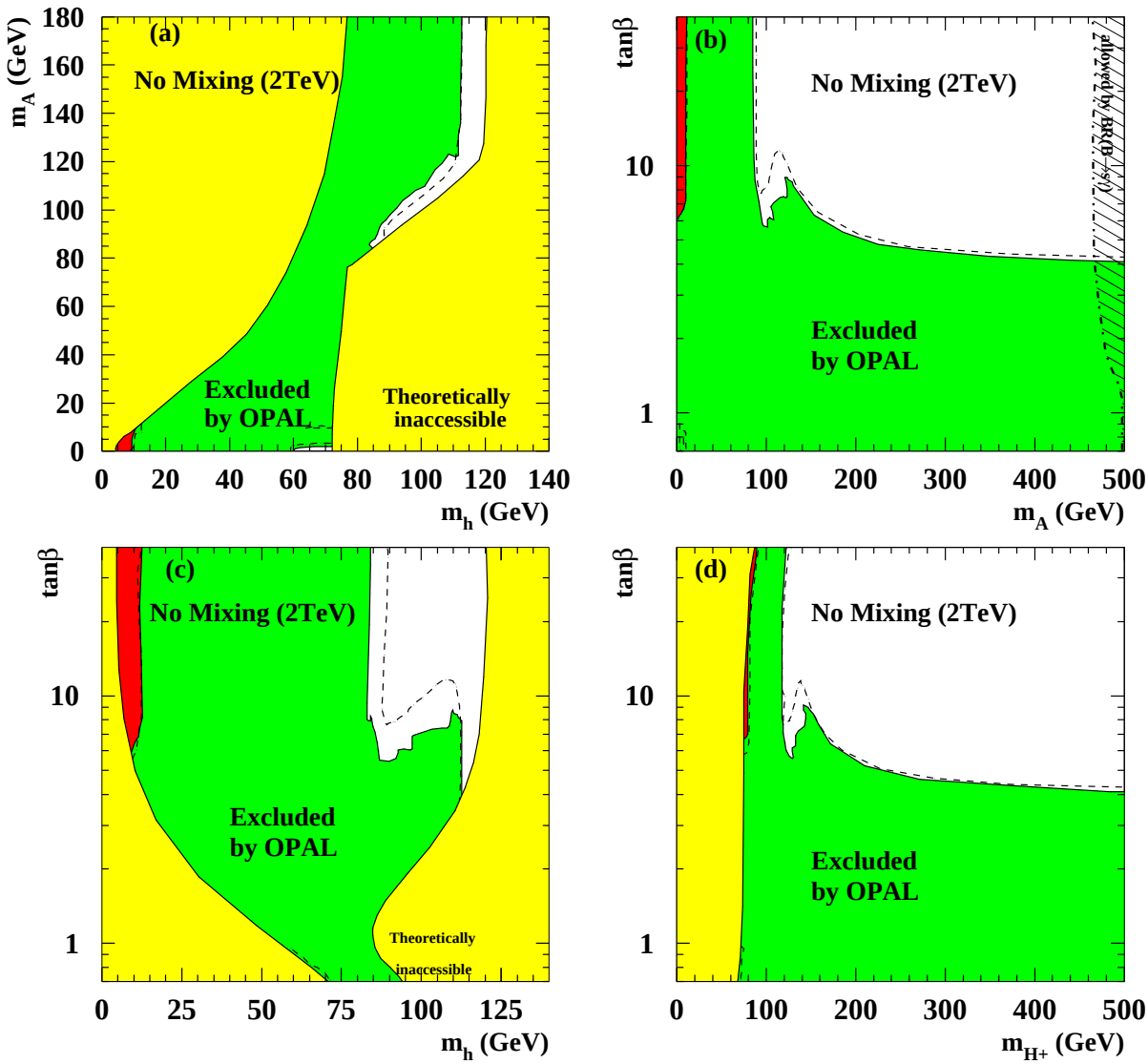

Figure 6.9: *Results for the "no mixing (2 TeV)" benchmark scenario described in the text of Section 6.4.1. See Fig. 6.8 for the notation.*

3. The "$m_{\mathrm{h}}-$max" benchmark set is designed to yield the largest range of m_{h} for a given $(m_{\mathrm{A}}, \tan\beta)$. This scenario is therefore the most conservative in terms of exclusion in $\tan\beta$. The other parameters are fixed as in the "no mixing" scenario, with the exception of the stop mixing parameter $X_t = \sqrt{6}$ TeV.

   The exclusion plots for this benchmark set are shown in Fig. 6.10. The following absolute limits are obtained at the 95% confidence level: $m_{\mathrm{h}} > 84.5$ GeV and $m_{\mathrm{A}} > 85.0$ GeV. Furthermore, values of $\tan\beta$ between 0.7 and 1.9 are excluded. For $m_{\mathrm{top}} = 179$ GeV this exclusion shrinks to the domain $1.0 < \tan\beta < 1.3$. Since the "$m_{\mathrm{h}}-$max" benchmark set yields the most conservative exclusion in $\tan\beta$, also $m_{\mathrm{top}} = 183$ GeV as the new $1\,\sigma$ upper bound of an increased world average of $m_{\mathrm{top}} = 178$ GeV was tested. This is illustrated in Fig 6.10 (b) and in Fig 6.10 (c), where the exclusion in the $(\tan\beta, m_{\mathrm{A}})$ plane respectively

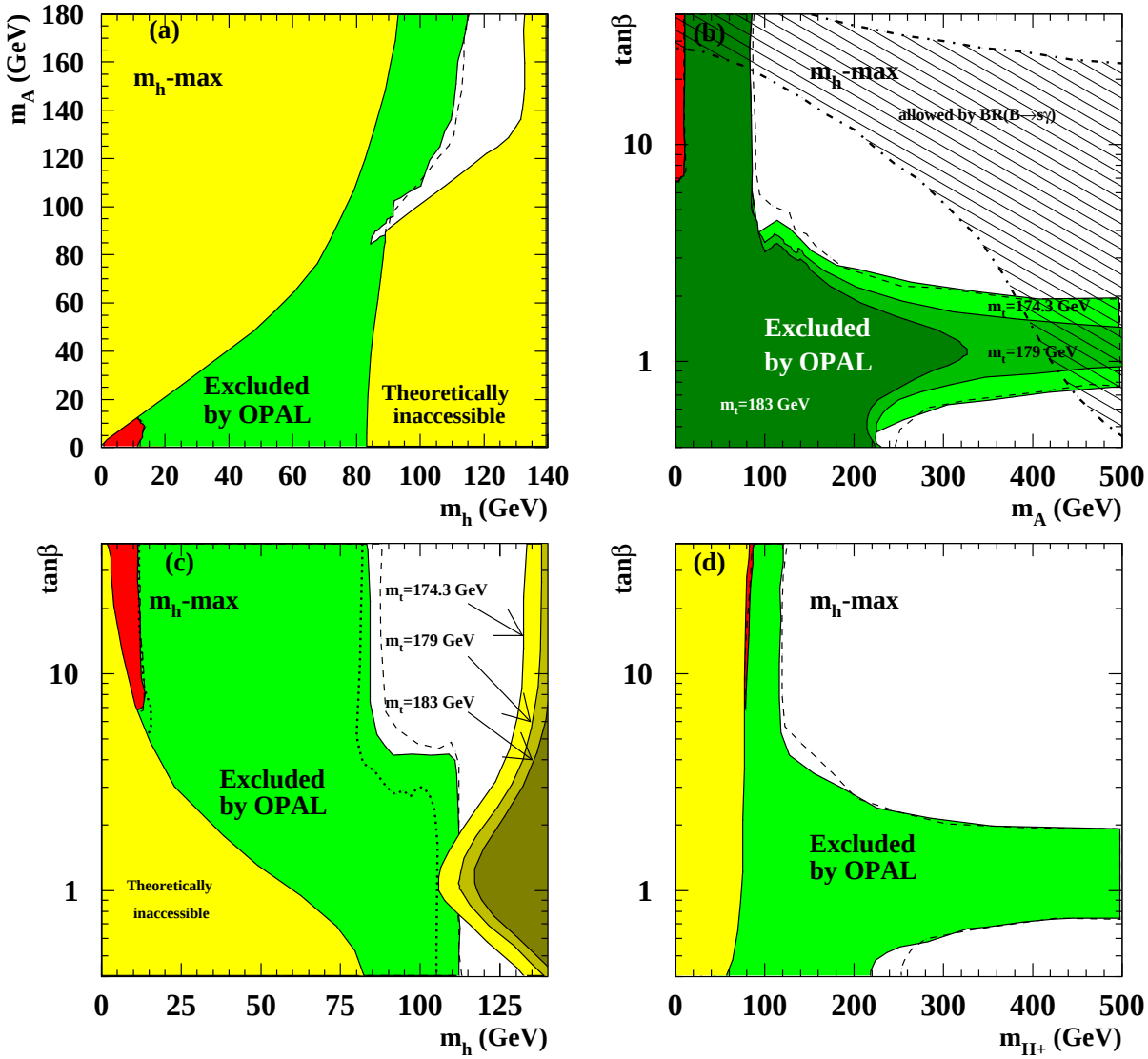

Figure 6.10: *Results for the $m_{\mathrm{h}}-$max benchmark scenario. See Fig. 6.8 for the notation. The dotted line in (c) shows the observed 99.9% confidence limit. The differently shaded regions in (b) show the exclusion for different values of m_{top}, as written in the Plot. The upper limit on m_{h} for different values of m_{top} is shown in (c), as expressed in the plot.*

the theoretical upper bounds on m_{h} for $m_{\mathrm{top}} = 179$ GeV and $m_{\mathrm{top}} = 183$ GeV are also shown. Should the world average of the top quark mass move beyond 179.5 GeV, the exclusion in $\tan\beta$ would vanish completely.

The supplementary constraint from the measured value of the BR(b→sγ) is shown in Fig. 6.10 (b).

4. The "$m_{\mathrm{h}}-\mathrm{max}^{+}$" benchmark set differs from the "$m_{\mathrm{h}}-$max" case only by the flipped sign of μ. This choice is favored by the presently available results on $(g-2)_{\mu}$ [145]. Since the Higgs boson properties depend only weakly on the sign of μ, the accessible Higgs mass range as well as the excluded domains are very similar to those of the "$m_{\mathrm{h}}-$max"

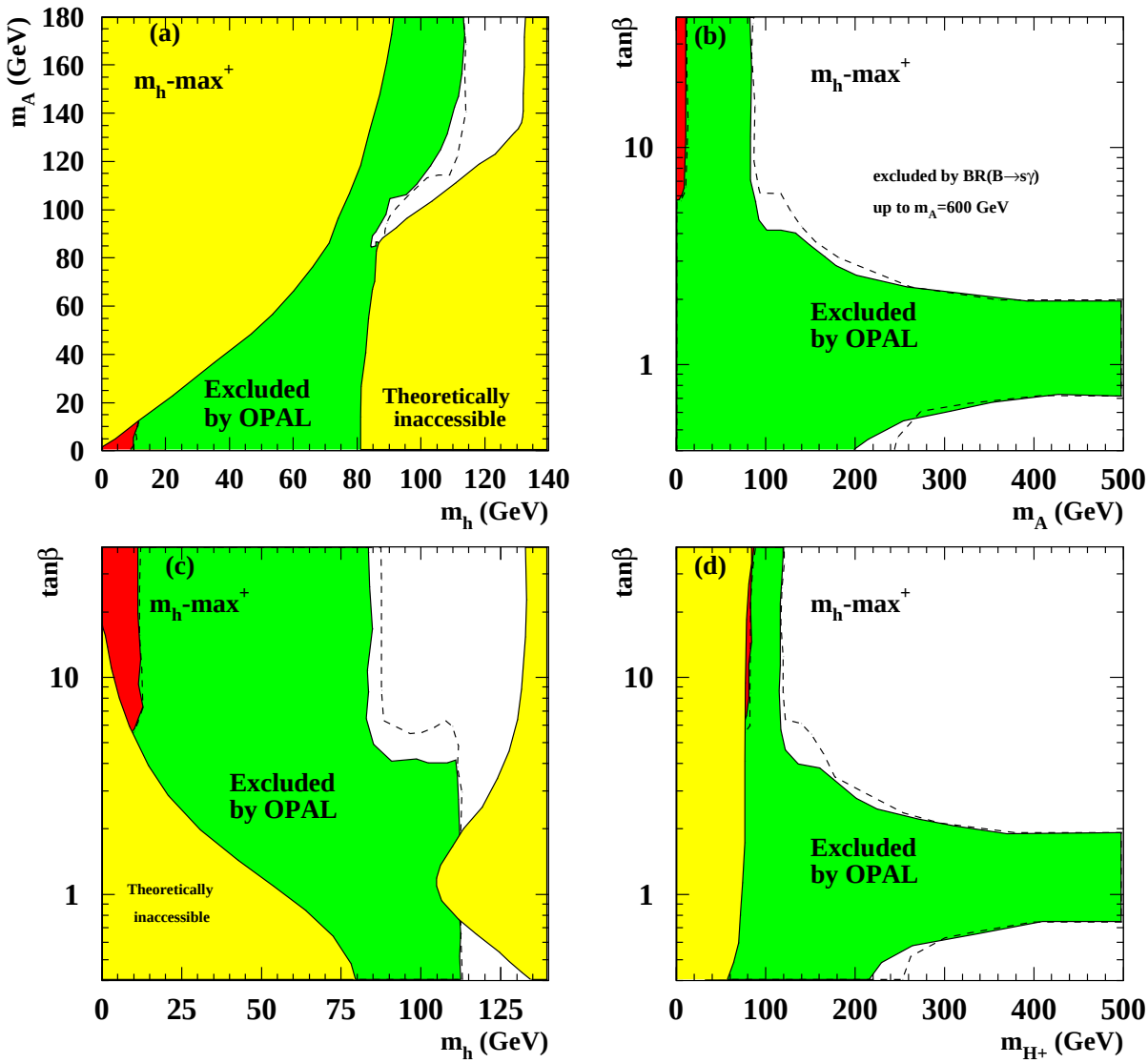

Figure 6.11: *Results for the "m_h−max$^+$" benchmark scenario described in the text of Section 6.4.1. See Fig. 6.8 for the notation.*

scenario; they are shown in Fig. 6.11.

The limits on the Higgs masses are $m_h > 84.5$ GeV and $m_A > 84.0$ GeV. The excluded range in $\tan\beta$ is $0.7 < \tan\beta < 1.9$, which decreases to $0.96 < \tan\beta < 1.4$ for $m_{top} = 179$ GeV.

The "m_h−max$^+$" scenario is excluded for $m_A < 600$ GeV by BR(b→sγ) measurements for all values of $\tan\beta$ considered (between 0.4 and 40). This means that only the decoupling limit with m_h at its maximum value for a given $\tan\beta$ is still allowed by BR(b→sγ).

5. The constrained "m_h-max" benchmark set differs from the "m_h−max$^+$" set by the flipped sign of X_t, which yields better agreement with BR(b → sγ) constraints. One

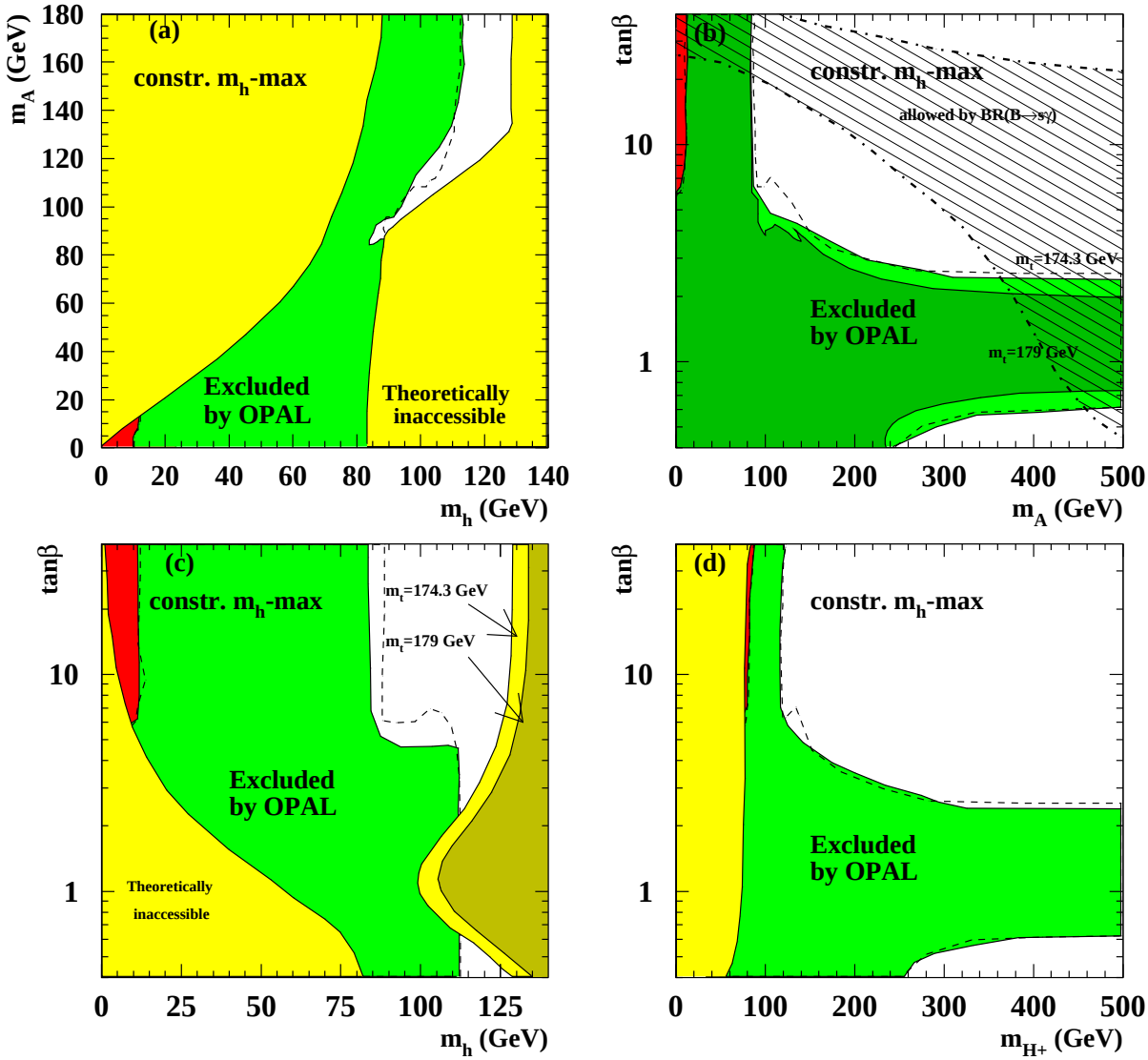

Figure 6.12: *Results for the constrained "$m_{\mathrm{h}}-$max" benchmark scenario described in the text of Section 6.4.1. See Fig. 6.8 for the notation. The differently shaded regions in (b) show the exclusion for different values of m_{top}, as written in the Plot. The upper limit on m_{h} for different values of m_{top} is shown in (c), as also expressed in the plot.*

observes that the maximum value of the Higgs boson mass at a given $\tan\beta$ is lowered by about 5 GeV.

The excluded areas for this scenario (see Fig. 6.12) show similar features as the "$m_{\mathrm{h}}-$max" and "$m_{\mathrm{h}}-\mathrm{max}^{+}$" scenarios. The limits on the Higgs masses are $m_{\mathrm{h}} > 84.0$ GeV and $m_{\mathrm{A}} > 85.0$ GeV. The excluded range in $\tan\beta$ is $0.6 < \tan\beta < 2.2$, which shrinks to $0.8 < \tan\beta < 1.8$ for $m_{\mathrm{top}} = 179$ GeV. This is illustrated in Fig. 6.12) (b) and (c).

The supplementary constraint from the measured value of the b$\to$sγ branching ratio is shown in Fig. 6.12 (b) as the band delimited by the two dash-dotted lines.

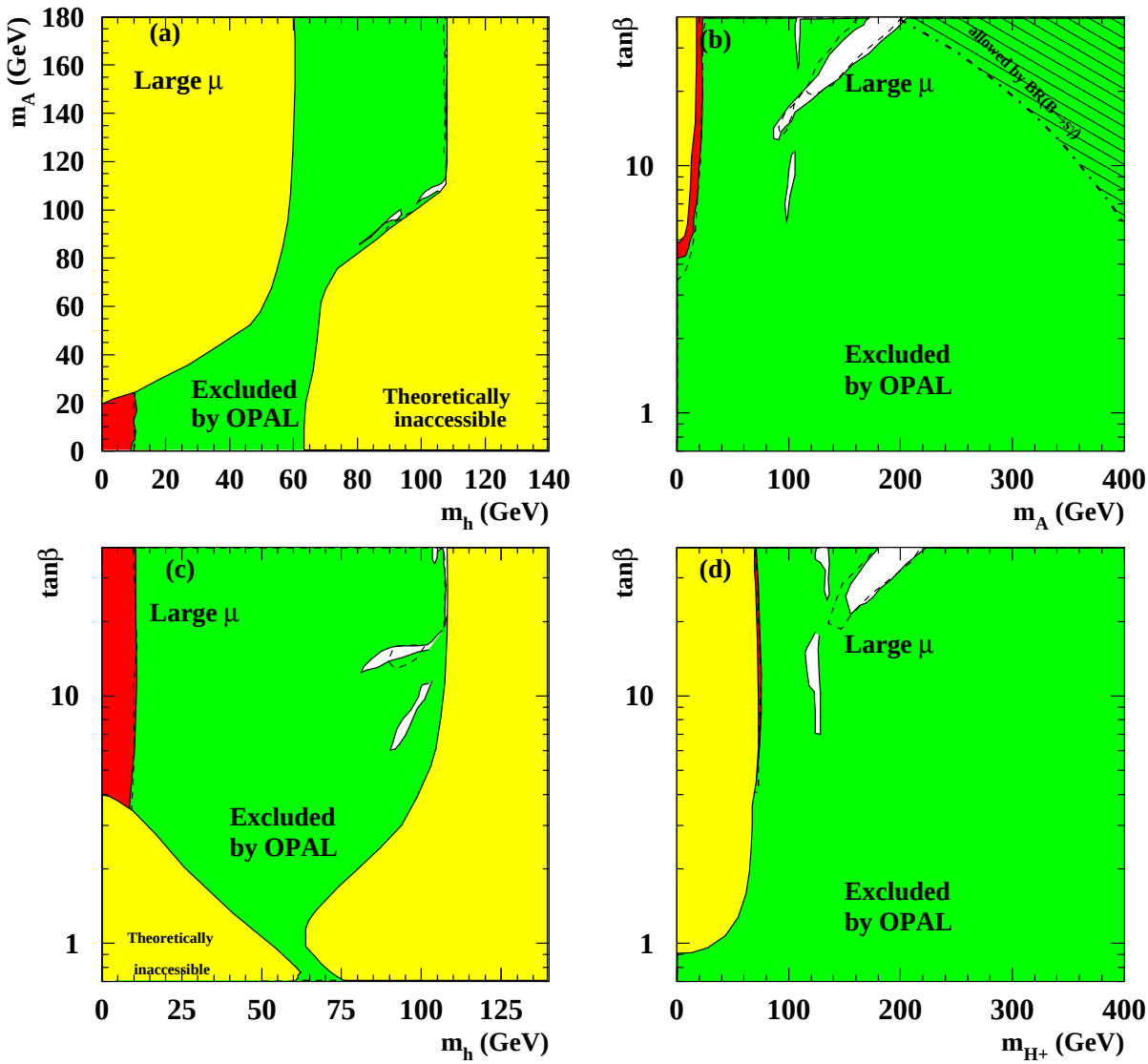

Figure 6.13: *Results for the "large μ" benchmark scenario described in the text of Section 6.4.1. See Fig. 6.8 for the notation.*

6. The "large μ" benchmark set is designed to illustrate choices of parameters for which the detection of the Higgs bosons is believed to be a priori difficult at LEP. The parameters are set to the following values: $m_{\rm SUSY}$=400 GeV, $\mu = 1$ TeV, $M_2 = 400$ GeV, $m_{\tilde{\rm g}} = 200$ GeV, $X_t = -300$ GeV. It is scanned from $\tan\beta = 0.7 - 40$ and $m_{\rm A} = 0 - 400$.

   For this set of parameters, the h boson is always kinematically accessible ($m_{\rm h} < 108$ GeV) but its decay to $\rm b\bar{b}$, on which most of the searches are based, is suppressed. For many of the scan points the decay $\rm h \to \tau^+\tau^-$ is also suppressed. The dominant decay modes are thus $\rm h \to c\bar{c}, gg$ or $\rm W^+W^-$, and the detection of Higgs bosons has to rely more heavily on flavour-independent searches.

   In some of the scan points the Higgsstrahlung process $\rm e^+e^- \to hZ$ is suppressed altogether ($\sin^2(\beta - \alpha)$ small). However, the heavy neutral scalar is relatively light in

such cases ($m_{\mathrm{H}} < 109$ GeV) and the cross-section for the process $\mathrm{e^+e^-} \to \mathrm{HZ}$, being proportional to $\cos^2(\beta - \alpha)$, is large.

The exclusions for this benchmark scenario are given in Fig. 6.13. They show that the parameter space is essentially excluded even in this difficult scenario, with the exception of a few isolated "islands". Those may slightly increase for higher values of the top quark mass. The origin of the islands can best be explained using Fig. 6.13 (b). The large diagonal island at $m_{\mathrm{A}} > 100$ GeV is due to the fact that $\mathrm{BR(h \to b\bar{b})}$ goes to 0 there. The two thin vertical islands around $m_{\mathrm{A}} > 100$ GeV are due to an overlap between $\mathrm{e^+e^- \to hZ}$ and $\mathrm{e^+e^- \to HZ}$ production. Both are kinematically accessible, but either one or the other can be used in the interpretation.

The supplementary constraint from the measured value of the $\mathrm{b \to s\gamma}$ branching ratio is shown in Fig. 6.13 (b).

7. The "gluophobic" benchmark set is constructed such that the Higgs coupling to gluons is suppressed due to a cancellation between the top and the stop loops at the hgg vertex. Since at the LHC the searches will rely heavily on the production of the Higgs boson by gluon-gluon fusion, such a scenario may be difficult to investigate there. The parameters chosen are : m_{SUSY}= 350 GeV, M_2 = 300 GeV, μ = 300 GeV, X_t = −750 GeV, $0.4 < \tan\beta < 40$, 0 GeV $< m_{\mathrm{A}} <$ 1 TeV and $m_{\tilde{\mathrm{g}}}$=500 GeV.

   The exclusion for this benchmark set is shown in Fig. 6.14. It is excluded to a large extend. The limits on the Higgs masses are $m_{\mathrm{h}} > 82$ GeV and $m_{\mathrm{A}} > 87.5$ GeV. The excluded range in $\tan\beta$ is $\tan\beta < 6.0$. The excluded range is reduced to $\tan\beta < 3.5$ for $m_{\mathrm{top}} = 179$ GeV.

   The supplementary constraint from the measured value of the $\mathrm{b \to s\gamma}$ branching ratio is shown in Fig. 6.14 (b).

8. In the "small α_{eff}" benchmark set the Higgs boson decay channels $\mathrm{h \to b\bar{b}}$ and $\mathrm{h \to \tau^+\tau^-}$ are suppressed with respect to their SM coupling due to corrections from $\tilde{\mathrm{b}} - \tilde{\mathrm{g}}$ loops. This scenario may also be difficult to investigate by the LHC experiments. Similarly to the large-μ scenario, such suppressions occur for large $\tan\beta$ and not too large m_A. The parameters chosen are: m_{SUSY} = 800 GeV, M_2 = 500 GeV, μ = 2 TeV, X_t = −1100 GeV, $0.4 < \tan\beta < 40$, and $m_{\tilde{\mathrm{g}}}$ =500 GeV.

   The exclusion for this benchmark set is shown in Fig. 6.15. The limits on the Higgs masses are $m_{\mathrm{h}} > 79.0$ GeV and $m_{\mathrm{A}} > 90.0$ GeV. The excluded range in $\tan\beta$ is $0.4 < \tan\beta < 3.6$, which is reduced to $0.5 < \tan\beta < 2.9$ for $m_{\mathrm{top}} = 179$ GeV. It appears that effects of suppression of the decays $\mathrm{h \to b\bar{b}}$ and $\mathrm{h \to \tau^+\tau^-}$ do not play a role in the region kinematically accessible at LEP.

   The constraint from the measured value of $\mathrm{BR(b \to s\gamma)}$ is shown in Fig. 6.15 (b).

In summary, no choice of parameters in the context of the CPC models was found in which either a statistically significant signal is found or in which the limit on the mass of the lightest Higgs boson vanishes. The lowest allowed CP even Higgs boson mass in the CPC models is $m_{\mathrm{h}} > 64$ GeV in the "no mixing" benchmark set. Disregarding the unexcluded region in the "no mixing" scenario due to its accessibility by charged Higgs searches, the lower CP-even Higgs mass limit is $m_{\mathrm{h}} > 79$ GeV. The smallest excluded area in $\tan\beta$ is $0.7 < \tan\beta < 1.9$ in the "m_{h}−max" scenario. The unexcluded area at very low m_{A} in the no mixing scenario is already excluded by the LEP combination in this scenario.

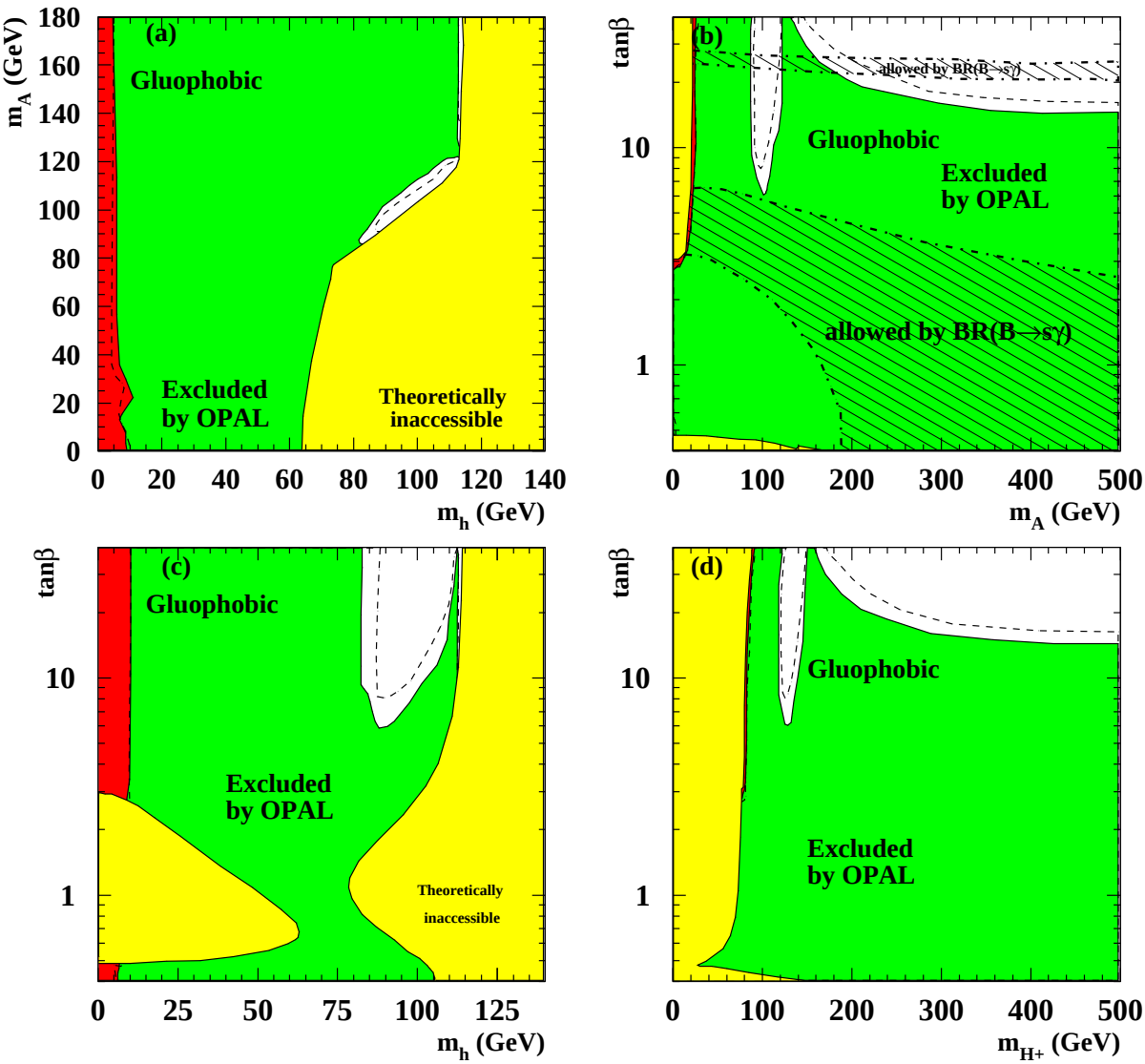

Figure 6.14: *Results for the "gluophobic" benchmark scenario described in the text of Section 6.4.1. See Fig. 6.8 for the notation. The hatched area in (c) is allowed by the BR(b→sγ) constraint.*

6.4.2 CP-Violating MSSM Scenarios

While CPC MSSM models do not help to explain the missing CP violation needed for baryogenesis [25], the additional CP violation introduced in the soft SUSY breaking lagrangian in the form of the complex phases of certain parameters can help to introduce enough CP violation to generate the cosmic matter-antimatter asymmetry [28]. The other advantage of the CPV models under study here is that they represent the most general case of parameter choices in the Higgs sector. On the other hand, the allowed amount of CP violation is limited by measurements of electric dipole moments.

For the CPV scenarios, also most of the searches from Tab. 6.1 and 6.2 are needed to cover the complete parameter space. Depending on the values of $\tan\beta$, m_{h} and m_{A} different

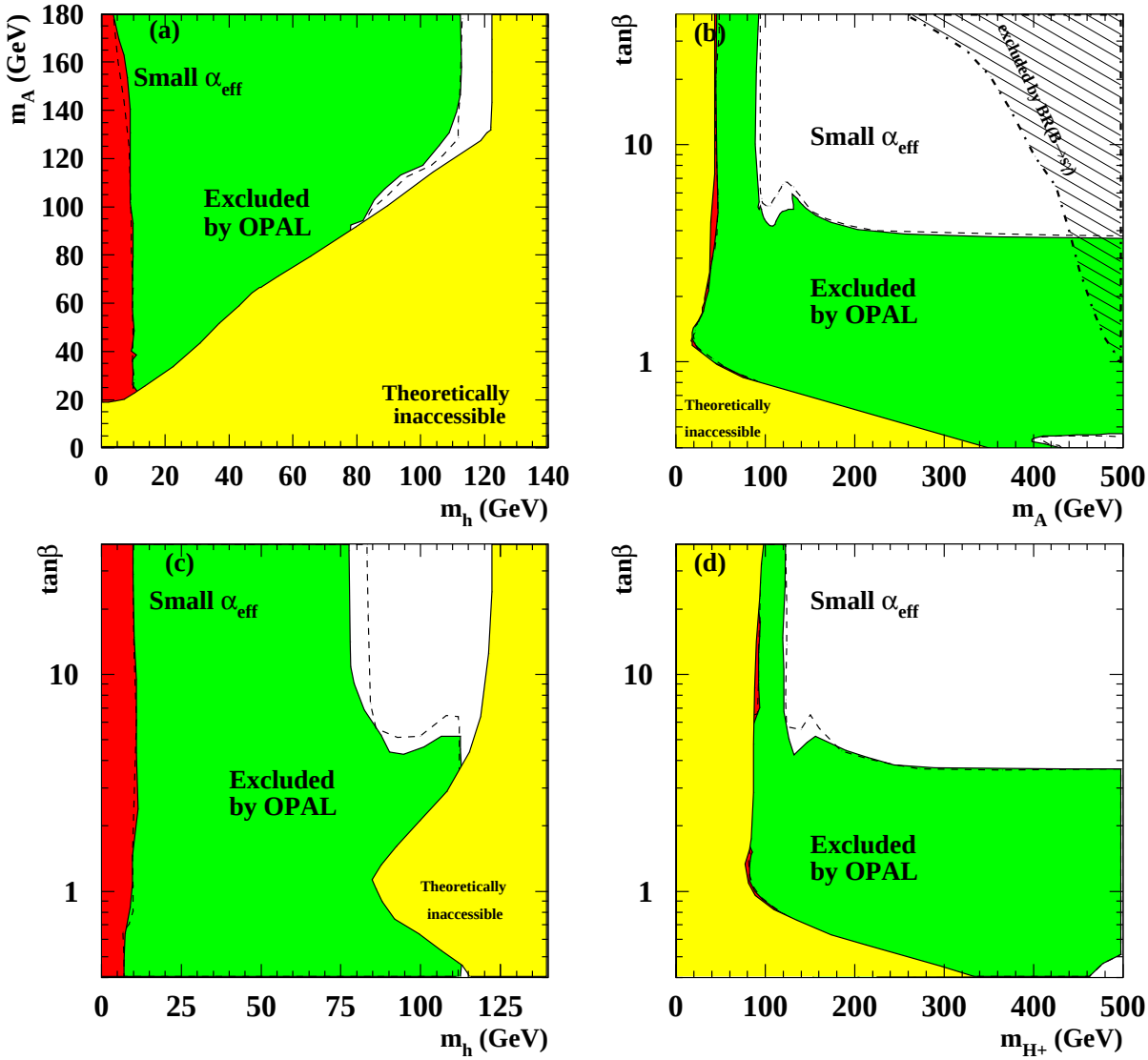

Figure 6.15: *Results for the "small $\alpha_{\rm eff}$" benchmark scenario described in the text of Section 6.4.1. See Fig. 6.8 for the notation.*

production and decay channels are dominant. The coverage of the parameter plane of the "CPX" scenario is shown in Fig. 6.16.

The areas of the dominance of different channels is shown in the boxes in Fig. 6.16. For large $\tan\beta$ and $m_{\rm H_1} < 12$ GeV, the Yukawa production channel $e^+e^- \to b\bar{b} \to H_1 b\bar{b} \to \tau^+\tau^- b\bar{b}$ can be used. For larger $m_{\rm h} > 12$ GeV, off-diagonal searches for $e^+e^- \to H_1H_2$ are dominant. For $\tan\beta < 10$, the Higgsstrahlung process $e^+e^- \to H_2Z$ begins to dominate over the pair production. Where kinematically allowed, i. e. for $m_{\rm H_1} < 50$ GeV, the decay $H_2 \to H_1H_1$ is strong, with severe consequences for the seach sensitivity. Finally, for $\tan\beta < 4$, the Higgsstrahlung process $e^+e^- \to H_1Z$ gradually takes over.

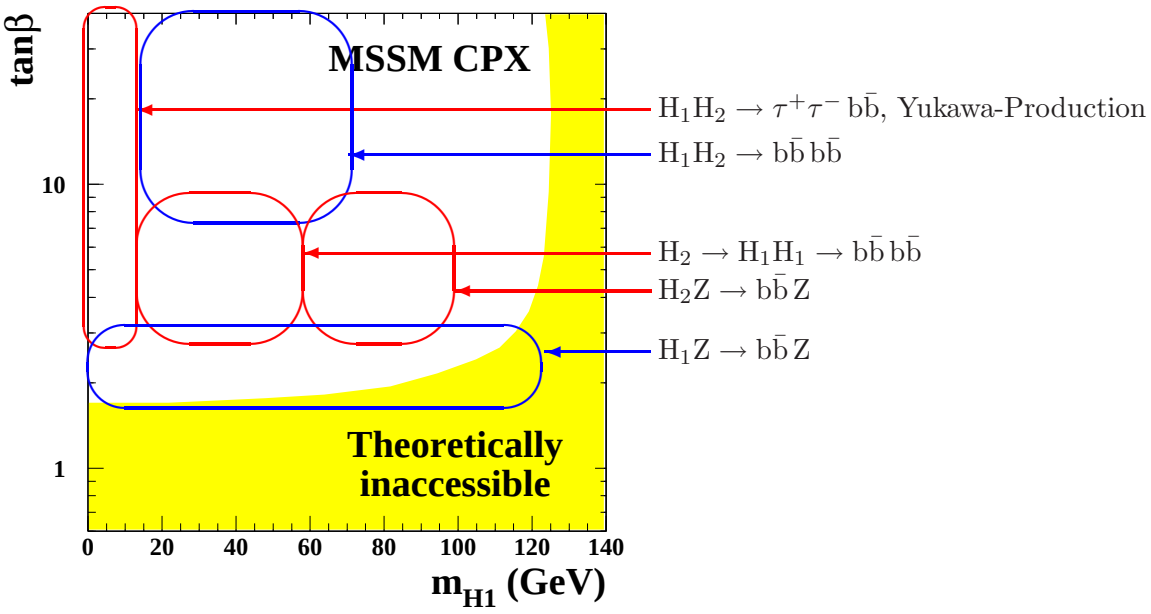

Figure 6.16: *The use of the individual searches in the "CPX" scenario. In red, the areas are shown were the exclusion is difficult, although the Higgs boson is kinematically accessible.*

Calculation of the Model Predictions

As outlined in Section 2.3.4, the size of the CPV off-diagonal elements of the Higgs boson mass matriximaginary contribution to μA_t and inversely proportional to the common SUSY breaking scale M_{SUSY} (2.58). As in the CPC scenarios, the top quark mass has a sizeable effect on the scenario.

When choosing the parameters, experimental constraints [52] from electric dipole moment (EDM) measurements of the neutron and the electron have to be fulfilled. However, cancellations among different contributions to the EDM may naturally emerge [50]; hence those measurements provide no universal exclusion in the MSSM parameter space, while direct searches at LEP provide a good testing ground for a CPV MSSM.

The basic CPV MSSM benchmark set is called "CPX". Its parameters are chosen such as to fulfill the EDM constraints for most of the values of $\tan\beta$ and $m_{\mathrm{H}^\pm}$ chosen, and to provide features that are the most dissimilar from a CPC scenario. The choice of parameters [51] is given in Table 6.5 (last column). In the definition of the "CPX" scenario [51] the relations $\mu = 4m_{\mathrm{SUSY}}$ and $|A_{\mathrm{t,b}}| = |m_{\tilde{\mathrm{g}}}| = 2m_{\mathrm{SUSY}}$ are fixed. Here, $m_{\mathrm{SUSY}} = 500$ GeV is chosen. The parameter M_2 is set to 200 GeV. Additionally the complex phases of $A_{\mathrm{t,b}}$ and $m_{\tilde{g}}$ are fixed at 90° degrees. Variants of the "CPX" scenario are investigated to check the stability of the "CPX" results with respect to the choice of its parameters. The phases of $A_{\mathrm{t,b}}$ and $m_{\tilde{g}}$ varied from from 0° to 180°, μ in between 500 and 4000 GeV. The scenario with $\arg(A_{\mathrm{t,b}}) = 90°$ has very different features from a CPC case and therefore has good properties for a CPV benchmark scenario.

The benchmark scan databases, containing masses, cross-sections and branching ratios for all three neutral Higgs bosons for a variety of different input parameters, are generated using both CPH [51], a modified version of SUBHPOLE, and FEYNHIGGS 2.0 [146]. They are implemented in a modified version of HZHA [76]. Initial-state radiation and interference between Higgsstrahlung and boson fusion processes are taken into account by HZHA. The

parameter $\tan\beta$ is scanned from 0.6 to 40, and $m_{\mathrm{H}^\pm}$ is scanned from 4 to 1000. In this region both H_1 and H_2 have a width below 1 GeV, negligible with respect to the experimental resolution of several GeV.

Also in the CPV scenarios there is good agreement between the data and the background estimation. The largest observed excess of the data over the background appears at $m_{\mathrm{H}_1} = 40$ GeV and $m_{\mathrm{H}_2} = 105$ GeV in the "CPX" benchmark set. It has a significance of $3.0\,\sigma$. As in case of the CPC interpretations, there it should be noted that there is a non-negligible statistical probability of such an excess to appear somewhere in the parameter space under study, therefore limits on the MSSM parameter space are derived. The observed excess is strongly influenced by the excess of data over background in one bin at $m_{\mathcal{H}_1} + m_{\mathcal{H}_2} = 150$ GeV in Fig. 5.6.

Exclusions on CP Violating MSSM models

In the following, the "CPX" scenario and variations of it are introduced and the excluded parameter ranges are explained.

1. Fig. 6.17 shows the combined exclusion result for the "CPX" scenario with all phases equal to 90°, $m_{\mathrm{SUSY}} = 500$ GeV and $\mu = 2$ TeV. Fig. 6.17 (a) shows both the expected and observed 95% CL exclusion areas in the plane of m_{H_1} and m_{H_2}. For heavy m_{H_2}, H_1 resembles the SM Higgs boson (almost completely CP-even) with very little effect from CP violation. The limit on the allowed mass of H_1 for large m_{H_2} is found to be $m_{\mathrm{H}_1} > 112$ GeV. In the region below $m_{\mathrm{H}_2} \approx 130$ GeV CPV effects play a major role.

   Fig. 6.17 (b) shows the 95% CL exclusion areas in the parameter space of $\tan\beta$ and m_{H_2}. One can see that $\tan\beta < 2.8$ is excluded. This lower limit holds for all CPV scenarios under study. The band at $\tan\beta < 2.8$ is excluded by searches for the SM-like H_1, while the band at $\tan\beta > 10$ and $m_{\mathrm{H}_2} < 120$ GeV is excluded by searches for ZH_2 and $\mathrm{H}_1\mathrm{H}_2$ topologies.

   Fig. 6.17 (c) displays the parameter space of $\tan\beta$ and m_{H_1}. The range $\tan\beta < 2.8$ is excluded, and a lower limit of $\tan\beta > 3.2$ exists if m_{H_1} is below 112 GeV. For $4 < \tan\beta < 10$, ZH_2 production is dominant. The large difference between the expected and observed exclusion regions in the area of $4 < \tan\beta < 10$ is mainly due to a less than 2σ excess in the data between $m_{\mathrm{h}} \approx 95$ GeV and $m_{\mathrm{h}} \approx 110$ GeV [114], which corresponds to the mass of H_2 in this region. For $m_{\mathrm{H}_1} < 50$ GeV there are also unexcluded regions in the expected exclusion, which is due to dominant $\mathrm{ZH}_2 \rightarrow \mathrm{ZH}_1\mathrm{H}_1$ production with relatively large m_{H_1}, yielding broad mass resolutions and therefore reduced sensitivity.

   In Fig. 6.17 (d) the exclusion area is shown in the parameter space of the theoretical input parameters $\tan\beta$ and $m_{\mathrm{H}^\pm}$, which are varied during the scan. Since the "CPX" scenario yields $m_{\mathrm{H}_2} \approx m_{\mathrm{H}^\pm}$ for most of the scan points, this is very similar to Fig. 6.17 (b).

   The uncertainty inherent to the two theoretical approaches, CPH and FEYNHIGGS, is illustrated in parts (e) and (f) of Fig. 6.17. The largest discrepancy occurs for large values of $\tan\beta$, where the FEYNHIGGS calculation (part (f)) predicts a higher cross-section for Higgsstrahlung, and hence a better search sensitivity than the CPH prediction (part(e)).

   The large impact of the value of the top quark mass on the exclusion limits is shown in Fig. 6.18. For $m_{\mathrm{top}} = 179.3$ GeV, the excluded range in $\tan\beta$ shrinks to $\tan\beta < 2.4$.

2. The effect of different choices of the CPV phases is illustrated in Figs. 6.19 and 6.20. Values of $\arg(A_{\mathrm{t,b}}) = \arg(m_{\tilde{\mathrm{g}}})$ from 0° to 180° are displayed. Fig. 6.19 shows exclusion

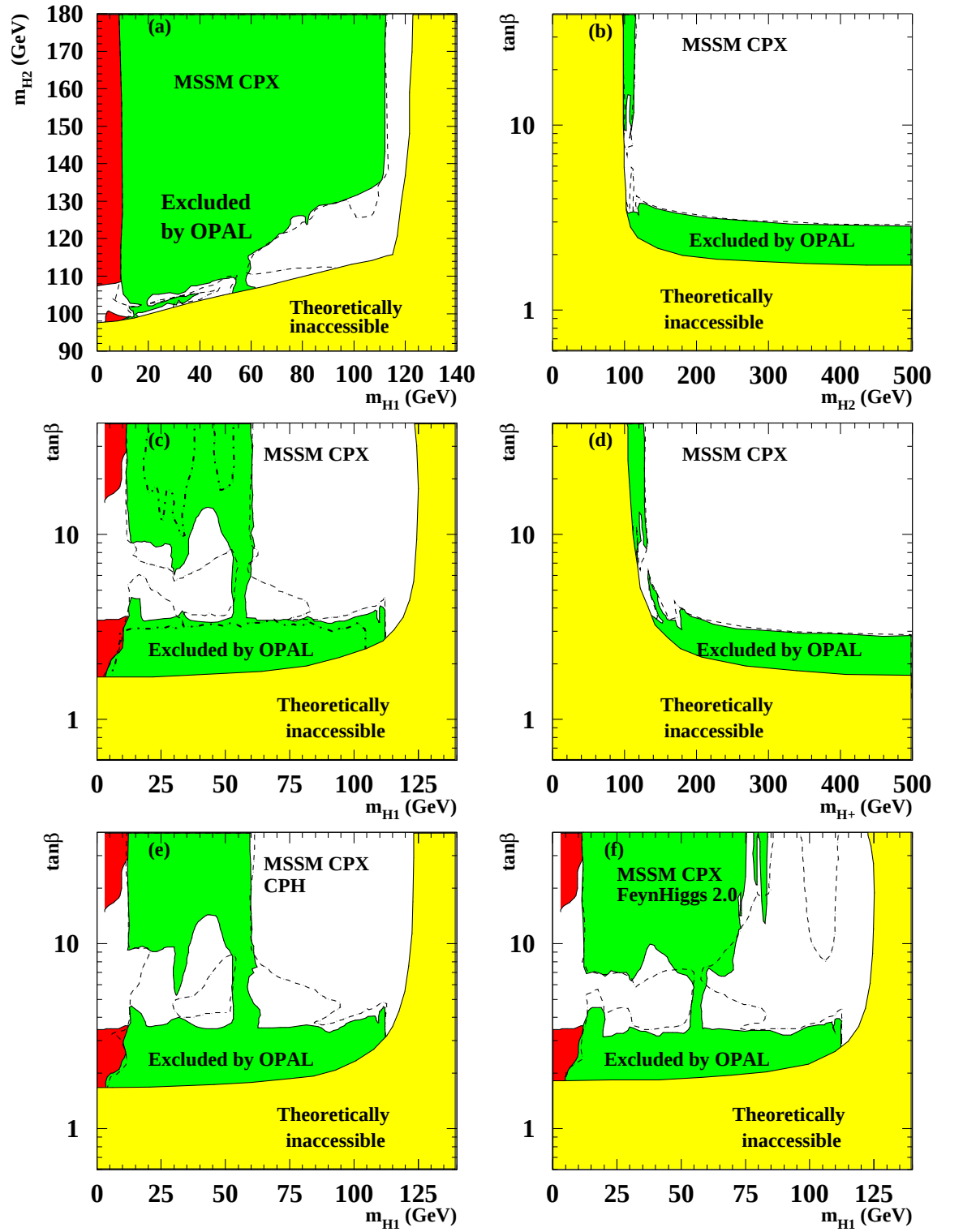

Figure 6.17: *The "CPX" MSSM* 95 % CL *exclusion areas. Excluded regions are shown for (a) the* (m_{H_1},m_{H_2}) *plane, (b) the* (m_{H_2},$\tan\beta$) *plane, (c) the* (m_{H_1},$\tan\beta$) *plane and (d) the* ($m_{\mathrm{H}^\pm}$,$\tan\beta$) *plane. Figure (e) shows the* (m_{H_1},$\tan\beta$) *of the CPH calculation alone, (f) shows the same projection of the FEYNHIGGS 2.0 calculation. See Fig. 6.8 for the notation. The dash-dotted line in (c) shows the area excluded on the 99.9% confidence level. In (b) and (d) the area excluded by* Z *width constraints or by decay independent searches is too small to be displayed.*

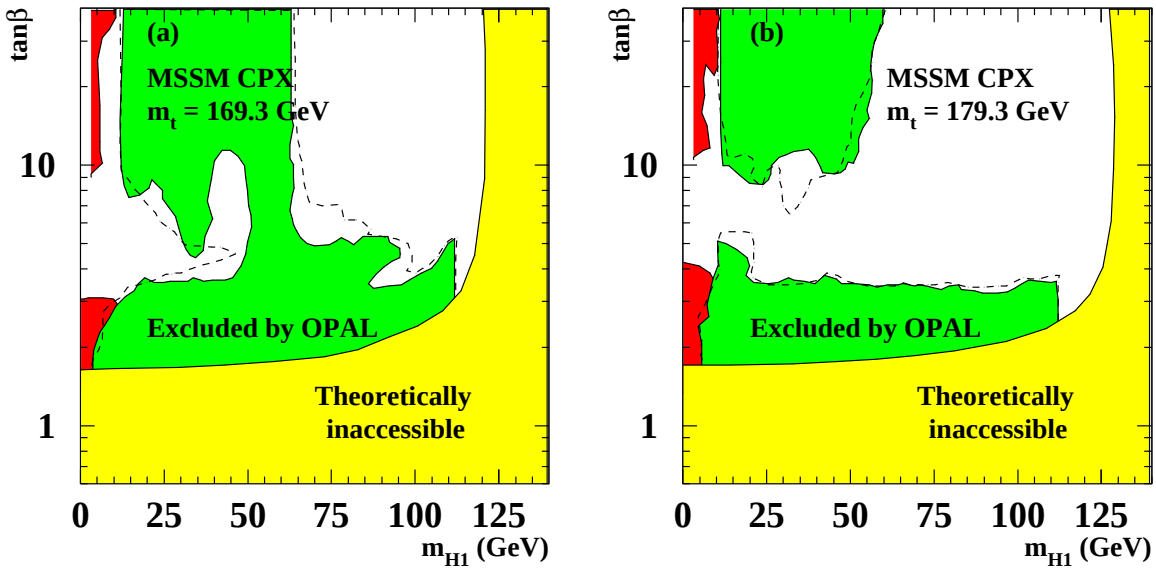

Figure 6.18: *The "CPX" MSSM* 95 % CL *exclusion areas in the* (m_{H_1},tan β) *plane, using scans with (a)* $m_{\mathrm{t}} = 179.3$ GeV *and (b)* $m_{\mathrm{t}} = 169.3$ GeV. *Due to the change in the top masses a strong difference is observed compared to Fig. 6.17 (c). See Fig. 6.8 for the notation.*

regions in the parameter space of tan β and m_{H_1} for $\arg(A_{\mathrm{t,b}}) = \arg(m_{\tilde{\mathrm{g}}}) = 90°, 60°, 30°$ and 0°. At 30° and at 0° all areas for low m_{H_1} and low tan β are excluded. The exclusion for the maximally CPV scenario "CPX" with 90° is very different from the exclusion of a CPC scenario ($\arg(A_{\mathrm{t,b}}) = \arg(m_{\tilde{\mathrm{g}}}) = 0°$). A variation of the second main parameter governing the size of CPV effects, m_{SUSY}, has similar effects on the exclusion to those of a variation of $\arg(A_{\mathrm{t,b}}) = \arg(m_{\tilde{\mathrm{g}}})$.

Fig. 6.20 shows exclusion regions in the parameter space of tan β and m_{H_1} for phases of (a) 135° and (b) 180°. The scenario in (a) is phenomenologically still similar to the original "CPX" scenario. The scenario in (b), which is in fact a CPC case, exhibits two allowed regions, of which the lower one from tan $\beta = 3$ to tan $\beta = 13$ has a low $\mathrm{H}_1\mathrm{Z}$ coupling. The unexcluded "hole" in the exclusion region for $90 < m_{\mathrm{H}_1} < 100$ GeV is due to an excess of the background in the Higgsstrahlung channels.

3. Since the "CPX" scenario has a relatively high value of $\mu = 2$ TeV, which influences the mixing of the CP eigenstates into the mass eigenstates (see Eq. (2.58)), μ is varied from $\mu = 500$ GeV to $\mu = 4$ TeV in Fig. 6.21. Also such a high value of μ in the presence of a low value of M_{SUSY} is disfavoured by the requirement of unification of parameters at the GUT scale. This means that it is very unlikely to derive such a model from SUSY breaking assumptions at the GUT scale. For $\mu = 500$ GeV (Fig. 6.21 (a)) and $\mu = 1$ TeV (Fig. 6.21 (b)) the CPV effects are small. Therefore no unexcluded regions occur at small m_{H_1}. The scenario with $\mu = 4$ TeV (Fig. 6.21 (d)) has strong mixing and a suppression of pair production at large tan β, resulting in an exclusion area that is considerably smaller than in the "CPX" scenario (Fig. 6.21 (c)).

4. The proposal of the "CPX" scenario in [51] leaves the choice of m_{SUSY} open, as long as the relations $|A_{\mathrm{t,b}}| = 2m_{\mathrm{SUSY}}$, $|m_{\tilde{\mathrm{g}}}| = 2m_{\mathrm{SUSY}}$ and $\mu = 4m_{\mathrm{SUSY}}$ are preserved. In

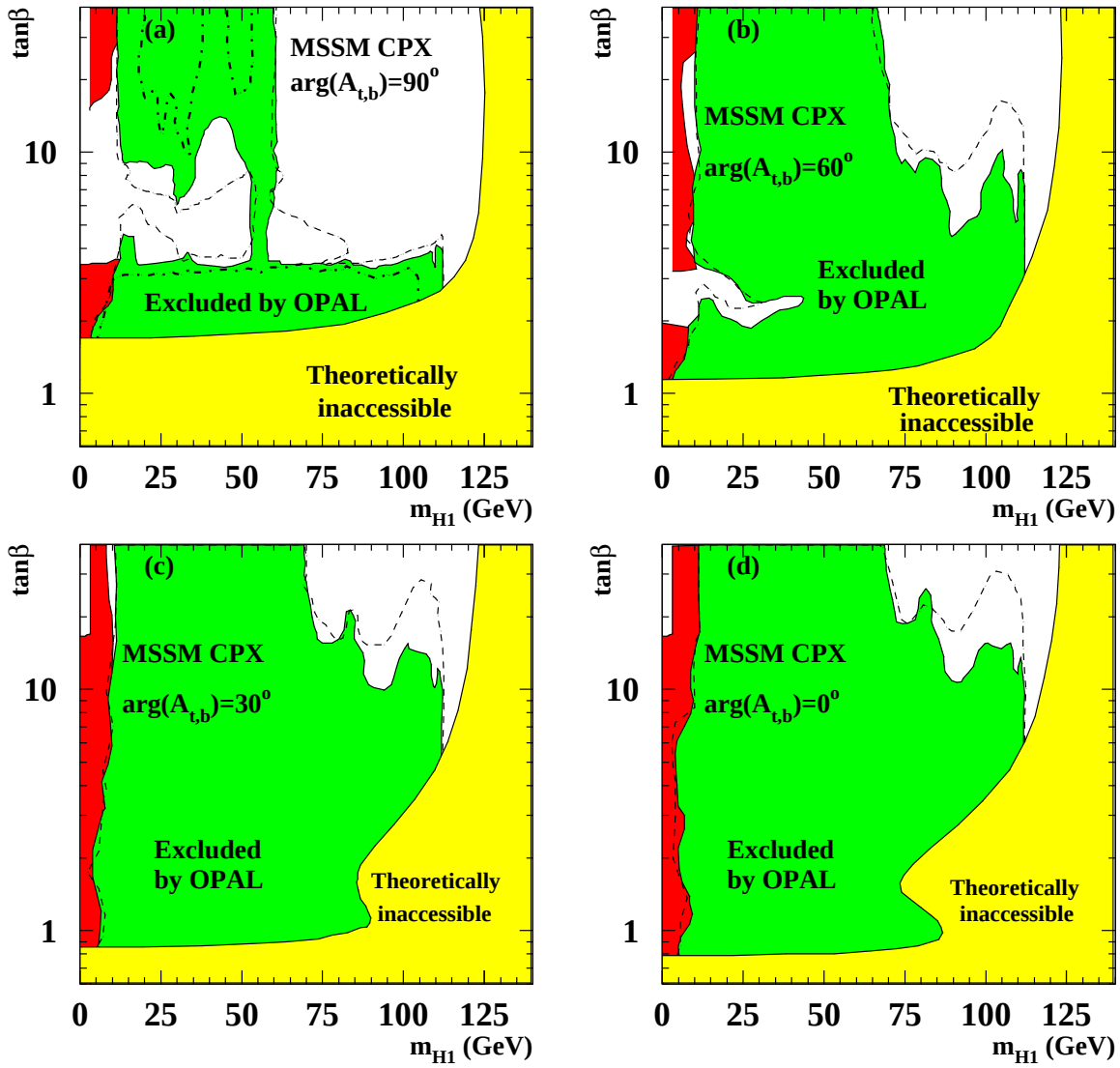

Figure 6.19: *The "CPX" MSSM* 95 % CL *exclusion areas in the* $(m_{\mathrm{H}_1}, \tan\beta)$ *plane, using scans with (a)* $\arg(A_{\mathrm{t,b}}) = \arg(m_{\tilde{\mathrm{g}}}) = 90°$, *(b)* $\arg(A_{\mathrm{t,b}}) = \arg(m_{\tilde{\mathrm{g}}}) = 60°$, *(c)* $\arg(A_{\mathrm{t,b}}) = \arg(m_{\tilde{\mathrm{g}}}) = 30°$ *and (d)* $\arg(A_{\mathrm{t,b}}) = \arg(m_{\tilde{\mathrm{g}}}) = 0°$. *While the CPV phases decrease, effects from CP violation like the strong* $\mathrm{H}_2 \to \mathrm{H}_1\mathrm{H}_1$ *contribution vanish. See Fig. 6.8 for the notation.*

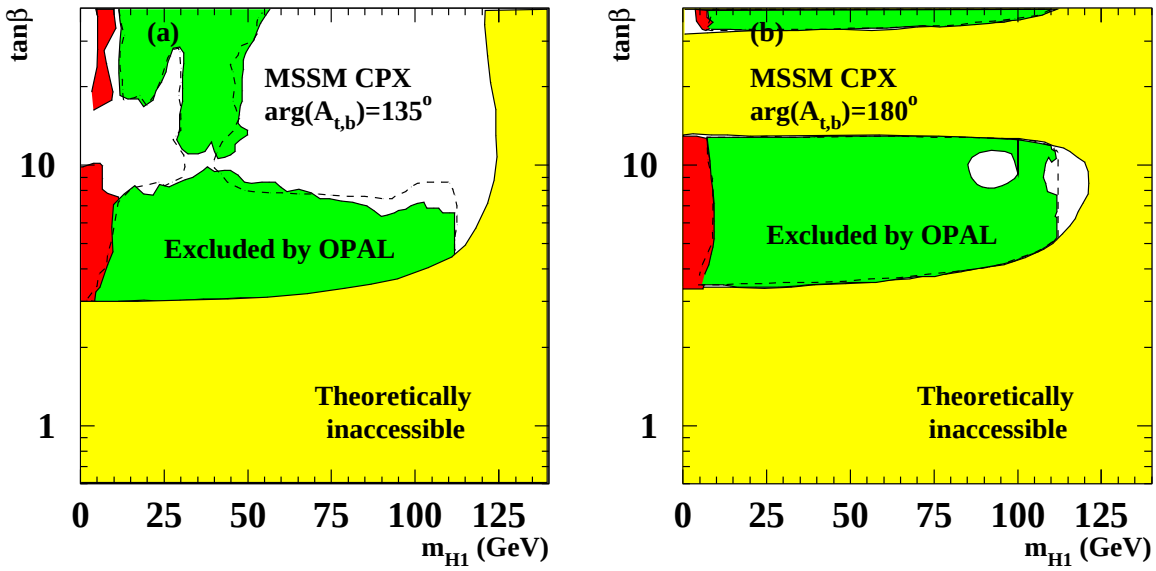

Figure 6.20: *The "CPX" MSSM* 95 % CL *exclusion areas in the* (m_{H_1},tan β) *plane, using scans with (a)* $\arg(A_{\mathrm{t,b}}) = \arg(m_{\tilde{\mathrm{g}}}) = 135°$ *and (b)* $\arg(A_{\mathrm{t,b}}) = \arg(m_{\tilde{\mathrm{g}}}) = 180°$. *See Fig. 6.8 for the notation.*

order to test the dependence on m_{SUSY}, two scenarios are tested: Fig. 6.22 (a) shows the scenario "$\mathrm{CPX}_{1.0}$", where the ratio between the parameters in the "CPX" proposal is preserved, while m_{SUSY} is increased from 500 GeV to 1 TeV. Only small differences with respect to the "CPX" scenario with $m_{\mathrm{SUSY}} = 500$ GeV can be seen. Fig. 6.22 (b) shows the "CPX" scenario as given in Table 6.5, but with only m_{SUSY} set to 1 TeV, while the values of $|A_{\mathrm{t,b}}|$, $|m_{\tilde{\mathrm{g}}}|$ and μ are kept fixed. This results in a decrease of the CPV effects and thus no unexcluded regions at small m_{H_1} are observed.

In summary, the CPV models show that there still is no absolute Higgs boson mass limit in the MSSM from OPAL data. Given the appropriate chice of parameters, as in the "CPX" scenario, regions of the MSSM parameter space at intermediate tan β remain uncovered. The absolute lower limit on tan β from all CPV benchmark sets under study is $\tan\beta > 2.8$.

6.5 Combination of the Results of the LEP Collaborations

The results of the interpretations can be improved significantly, if the full information from all four LEP experiments, ALEPH [154], DELPHI [155], L3 [156] and OPAL is used. All collaborations performed extensive searches for the Higgs boson in basically all the final states listed in Tab. 6.1 and 6.2. All searches of the four experiments are combined in the same way as the searches of the OPAL experiment are combined (see Section 6.1). The statistical uncertainties and most of the systematic uncertainties of the four experiments are independent. The correlation of the systematic uncertainties stemming from theoretical sources (such as background cross-sections) is taken into account. The searches of the ALEPH experiment are described in [157], the DELPHI searches are listed in [158], the L3 searches in [159] and the OPAL searches in [5].

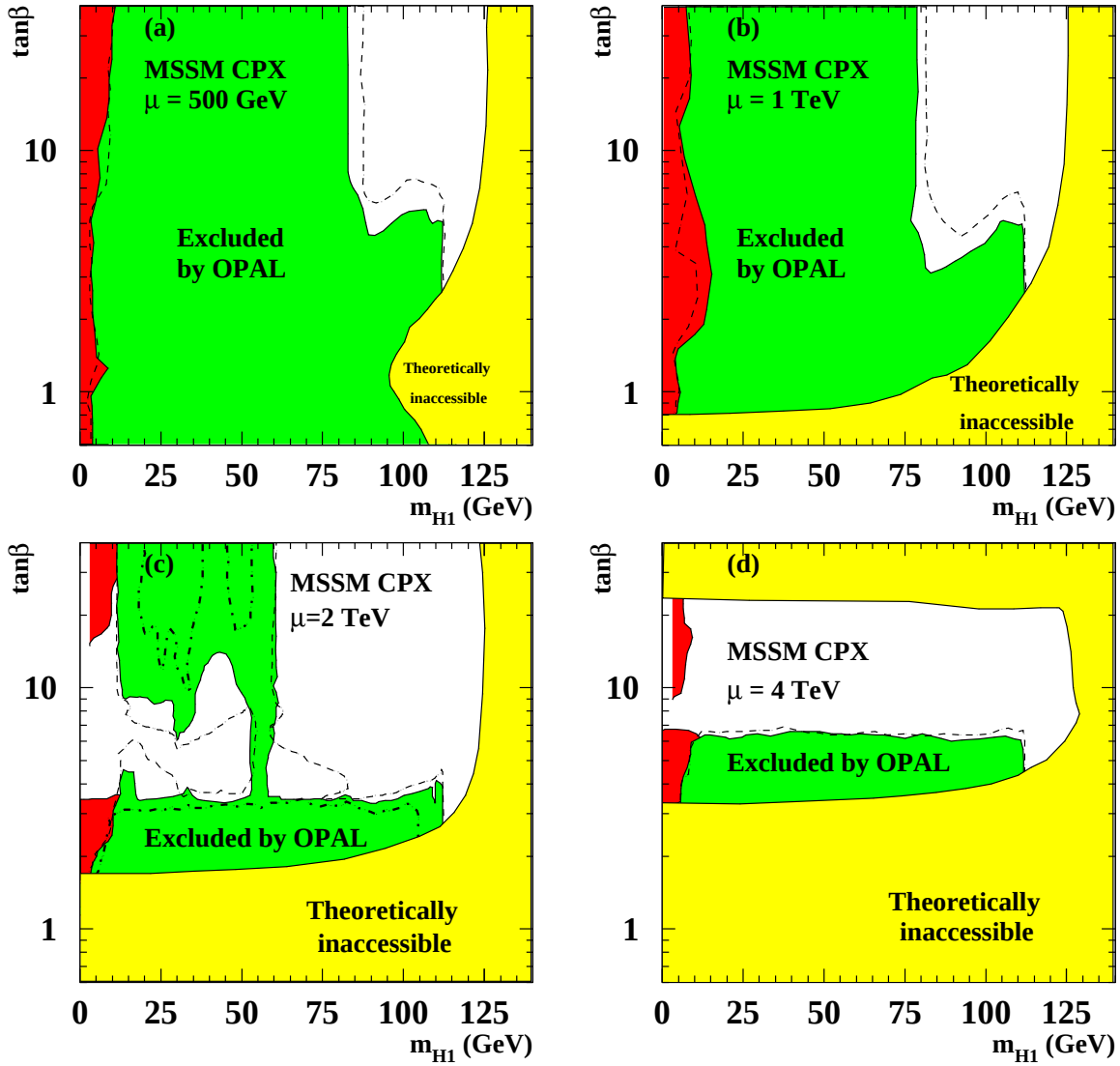

Figure 6.21: *The "CPX" MSSM* 95 % CL *exclusion areas in the* (m_{H_1},tan β) *plane, using scans with (a)* $\mu = 500$ *GeV, (b)* $\mu = 1000$ *GeV, (c)* $\mu = 2000$ *GeV ("CPX") and (d)* $\mu = 4000$ *GeV. See Fig. 6.8 for the notation.*

The combination of the results is especially helpful in case of the CPV scenarios. The excluded areas in the CPC scenarios are not expected to be subject to strong change, since there the values of CL_s vary steeply with the Higgs boson masses at the masses where the limits are set. Therefore a variation of the statistics, hence a variation of CL_s, transfers only into a small change in the mass limit. In the "CPX" scenario, however, the area unexcluded by OPAL at $4 < \tan\beta < 10$ and $m_{\mathrm{H}_1} < 50$ GeV is close to being excluded ($\mathrm{CL}_{s,\mathrm{exp}} \approx 0.1$) and the variation of the confidence limit with the masses is small. Therefore a variation of CL_s transfers into a large difference in the excluded mass range.

The preliminary result of the LEP combination in the "CPX" scenario is shown in Fig. 6.23. No significant excess of the data over the expected background has been found. The strongest

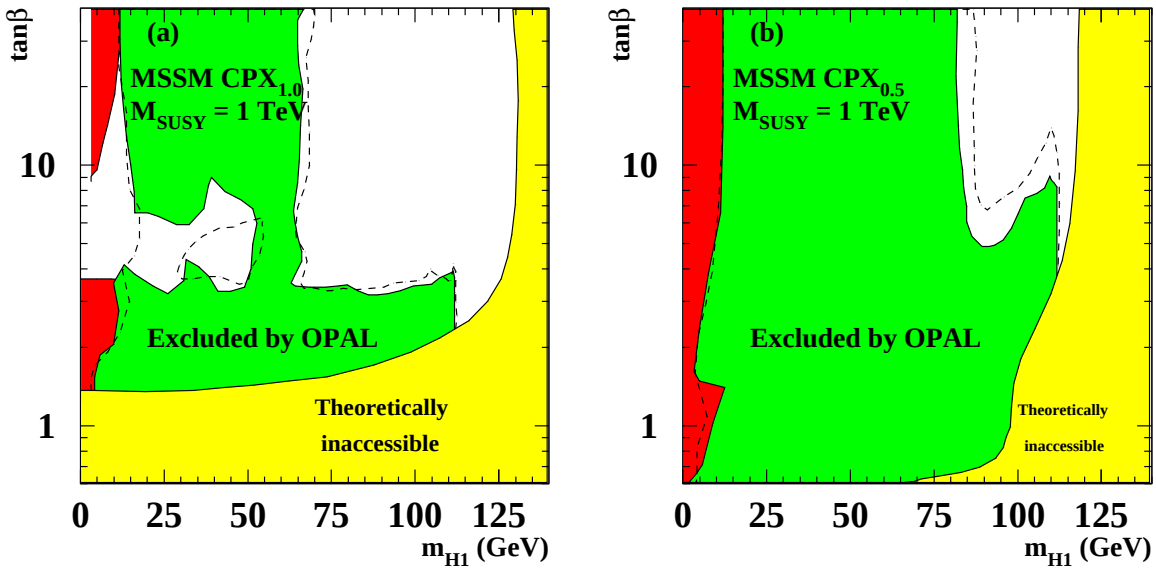

Figure 6.22: *The "CPX" MSSM* 95 % CL *exclusion areas in the* $(m_{\mathrm{H}_1}, \tan\beta)$ *plane, using scans (a) preserving the "CPX" ratios of* μ, $A_{\mathrm{b,t}}$ *and* m_{SUSY}, *using* $m_{\mathrm{SUSY}} = 1$ *TeV, and (b)* $m_{\mathrm{SUSY}} = 1$ *TeV keeping* μ *and* $A_{\mathrm{b,t}}$ *at their "CPX" values. See Fig. 6.8 for the notation.*

excess has a significance of $2\,\sigma$ at $m_{\mathrm{H}_1} = 40$ GeV and $m_{\mathrm{H}_2} = 105$ GeV, at the position of the strongest excess of the OPAL data over the background. Since no significant excess is found, limits on the MSSM parameters are derived. In Fig. 6.23 (a), the result of the combination using a top quark mass of $m_{\mathrm{top}} = 174.3$ GeV is shown. In the expected mass limit, the complete mass range of $12\,\mathrm{GeV} < m_{\mathrm{H}_1} < 67\,\mathrm{GeV}$ is excluded. However, in the observed limit an unexcluded region remains around the position of the above mentioned excess. The improvement in terms of the $\tan\beta$ exclusions are marginal. The improvement with respect to the OPAL exclusion in 6.17 is mainly due to the searches of the DELPHI experiment. The selections of the DELPHI searches are not test mass dependent, therefore the signals of the channels $\mathrm{e^+e^-} \to \mathrm{H_1Z}$ and $\mathrm{e^+e^-} \to \mathrm{H_2Z}$ can be added, increasing the sensitivity with respect to the OPAL searches, where either $\mathrm{e^+e^-} \to \mathrm{H_1Z}$ or $\mathrm{e^+e^-} \to \mathrm{H_2Z}$ can be used. The experiments ALEPH and L3 only contribute at $\tan\beta < 4$, since there no off-diagonal $\mathrm{e^+e^-} \to \mathrm{H_1H_2}$ searches and no significant $\mathrm{e^+e^-} \to \mathrm{H_2Z} \to \mathrm{H_1H_1Z}$ searches exist.

Fig. 6.23 (b) shows the result of the LEP combination for $m_{\mathrm{top}} = 179.3$ GeV, close to the current world average of $m_{\mathrm{top}} = 178$ GeV. Due to the increasing CP-mixing off-diagonal elements (2.58) with increasing m_{top} and the increasing mass m_{H_2} for given $(\tan\beta, m_{\mathrm{H}_1})$, the exclusion area shrinks with respect to the plot with the smaller top quark mass. No absolute limit on m_{H_1} can be set in this case by the LEP combination.

6.6 Summary

The searches for neutral Higgs bosons described in this section are based on all data collected by the OPAL experiment, at energies in the vicinity of the Z resonance (LEP 1 phase) and between 130 and 209 GeV (LEP 2 phase). The corresponding integrated luminosities are about $720\,\mathrm{pb}^{-1}$. The searches addressing the Higgsstrahlung process $\mathrm{e^+e^-} \to \mathcal{H}Z$ and those

Table 6.6: *Limits on m_{h} m_{A} and $\tan\beta$ for the various benchmark sets. The median expected limits in an ensemble of SM background-only experiments are listed in parentheses. The lower limits on m_{h} and m_{A} in the "no mixing (2 TeV)" scenario are only valid for $m_{\mathrm{A}} > 2$ GeV.*

Limits on the MSSM scenarios			
Benchmark set	Lower limit on m_{h} (GeV)	Lower limit on m_{A} (GeV)	Excluded $\tan\beta$
no mixing	64.0 (60.0)	–	$0.8 < \tan\beta < 6.2$ $(0.9 < \tan\beta < 7.2)$
no mixing (2 TeV)	83.3 (88.0)	84.3 (88.8)	$0.9 < \tan\beta < 4.2$ $(0.9 < \tan\beta < 4.3)$
m_{h}−max	84.5 (88.5)	85.0 (89.0)	$0.7 < \tan\beta < 1.9$ $(0.7 < \tan\beta < 1.9)$
m_{h}−max^{+}	84.5 (88.0)	84.0 (89.5)	$0.7 < \tan\beta < 1.9$ $(0.7 < \tan\beta < 1.9)$
constr. m_{h}−max	84.0 (88.0)	85.0 (89.0)	$0.6 < \tan\beta < 2.2$ $(0.6 < \tan\beta < 2.2)$
gluophobic	82.0 (87.0)	87.5 (90.5)	$\tan\beta < 6.0$ $(\tan\beta < 8.0)$
small α_{eff}	79.0 (83.0)	90.0 (95.0)	$0.4 < \tan\beta < 3.6$ $(0.4 < \tan\beta < 3.6)$
CPX	–	–	$\tan\beta < 2.8$ $(\tan\beta < 2.8)$
Allowed regions in the "large μ" scenario			
large μ	$80.0 < m_{\mathrm{h}} < 107.0$ $(81.0 < m_{\mathrm{h}} < 107.0)$	$87.0 < m_{\mathrm{A}}$ $(87.0 < m_{\mathrm{A}})$	$\tan\beta > 6$ $(\tan\beta > 12)$

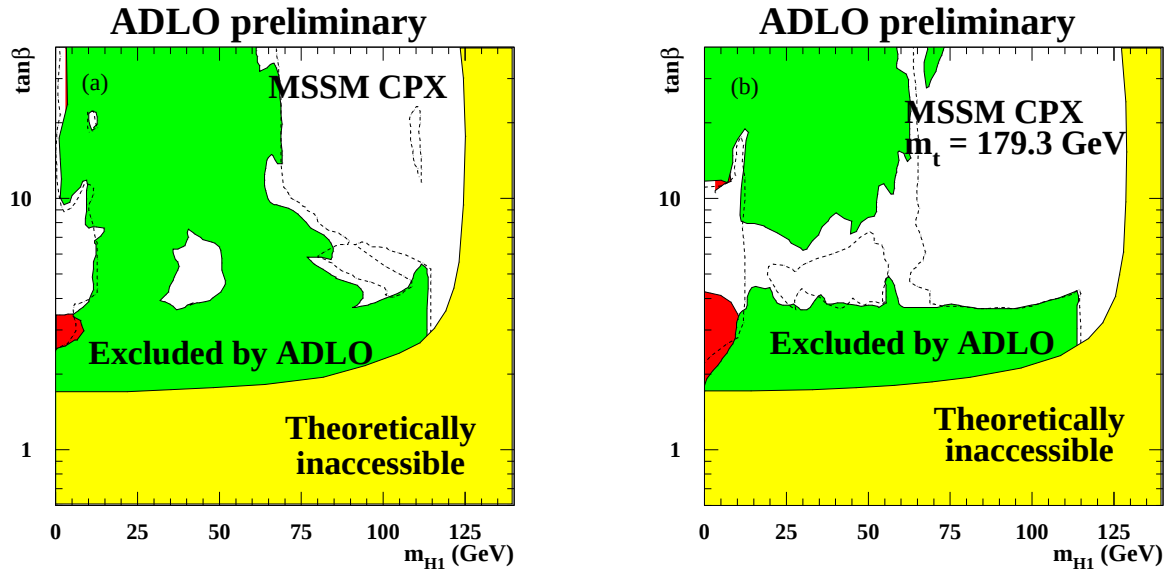

Figure 6.23: *The "CPX" MSSM* 95 % CL *exclusion areas in the* (m_{H_1},$\tan\beta$) *plane for the combination of the data of all four LEP experiments, using (a) a central value of* $m_{\mathrm{top}} = 174.3$ *GeV for the top quark mass and (b) a value of* $m_{\mathrm{top}} = 179.3$ *GeV.*

for the pair production process $\mathrm{e^+e^-} \rightarrow \mathcal{H}_1\mathcal{H}_2$ are statistically combined. None of these searches reveals a significant excess of events beyond the predicted background level, which would indicate the production of Higgs bosons.

From these results, model-independent limits are derived for the cross-section of a number of event topologies that could be associated to Higgs boson pair production. These limits cover a wide range of Higgs boson masses and are typically much lower than the largest cross-sections predicted by the MSSM.

The search results are also used to test a number of benchmark scenarios of the MSSM, with and without the inclusion of CP-violating effects. The nine CP-violating models and 5 of the eight CP-conserving models are studied experimentally for the first time in the context of this thesis. Since no statistically significant signal has been found, which could be used to find the regions in the MSSM parameter space connected to this signal, the parameter space has to be tested point-by-point as close as possible in order to place limits on the parameters by comparing the predicted signal at each point with the data. The most advanced available statistical methods have been used to perform this comparison.

In the CP-conserving case, new benchmark situations are investigated as compared to earlier publications. These are motivated either by new measurements of the b→sγ branching ratio and the muon anomalous magnetic moment $(g-2)_\mu$, or in anticipation of the forthcoming searches at the proton-proton collider LHC. In all these scenarios the searches conducted by OPAL exclude sizeable domains of the MSSM parameter space, even in those situations where the sensitivity of the LHC experiments is expected to be low. An overview of the results is given in Table 6.6. Generally limits of around $m_{\mathrm{h}} > 85$ GeV and $m_{\mathrm{A}} > 85$ GeV can be set on the Higgs boson masses. A very important development in recent times is the increase of the world average value of m_{top}. As outlined in this section, this has dramatic impacts on the $\tan\beta$ exclusion from LEP. This is especially important for the LHC experiments and their prospect of MSSM Higgs searches, which will have to cover a larger range in $\tan\beta$ as planned

before.

In the case of the CP-violating MSSM scenarios, where the CP-violating effects are introduced in the Higgs potential by radiative corrections, the "CPX" benchmark scenario is designed to maximize the phenomenological differences in the Higgs sector with respect to the CP-conserving scenarios. In this case the region $\tan\beta < 2.8$ is excluded at 95% confidence level but no universal limit is obtained for either of the Higgs boson masses.

In the preliminary combination of the MSSM Higgs searches of the LEP experiments, the increase of sensitivity is especially strong in the CPV case. No Higgs boson signal has been found. However, also in this case no absolute lower limit can be set on the lightest Higgs boson mass m_{H_1}. The experimentally accessible region in the parameter space is further reduced for enlarged top quark masses.

Chapter 7

MSSM Parameter Fits with Fittino

In the previous section, the extraction of limits on specific MSSM parameters connected to the Higgs sector has been discussed. It was only possible to calculate limits, since no statistically significant signal in any search channel was found. Therefore as many different parameter combinations in a 7-dimensional (for the CPC scenarios) or 8-dimensional (for the CPV scenarios) parameter space as possible had to be tested. The combination of different small excesses in different channels could well have shown a statistically significant signal, which was not the case in reality.

At the future collider experiments at the LHC and the Linear Collider (LC), the situation will most likely be different. If a Higgs boson exists, either in the SM or the MSSM, it will most likely be discovered at the LHC. Large parts of the MSSM particle spectrum will be visible at both machines in most natural MSSM scenarios [160]. Since individual signals for Higgs bosons, gauginos, sleptons and squarks exist, it will not be needed to scan large parts of the parameter space, as done in Section 6 in the case of LEP. Instead, the individually established and identified signals, as well as branching ratios, widths, asymmetries and cross-sections, can be used to directly determine the MSSM parameters. Such a parameter determination needs precise theoretical predictions, including all available loop corrections. Based on these predictions as well as on the anticipated accuracy of future measurements the MSSM parameter fit program Fittino [161] was developed in the context of this thesis.

The program Fittino extracts the parameters of the SUSY Lagrangian from simulated measurements at LHC and the LC in a global fit. No prior knowledge of the parameters is assumed. Tree-level relations between observables and SUSY parameters are used to obtain start values for the fit. A model fit is performed for the benchmark parameter set SPS1a [160], assuming unification in the first two generations. As a result of the fit, a full error matrix of the parameters and two-dimensional uncertainty contours of the parameters are obtained.

First the general concepts of MSSM parameter determination is introduced, followed by a description of the fit program Fittino. A documentation of Fittino is given in Appendix A.2. Then the results of MSSM parameter fits at the LC alone and at LHC+LC are discussed. Finally, the obtained results of the fitted parameters and their uncertainties can be used to extract the MSSM parameters at the GUT scale, and thus to identify the SUSY breaking scenario.

7.1 MSSM Signals at e^+e^- Colliders

In this section an overview of the typical expected production processes for supersymmetric (SUSY) particles in e^+e^- collisions at energies up to about 1 TeV is given. It is expected

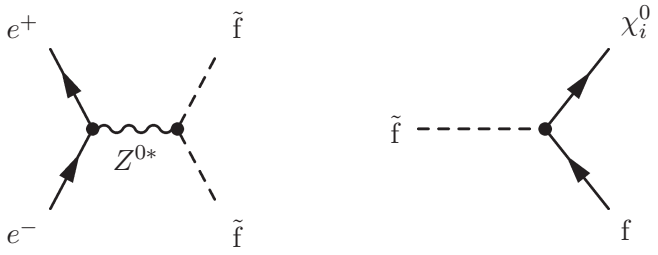

Figure 7.1: *Production and decay of sfermions at* e^+e^- *colliders. It is assumed that the lightest neutralino is the LSP.*

that the production and decay of sparticles can be studied in great detail at the future e^+e^- linear collider project, e.g. TESLA. The expected signatures are governed by the following principles:

- *Sparticles will be pair-produced*
  This is a direct consequence of the conservation of R-parity, which is assumed here. Thus no single SUSY-particle can be produced, limiting the kinematically accessible range in case of the production of a particle-antiparticle pair to sparticle masses of $m_{\tilde{p}} < 1/2\sqrt{s}$. In case of the production of charginos and neutralinos, the mass reach is higher due to production mechanisms of the type $e^+e^- \to \chi_i\chi_j$ with $i \neq j$.

- *All sparticles besides the LSP decay*
  Since no sparticles are observed up to now, all sparticles interacting electromagnetically or strongly must be unstable. In most scenarios sparticles decay with no measurable decay length.

- *The LSP is stable and escapes direct detection*
  The lightest supersymmetric particle LSP serves as a candidate for cosmic dark matter. It is stable, since R-parity is assumed to be conserved. It can be only weakly interacting if it is a candidate for the dark matter. Therefore a dominating signature of SUSY will be the missing energy carried away by the undetected LSP. Candidates for the LSP in SUSY models are the lightest neutralino χ_1^0, the sneutrino or the gravitino.

At a future e^+e^- linear collider with $\sqrt{s} \leq 1$ TeV, the production of stop quarks, all sleptons and most charginos and neutralinos is accessible in typical SUSY models [160].

The production and decay of sfermions is shown in Fig. 7.1. The signature for sleptons are two like-flavour leptons with opposite charge and missing energy in the final state. The mass of the slepton can be extracted from the invariant mass spectrum of the leptons [162]. This however can be impossible for sneutrinos, if their preferred decay is $\tilde{\nu} \to \nu\chi_1^0$.

Charginos are pair-produced either in the s-channel via Z or γ exchange or in the t-channel via sneutrino exchange. Figure 7.2 shows diagrams for production and decay. The decay signature of the chargino depends strongly on its mass. If kinematically allowed, the decay into a lighter neutralino and a $W^\pm$ dominates. If this is kinematically suppressed, also more complicated decay patterns involving cascade decays of sneutrinos are important. The analysis of the decay also allows to extract information about intermediate particles and the lightest neutralino.

The production and decay of neutralinos is similar to that of charginos, as shown in Fig. 7.3. However the experimental analysis is more difficult, since the lightest neutralino is the LSP and escapes undetected, therefore in the case of $e^+e^- \to \chi_1^0\chi_1^0$ production the only experimental signature accessible is the measurement of single ISR photons from $e^+e^- \to \chi_1^0\chi_1^0\gamma$. In $e^+e^- \to \chi_1^0\chi_i^0$ (with $i > 1$) production only a small part of the event is accessible.

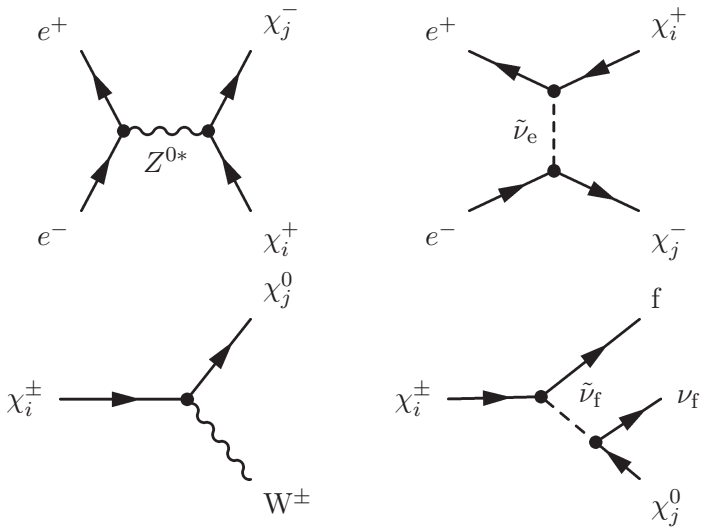

Figure 7.2: *Production and decay of charginos at* e^+e^- *colliders. It is assumed that the lightest neutralino is the LSP.*

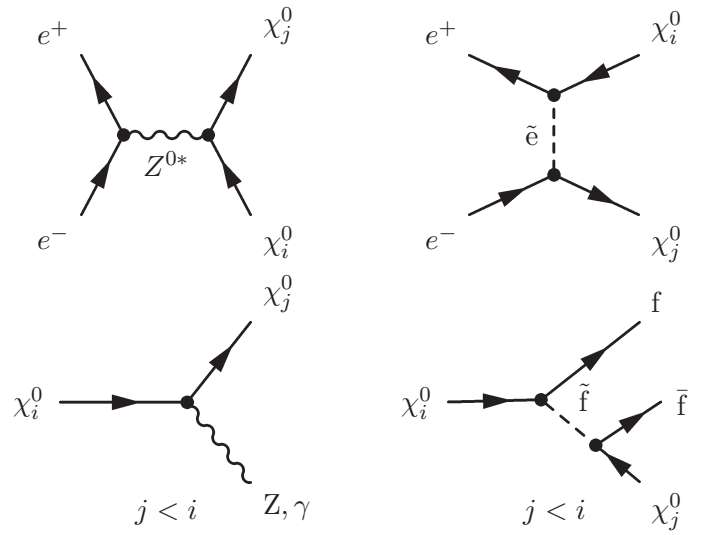

Figure 7.3: *Production and decay of neutralinos at* e^+e^- *colliders. It is assumed that the lightest neutralino is the LSP.*

The t-channel contribution to the chargino and neutralino production, and also to $\tilde{e}\tilde{e}$ and $\tilde{\nu}_e\tilde{e}_e$, can be sizeable if the exchanged particle is light. Its interference with the s-channel contribution can be either positive or negative. Typical cross-sections for the production of sparticles, computed on tree-level, can be found in [162]. If the lightest neutralino χ_1^0 is not the LSP, as generally assumed here, the additional decay $\chi_1^0 \to \gamma\tilde{g}r$ occurs.

The study of these signatures will allow the determination of the sparticle masses, parity and spin. Together with the Higgs boson signatures described in Section 3.1, these measurements will allow the extraction of the parameters of the MSSM Lagrangian, as will be shown in the following sections of this chapter.

7.2 MSSM Parameter Determination

In this section, first the general possibilities of parameter determination of any theory are introduced. This is followed by a description of the goals and properties of Fittino, the MSSM parameter fit program developed in the context of this thesis.

General Concepts of MSSM Parameter Determination

The following three possibilities exist, if a parameter of any given theory shall be extracted from the observables.

- *Parameter = Observable*
  In the case that a parameter is also a direct observable, as for example in the case of the CP-odd Higgs boson mass m_{A}, the parameter can be measured directly. However, also in this case the measured observable $m_{\mathrm{A}}(\Lambda = m_{\mathrm{A}})$ is determined at the energy scale Λ of its own mass. This can be different from the input scale of the theory, i. e. due to the running of the observables with the energy scale correlations with other parameters can also occur in this case. Therefore such a simple direct measurement without any discussion of the effect of other parameters is not possible for a precise determination of the parameters and their uncertainties and correlations.

- *Parameter determination on tree-level*
  In many cases the tree-level relations between the parameters and the observables (e. g. (2.36)) can be used to determine a parameter, which is not directly observable. Such a case is for example the third generation squark mass parameter

  $$M_{\tilde{\mathrm{t}}_L} = f(m_{\tilde{\mathrm{t}}_1}, m_{\tilde{\mathrm{t}}_2}, \ldots),$$

  which is a function of only a few observables. However, loop level effects are completely ignored. On loop level, in principle *every* parameter can influence *every* observable. These corrections can be large in the MSSM. For example, as outlined in Section 2.3.3, the tree-level upper mass bound on the lightest CP-even Higgs mass is $m_{\mathrm{h}} < m_{\mathrm{Z}}$. On loop-level the current upper mass bound for two loops is $m_{\mathrm{h}} < 135$ GeV [48, 46, 47], which is roughly a factor of 1.5 times the original upper bound. Neglecting these effects will give wrong results for the parameters.

  The result of the neglection of correlations of parameters is schematically shown in Fig. 7.4. Assuming two correlated parameters P_1 and P_2, a determination of P_1 with fixed P_2 shows two problems. First, the determined uncertainty on P_1 is much too small. Second, if the assumed value of P_2 is wrong, which in principle can not be determined unambiguously before since P_1 is unknown, then also the determined value of P_1 is wrong, often outside the uncertainty bounds.

  For these reasons, in the presence of very good experimental accuracy, also this method is depreciated for a correct parameter and uncertainty determination, since parameters tend to be systematically off their true values and since correlations can not be fully taken into account. This plays a role if the relative uncertainties of the measured observables O_i are smaller than the largest contribution from loop effects

  $$\frac{\Delta O_i^{\mathrm{meas}}}{O_i} \lesssim \frac{\Delta O_i^{\mathrm{loop}}}{O_i},$$

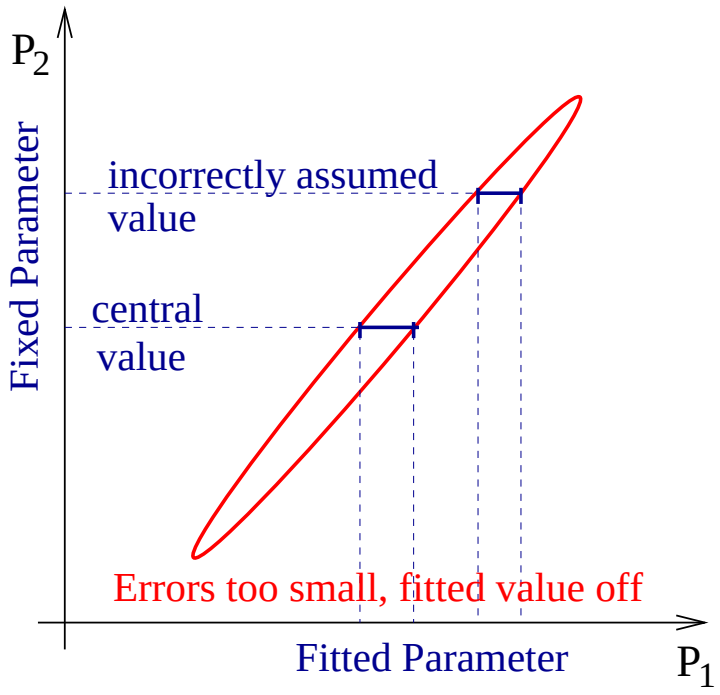

Figure 7.4: *The effect of correlations among parameters on the uncertainty. If only parameter P_1 is fitted and P_2 is kept fixed, the uncertainty on P_1 is too small. Additionally, if P_2 is kept fixed on a slightly wrong value, the result on P_1 can be wrong, too.*

as in case of the LC. If the uncertainties of the measurements are much larger than the expected contribution from loop effects, the tree-level parameter determination is sufficient.

- *Full loop corrections and correlations among parameters*
  In the approach used for the fit program Fittino, all available loop corrections are taken into account, in order to achieve the highest possible precision. This means that all observables O_i are treated as functions of all parameters P_j:

$$\text{Observable } O_i = f(\text{all parameters } P_j).$$

  Additionally, in order to account for the uncertainties from the limited precision of SM parameters (parametric uncertainties), the SM parameters can be fitted simultaneously with MSSM parameters. This approach also allows to extract the full correlation among all parameters. No bias is introduced due to a priori assumptions on fixed parameters. In order to be bias-free, this approach requires that no use of start values of parameters is made, which have to be chosen by the user. Instead, the start values of the parameters for the global fit to all observables are determined from tree-level formulae in an initialisation step, as described in the previous step. The drawbacks of the tree-level parameter determination are avoided by the parameter fit, which is performed in the main step of the parameter determination.

In the following, the iterative fit procedure developed for the fit program Fittino is described in detail.

The Fittino Approach

The aim of Fittino is the unbiased determination of the parameters of the MSSM. It is implemented in C++ and focuses on the determination of the parameters of the MSSM Lagrangian $\mathcal{L}_{\text{MSSM}}$, obeying the following principles:

- No a priori knowledge of SUSY parameters is assumed (but can be used if desired by the user)
- All measurements from future colliders could be used
- All correlations among parameters and all influences of loop-induced effects, where parameters of one sector affect observables of other sectors of the theory, are taken into account

In this way an unbiased global fit is obtained. No attempt to extract SUSY parameters at the GUT scale is made, since the evolution of the parameters and their determination on the low scale can be treated separately. The result of Fittino with the full errors of the low energy SUSY parameters can therefore be used later to extrapolate to the GUT scale.

However, all 104 possible parameters of $\mathcal{L}_{\text{MSSM}}$ can not be determined simultaneously. Therefore, assumptions on the structure of $\mathcal{L}_{\text{MSSM}}$ are made. All phases are set to 0, no mixing between generations is assumed and the mixing within the first two generations is set to 0. Thus the number of free parameters in the SUSY breaking sector is reduced to 24. Further assumptions can be specified by the user. Observables used in the fit can be

- Masses, limits on masses of unobserved particles
- Widths
- Cross-sections (momentarily in e^+e^- collisions only)
- Branching ratios
- Edges in mass spectra of decay products. For example in slepton decays $\tilde{\mu}^+\tilde{\mu}^- \rightarrow \mu^+\chi_1^0\mu^-\chi_1^0$, the lepton energy spectrum has a box-like shape. Its edges are correlated to the masses of the $\tilde{\mu}$ and the χ_1^0. By using the edge positions instead of the reconstructed masses, correlations among the observables can be reduced or omitted (see e.g. [163]).

Correlations among observables and both experimental and theoretical errors can be given. Theoretical uncertainties can be important, if they are in the order of magnitude of the experimental uncertainties. Both SM and MSSM observables can be used in the fit. Parametric uncertainties of SUSY observables can be taken into account by fitting the relevant SM parameters simultaneously with the MSSM parameters. For the interface between Fittino and the code providing the theoretical predictions, the SUSY Les Houches Accord [164] (SLHA) is used. The SLHA is a format for a text-file based interface between spectrum calculators, event generators and other programs in the context of the MSSM. Any theoretical code compliant with SLHA can be easily interfaced with Fittino. In the current implementation, the prediction of the MSSM observables for a given set of parameters is obtained from SPheno [165]. MINUIT [166] is used for the fitting process.

In the following, the principles of Fittino are outlined in more detail, followed by an example for a fit based on SPS1a.

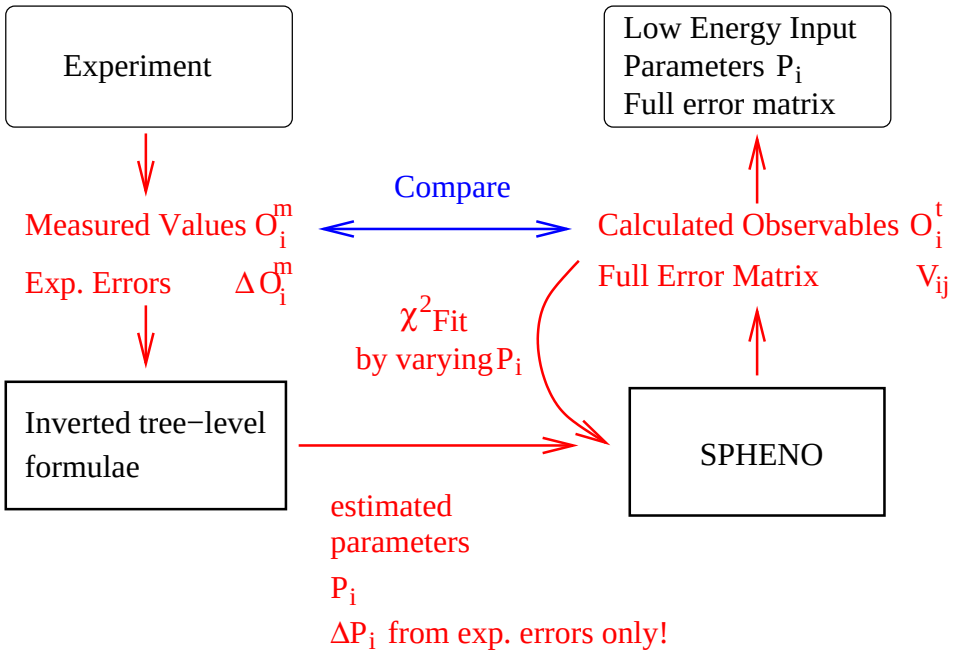

Figure 7.5: *The iterative fit procedure of Fittino. From the observables O_i and their uncertainties ΔO_i, the start values for parameters P_j of the fit are calculated in a bias-free way using tree-level relations. After the fit, the fitted parameters P_j and their uncertainties ΔP_j are obtained, including their full correlation matrix.*

7.3 The Fit Program Fittino

In the following, the program Fittino is described, which is able to determine the 24 parameters of the SUSY Lagrangian without a priori assumptions on the parameters. In order to account for parametric uncertainties, SM parameters can be fitted simultaneously. First the fit procedure and the fit method is explained, followed by an introduction into the steering of Fittino using ASCII input files.

The Iterative Fit Procedure

The full MSSM parameter space in Fittino, consisting of maximally 24 MSSM parameters plus SM parameters, can not be scanned completely, neither in a fit nor in a grid approach. Therefore, in order to find the true parameters in a fit by minimising a χ^2 function, it is essential to begin with reasonable start values, allowing for a smooth transition to the true minimum. As default, no a priori knowledge of the parameters can be used in a realistic attempt of a fit, since in a real measurement no information on true parameters will be available either.

The program Fittino uses an iterative procedure to determine the start values for the fit. It is displayed in Fig. 7.5. In a first step, the SUSY parameters are estimated using tree-level-relations as follows:

1. $\mu, m_A, \tan\beta, M_1, M_2, M_3$ are determined from the gaugino and Higgs sector using formulae from [167]. In order to extract these parameters, information from chargino cross-sections is needed, which enters in form of the chargino mixing angles $\cos 2\phi_L$ and

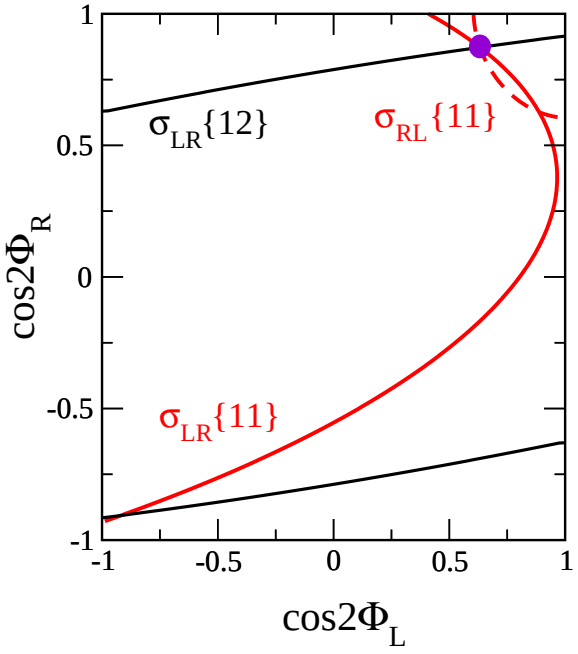

Figure 7.6: *The approximate initial determination of the chargino mixing angles from LR and RL chargino cross-sections. From the measurements of three chargino cross-sections at different beam polarisation, the chargino mixing angles can be initially determined [168].*

$\cos 2\phi_R$. These pseudo observables are just used for the determination of the start values, no use is made of them for the fit. Their approximate determination from chargino cross-sections at different polarisations is shown in Fig. 7.6. In most models, m_{A} can be directly measured. For the other parameters, the following individual calculations are performed, based on the eigenvalues of the chargino mixing matrix (2.37).

$$|\mu| = m_W \left(\Sigma + \Delta(\cos 2\phi_L + \cos 2\phi_R)\right)^{\frac{1}{2}} \tag{7.1}$$

$$\tan\beta = \left(\frac{1 + \Delta(\cos 2\phi_R - \cos 2\phi_L)}{1 - \Delta(\cos 2\phi_R - \cos 2\phi_L)}\right)^{\frac{1}{2}} \tag{7.2}$$

$$M_2 = m_W \left(\Sigma - \Delta(\cos 2\phi_L + \cos 2\phi_R)\right)^{\frac{1}{2}} \tag{7.3}$$

$$\mathrm{sign}(\mu) = -\frac{\Delta^2 - (\mu^2 - M_2^2)^2 - 4m_W^2(\mu^2 + M_2^2) - 4m_W^2 \cos^2 2\beta}{8m_W^2 M_2 |\mu| \sin 2\beta} \tag{7.4}$$

$$M_3 = m_{\tilde{\mathrm{g}}} \tag{7.5}$$

using

$$\Sigma = \frac{m^2_{\chi_2^\pm} + m^2_{\chi_1^\pm}}{2m_W^2} - 1 \tag{7.6}$$

$$\Delta = \frac{m^2_{\chi_2^\pm} - m^2_{\chi_1^\pm}}{4m_W^2} \tag{7.7}$$

After these parameters have been determined at tree-level, a tree-level estimate of M_1 can be calculated from the neutralino mass matrix (2.40) eigenvalues. They depend on

$\mu, \tan\beta, M_2$ and M_1. The first three of these parameters have been determined already in the first step. Thus the neutralino system can be used to finally determine M_1. In fact, the neutralino system is the only sector where M_1 can be measured directly. The characteristic equation of the neutralino mass matrix can be written as a quadratic equation in M_1

$$YY^\dagger = 0 = xM_1^2 + yM_1 + z.$$

where x, y and z are functions of $\mu, \tan\beta$ and M_2. The full form of these functions can be found in [167].

2. $X_{\text{top}}, X_{\text{bottom}}, M_Q, M_U, M_D$ are determined from the squark sector masses, using formulae from [169]. No mixing in the third generation is assumed at this step of the procedure, i. e. the mixing parameters X are set to zero for the determination of the squark mass parameters. These parameters are defined as the off-diagonal elements $X_{\text{top}} = A_t - \mu/\tan\beta$ and $X_{\text{bottom}} = A_b - \mu\tan\beta$ in (2.36). They are chosen as fit parameters instead of A because their correlation with $\tan\beta$ is reduced. After $\tan\beta$ and μ have been determined in the previous step, the following tree-level relations are obtained from (2.36), neglecting the mixing terms. As an example, only the third generation is shown explicitely.

$$\begin{aligned}
M_{\mathrm{t}_L} &= -{m_{\mathrm{Z}}}^2 \cos 2\beta(\frac{1}{2} - \frac{2}{3}\sin^2\theta_W) - m_{\mathrm{t}}^2 + \frac{1}{2}(m_{\tilde{\mathrm{t}}_1}^2 + m_{\tilde{\mathrm{t}}_2}^2) && (7.8)\\
&= {m_{\mathrm{Z}}}^2 \cos 2\beta(\frac{1}{2} - \frac{1}{3}\sin^2\theta_W) - m_{\mathrm{b}}^2 + \frac{1}{2}(m_{\tilde{\mathrm{b}}_1}^2 + m_{\tilde{\mathrm{b}}_2}^2) && (7.9)\\
M_{\mathrm{t}_R} &= -{m_{\mathrm{Z}}}^2 \cos 2\beta\frac{2}{3}\sin^2\theta_W - m_{\mathrm{t}}^2 + \frac{1}{2}(m_{\tilde{\mathrm{t}}_1}^2 + m_{\tilde{\mathrm{t}}_2}^2) && (7.10)\\
M_{\mathrm{b}_R} &= {m_{\mathrm{Z}}}^2 \cos 2\beta\frac{1}{3}\sin^2\theta_W - m_{\mathrm{b}}^2 + \frac{1}{2}(m_{\tilde{\mathrm{b}}_1}^2 + m_{\tilde{\mathrm{b}}_2}^2) && (7.11)\\
X_{\text{top}} &= -\mu/\tan\beta && (7.12)\\
X_{\text{bottom}} &= -\mu\tan\beta && (7.13)
\end{aligned}$$

The parameters of the other generations can be obtained analogously. The initial determination of X_{top} and X_{bottom} is only very rough and therefore refined in an additional step, which is explained below.

3. X_τ, M_L, M_E are determined from the slepton sector masses, using formulae from [169]. No mixing in the third generation is assumed. Here $X_\tau = A_\tau - \mu\tan\beta$ from (2.34) is set to zero, too. The tree-level formulae derived from (2.34) read for the third generation:

$$\begin{aligned}
M_{\mathrm{t}_L} &= {m_{\mathrm{Z}}}^2 \cos 2\beta(\frac{1}{2} - \sin^2\theta_W) - m_\tau^2 + \frac{1}{2}(m_{\tilde{\tau}_1}^2 + m_{\tilde{\tau}_2}^2) && (7.14)\\
M_{\mathrm{t}_R} &= -{m_{\mathrm{Z}}}^2 \cos 2\beta \sin^2\theta_W - m_\tau^2 + \frac{1}{2}(m_{\tilde{\tau}_1}^2 + m_{\tilde{\tau}_2}^2) && (7.15)\\
X_\tau &= -\mu\tan\beta && (7.16)
\end{aligned}$$

The determination of X_τ is refined later as explained below.

In order to estimate the uncertainty of this determination of the parameters from tree-level formulae, the calculation is repeated 10 000 times with observables randomly smeared within their uncertainties according to a Gaussian probability distribution. The starting value of the fit is the mean of the distribution of each parameter. From the variance of the calculated parameter distribution the initial uncertainty is estimated.

Since the possibility of mixing in the third generation has been neglected in the calculation of the tree-level estimates, the parameters $X_{\text{top}}, X_{\text{bottom}}, X_\tau$ are only roughly initialised. A global fit with these starting values would most likely not converge. Therefore next the estimates from the slepton sector are improved by fitting only the slepton parameters X_τ, M_L, M_E to the observables from the slepton sector, i. e. slepton masses, widths and cross-sections. Observables not directly related to the slepton sector can degrade the fit result, since parameters of other sectors are likely to be still wrong. In such a case a parameter of the slepton sector will be pulled into a wrong direction, in order to compensate for the wrong parameters of other sectors. All parameters not from the slepton sector are fixed to their estimated tree-level values. In this fit with reduced number of dimensions MINUIT can handle the correlations among the parameter better than in a global fit with all parameters free.

Then the third generation squark parameters are improved by only fitting $X_{\text{top}}, X_{\text{bottom}}, M_Q, M_U, M_D$ to the observables of the squark sector, masses, widths and cross-sections. All other parameters are fixed to their previous values.

After this step the correlations among $\tan\beta$ and the third generation slepton and squark parameters are still not optimally modelled. Therefore another intermediate step is introduced, where $\tan\beta, X_{\text{top}}, X_{\text{bottom}}, X_\tau$ and $M_{t,L,R}$ are fitted to all observables and all other parameters are fixed to their present values.

After this, all parameters are released and a global fit is done, using the method MINIMIZE in MINUIT. If this fit converges, a MINOS error analysis is performed, yielding asymmetrical uncertainties, the full correlation matrix and 2D fit contours. The mathematical procedures used by MINUIT are briefly described in Appendix A.1.

A documentation of the program Fittino is given in Appendix A.2.

Calculations of Observables in SPheno

In the current implementation, the program SPheno [165] is used as a tool to predict the observables for a given set of input parameters. SPheno is a SUSY spectrum calculator, incorporating a huge number of available loop calculations to the sparticle masses. After calculating the masses and couplings, also widths, branching ratios and e^+e^- cross-sections for various centre-of-mass energies and polarisations, including ISR, are determined. Either low-energy parameters of $\mathcal{L}_{\text{SUSY}}$ can be given as input, or high-scale parameters at the scale Λ_{GUT} can be used, in which case the low-energy parameters of $\mathcal{L}_{\text{SUSY}}$ are calculated using one-loop renormalisation group equations. The following levels of loop corrections are included:

- *Sparticles*: All sparticle masses are determined at one-loop-level.
- *Higgs sector*: The Higgs sector masses are determined on the two-loop level, incorporating the latest $\mathcal{O}(\alpha_t^2)$ corrections [47] also incorporated in FEYNHIGGS, which was used as a spectrum calculator in the calculations in Section 6.
- *Couplings*: All widths and branching ratios are determined on tree-level.
- *Cross-Sections*: The leading electromagnetic correction ISR is included using formulae from [170].

It is interfaced to Fittino using the SLHA, which has been extended for the purpose of this project with a block for cross-section information.

7.4 The SPS1a Fit

The program Fittino is used to demonstrate the feasibility of a bias-free fit of the MSSM parameters to the observables of LHC and the LC. No a priori assumption on the parameters is used. The complete MSSM spectrum is fitted simultaneously in order to determine the full uncertainties of all parameters and their full correlation matrix.

In the following, a specific example for one set of MSSM parameters (the benchmark points SPS1a) is carried out. Available experimental studies are used to determine the anticipated precision of future measurements at LHC and LC. The MSSM model under study and the inputs are explained. Then the fit result is discussed. This section is closed with a discussion of the difficulties of parameter determinations in subspaces of the complete parameter space. This is demonstrated by a fit in the gaugino sector, using observables of a 500 GeV LC only.

7.4.1 Assumptions and Simplifications

The MSSM benchmark point SPS1a [160] is chosen for a global MSSM parameter fit. It is derived from the following parameter choice at the GUT scale:

$$\begin{aligned} m_0 &= 100\,\text{GeV} && \text{common sparticle mass scale} \\ m_{1/2} &= 250\,\text{GeV} && \text{common gaugino mass scale} \\ A_0 &= -100\,\text{GeV} && \text{common trilinear coupling} \\ \tan\beta &= 10 \\ \text{sign}(\mu) &> 0. \end{aligned}$$

From this choice, the low-energy parameters have been derived using Isajet 7.48 [171]. The low-energy-parameters are then fixed and define the parameter point SPS1a. In the context of this thesis, the parameters have been derived from the above choice of high-scale parameters using SPheno. For points with small and intermediate $\tan\beta$, the first and second generation of sparticles is almost degenerate and the corresponding mass parameters of the first and second generation are almost unified. Therefore in this fit unification among the first and second generation is assumed.

The resulting parameters of this modified SPS1a point, here called $\text{SPS1a}_{\text{mod}}$, are shown in Tab. 7.2. No relevant change of the phenomenological behaviour of this MSSM point with respect to the original SPS1a point is observed.

Generally also SM parameters have to be determined in a simultaneous fit together with the MSSM parameters. Since SM parameters such as $\sin^2\theta_W$ or m_Z are generally measured to a great precision, it is omitted to fit them here. The top quark mass m_{top}, on the other hand, has a rather large uncertainty and influences parts of the MSSM observables very strongly, such as the Higgs boson mass. Therefore m_{top} is fitted simultaneously with the MSSM parameters.

The uncertainty of the theory predictions is not known for all observables. It is expected that the influence of theoretical uncertainty is strongest in the Higgs sector, where very precise measurements can be made. For the Higgs sector an estimate of the theoretical uncertainty of the prediction is available [47]. Since no information about the probability distribution inside the uncertainty band is available, it is assumed to be Gaussian. For the time of the LC data taking, a theoretical uncertainty of 500 MeV on the mass of the lightest CP-even Higgs boson h is assumed. This is about a factor of 10 larger than the anticipated experimental uncertainty. No estimate of the theoretical uncertainties is available in other sectors, This is needed for precise studies of the parameter determination in the future.

Since the tree-level estimation of the third generation mixing parameters X_τ, X_{top} and X_{bottom} is difficult, these parameters are roughly constrained to the range $-6000\,\text{GeV} < X <$

2000 GeV, which covers the region in which they are to be expected naturally for the values of μ and $\tan\beta$ derived on tree-level.

7.4.2 Simulated Measurements

Using the low-energy parameters of $\text{SPS1a}_{\text{mod}}$, the observables at the LHC and a 500 GeV and 1 TeV LC are calculated using SPheno. The observables used in this fit are shown in Tab. 7.1.

The uncertainties of the observables are obtained in the following way:

- *SM precision observables*: For $m_{\text{W}}, m_{\text{Z}}$ and $\sin^2\theta_W$ the present uncertainties are used as a conservative estimate of the future precision.
- *Mass measurements*: The precision on the mass measurements are taken from [6]. This analysis contains measurements at the LHC (primarily the squark sector and the gluino) and a 500 GeV and 1 TeV LC, which dominates the precision in the gaugino sector and the Higgs sector. The benefit of combined analyses at LHC and LC is taken into account. In these analyses, observables obtained at the LC are used to eliminate uncertainties (primarily from intermediate particles in cascade decays) at the LHC, and vice versa. Also the uncertainty of the top quark mass assumes that it is measured at the LC with high precision.
- *Cross-sections*: Since the measurement of cross-sections is non-trivial at the LHC, only cross-section measurements at the LC are included. Since no comprehensive study of the precision of different cross-section measurements is available, the uncertainty is taken to be the statistical error of a counting experiment, using the following assumptions:
  - 50 % efficiency of each search
  - 80 % polarisation of the e^- beam, 60 % polarisation of the e^+ beam
  - 500 fb^{-1} per $\sqrt{s}$ and polarisation
  - To account for possible systematical effects: no relative precision better than 1 %, no absolute precision better than 0.1 fb.

  In total 8 different combinations of $\sqrt{s}$ and beam polarisations are used, corresponding to about 8 years of LC data taking. Once a limited knowledge of the SUSY parameters is available, the results obtained with this study can then be used to balance the luminosity delivered from the LC at various $\sqrt{s}$ and beam polarisations such that the highest precision on the SUSY parameters is achieved with the smallest amount of luminosity.
- *Branching Ratios*: Only three Higgs branching ratios are included. The uncertainty on $\text{BR}(\text{h} \to \text{b}\bar{\text{b}})$ is taken from [172], the uncertainty on the other branching ratios is estimated conservatively (compare with [162]).
- *Mixing angles*: For tree-level estimation of $\tan\beta$, μ and the parameters of the gaugino sector the chargino mixing angles $\cos 2\phi_L$ and $\cos 2\phi_R$ are used. Their uncertainty is irrelevant for the fit result.

No effect of experimental correlations of observables among each other is included. Also no use is made of total width measurements, limits on undetected particles and edges in mass spectra.

It is assumed that all particles are uniquely identified. In most cases this will be possible, since there are measurements of angular distributions, threshold behaviour, asymmetries and

Table 7.1: *Simulated measurements at LHC and a 0.5 and 1 TeV LC. The values of the observables are taken from the prediction of SPheno for the SPS1a MSSM parameter set. The uncertainties on the masses are taken from [6]. The uncertainties on the cross-sections are estimated for a luminosity of* $\mathcal{L}^{\text{int}} = 500\,\text{fb}^{-1}$ *at each polarisation and energy with* 50 % *selection efficiency.*

Observable	Value	Experimental uncertainty	Source
m_{W}	80.3382 GeV	0.039 GeV	current Exp.
m_{Z}	91.1187 GeV	0.0021 GeV	current Exp.
m_{top}	174.3 GeV	0.3 GeV	LC
m_{bottom}	4.2 GeV	0.5 GeV	current Exp.
$\sin 2\theta_W$	0.23113	0.00015	current Exp.
m_{h}	110.211 GeV	0.05 GeV $\pm$ 0.5 GeV	LC
m_{A}	399.767 GeV	1.3 GeV	LC
m_{H}	400.803 GeV	1.3 GeV	LC
$m_{\text{H}^\pm}$	407.695 GeV	1.1 GeV	LC
$m_{\tilde{\text{d}}_L}$	586.734 GeV	9.8 GeV	LHC+LC
$m_{\tilde{\text{d}}_R}$	566.257 GeV	23.6 GeV	LHC
$m_{\tilde{u}_L}$	583.546 GeV	9.8 GeV	LHC+LC
$m_{\tilde{u}_R}$	566.516 GeV	23.6 GeV	LHC
$m_{\tilde{s}_L}$	586.736 GeV	9.8 GeV	LHC+LC
$m_{\tilde{s}_R}$	566.254 GeV	23.6 GeV	LHC
$m_{\tilde{c}_L}$	583.552 GeV	9.8 GeV	LHC+LC
$m_{\tilde{c}_R}$	566.510 GeV	23.6 GeV	LHC
$m_{\tilde{b}_1}$	532.146 GeV	5.7 GeV	LHC+LC
$m_{\tilde{b}_2}$	565.561 GeV	6.2 GeV	LHC+LC
$m_{\tilde{t}_1}$	417.516 GeV	2.0 GeV	LC
$m_{\tilde{e}_L}$	208.002 GeV	0.2 GeV	LC
$m_{\tilde{e}_R}$	143.906 GeV	0.05 GeV	LC
$m_{\tilde{\nu_{e_L}}}$	192.300 GeV	0.7 GeV	LC
$m_{\tilde{\mu}_L}$	208.02 GeV	0.5 GeV	LC
$m_{\tilde{\mu}_R}$	143.878 GeV	0.2 GeV	LC
$m_{\tilde{\tau}_1}$	134.283 GeV	0.3 GeV	LC
$m_{\tilde{\tau}_2}$	211.792 GeV	1.1 GeV	LC
$m_{\tilde{\text{g}}}$	630.449 GeV	6.4 GeV	LHC
$m_{\chi_1^0}$	95.7412 GeV	0.05 GeV	LC
$m_{\chi_2^0}$	182.396 GeV	0.08 GeV	LHC+LC
$m_{\chi_1^\pm}$	180.461 GeV	0.55 GeV	LC
$m_{\chi_2^\pm}$	379.967 GeV	3.0 GeV	LC
σ ($\text{e}^+\text{e}^-{}_{LL} \to \chi_1^0\chi_2^0$) 500 *GeV*	22.7048 fb	0.3 fb	LC
σ ($\text{e}^+\text{e}^-{}_{LL} \to \chi_2^0\chi_2^0$) 500 *GeV*	19.4676 fb	0.28 fb	LC
σ ($\text{e}^+\text{e}^-{}_{LL} \to \tilde{\text{e}}_L\bar{\tilde{\text{e}}}_L$) 500 *GeV*	204.974 fb	2.0 fb	LC
σ ($\text{e}^+\text{e}^-{}_{LL} \to \tilde{\mu}_L\bar{\tilde{\mu}}_L$) 500 *GeV*	36.8348 fb	0.4 fb	LC
σ ($\text{e}^+\text{e}^-{}_{LR} \to \tilde{\tau}_1\bar{\tilde{\tau}}_1$) 500 *GeV*	45.4683 fb	0.46 fb	LC
σ ($\text{e}^+\text{e}^-{}_{RL} \to \tilde{\tau}_1\bar{\tilde{\tau}}_1$) 500 *GeV*	139.109 fb	1.4 fb	LC
σ ($\text{e}^+\text{e}^-{}_{LL} \to \chi_1^+\chi_1^-$) 500 *GeV*	46.6626 fb	0.46 fb	LC
σ ($\text{e}^+\text{e}^-{}_{RL} \to \text{hZ}$) 500 *GeV*	38.3684 fb	0.38 fb	LC
σ ($\text{e}^+\text{e}^-{}_{LR} \to \text{hZ}$) 500 *GeV*	28.9897 fb	0.35 fb	LC
σ ($\text{e}^+\text{e}^-{}_{RR} \to \chi_1^+\chi_1^-$) 500 *GeV*	104.746 fb	1.0 fb	LC
σ ($\text{e}^+\text{e}^-{}_{RR} \to \chi_1^0\chi_2^0$) 500 *GeV*	43.9503 fb	0.4 fb	LC

continued on next page

continued from last page			
Observable	Value	Experimental uncertainty	Source
σ ($e^+e^-_{RR} \to \chi_2^0\chi_2^0$) 500 GeV	43.7745 fb	0.4 fb	LC
σ ($e^+e^-_{RR} \to \tilde{e}_L\bar{\tilde{e}}_L$) 500 GeV	97.4164 fb	1.0 fb	LC
σ ($e^+e^-_{RR} \to \tilde{e}_L\bar{\tilde{e}}_R$) 500 GeV	223.676 fb	2.2 fb	LC
σ ($e^+e^-_{RR} \to \tilde{e}_R\bar{\tilde{e}}_R$) 500 GeV	28.9840 fb	0.35 fb	LC
σ ($e^+e^-_{RR} \to \tilde{\mu}_L\bar{\tilde{\mu}}_L$) 500 GeV	22.6951 fb	0.3 fb	LC
σ ($e^+e^-_{RR} \to \tilde{\tau}_1\bar{\tilde{\tau}}_1$) 500 GeV	25.7371 fb	0.32 fb	LC
σ ($e^+e^-_{RL} \to \chi_1^+\chi_1^-$) 1 TeV	11.8156 fb	0.2 fb	LC
σ ($e^+e^-_{LR} \to \chi_1^+\chi_1^-$) 1 TeV	405.536 fb	4.0 fb	LC
σ ($e^+e^-_{RL} \to \chi_1^+\chi_2^-$) 1 TeV	6.44726 fb	0.15 fb	LC
σ ($e^+e^-_{LR} \to \chi_1^+\chi_2^-$) 1 TeV	41.7643 fb	0.4 fb	LC
σ ($e^+e^-_{RL} \to \chi_2^+\chi_2^-$) 1 TeV	43.7696 fb	0.4 fb	LC
σ ($e^+e^-_{LR} \to \chi_2^+\chi_2^-$) 1 TeV	206.527 fb	2.0 fb	LC
σ ($e^+e^-_{LR} \to \chi_1^+\chi_1^-$) 500 GeV	418.759 fb	4.2 fb	LC
σ ($e^+e^-_{RL} \to \chi_1^+\chi_1^-$) 500 GeV	12.1741 fb	0.22 fb	LC
σ ($e^+e^-_{LR} \to \chi_1^0\chi_2^0$) 500 GeV	169.215 fb	1.7 fb	LC
σ ($e^+e^-_{RL} \to \chi_2^0\chi_2^0$) 500 GeV	4.92392 fb	0.15 fb	LC
σ ($e^+e^-_{RL} \to \chi_1^0\chi_2^0$) 500 GeV	20.4959 fb	0.3 fb	LC
σ ($e^+e^-_{LR} \to \chi_2^0\chi_2^0$) 500 GeV	175.073 fb	1.8 fb	LC
σ ($e^+e^-_{LR} \to \chi_1^+\chi_1^-$) 400 GeV	135.403 fb	1.4 fb	LC
σ ($e^+e^-_{RL} \to \chi_1^+\chi_1^-$) 400 GeV	3.8592 fb	0.13 fb	LC
σ ($e^+e^-_{LR} \to \chi_1^0\chi_2^0$) 400 GeV	135.518 fb	1.4 fb	LC
σ ($e^+e^-_{RL} \to \chi_2^0\chi_2^0$) 400 GeV	1.24456 fb	0.1 fb	LC
σ ($e^+e^-_{RL} \to \chi_1^0\chi_2^0$) 400 GeV	18.0209 fb	0.3 fb	LC
σ ($e^+e^-_{LR} \to \chi_2^0\chi_2^0$) 400 GeV	44.0553 fb	0.4 fb	LC
σ ($e^+e^-_{RL} \to \tilde{e}_L\bar{\tilde{e}}_L$) 500 GeV	806.778 fb	8.0 fb	LC
σ ($e^+e^-_{LR} \to \tilde{e}_L\bar{\tilde{e}}_L$) 500 GeV	53.8728 fb	0.54 fb	LC
σ ($e^+e^-_{RL} \to \tilde{e}_L\bar{\tilde{e}}_L$) 400 GeV	549.688 fb	5.5 fb	LC
σ ($e^+e^-_{LR} \to \tilde{e}_L\bar{\tilde{e}}_L$) 400 GeV	42.7344 fb	0.4 fb	LC
σ ($e^+e^-_{LR} \to \tilde{\mu}_L\bar{\tilde{\mu}}_L$) 500 GeV	35.2265 fb	0.35 fb	LC
σ ($e^+e^-_{RL} \to \tilde{\mu}_L\bar{\tilde{\mu}}_L$) 500 GeV	134.205 fb	1.4 fb	LC
σ ($e^+e^-_{LR} \to \tilde{\mu}_L\bar{\tilde{\mu}}_L$) 400 GeV	30.8649 fb	0.35 fb	LC
σ ($e^+e^-_{RL} \to \tilde{\mu}_L\bar{\tilde{\mu}}_L$) 400 GeV	120.872 fb	1.2 fb	LC
σ ($e^+e^-_{RL} \to \tilde{\nu}_{e_L}\bar{\tilde{\nu}}_{e_L}$) 500 GeV	46.4731 fb	0.5 fb	LC
σ ($e^+e^-_{LR} \to \tilde{\nu}_{e_L}\bar{\tilde{\nu}}_{e_L}$) 500 GeV	1132.59 fb	12.0 fb	LC
σ ($e^+e^-_{RL} \to \tilde{e}_R\bar{\tilde{e}}_R$) 500 GeV	11.655 fb	0.2 fb	LC
σ ($e^+e^-_{LR} \to \tilde{e}_R\bar{\tilde{e}}_R$) 500 GeV	112.377 fb	1.2 fb	LC
BR (h $\to$ Bottom Bottom)	0.824057	0.01	LC
BR (h $\to$ Charm Charm)	0.0405547	0.01	LC
BR (h $\to$ Tau Tau)	0.134444	0.01	LC
Observables only used for tree-level initialisation			
$\cos 2\phi_L$	0.674	0.005	LC
$\cos 2\phi_R$	0.898	0.005	LC

branching ratios which can be used to identify the particles and which are not directly included as measurements in this fit. However, it is impossible to distinguish the first and second generation squarks at LHC from each other. As Tab. 7.4 shows, this identification is not crucial for the fit.

In case of ambiguities among particle identifications which are not resolvable using the measurements mentioned above, the Fittino fit can in principle be performed several times for all combinations of the ambiguities. The optimum identification of the observed particles can then be derived from the fit with the best χ^2.

Table 7.2: *The Fittino SPS1a fit result. The left column shows the assumed SPS1a values, the middle column represents the result of the intermediate fit without m_{top}, and the right column shows the result of the final fit. All SPS1a input values of the parameters are reconstructed.*

Parameter	$\text{SPS1a}_{\text{mod}}$ value	Tree-level estimate	Intermediate fit result	Final fit result
$\tan\beta$	10.0	9.97	10.2	10.0 ± 0.33
μ	358.64 GeV	354.4 GeV	358.7 GeV	358.6 ± 1.14 GeV
X_τ	-3837.23 GeV	-3533.0 GeV	-4003.3 GeV	-3837.2 ± 131.0 GeV
$M_{\tilde{e}_R}$	135.76 GeV	150.2 GeV	135.76 GeV	135.76 ± 0.39 GeV
$M_{\tilde{\tau}_R}$	133.33 GeV	141.0 GeV	134.13 GeV	133.33 ± 0.75 GeV
$M_{\tilde{e}_L}$	195.21 GeV	202.7 GeV	195.20 GeV	195.21 ± 0.18 GeV
$M_{\tilde{\tau}_L}$	194.39 GeV	206.6 GeV	193.9 GeV	194.4 ± 1.18 GeV
X_{top}	-506.388 GeV	-43.5 GeV	-503.1 GeV	-506.4 ± 29.5 GeV
X_{bottom}	-4441.0 GeV	-3533.0 GeV	-4465.5 GeV	-4441.1 ± 1765 GeV
$M_{\tilde{d}_R}$	528.14 GeV	567.3 GeV	528.1 GeV	528.2 ± 17.6 GeV
$M_{\tilde{b}_R}$	524.718 GeV	566.0 GeV	524.6 GeV	524.7 ± 7.67 GeV
$M_{\tilde{u}_R}$	530.253 GeV	566.9 GeV	530.3 GeV	530.2 ± 19.1 GeV
$M_{\tilde{t}_R}$	424.382 GeV	373.7 GeV	423.6 GeV	424.4 ± 8.54 GeV
$M_{\tilde{u}_L}$	548.705 GeV	581.3 GeV	548.7 GeV	548.7 ± 5.16 GeV
$M_{\tilde{t}_L}$	499.972 GeV	575.4 GeV	500.0 GeV	500.0 ± 8.06 GeV
M_1	101.809 GeV	99.07 GeV	101.78 GeV	101.81 ± 0.06 GeV
M_2	191.7556 GeV	195.08 GeV	191.67 GeV	191.76 ± 0.10 GeV
M_3	588.797 GeV	630.5 GeV	588.8 GeV	588.8 ± 7.88 GeV
m_{A}	399.767 GeV	399.8 GeV	399.8 GeV	399.8 ± 0.71 GeV
m_{top}	174.3 GeV	174.3 GeV	fixed	174.3 ± 0.34 GeV
χ^2 for unsmeared observables: 0.28×10^{-4}				

7.4.3 Fit Results

The global fit to the SPS1a MSSM benchmark point is divided into three parts. First, it is demonstrated that for a fit to the observables as predicted by $\text{SPS1a}_{\text{mod}}$ the $\text{SPS1a}_{\text{mod}}$ parameters are exactly reproduced. No smearing of the observables is introduced at this step. Then, systematical biases to the parameter reconstruction are checked using a statistical smearing of all observables within their uncertainties before the fit. This step is also used to test the uncertainty of the fitted parameters. Finally, the importance of the individual observables for the parameter determination is determined.

Fit to the Unsmeared Observables

The global SPS1a fit has been performed in several steps, as shown in Tab. 7.2. First, the tree-level estimate of the parameters is made. Apart from the mixing parameters, all parameters are derived in the correct order of magnitude. Then an intermediate fit is performed to improve the tree-level estimates. For simplicity, the fit of the directly measurable parameter (and observable) m_{top} is omitted at this step. Also only cross-sections at $\sqrt{s} = 500$ GeV are used, since the cross-section calculation is the most time consuming step in the fit. The intermediate fit result is also shown in Tab. 7.2.

After this step, the final SPS1a fit is performed using MIGRAD for minimisation and MINOS for the uncertainty analysis. As Tab. 7.2 shows, it converges exactly to the input parameters of $\text{SPS1a}_{\text{mod}}$. Since this fit is performed using unsmeared observables, the χ^2 of the fit is close to 0 at $\chi^2 = 0.28 \times 10^{-4}$. Most parameters are reconstructed with a relative precision better than 4 %. Typically the mixing parameters are determined with the smallest precision. The relatively large precision in the slepton sector allows to determine X_τ to a precision of 3.4 %. The large mass splitting in the stop sector and its influence on the Higgs sector yield a relative precision on X_{top} of 6 %. The sbottom mixing parameter X_{bottom} is only weakly constrained by the sbottom masses and has small effects on the Higgs sector, therefore it is the parameter with the smallest relative precision of 40 %.

The parameters of the Higgs, slepton and the gaugino sectors are generally measured with the best precision. $\tan\beta$ is measured to a precision of 3.3 %, which is a good value for a parameter which is not directly connected to one single precisely measured observable and which has strong correlations to other parameters.

Since all parameters have been determined simultaneously, the information on their full correlations is available in form of their covariance and correlation matrices. The covariance matrix of the parameters of the SPS1a fit is shown in Appendix B.3 in Tables B.1 and B.2. The correlation matrix is shown in Tables B.3 and B.4. The correlation matrix shows that generally correlations among the same sector can be strong and that, most notably, correlations between different sectors are not negligible. For example, there is a strong correlation among the parameters of the gaugino sector. The parameters $\tan\beta$, μ, M_1 and M_2 are all correlated to a degree of more than 29 %. $\tan\beta$ and μ along are anti-correlated to a degree of 82 %. This effect already is visible on tree level, given that using (7.2) and (7.1) $\tan\beta$ and μ depend on the same observables.

These correlations among the parameters of one single sector can also be taken into account in a parameter determination in one sector only. The correlations (and their impact on the parameter uncertainty) among parameters of different sectors, however, can only be determined in a global fit and using loop-level calculations. For example, the slepton sector $M_{\tilde{\text{e}}_R}$ has a correlation of 87 % with the squark sector parameter $M_{\tilde{\text{u}}_R}$, induced by F- and D-term graphs on one-loop level [173]. Also the relatively robust gaugino sector is affected by these correlations. M_1, for example, has correlations of more than 20% with $M_{\tilde{\text{e}}_R}$, $M_{\tilde{\text{u}}_R}$ and $M_{\tilde{\text{t}}_R}$.

These correlations are graphically displayed in two-dimensional uncertainty contours. An example for these contours is given in Figure 7.7. Every graph represents the contour in the two-dimensional parameter space of two parameters, at which the difference $\Delta\chi^2$ to the minimal χ^2 of the fit is +1, representing the one-dimensional $1\,\sigma$ borders of the individual parameters. All other parameters are kept fixed to their central values in the fit. A thin and diagonal shape of one of the graphs shows a strong positive (positive slope of the ellipse main axis) or negative (negative slope) correlation among the parameters.

Most of the uncertainty contours are almost elliptical, showing that close to the minimum of the χ^2 the dependence of the observables on the parameters is almost linear. In Fig. 7.7, the upper left plot shows the correlation between $\tan\beta$ and μ, which is already visible from (7.1) and (7.2). Other parameters are uncorrelated, as the upper right plot shows for M_3 and $\tan\beta$. The lower plots in Fig. 7.7 show the correlations of parameters of different sectors of the MSSM. For the correlation coefficients, see Tables B.1 and B.2.

The strong correlations in the gaugino sector can only be resolved using precise information in the couplings in this sector. Without the use of precise cross-section measurements at various beam polarisations at the LC no determination of the correlation matrix is possible. Correlations among the parameters are too strong to be precisely measured and the dependence

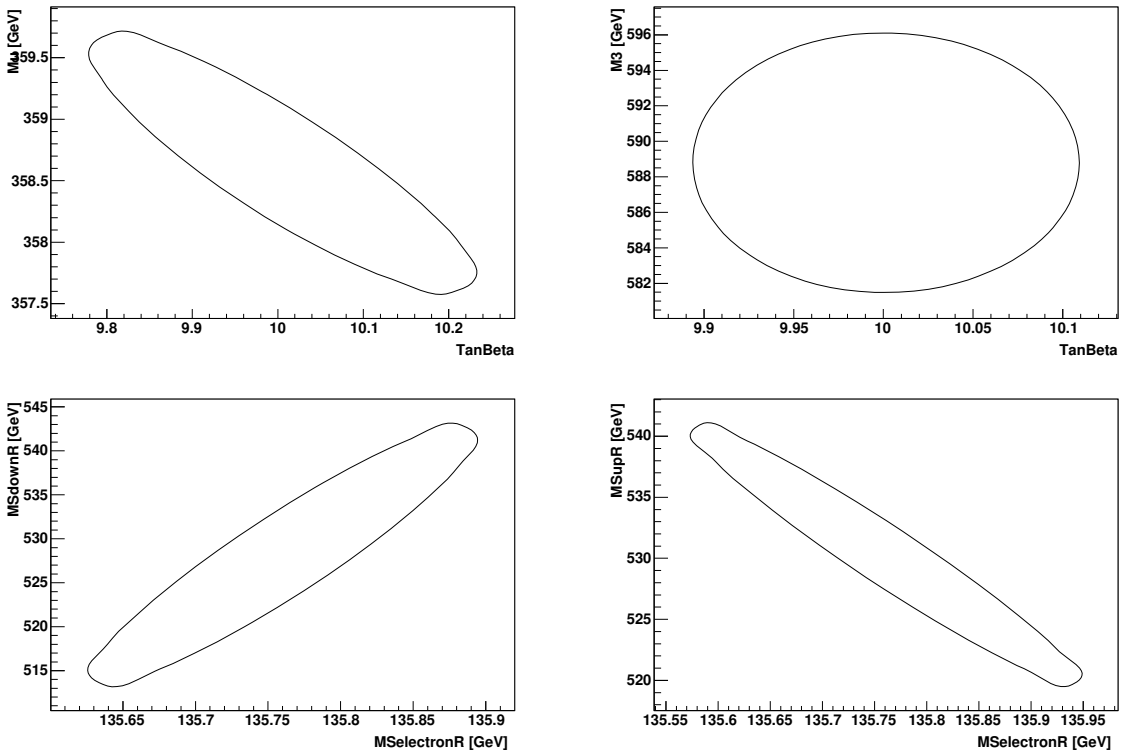

Figure 7.7: *Examples of the two-dimensional uncertainty contours of the Fittino SPS1a fit.*

of the observables on the parameters is too non-linear to be approximated by a quadratical uncertainty function. However, the parameters can only be determined correctly if also the correlation with other sectors are treated properly. This shows the strong benefit of using both LHC and LC data.

Pull Distributions

The fit result as presented above is based on the use of the observables at their central values as predicted by SPheno in the $\text{SPS1a}_{\text{mod}}$ scenario. This is done in order to demonstrate that the exact value of the input parameters can be reconstructed. However, in a real measurement at LHC or LC the central value of the measurement will not exactly match the true value of the observable due to statistical and systematical uncertainties. The effect of the variation of the observables within their uncertainties is tested using the calculation of pull distributions for the parameters. For this purpose, 120 individual global fits to $\text{SPS1a}_{\text{mod}}$ have been performed. Before each fit, the observables have been smeared randomly in a Gaussian way according to their covariance matrix. Then the distribution of the obtained χ^2 values of the fits and the distributions of $(P_i^{\text{true}} - P_i^{\text{fit}})/\sigma_i^{\text{fit}}$ for each parameter is plotted.

This method is also used to cross-check the parameter uncertainties measured in the global fit. If the uncertainties are correct, then the distribution of $(P_i^{\text{true}} - P_i^{\text{fit}})/\sigma_i^{\text{fit}}$ has to follow a Gaussian distribution with $\sigma = 1$ and mean zero. The distribution of the χ^2 values has to follow the probability distribution for the χ^2 values with $n = o - p = 62$ degrees of freedom (d.o.f.), for o observables and p parameters, since no correlations among the observables are taken into account.

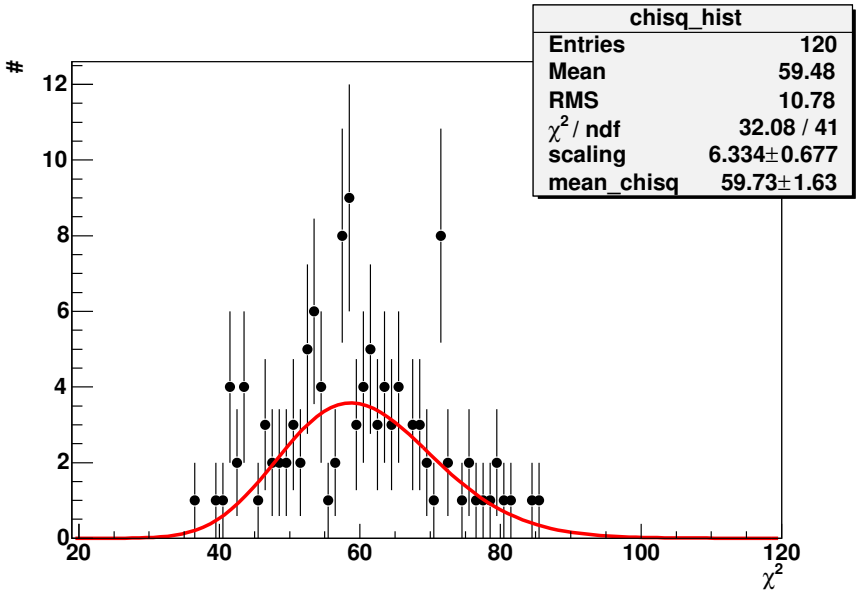

Figure 7.8: *Distribution of χ^2 for the SPS1a fit. 120 fits with 62 d.o.f. are performed. The observables of the simulated measurements are smeared in each fit according to their uncertainties. The mean of the distribution is $\chi^2_{\text{mean}} = 59.7 \pm 1.6$.*

Figure 7.8 shows the χ^2 distribution of the 120 fits. The χ^2 probability function [129]

$$P(\chi^2, n) = \frac{e^{-\chi^2/2}\chi^{n-1}2^{1-n/2}}{\Gamma\left(\frac{n}{2}\right)} \tag{7.17}$$

is fitted to this distribution. The agreement of the observed χ^2 distribution with the fitted function is very good. This fit yields $\chi^2 = 32$ for 41 d.o.f. The mean χ^2 of the SPS1a fit is $\chi^2_{\text{mean}} = 59.7 \pm 1.6$ for 62 d.o.f., which is in good agreement. This test shows that generally the values of the parameter uncertainties are determined correctly.

The pull distributions of the individual parameters are shown in Figures 7.9 to 7.12. In each distribution, the quantity $(P_i^{\text{true}} - P_i^{\text{fit}})/\sigma_i^{\text{fit}}$ is shown, together with a Gaussian distribution fitted to the observed values. The widths of the fitted Gaussian functions for each parameter are shown in Tab. 7.3. In all distributions apart from X_{bottom}, the agreement between the expected Gaussian with $\sigma = 1$ and mean zero is good. As expected by a statistical distribution of the results, there exist some distributions with a deviation between 1 and $2\,\sigma$ from the expectation. The Gaussian widths in Tab. 7.3 are all close to 1, showing that the uncertainties of all parameters are determined correctly in the SPS1a fit. No significant systematical shift to either higher or lower fitted parameter values with respect to the $\text{SPS1a}_{\text{mod}}$ values is observed.

The only deviation from the expected distribution occurs in the case of X_{bottom}. This parameter has the largest relative and by far the largest absolute uncertainty. Additionally, it is constrained to the range $-6000\,\text{GeV} < X_{\text{bottom}} < 2000\,\text{GeV}$. This distorts the the pull distribution. In a future step, the constraint on the parameter should be removed in the final fit.

As a result, the uncertainties determined by the SPS1a fit are fully confirmed. In principle this technique to cross-check the fit result can also be performed with real measurements, which are smeared within their uncertainties and according to their correlations.

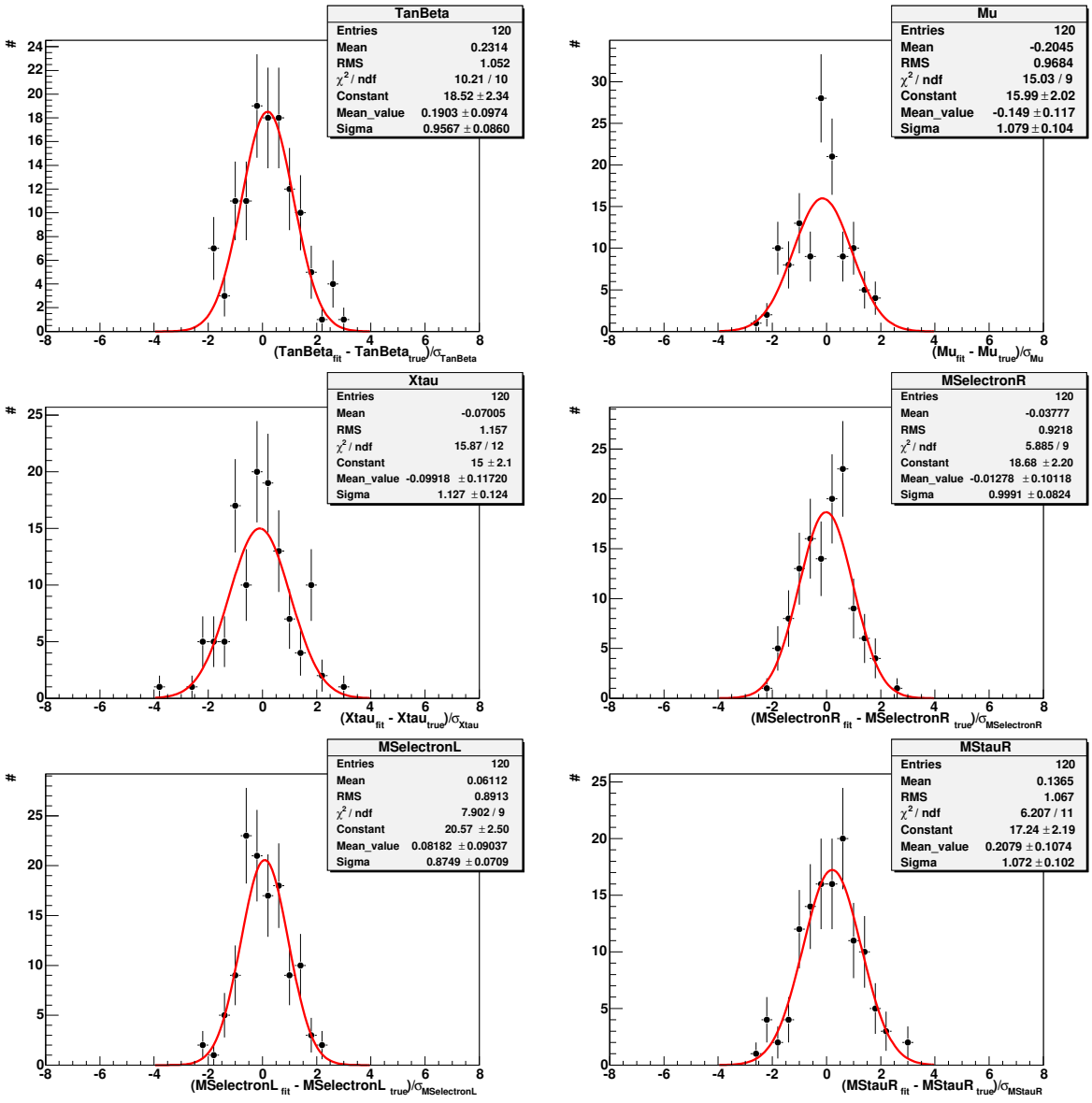

Figure 7.9: *Pull distributions of the parameters of the SPS1a fit for 120 independent fits with observables smeared within their uncertainties. The uncertainties of all parameters are well described.*

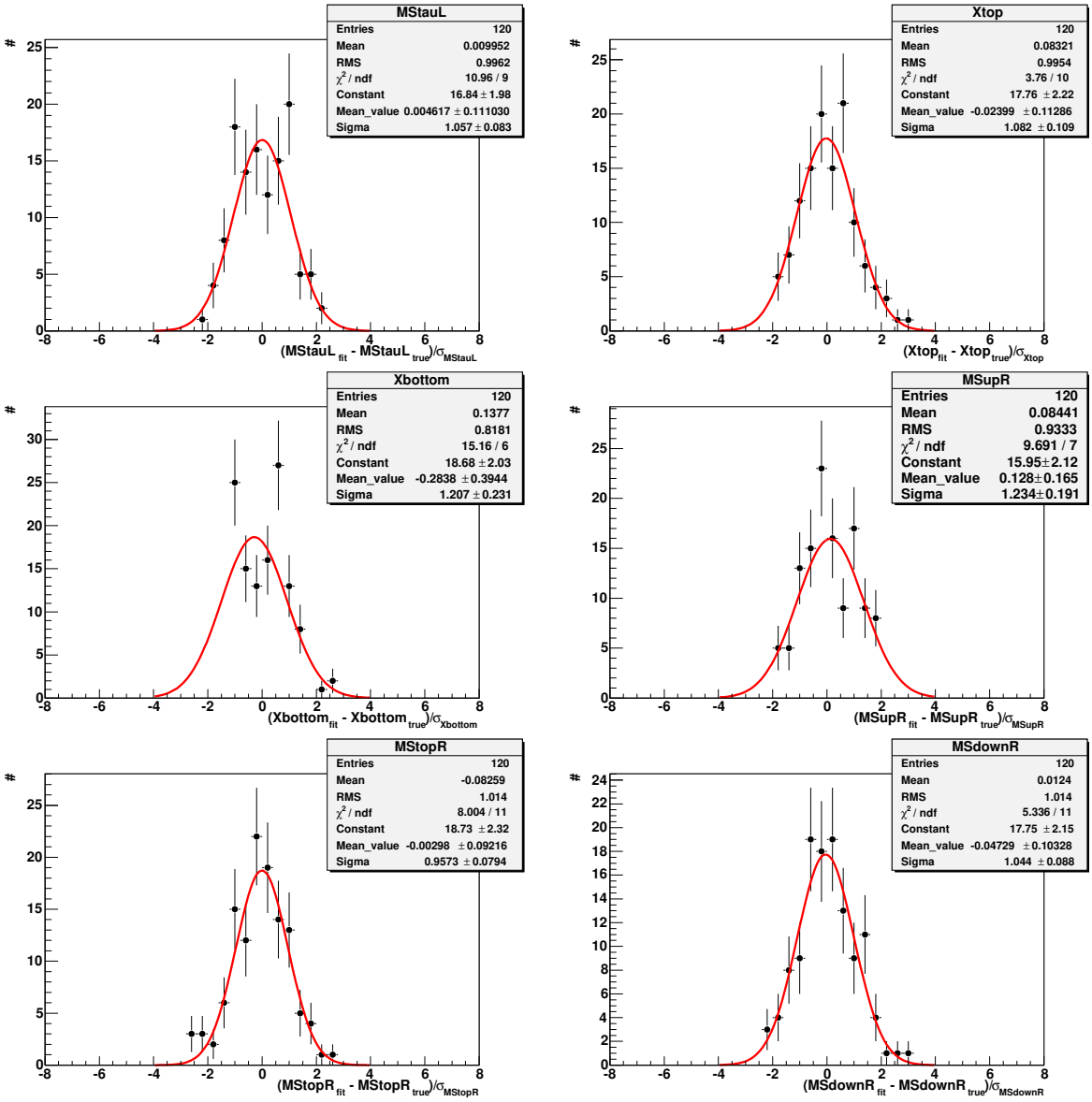

Figure 7.10: *Pull distributions of the parameters of the SPS1a fit for 120 independent fits with observables smeared within their uncertainties. The uncertainties of all parameters are well described, apart from* X_{bottom}.

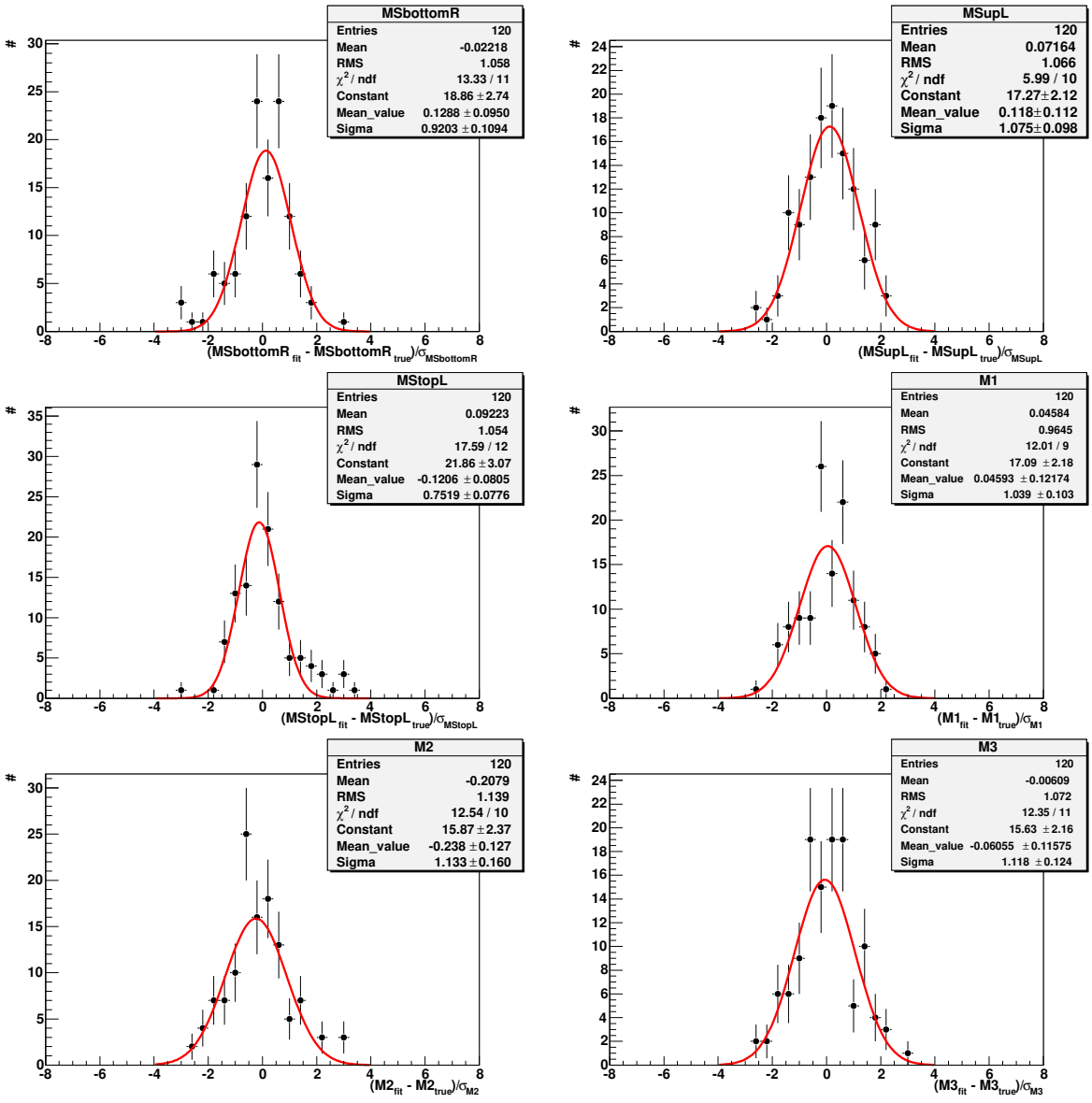

Figure 7.11: *Pull distributions of the parameters of the SPS1a fit for 120 independent fits with observables smeared within their uncertainties. The uncertainties of all parameters are well described.*

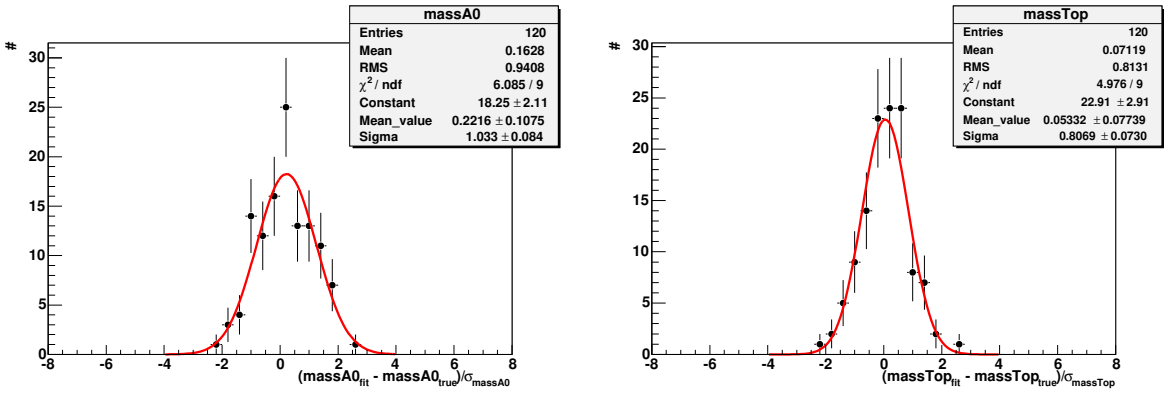

Figure 7.12: *Pull distributions of the parameters of the SPS1a fit for 120 independent fits with observables smeared within their uncertainties. The uncertainties of all parameters are well described.*

Observable Importance Determination

The technique of determining the parameters of the MSSM simultaneously in a global fit to all observables has the disadvantage that it is not directly obvious which observables influence the determination of which parameter. Thus also the reasons for parameter correlations are not directly visible.

This disadvantage can be resolved by determining the contribution of each observable to the value $\Delta\chi^2 = \chi^2_{1\sigma} - \chi^2_{\text{min}}$. Here χ^2_{min} is the minimal χ^2 of the fit and $\chi^2_{1\sigma}$ is the χ^2 for the variation of one parameter by plus or minus $1\,\sigma$. The higher the total $\Delta\chi^2_i$ for the variation of parameter P_i is, the larger is the total correlation of the parameter with other parameters. And the higher the individual contribution $\Delta\chi^2_{i,j}$ of the observable O_j with respect to all other observables is, the higher is the importance of the observable O_j for the determination of parameter P_i.

The individual $\Delta\chi^2$ are evaluated in the following way after the SPS1a fit has been performed:

1. The χ^2_{min} for the central value of the fitted parameters is calculated.

2. Each parameter is first changed by $+1\,\sigma$ and then by $-1\,\sigma$ with respect to its central value. All other parameters are kept at their central values. For each parameter variation, the total $\Delta\chi^2_i$ of the parameter P_i and the individual $\Delta\chi^2_{i,j}$ from each observable O_j is determined.

3. The average of the $\Delta\chi^2$ contributions from the variation of each parameter by $+1\,\sigma$ and $-1\,\sigma$ is taken as final value. Since for variations from the central value of the fitted parameters all $\Delta\chi^2$ have to be positive, no cancellation between the $\Delta\chi^2$ values from $+1\,\sigma$ and $-1\,\sigma$ variations can occur.

The results of this determination of the importance of the individual observables is listed in Tab. 7.4. As visible from the total $\Delta\chi^2$, there are parameters with very small correlations to other parameters, such as m_{A} or M_3, which have a total $\Delta\chi^2$ very close to 1. Other parameters are highly correlated, such as $M_{\tilde{\text{e}}_R}$ or $M_{\tilde{\text{u}}_R}$. Since their correlation is so large, the total $\Delta\chi^2$ is very large in case that just one of the correlated parameters is varied and none of the other parameters.

Table 7.3: *Scaling factors of the uncertainties obtained from the pull distributions. Each scaling factor is compatible with 1, showing that the uncertainty determination in the SPS1a fit is correct. For X_{bottom}, the distorted pull distribution has to be taken into account.*

Parameter	Uncertainty scaling factor
$\tan\beta$	0.956
μ	1.079
X_τ	1.126
$M_{\tilde{e}_R}$	0.999
$M_{\tilde{\tau}_R}$	1.071
$M_{\tilde{e}_L}$	0.874
$M_{\tilde{\tau}_L}$	1.056
X_{top}	1.081
X_{bottom}	1.206
$M_{\tilde{d}_R}$	1.044
$M_{\tilde{b}_R}$	0.920
$M_{\tilde{u}_R}$	1.233
$M_{\tilde{t}_R}$	0.957
$M_{\tilde{u}_L}$	1.074
$M_{\tilde{t}_L}$	0.751
M_1	1.038
M_2	1.133
M_3	1.118
m_{A}	1.033
m_{top}	0.806

It can also be noted that some parameters are almost solely determined by one measurement alone. This is the case for M_1, which is almost solely determined by $m_{\chi_1^0}$. However, this does not mean that there are no correlations of this parameter with other parameters. Other parameters like m_{A}, μ or $\tan\beta$ are almost equally determined by several observables. However, each of those observables is important, since leaving out one of those observables can have strong impacts on how the correlations are resolved.

It is interesting to note that some of the parameters of one SUSY sector are determined mostly by observables from another SUSY sector. This is the case for some of the squark mass parameters, which are most strongly constrained by measurements of slepton masses at the LC. The reason for this is the large precision of the slepton mass observables at the LC compared with the relatively large uncertainty of the squark masses in combined LHC and LC analyses (see Tab. 7.1).

Tab. 7.4 also shows the importance of the coupling measurements. In this fit they are mostly taken from cross-section measurements at various $\sqrt{s}$ and beam polarisations. Different polarisations are essential to disentangle the mixing in the chargino sector and thus to determine the very important parameters $\tan\beta$ and μ, which influence almost every sector of the theory. Other sources of coupling measurements could be branching ratio measurements or ratios of branching ratios at LHC and LC.

Table 7.4: *Individual $\Delta\chi^2$ contributions in the Fittino SPS1a fit. In the first column the parameter and its fitted value is shown. The second column shows the total $\Delta\chi^2$ for this parameter, if the parameter is varied by $1\,\sigma$. The third and fourth column show the parameters and their contribution to the $\Delta\chi^2$ of the parameter in per cent.*

Parameter Value	Total $\Delta\chi^2$	Observable	Contribution to the $\Delta\chi^2$ in %
$\tan\beta$	9.62	$m_{\chi_2^0}$	28
10.0 ± 0.33		$\sigma(\mathrm{e^+e^-}_{\mathrm{LR}} \to \chi_2^0\chi_2^0)$ 400 *GeV*	19
		$\sigma(\mathrm{e^+e^-}_{\mathrm{LR}} \to \chi_1^+\chi_1^-)$ 400 *GeV*	13
		$m_{\chi_1^0}$	8.8
		$\sigma(\mathrm{e^+e^-}_{\mathrm{RL}} \to \chi_1^0\chi_2^0)$ 500 *GeV*	7.2
μ	5.18	$\sigma(\mathrm{e^+e^-}_{\mathrm{LR}} \to \chi_1^+\chi_2^-)$ 1 *TeV*	25
358.6 ± 1.14		$m_{\chi_2^0}$	23
		$\sigma(\mathrm{e^+e^-}_{\mathrm{LR}} \to \chi_1^+\chi_1^-)$ 400 *GeV*	10
		$\sigma(\mathrm{e^+e^-}_{\mathrm{RL}} \to \chi_1^0\chi_2^0)$ 500 *GeV*	9.5
		$\sigma(\mathrm{e^+e^-}_{\mathrm{LR}} \to \chi_2^0\chi_2^0)$ 400 *GeV*	8.9
$X_{\tilde\tau}$	5.30	$m_{\tilde\tau_1}$	60
-3837.2 ± 131.6		$\sigma(\mathrm{e^+e^-}_{LR} \to \tilde\tau_1\bar{\tilde\tau}_1)$ 500 *GeV*	32
		$\sigma(\mathrm{e^+e^-}_{RR} \to \tilde\tau_1\bar{\tilde\tau}_1)$ 500 *GeV*	5.7
		$m_{\tilde\tau_2}$	1.0
		$\sigma(\mathrm{e^+e^-}_{RL} \to \tilde\tau_1\bar{\tilde\tau}_1)$ 500 *GeV*	0.6
$M_{\tilde{\mathrm{e}}_R}$	61.93	$m_{\tilde{\mathrm{e}}_R}$	87
135.76 ± 0.39		$m_{\tilde\mu_R}$	5.5
		$\sigma(\mathrm{e^+e^-}_{RL} \to \tilde{\mathrm{e}}_L\bar{\tilde{\mathrm{e}}}_L)$ 400 *GeV*	1.5
		$\sigma(\mathrm{e^+e^-}_{RL} \to \tilde\mu_L\bar{\tilde\mu}_L)$ 400 *GeV*	1.4
		$\sigma(\mathrm{e^+e^-}_{LR} \to \tilde{\mathrm{e}}_L\bar{\tilde{\mathrm{e}}}_L)$ 400 *GeV*	1.2
$M_{\tilde\tau_R}$	6.59	$m_{\tilde\tau_1}$	80
133.33 ± 0.75		$\sigma(\mathrm{e^+e^-}_{RL} \to \tilde\tau_1\bar{\tilde\tau}_1)$ 500 *GeV*	11
		$\sigma(\mathrm{e^+e^-}_{RR} \to \tilde\tau_1\bar{\tilde\tau}_1)$ 500 *GeV*	5.0
		$\sigma(\mathrm{e^+e^-}_{LR} \to \tilde\tau_1\bar{\tilde\tau}_1)$ 500 *GeV*	4.3
		$m_{\tilde{\mathrm{e}}_R}$	0.03
$M_{\tilde{\mathrm{e}}_L}$	2.11	$m_{\tilde{\mathrm{e}}_L}$	36
195.21 ± 0.19		$\sigma(\mathrm{e^+e^-}_{LR} \to \tilde{\mathrm{e}}_R\bar{\tilde{\mathrm{e}}}_R)$ 500 *GeV*	15
		$\sigma(\mathrm{e^+e^-}_{RR} \to \tilde{\mathrm{e}}_R\bar{\tilde{\mathrm{e}}}_R)$ 500 *GeV*	11
		$\sigma(\mathrm{e^+e^-}_{RL} \to \tilde\nu_{\mathrm{e}L}\bar{\tilde\nu}_{\mathrm{e}L})$ 500 *GeV*	7.8
		$\sigma(\mathrm{e^+e^-}_{LR} \to \tilde\nu_{\mathrm{e}L}\bar{\tilde\nu}_{\mathrm{e}L})$ 500 *GeV*	7.5
$M_{\tilde\tau_L}$	1.39	$m_{\tilde\tau_2}$	59
194.39 ± 1.18		$\sigma(\mathrm{e^+e^-}_{LR} \to \tilde\tau_1\bar{\tilde\tau}_1)$ 500 *GeV*	24
		$m_{\tilde\tau_1}$	13
		$\sigma(\mathrm{e^+e^-}_{RR} \to \tilde\tau_1\bar{\tilde\tau}_1)$ 500 *GeV*	1.9
		$\sigma(\mathrm{e^+e^-}_{RL} \to \tilde\tau_1\bar{\tilde\tau}_1)$ 500 *GeV*	0.7
X_{top}	8.61	$m_{\tilde{\mathrm{t}}_1}$	86
-506.7 ± 29.5		m_{h}	11
		$\sigma(\mathrm{e^+e^-}_{LR} \to \mathrm{hZ})$ 500 *GeV*	0.5

continued on next page

continued from last page			
Parameter Value	Total $\Delta\chi^2$	Observable	Contribution to the $\Delta\chi^2$ in %
		$m_{\tilde{\mathrm{e}}_R}$	0.4
		$\sigma(\mathrm{e}^+\mathrm{e}^-{}_{RL} \to \mathrm{hZ})$ 500 GeV	0.4
X_{bottom}	1.26	$\mathrm{BR}(\mathrm{h} \to \mathrm{b\bar{b}})$	43
-4441 ± 1765		$\mathrm{BR}(\mathrm{h} \to \tau^+\tau^-)$	25
		$m_{\tilde{\mathrm{b}}_1}$	23
		$m_{\tilde{\mathrm{b}}_2}$	3.9
		$\mathrm{BR}(\mathrm{h} \to \mathrm{c\bar{c}})$	2.3
$M_{\tilde{\mathrm{d}}_R}$	10.2	$m_{\tilde{\mathrm{e}}_R}$	75
528.2 ± 17.7		$m_{\tilde{\mathrm{d}}_R}$	4.9
		$m_{\tilde{\mathrm{s}}_R}$	4.9
		$m_{\tilde{\mu}_R}$	4.7
		$m_{\tilde{\tau}_1}$	1.9
$M_{\tilde{\mathrm{b}}_R}$	1.54	$m_{\tilde{\mathrm{b}}_2}$	70
524.7 ± 7.7		$m_{\tilde{\mathrm{e}}_R}$	24
		$m_{\tilde{\mu}_R}$	1.5
		$m_{\tilde{\mathrm{b}}_1}$	1.4
		$m_{\tilde{\tau}_1}$	0.6
$M_{\tilde{\mathrm{u}}_R}$	44.8	$m_{\tilde{\mathrm{e}}_R}$	81
530.2 ± 19.2		$m_{\tilde{\mu}_R}$	5.0
		$m_{\tilde{\tau}_1}$	0.2
		$\sigma(\mathrm{e}^+\mathrm{e}^-{}_{LR} \to \tilde{\mathrm{e}}_L\bar{\tilde{\mathrm{e}}}_L)$ 400 GeV	0.1
		$m_{\tilde{\mathrm{c}}_R}$	0.1
$M_{\tilde{\mathrm{t}}_R}$	12.2	$m_{\tilde{\mathrm{t}}_1}$	80
424.4 ± 8.5		$m_{\tilde{\mathrm{e}}_R}$	16
		$m_{\tilde{\mu}_R}$	1.0
		$m_{\tilde{\tau}_1}$	0.4
		$\sigma(\mathrm{e}^+\mathrm{e}^-{}_{LR} \to \tilde{\mathrm{e}}_L\bar{\tilde{\mathrm{e}}}_L)$ 400 GeV	0.2
$M_{\tilde{\mathrm{u}}_L}$	2.01	$m_{\tilde{\mathrm{e}}_R}$	31
548.7 ± 5.2		$m_{\tilde{\mathrm{u}}_L}$	13
		$m_{\tilde{\mathrm{c}}_L}$	1.3
		$m_{\tilde{\mathrm{d}}_L}$	1.2
		$m_{\tilde{\mathrm{s}}_L}$	1.2
$M_{\tilde{\mathrm{t}}_L}$	4.30	$m_{\tilde{\mathrm{t}}_1}$	46
500.0 ± 8.06		$m_{\tilde{\mathrm{b}}_1}$	32
		$m_{\tilde{\mathrm{e}}_R}$	8.8
		$m_{\chi_2^0}$	4.3
		$\sigma(\mathrm{e}^+\mathrm{e}^-{}_{\mathrm{LR}} \to \chi_1^+\chi_1^-)$ 400 GeV	2.6
M_1	1.57	$m_{\chi_1^0}$	97
101.809 ± 0.065		$\sigma(\mathrm{e}^+\mathrm{e}^-{}_{RL} \to \tilde{\mathrm{e}}_L\bar{\tilde{\mathrm{e}}}_L)$ 400 GeV	0.7
		$\sigma(\mathrm{e}^+\mathrm{e}^-{}_{LL} \to \tilde{\mathrm{e}}_L\bar{\tilde{\mathrm{e}}}_L)$ 500 GeV	0.5
		$\sigma(\mathrm{e}^+\mathrm{e}^-{}_{RL} \to \tilde{\mathrm{e}}_L\bar{\tilde{\mathrm{e}}}_L)$ 500 GeV	0.5
		$\sigma(\mathrm{e}^+\mathrm{e}^-{}_{\mathrm{RL}} \to \chi_1^0\chi_2^0)$ 400 GeV	0.5
M_2	3.23	$m_{\chi_2^0}$	45
continued on next page			

continued from last page			
Parameter Value	Total $\Delta\chi^2$	Observable	Contribution to the $\Delta\chi^2$ in %
191.76 ± 0.11		$\sigma(e^+e^-_{LR} \to \chi_2^0\chi_2^0)$ 400 *GeV*	26
		$\sigma(e^+e^-_{LR} \to \chi_2^+\chi_2^-)$ 400 *GeV*	17
		$\sigma(e^+e^-_{RL} \to \chi_2^+\chi_2^-)$ 400 *GeV*	1.5
		$\sigma(e^+e^-_{RR} \to \chi_2^+\chi_2^-)$ 500 *GeV*	1.4
M_3	1.16	$m_{\tilde{g}}$	91
588.8 ± 7.9		$m_{\tilde{t}_1}$	6.1
		$m_{\tilde{b}_1}$	0.7
		$m_{\tilde{b}_2}$	0.6
		$m_{\tilde{d}_L}$	0.2
m_A	1.02	$m_{H^\pm}$	40
399.77 ± 0.72		m_A	30
		m_H	30
		$m_{\tilde{e}_R}$	0.01
		$m_{\tilde{\mu}_R}$	0.001
m_{top}	1.44	m_{top}	92
174.3 ± 0.35		m_h	6.2
		$\sigma(e^+e^-_{RL} \to hZ)$ 500 *GeV*	0.4
		$\sigma(e^+e^-_{LR} \to hZ)$ 500 *GeV*	0.2
		$m_{\tilde{t}_1}$	0.02

7.4.4 Fits in Subspaces of the Parameter Space

In Section 7.4.3 it is shown that a global fit to the MSSM parameters in the SPS1a benchmark point is possible and that all parameters can be determined correctly with all their correlations. However, it might be interesting to study also the possibility to extract limited information on the SUSY parameters in a certain sector only, for example if just the information of either LHC or the LC should be used.

In this section a fit of the gaugino sector of the MSSM using primarily data from the LC is examined. However, with fixed parameters in the other sectors, such a fit will not yield the full uncertainties of the fitted parameters. The fit has been performed using the following observables from Tab. 7.1:

- All SM observables.
- All mass measurements at the 500 GeV LC in the gaugino sector, plus the measurement of $m_{\tilde{e}_{L,R}}$.
- All chargino, neutralino and $\tilde{e}$ cross-sections at $\sqrt{s} = 400$ GeV and $\sqrt{s} = 500$ GeV.
- In order to have a complete coverage of the gaugino sector, the measurement of $m_{\tilde{g}}$ at the LHC is included. It has hardly any effect on the gaugino parameters apart from M_3.

The fixed and fitted parameters are listed in Tab. 7.5. The fit is performed once for all fixed parameters at their correct values. The central values of the fitted parameters exactly reproduce the $SPS1a_{mod}$ input parameters. The uncertainties, due to the reduced correlations and the reduced number of observables, are in the same order of magnitude as in Tab. 7.2.

Another fit of the same parameters to the same observables is performed for different values of the fixed parameters. An arbitrary but realistic choice of the parameters of the

Table 7.5: *Fittino fit of a subspace of SPS1a. This fit shows that assuming parameters of one sector and fitting the parameters of another sector can lead to distortions in the spectrum, which can not be detected by a bad χ^2 value of the fit.*

Parameter	$\text{SPS1a}_{\text{mod}}$ value	Fit with correct fixed parameters	Fit with incorrect fixed parameters	Uncertainty
Fixed parameters				
X_τ	-3837.23 GeV	-3837.23 GeV	-3000 GeV	fixed
$M_{\tilde{\tau}_R}$	133.33 GeV	133.33 GeV	200 GeV	fixed
$M_{\tilde{\tau}_L}$	194.39 GeV	194.39 GeV	250 GeV	fixed
X_{top}	-506.388 GeV	-506.388 GeV	-600 GeV	fixed
X_{bottom}	-4441.0 GeV	-4441.0 GeV	-2000 GeV	fixed
$M_{\tilde{d}_R}$	528.14 GeV	528.14 GeV	600 GeV	fixed
$M_{\tilde{b}_R}$	524.718 GeV	524.718 GeV	600 GeV	fixed
$M_{\tilde{u}_R}$	530.253 GeV	530.253 GeV	600 GeV	fixed
$M_{\tilde{t}_R}$	424.382 GeV	424.382 GeV	500 GeV	fixed
$M_{\tilde{u}_L}$	548.705 GeV	548.705 GeV	600 GeV	fixed
$M_{\tilde{t}_L}$	499.972 GeV	499.972 GeV	600 GeV	fixed
m_{A}	399.767 GeV	399.767 GeV	399.767 GeV	fixed
m_{top}	174.3 GeV	174.3 GeV	174.3 GeV	fixed
Fitted parameters				
$\tan\beta$	10.0	10.0	9.15	0.50
μ	358.64 GeV	358.6 GeV	360.4 GeV	2.0 GeV
M_1	101.809 GeV	101.81 GeV	101.70 GeV	0.070 GeV
M_2	191.756 GeV	191.76 GeV	191.17 GeV	0.16 GeV
M_3	588.797 GeV	588.8 GeV	570.1 GeV	7.6 GeV
$M_{\tilde{e}_R}$	135.76 GeV	135.76 GeV	135.74 GeV	0.054 GeV
$M_{\tilde{e}_L}$	195.21 GeV	195.21 GeV	195.31 GeV	0.15 GeV
χ^2		0.12×10^{-4}	3.03	

squark sector and the third generation slepton sector is given in Tab. 7.5. The values chosen are realistic estimates in a situation where the squark sector parameters are not measured precisely. As visible in Tab. 7.5, in this case the fitted parameters of the gaugino sector are off by 1 to $4\,\sigma$. The χ^2 of this fit anyhow differs by only 3 from the χ^2 of the fit for the SPS1a values of the fixed parameters. In this fit with 41 d.o.f. this difference would not allow to discard the fit result.

This test shows that fitting just subsets of the parameter space can lead to results in the correct order of magnitude. Therefore this method is justified in the presence of large experimental errors. However it is dangerous if no reliable information on the other SUSY sectors is available and experimental precision is high. Such a problem automatically occurs if the full loop-level information is taken into account. Such a fit of a subset of the parameter space can give valuable information for the determination of the starting values of a global fit. A reliable parameter determination in the presence of very high experimental accuracy however can only be made in the global fit, as this example shows.

Compared with existing parameter determinations using tree-level relations [167], the uncertainties obtained in this fit of the gaugino sector are small, due to the large number of

Table 7.6: *Fitted values of the high-scale parameters at* Λ_{GUT}.

Parameter	SPS1a value	Fitted value
$\tan\beta$	10	10.0 ± 0.4
A_0	-100 GeV	-100.18 ± 16.2
M_0	100 GeV	100 ± 0.19
$M_{1/2}$	250 GeV	250 ± 0.29

cross-section measurements used for the fit.

7.5 Evolution to the SUSY Breaking Scale

Using the results of the fit of the low-energy MSSM parameters in Section 7.4.3, an attempt to obtain the high-scale parameters at the GUT scale can be made. Two possible approaches can be used. Either, the GUT-scale parameters of a certain breaking scenario are fitted to the low energy parameters obtained in the fit of Tab. 7.2 or directly to the observables of Tab. 7.1. This is called top-down approach. The other possibility is to extrapolate the fitted low energy parameters of Tab. 7.2 using renormalisation-group equations (RGE) from the scale Λ_{MSSM} where they are determined, to the scale Λ_{GUT}. This is called bottom-up approach.

With the results of the SPS1a fit, both approaches are pursued [174]. The results of the top-down fit of the mSUGRA parameters $\tan\beta, A_0, M_0$ and $M_{1/2}$ to the low-energy parameters is shown in Figs. 7.13 (a) and (b). In this case identical results are obtained for a fit to the observables as well as for a fit to the low-energy-parameters. The plots show the two-dimensional uncertainty contours of the parameters $\tan\beta$ and A_0 in (a) and of M_0 and $M_{1/2}$ in (b). The high-scale parameter values of the SPS1a scenario as given in Section 7.4.1 are reproduced. The fitted values of the high scale parameters and their uncertainties are given in Tab. 7.6. The small deviations of the central values from the SPS1a values are due to the fact that the point $\mathrm{SPS1a_{mod}}$, slightly different from SPS1a, is fitted.

The results of the bottom-up approach are shown in Figs. 7.13 (c), (d) and (e). In (c), the unification of the gaugino mass parameters M_1, M_2 and M_3 at the scale Λ_{GUT} of 3×10^{16} GeV is shown. Their evolution is given in terms of the inverse of the mass parameters. As expected from a realistic SUSY scenario, the unification is realized at the inverse of the common fermion mass scale $M_{1/2} = 250$ GeV. Fig. 7.13 (d) shows the evolution of the mass parameters of the first and second generation and the mass parameter M_{H_1} of the first Higgs doublet (see (2.45)). The scalar mass parameters of the down-type righthanded squarks M_{D_1}, the lefthanded squark doublets M_{Q_1}, the up-type righthanded squarks M_{U_1}, the righthanded sleptons M_{E_1} and the lefthanded slepton doublets M_{L_1} unite at the scale Λ_{GUT} at the value of M_0. The uncertainty in the trilinear couplings, which effect the Higgs mass parameter M_{H_1}, causes a rather large uncertainty in this parameter with respect to the other parameters. In Fig. 7.13 (e) the same RGE evolution with the parameters of the third sparticle generation and the second Higgs mass parameter is shown. The uncertainties are larger than in case of the second generation, mainly because of the increased impact of the trilinear couplings, which have large uncertainties.

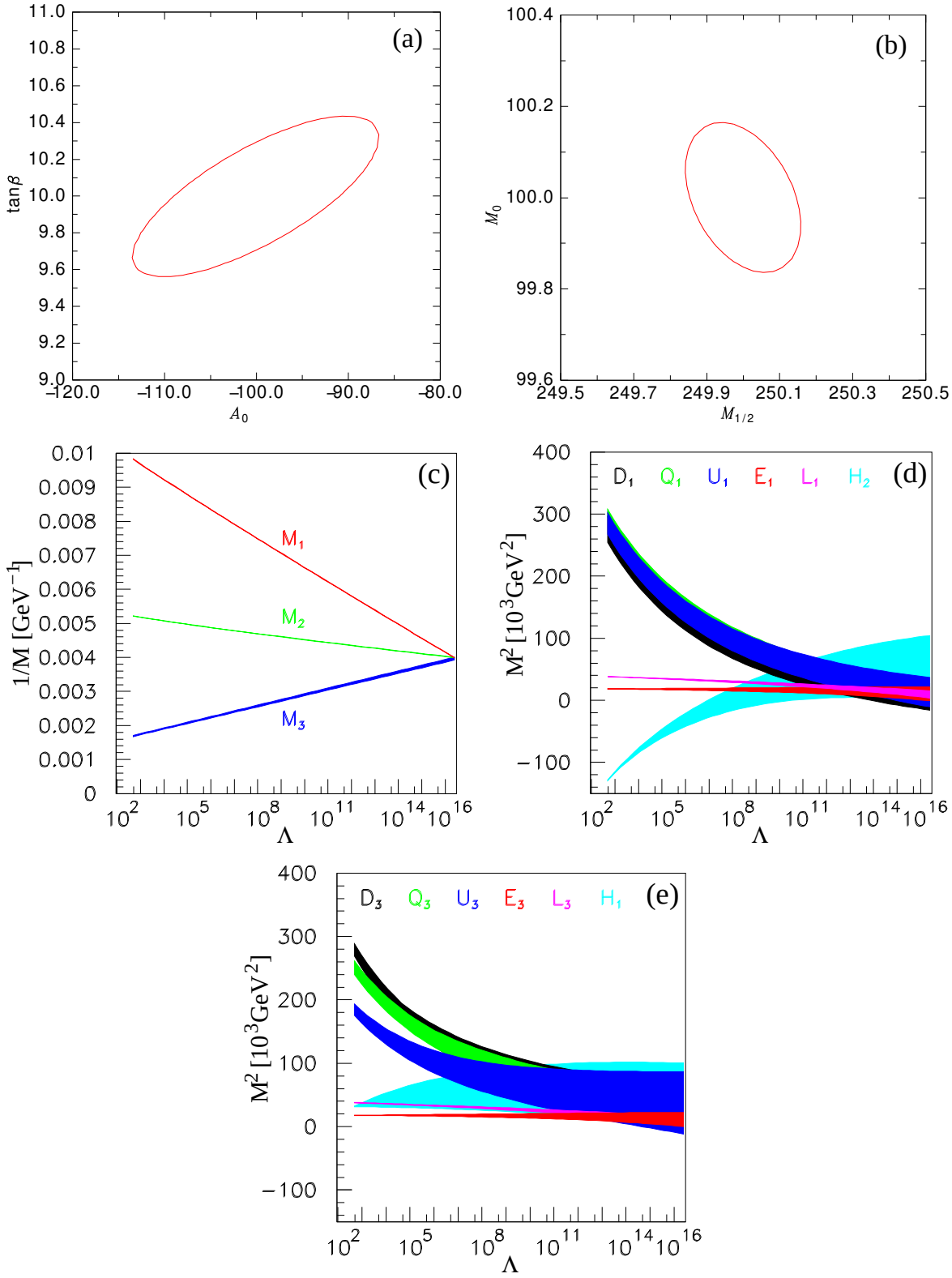

Figure 7.13: *Determination of the mSUGRA parameters, using the results of the MSSM parameter fit from Tab. 7.2. In (a) and (b), the two-dimensional uncertainty contours of the results of a top-down fit of the mSUGRA parameters is shown. (c), (d) and (e) present the evolution of the MSSM parameters to* Λ_{GUT} *[174].*

7.6 Summary

Fittino is a program to determine the soft SUSY breaking parameters from a fit to measurements at future colliders, such as the LHC and a future Linear Collider. Global fits or fits in parts of the parameter space can be performed with any combination of parameters and observables. No prior knowledge of any of the parameters is needed, but can be used if desired. To get reasonable start values for the fit, tree-level formulae are used to relate the observables to the SUSY parameters.

Fittino allows to test the fit result in various ways. The contribution of the individual observables to the variation of the χ^2 can be used to examine the importance of the individual observables for the constraint of a given parameter. Pull distributions can be automatically made, allowing an independent test of the parameter uncertainties and central values. Two-dimensional uncertainty contours show correlations of any parameter combination.

First results obtained with Fittino clearly reveal the benefit from combining the LHC and LC results. The comprehensive SUSY particle spectrum accessible at LHC is needed to converge to all input parameters of the SUSY spectrum. On the other hand, the precise measurements of the light SUSY particles at a Linear Collider and the precise information on the coupling and mixing, which is obtained using cross-section measurements at various centre-of-mass energies and polarisations, are crucial to constrain the parameter space. Without the information from the LC, due to non-linearities in the dependence between observables and parameters the parameter space is too free to perform a successful analysis of the uncertainties of the parameters, thus no information on the precision of the parameters and their correlations is obtained. Also no successful test of the fit results using pull distribution calculations can be made. Thus the complementary nature of the measurements at LHC and the LC is obvious from this study. It shows the great value of the LHC as a discovery machine and the importance of the LC for any precise SUSY parameter analysis.

As a result of the SPS1a fit, most parameters are determined with a very good precision of more than 4 %. However, more experimental information on the slepton and squark mixing in the third generation would be beneficial. Measurements of τ polarisation from $\tilde{\tau}$ decays would improve the determination of X_τ.

Attempts to fit only individual sectors of the theory, using the results of only one of the future colliders, are difficult at the high-precision level. Wrong assumptions on yet unmeasured parameters in one sector of the SUSY parameter space can influence the best fit results in the other sector via loop-level effects. The χ^2 of the fit can not always be used to detect such wrong assumptions. Therefore this study shows clearly that a global fit of the SUSY parameters is necessary to determine all parameters bias-free and with their full uncertainties.

The results obtained with Fittino on the low-energy parameters of the SUSY theory and their uncertainties and correlations can be evolved to the GUT scale using RGE techniques, assuming different breaking scenarios. The requirement of convergence of the couplings and parameters can be used to distinguish the breaking scenarios. The results of the fit of the mSUGRA parameters at the scale Λ_{GUT} to the low energy parameters at Λ_{MSSM} shows that the high scale parameters can be determined with good precision and that the consistency of different breaking scenarios with the low energy parameters can be tested.

In the future, Fittino can be used for systematical studies of the dependence on measurement uncertainties. The most crucial observables for the parameter determination can be identified and the detector and machine, especially the distribution of the luminosities with different centre-of-mass energies and beam polarisations, can be optimised for most precise parameter measurements. Also different sets of SUSY parameters and their phenomenology can be studied. The influence of theoretical uncertainties can be determined and regions with need for improvement can be identified. Also other theoretical tools should be interfaced with Fittino, such as more complete treatments of the Higgs sector as in FEYNHIGGS [54, 146].

Chapter 8

Summary and Conclusions

In this thesis the search for Higgs bosons in the context of the Minimal Supersymmetric Standard Model (MSSM), the interpretation of Higgs searches in the CP-conserving and, for the first time experimentally at LEP, the CP-violating MSSM is performed. A program for the MSSM parameter determination at future experiments is presented.

The data used for the topological search for the Higgs boson production process $e^+e^- \to \mathcal{H}_1\mathcal{H}_2 \to b\bar{b}b\bar{b}$, where $\mathcal{H}_1$ and $\mathcal{H}_2$ are two neutral Higgs boson mass eigenstates in the MSSM, decaying each into a pair of b quarks, is collected at centre-of-mass energies $\sqrt{s} = 192 - 209$ GeV using the OPAL detector at the LEP storage ring at CERN in the years 1999 and 2000. For the selection of candidates, a likelihood analysis has been used. Two different kinematical regimes are covered with differently optimised selections. Advanced tools for the statistical interpretation of the result and the use of the reconstructed masses of the candidates are used and developed. No statistically significant signal of Higgs boson production has been found. Therefore limits in a model-independent framework and in the MSSM are deduced.

The searches for neutral Higgs bosons used in this thesis for the interpretation in the MSSM are based on all data collected by the OPAL experiment, at energies in the vicinity of the Z resonance (LEP 1 phase) and between 130 and 209 GeV (LEP 2 phase). The corresponding integrated luminosities are of about $720\,\mathrm{pb}^{-1}$. The searches addressing the Higgsstrahlung process $e^+e^- \to \mathcal{H}Z$ and those for the pair production process $e^+e^- \to \mathcal{H}_1\mathcal{H}_2$ are statistically combined. None of these searches reveals a significant excess of events beyond the predicted background level, which would indicate the production of Higgs bosons.

From these results, model-independent limits are derived for the cross-section of a number of event topologies that could be associated to Higgs boson pair production. These limits cover a wide range of Higgs boson masses and are typically much lower than the largest cross-sections predicted by the MSSM.

The search results are also used to test a number of "benchmark scenarios" of the MSSM, with and without the inclusion of CP-violating effects.

In the CP-conserving case, new benchmark situations are investigated as compared to earlier publications. These are motivated either by new measurements of the b→sγ branching ratio and the muon anomalous magnetic moment $(g-2)_\mu$, or in anticipation of the forthcoming searches at the proton-proton collider LHC. In all these scenarios the searches conducted by OPAL exclude sizeable domains of the MSSM parameter space, even in those situations where the sensitivity of the LHC experiments is expected to be low. An overview of the results is given in Table 6.6. In the "m_h-max" scenario which, among all scenarios predicts the widest range of m_h values, the following limits can be set at the 95% confidence level: $m_\mathrm{h} > 84.5$ GeV and $m_\mathrm{A} > 85.0$ GeV; furthermore, if the top quark mass is fixed at the current experimental value of 174.3 GeV, the range $0.7 < \tan\beta < 1.9$ GeV can be excluded. However, this range

shrinks for higher values of m_{top}. For $m_{\text{top}} > 179.5$ GeV, no limit can be set on $\tan\beta$. This strengthens the need for a very precise determination of the top quark mass and potentially opens new $\tan\beta$ regimes for Higgs and sparticle searches at the Large Hadron Collider.

For the first time, a number of CP-violating MSSM scenarios are studied experimentally, where the CP-violating effects are introduced in the Higgs potential by radiative corrections. The "CPX" benchmark scenario is designed to maximise the phenomenological differences in the Higgs sector with respect to the CP-conserving scenarios. In this case the region $\tan\beta < 2.8$ is excluded at 95% confidence level but no universal limit is obtained for either of the Higgs boson masses. However, for $\tan\beta < 3.3$, the limit $m_{\text{H}_1} > 112$ GeV can be set for the mass of the lightest neutral Higgs boson of the model.

These results on Higgs searches at LEP will be improved by the statistical combination of the searches of the LEP experiments. The preliminary analysis of the LEP combination for the "CPX" scenario shows that the increase in sensitivity is large. However, also the LEP combination can set no absolute lower limit on the lightest Higgs boson mass. After the final analyses of the LEP data, the Tevatron experiments could contribute to the search for the MSSM Higgs bosons, preferably if it behaves similar to a Standard Model Higgs boson. If the MSSM is realized but if the Higgs boson is not found at the Tevatron, the the Large Hadron Collider will cover the complete parameter space of the CP-even MSSM and find at least one of the Higgs bosons. If more than one Higgs bosons is found, a very strong indication for the realization of Supersymmetry is found. However, also if only one Higgs boson can be found, the measurement of the Higgs boson mass and its couplings to the SM particles will provide a stringent test of the Standard Model and hence a possibility to discover physics beyond the Standard Model. Finally the Liner Collider will also find at least one of the MSSM Higgs bosons, provided they exist, and measure all its properties with unprecedented precision, allowing even more stringent tests of the Standard Model and possible extensions.

In this thesis, studies for the consistent determination of the parameters of the MSSM are presented, taking into account most of the potentially available observables at future colliders and the full correlations among the parameters as well as the most precise presently available predictions of MSSM observables. The results reveal that using measurements from the Large Hadron Collider LHC and the future Linear Collider LC a precise parameter determination without a priori assumptions on the parameter values is possible. For example, in a global fit the parameter $\tan\beta$ can be measured to a relative precision of 3 % for the SPS1a MSSM scenario. In this fit, the information from both the LHC and the LC is crucial. Without the mass information from almost the full MSSM spectrum in the combination of LHC and LC, the convergence to the exact parameter values proves to be difficult. On the other hand, without the very precise measurements of the sparticle masses and couplings from the LC the dependence of the observables from the parameters can not successfully be approximated linearly, thus no reliable determination of the parameter uncertainties and correlations is possible without the LC data.

In the future, the experimental studies missing to better constrain the set of MSSM parameters should be investigated. Especially, observables constraining the trilinear couplings more directly are needed. For example, the measurement of the polarisation of bottom quarks from sbottom decays should be included in order to improve the precision of X_{bottom}. Also blind tests of the fitting procedures can be performed, where the observables are fitted to a set of observables with hidden true values of the MSSM parameters, and the fit procedure should be tested over a large range of different MSSM scenario in order to test the reliability of the fit result for all possible scenarios.

Appendix A

Fittino Documentation

A.1 The MINUIT Fit Methods

The program MINUIT [166] is a tool to minimise functions. Additionally, it is able to determine the range of uncertainty of the parameters that have been adjusted to minimise the function. In the case of Fittino, MINUIT is used to minimise a function $\chi^2(P_i, O_j, \Delta O_j)$ of (variable) parameters P_i and fixed (measured) observables O_j with fixed uncertainties ΔO_j. The χ^2 is calculated as follows:

$$\chi^2 = \sum_{j=1}^{N}\sum_{k=1}^{N}(O_j^t(P_i) - O_j^m)V_{jk}^{-1}(O_k^t(P_i) - O_k^m) \tag{A.1}$$

for N observables. The matrix V_{jk} is the covariance matrix of the observables O_j. The χ^2 is a measure of the difference of the measured observables O_j^m with respect to the predicted observables $O_j^t(P_i)$, weighted with the inverse of the squared uncertainties. The theoretically predicted observables $O_j^t(P_i)$ are in general a function of all parameters P_i.

The MIGRAD minimisation method in MINUIT attempts to find the minimum of the χ^2 using a method based on the knowledge of the first derivatives of the χ^2 function $\partial\chi^2/\partial P_i$ and on the inverse of the second derivative matrix

$$H = \begin{pmatrix} \frac{\partial^2\chi^2}{\partial P_1 \partial P_1} & \cdots & \frac{\partial^2\chi^2}{\partial P_i \partial P_1} \\ \vdots & \ddots & \vdots \\ \frac{\partial^2\chi^2}{\partial P_1 \partial P_i} & \cdots & \frac{\partial^2\chi^2}{\partial P_i \partial P_i} \end{pmatrix}^{-1} \tag{A.2}$$

which is also called Hesse-matrix and which is identical to the covariance matrix V of the parameters P_i. At each step of the minimisation, the Hesse-matrix is calculated from finite differences at a given starting point. If it is positive definite, this is repeated using the minimum of the hyperbolic function described by the first derivatives and the second-derivative matrix as the next starting value.

As a by-product of this minimisation, the covariance matrix is known at each step. However, the parameter uncertainties of the covariance matrix are only realistic if the matrix is positive definite.

This method is fast and stable as long as the starting point of the minimisation is close enough to the true minimum, because in this case each physical problem can be approximated by a linear function of the parameters P_i. Therefore the initialisation of the MSSM parameters using tree-level functions is important.

Since the MSSM at loop-level is not a linear problem, a more precise determination of the parameter uncertainties is possible using the MINOS tool in MINUIT. It determines the asymmetric parameter uncertainties for each parameter by varying P_i. For each varied P_i the χ^2 is minimised with respect to all other $i-1$ parameters. This is repeated until the maximum possible variation of P_i is found, for which the deviation of the $\Delta\chi^2 = \chi^2 - \chi^2_{\text{min}}$ with respect to the minimal χ^2_{min} at the function minimum is $\Delta\chi^2 < 1$.

A.2 The Fittino Steering File

The fit program Fittino is controlled using an ASCII input file called `fittino.in`. The user can specify the observables, their values and uncertainties, their correlations, the fitted and fixed parameters and universalities among generations. Flags can be used to control the general behaviour of the fit program. A list of the available commands is given in Tab. A.1. In the following, the syntax of the commands is explained.

Keys The commands in this group act on the contents of the line after the key. Available keys are:

- `#`
  Comment line. Everything after `#` is ignored by Fittino.
- `nofit <observable> <value> +- <uncertainty>`
  This key can be used to specify observables which shall only be used in the step of the initialisation of parameters using tree-level relations. A typical example are the chargino mixing angles $\cos 2\phi_L$ and $\cos 2\phi_R$.

Observables The commands in this group specified the measured (or simulated) observables and their values and uncertainties. The following types of observables are available:

- `mass<name> <value> +- <uncertainty> [ +- <theo_uncertainty> ]`
  Specifies the mass of the particle `<name>`. All available particles are listed in Tab. A.2. If no uncertainty is given, the particle mass is not used in the χ^2 of the fit. If more than one uncertainty is given, the uncertainties are added in quadrature. This is useful in case large theoretical uncertainties on the predicted particle mass exist. For the time being it is assumed that treating the theoretical uncertainties as uncorrelated with the experimental error and assuming a Gaussian probability distribution is precise enough. No assumption on the probability distribution of the theoretical uncertainties is preferred on theoretical grounds.

  If no unit is given in `<value>` and `<uncertainty>`, they are assumed to be given in GeV. Other supported units range from eV to PeV.
- `edge <alias> <type> <mass1> <mass2> [more masses] <value> +- <uncertainties>`
  Specifies the edge in a mass spectrum. Since SUSY particles tend to decay in cascade decays, the masses of intermediate particles can often be reconstructed from edges in mass spectra. If the edges are transformed into masses before the fit is made, the correlations among the reconstructed masses from one spectrum have to be specified using `correlationCoefficient`. The command `edge` offers the more simple and straightforward possibility to use the edge positions in the mass spectra directly in the fit. Momentarily, the following types `<type>` are available:
  1 `<mass1>+<mass2>`
  2 `|<mass1>-<mass2>|`
  The list of formulas can be easily extended.
- `sigma ( <initial_state> -> <final_state_particles>,<Ecms>,<polarisation1>, <polarisation2>) <value> +- <uncertainties> alias <alias>`
  Specifies the cross section of a given process `<initial_state> -> <final_state_particles>`, where `<final_state_particles>` is a list of particle

Table A.1: *Commands in the Fittino steering file* `fittino.in`*. The full form of the commands is given in the text. The correlations must be specified after all observables.*

Command	Explanation
Keys before any line	
`#`	Comment line
`nofit`	The observable after `nofit` is not used in the fit
Observables	
`mass<name>`	Mass of the particle `<name>`, see Tab. A.2
`edge`	Position of an edge in a mass spectrum
`sigma`	cross section of a process in e^+e^- collisions
`BR`	Branching ratio
`width`	Total width of a particle
`limit`	Limits on particle masses
`sin2thetaW`	The value of $\sin^2\theta_W$
`cos2phiL`	The value of $\cos 2\phi_L$
`cos2phiR`	The value of $\cos 2\phi_R$
Correlations	
`correlationCoefficient`	Correlation coefficient of two observables
Parameters	
`fitParameter`	Name and eventually value of a fitted parameter
`fixParameter`	Name and value of a fixed parameter
`universality`	Specifies which two parameters are unified
Flags	
`OneLoopCorrections`	Use full SPHENO loop corrections
`ISR`	Switch on ISR
`UseGivenStartValues`	Start from parameter values in `fitParameter`
`FitAllDirectly`	Fit all parameters at once
`CalcPullDist`	Calculate pull distributions
`CalcIndChisqContr`	Calculate individual $\Delta\chi^2$ contributions
`BoundsOnX`	Set bounds on X_τ, X_{top} and X_{bottom}
`ScanX`	Scan X_{top} and X_{bottom} before fitting
`SepFitTanbX`	Perform separate fit of $\tan\beta$, $M_{\tilde{t}_R}$, $M_{\tilde{t}_L}$, X_{top} and X_{bottom}
`Generator`	Use generator `Generator`
`UseMinos`	Use Minos error calculation
`UseHesse`	Use Hesse error matrix calculation
`NumberOfMinimizations`	Number of minimisation steps
`ErrDef`	The error definition used in Minos
`NumberPulls`	Number of pull fits

Table A.2: *Particles known to Fittino. The following particles can be used after* `mass`, `sigma`, `BR` *and* `width`. *Antiparticles are identified by* `~` *after the particle name.*

Particle Name	Explanation	Particle Name	Explanation
`W`	W boson	`SelectronL`	$\tilde{\mathrm{e}}_L$ selectron
`Z`	Z boson	`SelectronR`	$\tilde{\mathrm{e}}_R$ selectron
`gamma`	γ	`SnueL`	$\tilde{\nu}_{\mathrm{e}_L}$ electron sneutrino
`gluon`	gluon	`SmuL`	$\tilde{\mu}_L$ smuon
`Up`	u quark	`SmuR`	$\tilde{\mu}_R$ smuon
`Down`	d quark	`SnumuL`	$\tilde{\nu}_{\mu_L}$ muon sneutrino
`Charm`	c quark	`Stau1`	$\tilde{\tau}_L$ stau
`Strange`	s quark	`Stau2`	$\tilde{\tau}_R$ stau
`Top`	t quark	`Snutau1`	$\tilde{\nu}_{\tau_1}$ tau sneutrino
`Bottom`	b quark	`Gluino`	$\tilde{\mathrm{g}}$ gluino
`Electron`	electron	`Neutralino1`	χ_1^0 neutralino
`Nue`	electron neutrino ν_{e}	`Neutralino2`	χ_2^0 neutralino
`Mu`	muon	`Neutralino3`	χ_3^0 neutralino
`Numu`	muon neutrino ν_μ	`Neutralino4`	χ_4^0 neutralino
`Tau`	tau	`Chargino1`	χ_1^+ chargino
`Nutau`	tau neutrino ν_τ	`Chargino2`	χ_2^+ chargino
`h0`	h CP-even Higgs boson		
`A0`	A CP-odd Higgs boson		
`H0`	H CP-even Higgs boson		
`Hplus`	$\mathrm{H}^\pm$ charged Higgs boson		
`SdownL`	$\tilde{\mathrm{d}}_L$ squark		
`SdownR`	$\tilde{\mathrm{d}}_R$ squark		
`SupL`	$\tilde{\mathrm{u}}_L$ squark		
`SupR`	$\tilde{\mathrm{u}}_R$ squark		
`SstrangeL`	$\tilde{\mathrm{s}}_L$ squark		
`SstrangeR`	$\tilde{\mathrm{s}}_R$ squark		
`ScharmL`	$\tilde{\mathrm{c}}_L$ squark		
`ScharmR`	$\tilde{\mathrm{c}}_R$ squark		
`Sbottom1`	$\tilde{\mathrm{b}}_1$ squark		
`Sbottom2`	$\tilde{\mathrm{b}}_2$ squark		
`Stop1`	$\tilde{\mathrm{t}}_1$ squark		
`Stop2`	$\tilde{\mathrm{t}}_2$ squark		

names. Antiparticles are specified by `<particle>~`. Momentarily only e^+e^- processes are implemented, identified by `<initial_state>=ee`. The centre-of-mass energy is given by `<Ecms>`, the polarisation of the incoming particles are given by `<polarisation1>` and `<polarisation2>`. If no unit of the cross-section and the uncertainty is given, they are assumed to be given in fb. The integer number `<alias>` identifies the cross-section in the `correlationCoefficient` commands.

- `BR <alias> ( <decaying_particle> -> <decay_products> ) <value> +- <uncertainties>`
  Specifies the branching ratio of a given particle `<decaying_particle>` into the decay products `<decay_products>`. The integer number `<alias>` identifies the cross-section in the `correlationCoefficient` commands.

- `width <particle> <value> +- <uncertainties> alias <alias>`
  Specifies the total width of the particle ¡particle¿. If no unit is given in `<value>` and `<uncertainty>`, they are assumed to be given in GeV.

- `limit mass<name> <|> <limit>`
  Allows the user to specify upper or lower mass limits of yet undiscovered SUSY particles. The limit is used in the calculation of the χ^2 of the fit in the following way: If the predicted mass is in agreement width the limit, the contribution of this observable to the total χ^2 is zero. If the limit is violated by the predicted mass m_p, the χ^2 contribution is $((\texttt{<limit>} - m_p)/(\texttt{<limit>}/10))^2$, i. e. a 10 % violation of the limit adds 1 to the χ^2 of the fit.

- Other observables dedicated for special cases are
  - `sin2thetaW <value> +- <uncertainties>`
    Specifies the value of $\sin^2\theta_W$
  - `cos2phiR <value> +- <uncertainties>`
  - `cos2phiL <value> +- <uncertainties>`
    Specify the values of the chargino mixing angles, used for initialisation.

Correlations among observables After all observables have been specified, the following command can be used to specify the correlation among observables.

- `correlationCoefficient <observable1> <observable2> <value>`
  If the observables are masses, they are identified by `mass<name>`. All other observables are identified by their alias number, such as `sigma_<alias>`.

Parameters The fit program Fittino can fit any combination of the MSSM and SM parameters given in Tab. A.3 to the observables given in `fittino.in`. The following commands can be used to specify the parameters that are fitted to the observables and the parameters which are kept fixed.

- `fitParameter <parameter> [ <value> [ +- <uncertainty>] ]`
  Specifies one of the parameters that should be fitted. The names which are available for `<parameter>` are listed in Tab. A.3. If a value `<value>` is given, then using `FitAllDirectly` it is possible to specify that `<value>` should be the initial value of the parameter in the fit. If additionally an uncertainty is given, then this can be used in the pull distribution calculation with `CalcPullDist`. If no unit for `<value>` is given for a dimension-full parameter, then it is assumed to be given in GeV.

Table A.3: *MSSM parameters known to Fittino. The following parameters can be used with* `fitParameter`, `fixParameter` *and* `universality`.

Parameter Name	Explanation
`TanBeta`	Ratio of Higgs vacuum expectation values
`Mu`	μ parameter, controls Higgsino mixing
`Xtau`	Tau mixing parameter
`Xtop`	Top mixing parameter
`Xbottom`	Bottom mixing parameter
`MSelectronR`	Right scalar electron mass parameter
`MSmuR`	Right scalar muon mass parameter
`MStauR`	Right scalar tau mass parameter
`MSelectronL`	Left 1st. gen. scalar lepton mass parameter
`MSmuL`	Left 2nd. gen. scalar lepton mass parameter
`MStauL`	Left 3rd. gen. scalar lepton mass parameter
`MSdownR`	Right scalar down mass parameter
`MSstrangeR`	Right scalar strange mass parameter
`MSbottomR`	Right scalar bottom mass parameter
`MSupR`	Right scalar up mass parameter
`MScharmR`	Right scalar charm mass parameter
`MStopR`	Right scalar top mass parameter
`MSupL`	Left 1st. gen. scalar quark mass parameter
`MScharmL`	Left 2nd. gen. scalar quark mass parameter
`MStopL`	Left 3rd. gen. scalar quark mass parameter
`M1`	$U(1)_Y$ gaugino (Bino) mass parameter
`M2`	$SU(2)_L$ gaugino (Wino) mass parameter
`M3`	$SU(3)_C$ gaugino (gluino) mass parameter
`massA0`	Pseudoscalar Higgs mass
`massW`	W boson mass
`massZ`	Z boson mass
`massTop`	Top quark mass $m_{\mathrm{t}}(m_{\mathrm{t}})$
`massBottom`	Bottom quark mass $m_{\mathrm{b}}(m_{\mathrm{b}})$
`massCharm`	Charm quark mass $m_{\mathrm{c}}(m_{\mathrm{c}})$

- `fixParameter <parameter> <value>`
  Specifies a parameter kept fixed during the fit.

- `universality <parameter1> <parameter2>`
  Specifies that `<parameter2>` should not be fitted on its own, but that it should be set to the value of `<parameter1>` during the fit. This is useful if unification among generations shall be assumed.

Flags The following flags can be used to control the behaviour of Fittino during the fit and to specify what operations Fittino should perform.

- `OneLoopCorrections on|off`
  If `OneLoopCorrections` is `off`, then no fit is performed but just the tree-level estimates of the parameters are calculated. By default it is `on`.

- `ISR on|off`
  Switches ISR corrections in the cross-section calculations `on` or `off`. By default it is `on`.

- `UseGivenStartValues on|off`
  If `UseGivenStartValues` is `on`, then the start values of the parameters in the fit are not determined from tree-level estimates, but from the values given in `fitParameter`. By default it is `off`.

- `FitAllDirectly on|off`
  If `FitAllDirectly` is `on`, then the initial fits of subsets of the parameter space (as described above in Section 7.3) are omitted. By default it is `off`.

- `CalcPullDist on|off`
  If `CalcPullDist` is `on`, then pull distributions for all parameters specified with `fitParameter` are calculated. It is necessary that each parameter is given with its value and uncertainty. The pull distribution is then calculated with respect to the parameter value and the width is compared with the parameter uncertainty. For each parameter, a `root` [175] histogram is created in the output file `PullDistributions.root`. The number of fits per Fittino run can be specified using the command `NumberPulls`. By default `CalcPullDist` is `off`. This command is very useful to test the fitted parameters and their uncertainties calculated in a previous run of Fittino.

- `CalcIndChisqContr on|off`
  If `CalcIndChisqContr` is `on`, for each parameter specified with `fitParameter` the individual contribution of each observable to the $\Delta\chi^2$ of the fit is calculated, if the parameter is varied by $\pm 1\,\sigma$. It is necessary that each parameter is given with its value and uncertainty. The parameter is varied once by $+1\,\sigma$ and once by $-1\,\sigma$. The resulting total $\Delta\chi^2$ and the individual $\Delta\chi^2_i$ of each observable O_i are averaged. The total $\Delta\chi^2$ gives the correlation of the parameter with all other parameters. The individual $\Delta\chi^2_i$ represent the contribution of observable O_i to the determination of the parameter. The output is given in the file `fittino_individual_chisq_contr.out`. By default, `CalcIndChisqContr` is `off`. This command is very useful to visualise the contributions of the individual observables to a fit performed in a previous run of Fittino.

- `BoundsOnX on|off`
  If `BoundsOnX` is `on`, then the parameters X_τ, X_{top} and X_{bottom} are bounded between $-6000 < X < 2000$. By default `BoundsOnX` is `on`.

- `ScanX on|off`
  If `ScanX` is `on`, then the parameters X_{top} and X_{bottom} are individually scanned in the range $-6000 < X < 2000$ before the main fit and before the separate fit of the squark sector. This helps to avoid local minima which typically occur at parameter values with the wrong sign. By default `ScanX` is `on`.

- `SepFitTanbX on|off`
  If `SepFitTanbX` is `on`, a separate fit of of $\tan\beta$, $M_{\tilde{t}_R}$, $M_{\tilde{t}_L}$, X_{top} and X_{bottom} is performed before the main fit and after the separate fit of the squark sector. By default `SepFitTanbX` is `on`.

- `Generator <generator_name> <path>`
  Specifies the tool for the calculation of the theory predictions. Currently SPheno is implemented, but also any other tool capable of input and output according to the SUSY Les Houches Accord [164] can be easily interfaced with Fittino.

- `UseMinos on|off`
  If `UseMinos` is `on`, then MINOS is used to perform a detailed uncertainty analysis after MINIMIZE converged. `UseMinos` implies automatically that `UseHesse` is `on` (see below). After MINOS, the two-dimensional uncertainty contours of all combinations of two parameters are calculated and stored in the output file `FitContours.root`. Since this can take very long (order of several weeks on a PIII 1.3GHz in a typical fit of the full MSSM spectrum), this option is `off` by default.

- `UseHesse on|off`
  If `UseHesse` is `on`, then the HESSE function in MINUIT is used to perform a detailed error matrix calculation after MINIMIZE converged, assuming parabolic errors. By default, `UseHesse` is `off`.

- `NumberOfMinimizations <number>`
  In very complex cases the first call to MINIMIZE often does converge near the true minimum of the fit, but the convergence criteria is often not fulfilled after the first call to MINIMIZE. Therefore, MINIMIZE can be called `<number>` times after each other. By default, `NumberOfMinimizations` is 1.

- `ErrDef <real_number>`
  If the parameter space of the fit is very complex, either due to a large number of d.o.f. or because of observables with large uncertainties, sometimes MINOS is not able to find a positive definite error matrix with the standard setting of $\Delta\chi^2 = 1$ for the definition of the $1\,\sigma$ bound of the parameters. Therefore, using `ErrDef`, the error definition can be changed from 1 to any other real number. After MINOS is finished, the uncertainties and the covariance matrix found by MINOS is retransformed such as to represent an error definition of 1. With small error definitions, MINOS finds the uncertainties more easily, since it is more seldom trapped in local minima close to the absolute minimum. On the other hand, the uncertainties on the parameters are less precise for small error definitions. By default, `ErrDef` is set to 1.

- `NumberPulls <number>`
  Specifies the number of individual fits for the calculation of pull distributions in one run of Fittino. For each fit, the observables are smeared in a Gaussian form according to their covariance matrix. The initialisation of the random number generator used for the

smearing uses the system time in seconds. By default, `NumberPulls` is set to 10. Only MINIMIZE is used in the fit, MINOS is switched off.

An example for a Fittino input file `fittino.in` can be found in Appendix B.1.

A.3 The Fittino Output Files

Depending on the requested operation, Fittino saves its results in the following files:

- `fittino.out`: Main output file. It contains the observables, their covariance matrix, the fixed and fitted MSSM parameters and their correlation and covariance matrices. Additionally, information on the χ^2 and the accuracy of the error matrix estimate is shown. An example of this output file is given in Appendix B.2.
- `FitContours.root`: In case a MINOS uncertainty analysis is requested using `UseMinos`, the two-dimensional uncertainty contours of each pair of parameters are stored in the ROOT [175] format in this file.
- `fittino_individual_chisq_contr.out`: In case that an analysis of which observables determine which parameters is requested using `CalcIndChisqContr`, the individual contributions to the $\Delta\chi^2$ are listed in this file.
- `PullDistributions.root`: In case pull distributions are calculated using `CalcPullDistr`, the pull distributions and the distribution of the total χ^2 of the fits is stored in this file in the ROOT format.

Appendix B

Fittino Inputs and Results

B.1 The Fittino Steering File

```
#########################################################################
###                          Fittino input file                       ###
#########################################################################
###                 This is an example steering file.                 ###
###                         P. Bechtle, 20040520                      ###
#########################################################################

# Electroweak precision measurements
massW                    80.3382  GeV +- 0.039  GeV
massZ                    91.1187 GeV +- 0.0021 GeV
massTop                  174.3   GeV +- 0.3    GeV
massBottom               4.2     GeV +- 0.5    GeV
sin2ThetaW               0.23113 +- 0.00015

# Higgs sector at LC 500 and LC 1000
massh0                   110.211 GeV +- 0.05 GeV +- 0.5 GeV # Degrassi et al
massA0                   399.767 GeV +- 1.3 GeV      # not in LHC
massH0                   400.803 GeV +- 1.3 GeV # not in LHC
massHplus                407.695 GeV +- 1.1 GeV # not in LHC

# Sparticles at LHC, LC 500 and LC 1000
massSdownL               586.734   GeV +- 9.8 GeV
massSdownR               566.257  GeV +- 23.6 GeV
massSupL                 583.546   GeV +- 9.8 GeV
massSupR                 566.516   GeV +- 23.6 GeV
massSstrangeL            586.736 GeV +- 9.8 GeV
massSstrangeR            566.254 GeV +- 23.6 GeV
massScharmL             583.552 GeV +- 9.8 GeV # ~c_L
massScharmR             566.510 GeV +- 23.6 GeV # ~c_R
massSbottom1            532.146 GeV +- 5.7  GeV # ~b_1
massSbottom2            565.561 GeV +- 6.2  GeV # ~b_2
massStop1                 417.516 GeV +- 2.0 GeV  # ~t_1 # not at LHC
nofit massStop2           600.037 GeV +- 20.0 GeV # ~t_2 # not at LHC
```

```
massSelectronL           208.002 GeV +- 0.2 GeV # ~e_L-
massSelectronR           143.906 GeV +- 0.05 GeV # ~e_R-
massSnueL                192.300 GeV +- 0.7 GeV # ~nu_eL # not at LHC
massSmuL                 208.02 GeV +- 0.5 GeV # ~mu_L-
massSmuR                 143.878 GeV +- 0.2 GeV # ~mu_R-
massStau1                134.283 GeV +- 0.3 GeV # ~tau_1-
massStau2                211.792 GeV +- 1.1 GeV # ~tau_2- # not at LHC

# Gauginos at LHC, LC 500 and LHC
massGluino               630.449 GeV +- 6.4 GeV # ~g
nofit massNeutralino1          95.7412 GeV +- 0.05 GeV # ~chi_10
nofit massNeutralino2          182.396 GeV +- 0.08 GeV # ~chi_20
massChargino1            180.461 GeV +- 0.55 GeV# ~chi_1+
massChargino2            379.967 GeV +- 3.0 GeV # ~chi_2+

edge 1 1 massNeutralino1 massNeutralino2 263.50279 GeV +- 1.2 GeV
edge 2 2 massNeutralino1 massNeutralino2 79.09719  GeV +- 1.2 GeV

# estimated chargino mixing angles from LC 500
nofit cos2PhiL                 0.6737 +- 0.05       # rough estimate
nofit cos2PhiR                 0.8978 +- 0.05       # rough estimate

# LC 500 Cross-sections
sigma ( ee -> Neutralino1 Neutralino2, 500.,0.8,0.6 )    22.7048 fb +- 2.0 fb alias 1
sigma ( ee -> Neutralino2 Neutralino2, 500.,0.8,0.6 )    19.4676 fb +- 2.0 fb alias 2
sigma ( ee -> SelectronL  SelectronL~, 500.,0.8,0.6 )   204.974 fb +- 4.0 fb alias 3
sigma ( ee -> SmuL  SmuL~, 500.,0.8,0.6 )                36.8348 fb +- 4.0 fb alias 4
sigma ( ee -> Stau1 Stau1~, 500.,0.8,0.6 )               39.1143 fb +- 4.0 fb alias 5
sigma ( ee -> Chargino1 Chargino1, 500.,0.8,0.6 )    46.6626 fb +- 1.0 fb alias 6
sigma ( ee -> Z h0, 500., 0.8, 0.6 )                  11.1633 fb +- 0.21 fb   alias 7

# LC 500 Branching Ratios
BR 1 ( h0 -> Bottom Bottom~ )                        0.824057   +- 0.01      alias 1
BR 2 ( h0 -> Charm  Charm~ )                         0.0405547  +- 0.01      alias 2
BR 3 ( h0 -> Tau  Tau~ )                             0.134444   +- 0.01      alias 3

# Correlations among observables
correlationCoefficient   massChargino1   massNeutralino1    0.05

# Parameters to be fitted
fitParameter  TanBeta          9.96662
fitParameter  Mu               358.635 GeV
fitParameter  Atau            -3884.46 GeV
fitParameter  MSelectronR      135.762 GeV
fitParameter  MStauR           133.564 GeV
fitParameter  MSelectronL       195.21 GeV
fitParameter  MStauL           194.277 GeV
fitParameter  Atop            -506.936 GeV
fitParameter  Abottom         -4444.56 GeV
```

```
fitParameter  MSdownR          528.135 GeV
fitParameter  MSbottomR        524.719 GeV
fitParameter  MSupR            530.244 GeV
fitParameter  MStopR           424.515 GeV
fitParameter  MSupL            548.704 GeV
fitParameter  MStopL           499.986 GeV
fitParameter  M1               101.814 GeV
fitParameter  M2               191.771 GeV
fitParameter  M3               588.798 GeV
fitParameter  massA0           399.763 GeV
fitParameter  massTop          174.3   GeV

# Fixed Parameters
fixParameter  massBottom      4.200e+00   GeV
fixParameter  massCharm       1.2e+00   GeV

# Universalities among parameters
universality MSelectronR MSmuR
universality MSelectronL MSmuL
universality MSdownR MSstrangeR
universality MSupR MScharmR
universality MSupL MScharmL

# switches
OneLoopCorrections    on          # Use full loop corrections in SPHENO
ISR                   on          # Switch on ISR

UseGivenStartValues   off
FitAllDirectly        off


ScanParameters        off
CalcPullDist          off
CalcIndChisqContr     off

# Generator             SPHENO  /home/bechtle/FLC/programs/SPheno2.2.0/SPheno

UseMinos              on

NumberOfMinimizations  1
ErrDef                 1.
NumberPulls            3
```

B.2 The Fittino Output File

```
#################### Fittino Fit Summary ####################
created by Fittino version 0.0.1
on Tuesday, June 01, 2004 at 13:36:05

Input values:
=============
              massh0        110.211 +-     0.502494
              massA0        399.767 +-          1.3
     massNeutralino1        95.7412 +-         0.05
     massNeutralino2        182.396 +-         0.08
       massChargino1        180.461 +-         0.55
       massChargino2        379.967 +-            3
ee  -> Neutralino1 Neutralino2       22.704800 +- 2.000000
ee  -> Neutralino2 Neutralino2       19.467600 +- 2.000000
ee  -> Chargino1 Chargino1       46.662600 +- 1.000000
        ee  -> Z h0         11.1633 +-         0.21
ee  -> Chargino1 Chargino1       104.746000 +- 3.500000
ee  -> Neutralino1 Neutralino2       43.950300 +- 2.000000
ee  -> Neutralino2 Neutralino2       43.774500 +- 2.000000

Covariance matrix for input value:
==================================
                                    massh0      massA0    all observables ...
              massh0              0.252500    0.000000    ...
              massA0              0.000000    1.690000    ...
                 .                   .           .
           all observables           .           .
                 .                   .           .
                 .                   .           .
                 .                   .           .

Fixed values:
=============
                Xtau       -3884.46
         MSelectronR        135.762
              MStauR        133.564
         MSelectronL         195.21
              MStauL        194.277
                Xtop       -506.936
             Xbottom       -4444.56
             MSdownR        528.135
           MSbottomR        524.719
               MSupR        530.244
              MStopR        424.515
               MSupL        548.704
              MStopL        499.986
                  M1        101.814
```

```
                M2        191.771
                M3        588.798
            massA0        399.763
             MSmuR         135.76
             MSmuL         195.21
          MSstrangeR         528.14
           MScharmR        530.253
           MScharmL        548.705
            massTop          174.3
          massBottom            4.2
           massCharm            1.2

Fitted values:
==============
             TanBeta        9.94391 +-     0.114925
                  Mu        358.914 +-     0.867347

Covariance matrix for fitted parameters:
========================================

                        TanBeta          Mu
             TanBeta    0.0132078  -0.0419162
                  Mu   -0.0419162    0.752291


Correlation matrix for fitted parameters:
=========================================

                        TanBeta          Mu
             TanBeta            1   -0.420508
                  Mu    -0.420508           1


Chisq of the fit:
=================

                  chisq = 1.476873


Status of the minimization:
===========================

                  Error Matrix accurate


###################### End of Fit Summary ####################
```

B.3 Correlation Matrices of Fittino Fits

Table B.1: *Covariance matrix of the Fittino SPS1a fit, part I.*

Parameter	$\tan\beta$	μ	X_τ	$M_{\tilde{e}_R}$	$M_{\tilde{\tau}_R}$
$\tan\beta$	0.111175	-0.315588	1.89651	-0.000895779	-0.0201037
μ	-0.315588	1.30946	-5.21081	-0.00196776	0.0495931
X_τ	1.89651	-5.21081	17344.8	-0.216795	-73.208
$M_{\tilde{e}_R}$	-0.000895779	-0.00196776	-0.216795	0.154075	0.151788
$M_{\tilde{\tau}_R}$	-0.0201037	0.0495931	-73.208	0.151788	0.564233
$M_{\tilde{e}_L}$	-0.00483114	0.0176371	-0.027209	-0.0519631	-0.0511075
$M_{\tilde{\tau}_L}$	-0.0162266	0.0460825	-45.6648	-0.0586238	-0.0197967
X_{top}	0.888352	-2.20943	16.7655	2.14995	1.99168
X_{bottom}	17.6128	60.5206	2481.58	-48.3702	-60.4599
$M_{\tilde{d}_R}$	-0.0437921	0.115654	-11.919	2.97347	3.00117
$M_{\tilde{b}_R}$	0.0279772	0.138872	1.66202	0.110171	0.0988665
$M_{\tilde{u}_R}$	-0.226218	0.547759	-6.02518	-6.58442	-6.45395
$M_{\tilde{t}_R}$	-0.151336	0.669135	0.482936	-0.853462	-0.839161
$M_{\tilde{u}_L}$	-0.127822	0.273813	-3.01459	0.230473	0.256344
$M_{\tilde{t}_L}$	-0.198402	-0.359759	-10.164	0.446669	0.50944
M_1	-0.00883466	0.0193444	-0.104197	0.00689816	0.00828826
M_2	-0.0222488	0.0389265	-0.252275	-0.00236722	0.0013743
M_3	0.0735719	-0.0446575	2.38435	0.142459	0.120686
m_{A}	0.0102731	-0.0244336	0.299631	0.00412286	0.00224587
m_{top}	-0.00788672	0.0360108	0.284704	0.00873464	0.00815595

Parameter	$M_{\tilde{e}_L}$	$M_{\tilde{\tau}_L}$	X_{top}	X_{bottom}	$M_{\tilde{d}_R}$
$\tan\beta$	-0.00483114	-0.0162266	0.888352	17.6128	-0.0437921
μ	0.0176371	0.0460825	-2.20943	60.5206	0.115654
X_τ	-0.027209	-45.6648	16.7655	2481.58	-11.919
$M_{\tilde{e}_R}$	-0.0519631	-0.0586238	2.14995	-48.3702	2.97347
$M_{\tilde{\tau}_R}$	-0.0511075	-0.0197967	1.99168	-60.4599	3.00117
$M_{\tilde{e}_L}$	0.0349508	0.0209954	-0.955774	14.0727	-1.00467
$M_{\tilde{\tau}_L}$	0.0209954	1.3928	-1.19829	8.69516	-1.03961
X_{top}	-0.955774	-1.19829	873.237	1643.22	-3.66798
X_{bottom}	14.0727	8.69516	1643.22	3.50×10^6	-302.461
$M_{\tilde{d}_R}$	-1.00467	-1.03961	-3.66798	-302.461	313.061
$M_{\tilde{b}_R}$	-0.0421496	-0.0491806	-1.35847	2906.67	0.485075
$M_{\tilde{u}_R}$	2.25748	2.31423	-40.2621	54.7287	-13.4928
$M_{\tilde{t}_R}$	0.334591	0.393525	-212.414	2821.82	1.00314
$M_{\tilde{u}_L}$	-0.0766215	-0.0744772	-0.992753	76.6723	1.82767
$M_{\tilde{t}_L}$	-0.125817	-0.110878	-15.675	-7606.35	2.74612
M_1	-0.00223675	-0.00180204	0.439357	-5.25497	-0.0583998
M_2	0.000645358	0.00168416	-0.186187	20.4471	-0.00863168
M_3	-0.053189	-0.0574816	7.0432	323.028	-17.8538
m_{A}	-0.00223656	-0.0039251	1.55455	142.822	0.04473
m_{top}	-0.00278614	-0.00178353	2.24027	1.90612	0.094059

Table B.2: *Covariance matrix of the Fittino SPS1a fit, part II.*

Parameter	$M_{\tilde{b}_R}$	$M_{\tilde{u}_R}$	$M_{\tilde{t}_R}$	$M_{\tilde{u}_L}$	$M_{\tilde{t}_L}$
$\tan\beta$	0.0279772	-0.226218	-0.151336	-0.127822	-0.198402
μ	0.138872	0.547759	0.669135	0.273813	-0.359759
X_τ	1.66202	-6.02518	0.482936	-3.01459	-10.164
$M_{\tilde{e}_R}$	0.110171	-6.58442	-0.853462	0.230473	0.446669
$M_{\tilde{\tau}_R}$	0.0988665	-6.45395	-0.839161	0.256344	0.50944
$M_{\tilde{e}_L}$	-0.0421496	2.25748	0.334591	-0.0766215	-0.125817
$M_{\tilde{\tau}_L}$	-0.0491806	2.31423	0.393525	-0.0744772	-0.110878
X_{top}	-1.35847	-40.2621	-212.414	-0.992753	-15.675
X_{bottom}	2906.67	54.7287	2821.82	76.6723	-7606.35
$M_{\tilde{d}_R}$	0.485075	-13.4928	1.00314	1.82767	2.74612
$M_{\tilde{b}_R}$	58.8949	0.312779	8.73357	0.861253	-17.4464
$M_{\tilde{u}_R}$	0.312779	367.187	13.2453	0.403993	0.809969
$M_{\tilde{t}_R}$	8.73357	13.2453	73.0989	1.40883	-25.5751
$M_{\tilde{u}_L}$	0.861253	0.403993	1.40883	26.6879	-0.238608
$M_{\tilde{t}_L}$	-17.4464	0.809969	-25.5751	-0.238608	65.0215
M_1	-0.0211334	-0.341557	-0.139911	0.00685591	0.0485836
M_2	0.0471537	0.0364831	0.123772	-0.103703	-0.166186
M_3	-5.07288	-21.0093	-4.78377	-6.703	-6.23905
m_{A}	0.118827	-0.288148	-0.253683	-0.00340125	-0.327189
m_{top}	-0.0913864	-0.242361	-0.500907	0.0177321	-0.0123086

Parameter	M_1	M_2	M_3	m_{A}	m_{top}
$\tan\beta$	-0.00883466	-0.0222488	0.0735719	0.0102731	-0.00788672
μ	0.0193444	0.0389265	-0.0446575	-0.0244336	0.0360108
X_τ	-0.104197	-0.252275	2.38435	0.299631	0.284704
$M_{\tilde{e}_R}$	0.00689816	-0.00236722	0.142459	0.00412286	0.00873464
$M_{\tilde{\tau}_R}$	0.00828826	0.0013743	0.120686	0.00224587	0.00815595
$M_{\tilde{e}_L}$	-0.00223675	0.000645358	-0.053189	-0.00223656	-0.00278614
$M_{\tilde{\tau}_L}$	-0.00180204	0.00168416	-0.0574816	-0.0039251	-0.00178353
X_{top}	0.439357	-0.186187	7.0432	1.55455	2.24027
X_{bottom}	-5.25497	20.4471	323.028	142.822	1.90612
$M_{\tilde{d}_R}$	-0.0583998	-0.00863168	-17.8538	0.04473	0.094059
$M_{\tilde{b}_R}$	-0.0211334	0.0471537	-5.07288	0.118827	-0.0913864
$M_{\tilde{u}_R}$	-0.341557	0.0364831	-21.0093	-0.288148	-0.242361
$M_{\tilde{t}_R}$	-0.139911	0.123772	-4.78377	-0.253683	-0.500907
$M_{\tilde{u}_L}$	0.00685591	-0.103703	-6.703	-0.00340125	0.0177321
$M_{\tilde{t}_L}$	0.0485836	-0.166186	-6.23905	-0.327189	-0.0123086
M_1	0.00424791	0.00203446	0.0224873	2.94021e-05	0.0017519
M_2	0.00203446	0.0111191	0.0369259	-0.00145371	0.00105683
M_3	0.0224873	0.0369259	62.2332	0.00206672	0.00838941
m_{A}	2.94021e-05	-0.00145371	0.00206672	0.514352	0.00279667
m_{top}	0.0017519	0.00105683	0.00838941	0.00279667	0.11917

Table B.3: *Correlation matrix of the Fittino SPS1a fit, part I.*

Parameter	$\tan\beta$	μ	X_τ	$M_{\tilde{e}_R}$	$M_{\tilde{\tau}_R}$
$\tan\beta$	1	-0.827124	0.0431884	-0.00684433	-0.0802679
μ	-0.827124	1	-0.034576	-0.00438088	0.0576961
X_τ	0.0431884	-0.034576	1	-0.0041937	-0.740021
$M_{\tilde{e}_R}$	-0.00684433	-0.00438088	-0.0041937	1	0.514805
$M_{\tilde{\tau}_R}$	-0.0802679	0.0576961	-0.740021	0.514805	1
$M_{\tilde{e}_L}$	-0.0775027	0.0824427	-0.0011051	-0.70811	-0.363938
$M_{\tilde{\tau}_L}$	-0.0412362	0.034123	-0.293801	-0.126551	-0.0223316
X_{top}	0.0901602	-0.0653383	0.0043079	0.185352	0.0897273
X_{bottom}	0.0282112	0.0282459	0.0100633	-0.0658127	-0.0429869
$M_{\tilde{d}_R}$	-0.00742295	0.00571214	-0.00511493	0.428138	0.225812
$M_{\tilde{b}_R}$	0.0109336	0.0158135	0.00164442	0.036573	0.0171507
$M_{\tilde{u}_R}$	-0.0354062	0.0249804	-0.00238749	-0.875403	-0.448386
$M_{\tilde{t}_R}$	-0.0530862	0.0683932	0.000428893	-0.25431	-0.130665
$M_{\tilde{u}_L}$	-0.0742072	0.0463182	-0.00443085	0.113657	0.0660598
$M_{\tilde{t}_L}$	-0.0737927	-0.0389886	-0.00957084	0.141121	0.0841075
M_1	-0.406535	0.259372	-0.012139	0.269637	0.169296
M_2	-0.632802	0.3226	-0.0181658	-0.0571924	0.0173507
M_3	0.0279703	-0.00494695	0.00229495	0.046006	0.0203665
m_{A}	0.0429604	-0.0297722	0.00317228	0.0146454	0.00416894
m_{top}	-0.0685185	0.0911597	0.00626218	0.0644608	0.0314529

Parameter	$M_{\tilde{e}_L}$	$M_{\tilde{\tau}_L}$	X_{top}	X_{bottom}	$M_{\tilde{d}_R}$
$\tan\beta$	-0.0775027	-0.0412362	0.0901602	0.0282112	-0.00742295
μ	0.0824427	0.034123	-0.0653383	0.0282459	0.00571214
X_τ	-0.0011051	-0.293801	0.0043079	0.0100633	-0.00511493
$M_{\tilde{e}_R}$	-0.70811	-0.126551	0.185352	-0.0658127	0.428138
$M_{\tilde{\tau}_R}$	-0.363938	-0.0223316	0.0897273	-0.0429869	0.225812
$M_{\tilde{e}_L}$	1	0.0951596	-0.173006	0.0402018	-0.303726
$M_{\tilde{\tau}_L}$	0.0951596	1	-0.0343598	0.00393488	-0.0497867
X_{top}	-0.173006	-0.0343598	1	0.0296981	-0.0070153
X_{bottom}	0.0402018	0.00393488	0.0296981	1	-0.0091296
$M_{\tilde{d}_R}$	-0.303726	-0.0497867	-0.0070153	-0.0091296	1
$M_{\tilde{b}_R}$	-0.0293783	-0.00543014	-0.00599024	0.202281	0.00357236
$M_{\tilde{u}_R}$	0.63016	0.102334	-0.0711028	0.00152535	-0.0397963
$M_{\tilde{t}_R}$	0.209329	0.0390007	-0.840742	0.176267	0.00663118
$M_{\tilde{u}_L}$	-0.0793351	-0.0122158	-0.00650307	0.00792646	0.0199952
$M_{\tilde{t}_L}$	-0.0834611	-0.0116513	-0.0657828	-0.503785	0.0192476
M_1	-0.18357	-0.0234279	0.22812	-0.0430606	-0.0506419
M_2	0.0327369	0.0135333	-0.0597515	0.103561	-0.00462643
M_3	-0.0360647	-0.0061741	0.0302129	0.0218689	-0.12791
m_{A}	-0.016681	-0.00463743	0.0733516	0.106356	0.00352496
m_{top}	-0.0431708	-0.00437776	0.219609	0.00294893	0.0153993

Table B.4: *Correlation matrix of the Fittino SPS1a fit, part II.*

Parameter	$M_{\tilde{b}_R}$	$M_{\tilde{u}_R}$	$M_{\tilde{t}_R}$	$M_{\tilde{u}_L}$	$M_{\tilde{t}_L}$
$\tan\beta$	0.0109336	-0.0354062	-0.0530862	-0.0742072	-0.0737927
μ	0.0158135	0.0249804	0.0683932	0.0463182	-0.0389886
X_τ	0.00164442	-0.00238749	0.000428893	-0.00443085	-0.00957084
$M_{\tilde{e}_R}$	0.036573	-0.875403	-0.25431	0.113657	0.141121
$M_{\tilde{\tau}_R}$	0.0171507	-0.448386	-0.130665	0.0660598	0.0841075
$M_{\tilde{e}_L}$	-0.0293783	0.63016	0.209329	-0.0793351	-0.0834611
$M_{\tilde{\tau}_L}$	-0.00543014	0.102334	0.0390007	-0.0122158	-0.0116513
X_{top}	-0.00599024	-0.0711028	-0.840742	-0.00650307	-0.0657828
X_{bottom}	0.202281	0.00152535	0.176267	0.00792646	-0.503785
$M_{\tilde{d}_R}$	0.00357236	-0.0397963	0.00663118	0.0199952	0.0192476
$M_{\tilde{b}_R}$	1	0.00212694	0.133106	0.0217238	-0.281929
$M_{\tilde{u}_R}$	0.00212694	1	0.0808469	0.00408106	0.00524199
$M_{\tilde{t}_R}$	0.133106	0.0808469	1	0.0318968	-0.370966
$M_{\tilde{u}_L}$	0.0217238	0.00408106	0.0318968	1	-0.00572795
$M_{\tilde{t}_L}$	-0.281929	0.00524199	-0.370966	-0.00572795	1
M_1	-0.0422517	-0.273484	-0.251078	0.020362	0.092443
M_2	0.0582696	0.0180556	0.137287	-0.19037	-0.195448
M_3	-0.0837924	-0.138981	-0.0709258	-0.164475	-0.0980797
m_{A}	0.0215897	-0.0209672	-0.0413718	-0.000918018	-0.0565769
m_{top}	-0.0344952	-0.0366383	-0.169714	0.00994307	-0.00442178

Parameter	M_1	M_2	M_3	m_{A}	m_{top}
$\tan\beta$	-0.406535	-0.632802	0.0279703	0.0429604	-0.0685185
μ	0.259372	0.3226	-0.00494695	-0.0297722	0.0911597
X_τ	-0.012139	-0.0181658	0.00229495	0.00317228	0.00626218
$M_{\tilde{e}_R}$	0.269637	-0.0571924	0.046006	0.0146454	0.0644608
$M_{\tilde{\tau}_R}$	0.169296	0.0173507	0.0203665	0.00416894	0.0314529
$M_{\tilde{e}_L}$	-0.18357	0.0327369	-0.0360647	-0.016681	-0.0431708
$M_{\tilde{\tau}_L}$	-0.0234279	0.0135333	-0.0061741	-0.00463743	-0.00437776
X_{top}	0.22812	-0.0597515	0.0302129	0.0733516	0.219609
X_{bottom}	-0.0430606	0.103561	0.0218689	0.106356	0.00294893
$M_{\tilde{d}_R}$	-0.0506419	-0.00462643	-0.12791	0.00352496	0.0153993
$M_{\tilde{b}_R}$	-0.0422517	0.0582696	-0.0837924	0.0215897	-0.0344952
$M_{\tilde{u}_R}$	-0.273484	0.0180556	-0.138981	-0.0209672	-0.0366383
$M_{\tilde{t}_R}$	-0.251078	0.137287	-0.0709258	-0.0413718	-0.169714
$M_{\tilde{u}_L}$	0.020362	-0.19037	-0.164475	-0.000918018	0.00994307
$M_{\tilde{t}_L}$	0.092443	-0.195448	-0.0980797	-0.0565769	-0.00442178
M_1	1	0.296025	0.043736	0.000629014	0.0778644
M_2	0.296025	1	0.0443899	-0.0192226	0.0290327
M_3	0.043736	0.0443899	1	0.000365292	0.00308061
m_{A}	0.000629014	-0.0192226	0.000365292	1	0.0112961
m_{top}	0.0778644	0.0290327	0.00308061	0.0112961	1

Bibliography

[1] H. Diels and W. Kranz, *Fragmente der Vorsokratiker*, Berlin (1961).

[2] M. W. Gruenewald, *Electroweak precision data: Global Higgs analysis* (2003), `hep-ex/0304023`.

S. Roth, *Standard model fits* (2004), Rencontres de Moriond, see `http://moriond.in2p3.fr/QCD/2004/ThursdayAfternoon/Roth.pdf`.

[3] ALEPH Collaboration, R. Barate *et al.*, *Search for the standard model Higgs boson at LEP*, Phys. Lett. **B565**(2003) 61, `hep-ex/0306033`.

[4] K. R. Popper, *Die Welt des Parmenides*, Piper, Muenchen (2001).

[5] OPAL Collaboration, G. Abbiendi *et al.*, *Search for neutral Higgs bosons in CP-conserving and CP-violating MSSM scenarios*, accepted by Eur. Phys. J. **C**(2004), `hep-ex/0406057`.

[6] G. Weiglein *et al.*, *The LHC/LC study group report* (2004), to be published.

[7] S. Weinberg, *A model of leptons*, Phys. Rev. Lett. **19**(1967) 1264.

S. L. Glashow, *Partial symmetries of weak interactions*, Nucl. Phys. **22**(1961) 579.

A. Salam, *Weak and electromagnetic interactions*, Proceedings of the Nobel Symposium held 1968 at Lerum, Sweden (1968) 367.

[8] J. Wess and B. Zumino, *Supergauge transformations in four-dimensions*, Nucl. Phys. **B70**(1974) 39.

[9] H. Fritzsch, M. Gell-Mann, and H. Leutwyler, *Advantages of the color octet gluon picture*, Phys. Lett. **B47**(1973) 365.

[10] P. W. Higgs, *Broken symmetries, massless particles and gauge fields*, Phys. Lett. **12**(1964) 132.

P. W. Higgs, *Broken symmetries and the masses of gauge bosons*, Phys. Rev. Lett. **13**(1964) 508.

F. Englert and R. Brout, *Broken symmetry and the mass of gauge vector mesons*, Phys. Rev. Lett. **13**(1964) 321.

G. S. Guralnik, C. R. Hagen, and T. W. B. Kibble, *Global conservation laws and massless particles*, Phys. Rev. Lett. **13**(1964) 585.

[11] G. 't Hooft and M. J. G. Veltman, *Regularization and renormalization of gauge fields*, Nucl. Phys. **B44**(1972) 189.

[12] S. L. Glashow, J. Iliopoulos, and L. Maiani, *Weak interactions with lepton–hadron symmetry*, Phys. Rev. **D2**(1970) 1285.

[13] J. E. Augustin *et al.*, *Discovery of a narrow resonance in e+ e- annihilation*, Phys. Rev. Lett. **33**(1974) 1406.

J. J. Aubert *et al.*, *Experimental observation of a heavy particle J*, Phys. Rev. Lett. **33**(1974) 1404.

[14] Gargamelle Neutrino Collaboration, F. J. Hasert *et al.*, *Observation of neutrino like interactions without muon or electron in the Gargamelle neutrino experiment*, Nucl. Phys. **B73**(1974) 1.

[15] JADE Collaboration, W. Bartel *et al.*, *Observation of planar three jet events in e+ e- annihilation and evidence for gluon bremsstrahlung*, Phys. Lett. **B91**(1980) 142.

TASSO Collaboration, R. Brandelik *et al.*, *Evidence for a spin one gluon in three jet events*, Phys. Lett. **B97**(1980) 453.

PLUTO Collaboration, C. Berger *et al.*, *Evidence for gluon bremsstrahlung in e+ e- annihilations at high-energies*, Phys. Lett. **B86**(1979) 418.

[16] UA1 Collaboration, G. Arnison *et al.*, *Experimental observation of isolated large transverse energy electrons with associated missing energy at* $\sqrt{s} = 540$ *GeV*, Phys. Lett. **B122**(1983) 103.

UA1 Collaboration, G. Arnison *et al.*, *Experimental observation of lepton pairs of invariant mass around 95 GeV at the CERN SPS collider*, Phys. Lett. **B126**(1983) 398.

[17] D0 Collaboration, S. Abachi *et al.*, *Observation of the top quark*, Phys. Rev. Lett. **74**(1995) 2632, `hep-ex/9503003`.

CDF Collaboration, F. Abe *et al.*, *Observation of top quark production in anti-p p collisions*, Phys. Rev. Lett. **74**(1995) 2626, `hep-ex/9503002`.

DONUT Collaboration, K. Kodama *et al.*, *Observation of tau-neutrino interactions*, Phys. Lett. **B504**(2001) 218, `hep-ex/0012035`.

[18] S. Eidelman *et al.*, *Review of Particle Physics*, Phys. Lett. **B592**(2004) 1, `http://pdg.lbl.gov`.

[19] SLD and LEP Collaboration, R. Barate *et al.*, *A combination of preliminary electroweak measurements and constraints on the standard model* (2003), `hep-ex/0312023`.

[20] CDF and D0 Collaboration, P. Azzi *et al.*, *Combination of CDF and D0 results on the top-quark mass* (2004), `hep-ex/0404010`.

[21] M. Spira and P. M. Zerwas, *Electroweak symmetry breaking and Higgs physics* (1997), Lectures given at 36. Internationale Universitaetswochen fuer Kernphysik und Teilchenphysik, Schladming, Austria, `hep-ph/9803257`.

[22] T. Hambye and K. Riesselmann, *Matching conditions and Higgs mass upper bounds revisited*, Phys. Rev. **D55**(1997) 7255, `hep-ph/9610272`.

[23] ALEPH Collaboration, R. Barate *et al.*, *Observation of an excess in the search for the standard model Higgs boson at ALEPH*, Phys. Lett. **B495**(2000) 1, `hep-ex/0011045`.

[24] *LEP and SLD electroweak working group* (2004), from `http://lepewwg.web.cern.ch/LEPEWWG/`.

[25] E. W. Kolb and M. S. Turner, *The Early universe*, Addison-Wesley, Redwood City, USA (1990), Frontiers in physics, 69.

[26] A. D. Sakharov, *Violation of CP invariance, C asymmetry, and baryon asymmetry of the universe*, Pisma Zh. Eksp. Teor. Fiz. **5**(1967) 32.

[27] N. Cabibbo, *Unitary symmetry and leptonic decays*, Phys. Rev. Lett. **10**(1963) 531.

[28] M. Carena, J. M. Moreno, M. Quiros, M. Seco, and C. E. M. Wagner, *Supersymmetric CP-violating currents and electroweak baryogenesis*, Nucl. Phys. **B599**(2001) 158, `hep-ph/0011055`.

[29] C. L. Bennett *et al.*, *First year wilkinson microwave anisotropy probe (WMAP) observations: Preliminary maps and basic results*, Astrophys. J. Suppl. **148**(2003) 1, `astro-ph/0302207`.

[30] Super-Kamiokande Collaboration, M. B. Smy *et al.*, *Precise measurement of the solar neutrino day/night and seasonal variation in Super-Kamiokande-I*, Phys. Rev. **D69**(2004) 011104, `hep-ex/0309011`.

[31] K2K Collaboration, M. H. Ahn *et al.*, *Indications of neutrino oscillation in a 250-km long- baseline experiment*, Phys. Rev. Lett. **90**(2003) 041801, `hep-ex/0212007`.

[32] SNO Collaboration, Q. R. Ahmad *et al.*, *Measurement of day and night neutrino energy spectra at SNO and constraints on neutrino mixing parameters*, Phys. Rev. Lett. **89**(2002) 011302, `nucl-ex/0204009`.

[33] KamLAND Collaboration, K. Eguchi *et al.*, *First results from KamLAND: Evidence for reactor anti–neutrino disappearance*, Phys. Rev. Lett. **90**(2003) 021802, `hep-ex/0212021`.

[34] J. Bonn *et al.*, *Newest results from the Mainz neutrino mass experiment*, Phys. Atom. Nucl. **63**(2000) 969.

[35] W. A. Bardeen, *Anomalous Ward identities in spinor field theories*, Phys. Rev. **184**(1969) 1848.

[36] W. de Boer and C. Sander, *Global electroweak fits in the SM, MSSM and CMSSM* (2002), Prepared for 10th International Conference on Supersymmetry and Unification of Fundamental Interactions (SUSY02), Hamburg, Germany, June 17th-23th.

[37] E. Witten, *Dynamical breaking of supersymmetry*, Nucl. Phys. **B188**(1981) 513.

[38] S. Dimopoulos, S. Raby, and F. Wilczek, *Supersymmetry and the scale of unification*, Phys. Rev. **D24**(1981) 1681.

[39] S. R. Coleman and J. Mandula, *All possible symmetries of the S matrix*, Phys. Rev. **159**(1967) 1251.

[40] G. L. Kane *et al.*, *Perspectives on supersymmetry*, Singapore (1998), World Scientific.

[41] L. Girardello and M. T. Grisaru, *Soft breaking of supersymmetry*, Nucl. Phys. **B194**(1982) 65.

[42] I. Simonsen, *A review of minimal supersymmetric electroweak theory* (1995), hep-ph/9506369.

[43] J. R. Ellis, J. S. Hagelin, D. V. Nanopoulos, K. A. Olive, and M. Srednicki, *Supersymmetric relics from the big bang*, Nucl. Phys. **B238**(1984) 453.

[44] H. E. Haber, *Introductory low-energy supersymmetry* (1993), hep-ph/9306207.

[45] J. R. Ellis, G. Ridolfi, and F. Zwirner, *Radiative corrections to the masses of supersymmetric Higgs bosons*, Phys. Lett. **B257**(1991) 83.

Y. Okada, M. Yamaguchi, and T. Yanagida, *Upper bound of the lightest Higgs boson mass in the minimal supersymmetric standard model*, Prog. Theor. Phys. **85**(1991) 1.

H. E. Haber and R. Hempfling, *Can the mass of the lightest Higgs boson of the minimal supersymmetric model be larger than m_Z?*, Phys. Rev. Lett. **66**(1991) 1815.

[46] G. Degrassi, S. Heinemeyer, W. Hollik, P. Slavich, and G. Weiglein, *Towards high-precision predictions for the MSSM higgs sector*, Eur. Phys. J. **C28**(2003) 133, hep-ph/0212020.

[47] A. Brignole, G. Degrassi, P. Slavich, and F. Zwirner, *On the $O(\alpha(t)^2)$ two-loop corrections to the neutral Higgs boson masses in the MSSM*, Nucl. Phys. **B631**(2002) 195, hep-ph/0112177.

[48] S. Heinemeyer, W. Hollik, and G. Weiglein, *The masses of the neutral CP-even Higgs bosons in the MSSM: Accurate analysis at the two-loop level*, Eur. Phys. J. **C9**(1999) 343, hep-ph/9812472.

[49] A. Pilaftsis and C. E. M. Wagner, *Higgs bosons in the minimal supersymmetric standard model with explicit CP violation*, Nucl. Phys. **B553**(1999) 3, hep-ph/9902371.

[50] M. Carena, J. R. Ellis, A. Pilaftsis, and C. E. M. Wagner, *Renormalization-group-improved effective potential for the MSSM Higgs sector with explicit CP-violation*, Nucl. Phys. **B586**(2000) 92, hep-ph/0003180.

[51] M. Carena, J. R. Ellis, A. Pilaftsis, and C. E. M. Wagner, *CP-violating MSSM Higgs bosons in the light of LEP 2*, Phys. Lett. **B495**(2000) 155, hep-ph/0009212.

[52] E. D. Commins, S. B. Ross, D. DeMille, and B. C. Regan, *Improved experimental limit on the electric dipole moment of the electron*, Phys. Rev. **A50**(1994) 2960.

P. G. Harris *et al.*, *New experimental limit on the electric dipole moment of the neutron*, Phys. Rev. Lett. **82**(1999) 904.

[53] N. Arkani-Hamed, A. G. Cohen, E. Katz, and A. E. Nelson, *The littlest Higgs*, JHEP **07**(2002) 034, hep-ph/0206021.

[54] S. Heinemeyer, W. Hollik, and G. Weiglein, *Feynhiggs: A program for the calculation of the masses of the neutral CP-even Higgs bosons in the MSSM*, Comput. Phys. Commun. **124**(2000) 76, hep-ph/9812320.

[55] E. Gross, G. Wolf, and B. A. Kniehl, *Production and decay of the Standard Model Higgs boson LEP- 200*, Z. Phys. **C63**(1994) 417, hep-ph/9404220.

[56] G. Altarelli, T. Sjstrand, F. Zwirner, *et al.*, *Workshop on physics at LEP2, Vol. 1* CERN-96-01-V-1.

[57] ALEPH Collaboration, A. Heister *et al.*, *Absolute mass lower limit for the lightest neutralino of the MSSM from e+ e- data at $\sqrt{s}$ up to 209 GeV*, Phys. Lett. **B583**(2004) 247.

[58] LEP Higgs Working for Higgs boson searches Collaboration, R. Barate *et al.*, *Searches for invisible Higgs bosons: Preliminary combined results using LEP data collected at energies up to 209 GeV* (2001), hep-ex/0107032.

[59] E. O. Lawrence and N. E. Edlefsen, *On the production of high speed protons*, Science **LXXII**(1930) 376.

[60] R. Assmann, M. Lamont, and S. Myers, *A brief history of the LEP collider*, Nucl. Phys. Proc. Suppl. **109B**(2002) 17.

[61] ATLAS Experiment, http://atlas.web.cern.ch/Atlas/Welcome.html.

[62] CMS Experiment, http://cmsinfo.cern.ch/Welcome.html.

[63] A. A. Sokolov and I. M. Ternov, *On polarization and spin effects in the theory of synchrotron radiation*, Phys. Dokl. **8**(1964) 1203.

[64] L. Arnaudon *et al.*, *Accurate determination of the LEP beam energy by resonant depolarization*, Z. Phys. **C66**(1995) 45.

[65] LEP Energy Working Group Collaboration, A. Blondel *et al.*, *Evaluation of the LEP centre-of-mass energy above the W pair production threshold*, Eur. Phys. J. **C11**(1999) 573, hep-ex/9901002.

C. Menot *et al.*, *The LEP spectrometer* (1999), Prepared for 9th LEP Performance Workshop, Chamonix, France, Januar 26th-29th.

[66] OPAL Collaboration, K. Ahmet *et al.*, *The OPAL detector at LEP*, Nucl. Instrum. Meth. **A305**(1991) 275.

[67] OPAL Collaboration, P. P. Allport *et al.*, *The OPAL silicon microvertex detector*, Nucl. Instrum. Meth. **A324**(1993) 34.

[68] R. D. Heuer and A. Wagner, *The OPAL jet chamber*, Nucl. Instrum. Meth. **A265**(1988) 11.

[69] O. Biebel *et al.*, *Performance of the OPAL jet chamber*, Nucl. Instrum. Meth. **A323**(1992) 169.

[70] M. Hauschild *et al.*, *Particle identification with the OPAL jet chamber*, Nucl. Instrum. Meth. **A314**(1992) 74.

[71] G. Aguillion *et al.*, *Thin scintillating tiles with high light yield for the OPAL endcaps*, Nucl. Instrum. Meth. **A417**(1998) 266.

[72] OPAL Collaboration, G. Abbiendi *et al.*, *Precision luminosity for Z0 lineshape measurements with a silicon-tungsten calorimeter*, Eur. Phys. J. **C14**(2000) 373, hep-ex/9910066.

[73] ALEPH, DELPHI, L3 and OPAL Collaboration, U. Parzefall *et al.*, *A combination of preliminary results on gauge boson couplings measured by the LEP collaborations* (2003), OPAL TN-739.

[74] R. Brun *et al.*, *GEANT: Simulation program for particle physics experiments. user guide and reference manual*, CERN-DD-78-2-REV 1978.

[75] OPAL Collaboration, J. Allison *et al.*, *The detector simulation program for the OPAL experiment at LEP*, Nucl. Instrum. Meth. **A317**(1992) 47.

[76] M. L. Mangano *et al.*, *Event generators for discovery physics* (1996), hep-ph/9602203.

[77] S. Jadach, B. F. L. Ward, and Z. Was, *Coherent exclusive exponentiation CEEX: The case of the resonant e+ e- collision*, Phys. Lett. **B449**(1999) 97, hep-ph/9905453.

S. Jadach, B. F. L. Ward, and Z. Was, *The precision monte carlo event generator KK for two- fermion final states in e+ e- collisions*, Comput. Phys. Commun. **130**(2000) 260, hep-ph/9912214.

[78] J. Fujimoto *et al.*, *grc4f v1.1: a four-fermion event generator for e+e- collisions*, Comput. Phys. Commun. **100**(1997) 128, hep-ph/9605312.

[79] R. Engel and J. Ranft, *Hadronic photon-photon interactions at high energies*, Phys. Rev. **D54**(1996) 4244, hep-ph/9509373.

[80] T. Sjostrand *et al.*, *High-energy-physics event generation with PYTHIA 6.1*, Comput. Phys. Commun. **135**(2001) 238, hep-ph/0010017.

[81] OPAL Collaboration, R. Akers *et al.* Documentation of ROPE in http://www.cern.ch/opal/manuals/ro/pro/ro.html.

[82] Consensus document available from http://sbhep1.physics.sunysb.edu/g̃rannis/wwlc_report.html.

[83] R. Brinkmann *et al.*, *TESLA: The superconducting electron positron linear collider with an integrated X-ray laser laboratory. technical design report. pt. 2: The accelerator* (2001), DESY-01-011.

[84] American Linear Collider Working Group Collaboration, T. Abe *et al.*, *Linear collider physics resource book for Snowmass 2001. 1: Introduction* (2001), hep-ex/0106055.

[85] ACFA Linear Collider Working Group Collaboration, K. Abe *et al.*, *Particle physics experiments at JLC* (2001), hep-ph/0109166.

[86] L. Lilje *et al.*, *Achievement of 35 MV/m in the superconducting nine-cell cavities for TESLA*, Nucl. Instrum. Meth. **A524**(2004) 1, physics/0401141.

[87] T. Behnke, S. Bertolucci, R. D. Heuer, R. Settles, *et al.*, *TESLA: The superconducting electron positron linear collider with an integrated X-ray laser laboratory. technical design report. pt. 4: A detector for TESLA* (2001), DESY-01-011.

[88] C. J. S. Damerell, *A CCD based vertex detector for TESLA* (2001), LC-DET-2001-023.

[89] M. Winter *et al.*, *A CMOS based VTX detector* (2001), LC-DET-2001-017.

[90] P. Fischer *et al.*, *A DEPFET based pixel vertex detector for the detector at TESLA* (2002), LC-DET-2002-004.

[91] M. Battaigla *et al.*, *A pixel vertex tracker for the detector at TESLA* (2001), LC-DET-2001-042.

[92] J. Hauschildt, *Studies on a silicon intermediate tracker for the TESLA detector* (2001), LC-DET-2001-036.

[93] R. Settles *et al.*, *A TPC for a future linear collider* (2002), LC-DET-2002-008.

[94] R. Bouclier *et al.*, *The gas electron multiplier (GEM)*, IEEE Trans. Nucl. Sci. **44**(1997) 646.

[95] Y. Giomataris, P. Rebourgeard, J. P. Robert, and G. Charpak, *MICROMEGAS: A high-granularity position-sensitive gaseous detector for high particle-flux environments*, Nucl. Instrum. Meth. **A376**(1996) 29.

[96] Medipix Collaboration, see
`http://www.nikhef.nl/pub/experiments/atlas/pixel/Medipix/`.

[97] T. Behnke *et al.*, *Performance study of the proposed TESLA detector using a realistic track reconstruction package* (2001), LC-DET-2001-029.

[98] F. Badaud *et al.*, *Si-W calorimeter performances* (2001), LC-DET-2001-058.

[99] P. Hassler *et al.*, *The hadronic tile calorimeter for the TESLA detector, design, construction and installation* (2001), LC-DET-2001-049.

[100] G. Acquistapace *et al.*, *CMS the magnet project: Technical design report* (1997), CERN-LHCC-97-10.

[101] R. Santonico and R. Cardarelli, *Development of resistive plate counters*, Nucl. Instrum. Meth. **187**(1981) 377.

[102] H. M. Araujo, A. Stahl, and D. J. Miller, *A lead tungstate detector with integrated light readout for the TESLA luminosity calorimeter* (2001), LC-DET-2001-080.

[103] OPAL Collaboration, K. Ackerstaff *et al.*, *Tests of the standard model and constraints on new physics from measurements of fermion pair production at 130 GeV to 172 GeV at LEP*, Eur. Phys. J. **C2**(1998) 441, `hep-ex/9708024`.

[104] OPAL Collaboration, K. Ackerstaff *et al.*, *A search for a mass peak in four-jet events produced in e+ e- collisions at* $\sqrt{s} = 130 - 172$ *GeV, following the selection of the ALEPH collaboration* (1997), OPAL PN-269.

[105] OPAL Collaboration, K. Ackerstaff *et al.*, *Search for the standard model Higgs boson in e+ e- collisions at* $\sqrt{s} = 161$ *GeV to 172 GeV*, Eur. Phys. J. **C1**(1998) 425, `hep-ex/9709003`.

[106] OPAL Collaboration, K. Ackerstaff *et al.*, *MT3.00: A new algorithm to calculate energy flow based on MT package* (1998), OPAL TN-575.

[107] OPAL Collaboration, H. Lafoux *et al.*, *Update of the neural electron id* (1995), OPAL TN-317.

[108] OPAL Collaboration, G. Abbiendi *et al.*, *Search for neutral Higgs bosons in e+ e- collisions at* $\sqrt{s} \approx 189$ *GeV*, Eur. Phys. J. **C12**(2000) 567, `hep-ex/9908002`.

[109] OPAL Collaboration, K. Ackerstaff *et al.*, *Attempt to develop new jet-particle association methods for four-jet topology with OPAL detector* (1998), OPAL TN-579.

[110] N. Brown and W. J. Stirling, *Finding jets and summing soft gluons: A new algorithm*, Z. Phys. **C53**(1992) 629.

[111] JADE Collaboration, W. Bartel *et al.*, *Experimental studies on multi–jet production in e+ e- annihilation at PETRA energies*, Z. Phys. **C33**(1986) 23.

[112] OPAL Collaboration, K. Ackerstaff *et al.*, *Upgraded b-tagging for LEP 2* (1998), OPAL TN-578.

[113] OPAL Collaboration, G. Abbiendi *et al.*, *Search for Higgs bosons in e+ e- collisions at 183 GeV*, Eur. Phys. J. **C7**(1999) 407, `hep-ex/9811025`.

[114] OPAL Collaboration, G. Abbiendi *et al.*, *Search for the standard model Higgs boson with the OPAL detector at LEP*, Eur. Phys. J. **C26**(2003) 479, `hep-ex/0209078`.

[115] C. Peterson and T. Rognvaldsson, *Lectures given at the 1991 CERN school of computing* (1991), Ystad, Sweden, August 23 to September 2, LU-TP-91-23.

[116] UA1 Collaboration, G. Arnison *et al.*, *Hadronic jet production at the CERN proton - anti-proton collider*, Phys. Lett. **B132**(1983) 214.

[117] OPAL Collaboration, O. Cooke, C. Jones, *et al.*, *Neural network electron and photon conversion identification* (1998), OPAL TN-556.

[118] M. Schumacher, *Suche nach neutralen Higgsbosonen mit dem OPAL-Detektor bei LEP2* (1999), Dissertation Univ. Bonn.

A. Quadt (2001), private communication.

[119] G. Parisi, *Super inclusive cross-sections*, Phys. Lett. **B74**(1978) 65.

J. F. Donoghue, F. E. Low, and S.-Y. Pi, *Tensor analysis of hadronic jets in quantum chromodynamics*, Phys. Rev. **D20**(1979) 2759.

[120] R. W. Brown and K. O. Mikaelian, *WW and ZZ pair production in e+ e-, p p, p anti-p colliding beams*, Phys. Rev. **D19**(1979) 922.

[121] B. List, *A simple figure of merit for searches* (1999), OPAL TN-619.

[122] SLD and LEP Collaboration, R. Barate *et al.*, *Parameters for the LEP/SLD electroweak heavy flavour results for summer 1998 conferences* (1998), LEPHF/98-01.

[123] S. Jadach, W. Placzek, M. Skrzypek, B. F. L. Ward, and Z. Was, *Monte carlo program KoralW 1.42 for all four-fermion final states in e+ e- collisions*, Comput. Phys. Commun. **119**(1999) 272, `hep-ph/9906277`.

[124] G. Marchesini *et al.*, *HERWIG: A monte carlo event generator for simulating hadron emission reactions with interfering gluons. Version 5.1 - April 1991*, Comput. Phys. Commun. **67**(1992) 465.

[125] M. W. Gruenewald, G. Passarino, *et al.*, *Four-fermion production in electron-positron collisions* (2000), `hep-ph/0005309`.

[126] K. S. Cranmer, *Kernel estimation in high-energy physics*, Comput. Phys. Commun. **136**(2001) 198, `hep-ex/0011057`.

[127] A. Kolmogorov, *On the empirical determination of a distribution function*, Giornale dell'Institutio Italiano degli Attuari (1933).

N. V. Smirnov, *On the estimation of the discrepancy between empirical curves of distributions for two independent samples*, Bull. Math. Univ. Moscow (1939).

[128] H. Akima, *A new method of interpolation and smooth curve fitting based on local procedures*, J.ACM **17**(1970) 589.

[129] R. Barlow, *Statistics: A Guide to the Use of Statistical Methods in the Physical Sciences*, John Wiley & Sons, Manchester (1989).

[130] T. Junk, *Confidence level computation for combining searches with small statistics*, Nucl. Instrum. Meth. **A434**(1999) 435, `hep-ex/9902006`.

[131] P. Bock, *Computation of confidence levels for exclusion or discovery of a signal with the method of fractional event counting* (2004), `hep-ex/0405072`.

[132] OPAL Collaboration, G. Abbiendi *et al.*, *Flavour independent search for Higgs bosons decaying into hadronic final states in e+ e- collisions at LEP* (2003), `hep-ex/0312042`.

[133] OPAL Collaboration, G. Alexander *et al.*, *Search for neutral Higgs bosons in Z0 decays using the OPAL detector at LEP*, Z. Phys. **C73**(1997) 189.

OPAL Collaboration, R. Akers *et al.*, *Search for neutral Higgs bosons in the minimal supersymmetric extension of the standard model*, Z. Phys. **C64**(1994) 1.

[134] OPAL Collaboration, K. Ackerstaff *et al.*, *A search for neutral Higgs bosons in the MSSM and models with two scalar field doublets*, Eur. Phys. J. **C5**(1998) 19, `hep-ex/9803019`.

[135] OPAL Collaboration, G. Abbiendi *et al.*, *Search for a low mass CP-odd Higgs boson in e+ e- collisions with the OPAL detector at LEP2*, Eur. Phys. J. **C27**(2003) 483, `hep-ex/0209068`.

[136] OPAL Collaboration, G. Abbiendi *et al.*, *Two Higgs doublet model and model independent interpretation of neutral Higgs boson searches*, Eur. Phys. J. **C18**(2001) 425, `hep-ex/0007040`.

[137] D. Y. Bardin *et al.*, *ZFITTER v.6.21: A semi-analytical program for fermion pair production in e+ e- annihilation*, Comput. Phys. Commun. **133**(2001) 229, `hep-ph/9908433`.

[138] OPAL Collaboration, G. Abbiendi *et al.*, *Decay-mode independent searches for new scalar bosons with the OPAL detector at LEP*, Eur. Phys. J. **C27**(2003) 311, `hep-ex/0206022`.

[139] OPAL Collaboration, G. Abbiendi *et al.*, *Search for yukawa production of a light neutral Higgs boson at LEP*, Eur. Phys. J. **C23**(2002) 397, hep-ex/0111010.

[140] P. L. Cho, M. Misiak, and D. Wyler, $K_l \to \pi^0 e^+ e^-$ *and* $B \to X_s \ell^+ \ell^-$ *decay in the MSSM*, Phys. Rev. **D54**(1996) 3329, hep-ph/9601360.

A. L. Kagan and M. Neubert, *QCD anatomy of* $B \to X_s \gamma$ *decays*, Eur. Phys. J. **C7**(1999) 5, hep-ph/9805303.

K. G. Chetyrkin, M. Misiak, and M. Munz, *Weak radiative B-meson decay beyond leading logarithms*, Phys. Lett. **B400**(1997) 206, hep-ph/9612313.

P. Gambino and M. Misiak, *Quark mass effects in* $\bar{B} \to X_s \gamma$, Nucl. Phys. **B611**(2001) 338, hep-ph/0104034.

J. R. Ellis, T. Falk, G. Ganis, K. A. Olive, and M. Srednicki, *The CMSSM parameter space at large* $\tan\beta$, Phys. Lett. **B510**(2001) 236, hep-ph/0102098.

[141] ALEPH Collaboration, R. Barate *et al.*, *A measurement of the inclusive* $b \to s\gamma$ *branching ratio*, Phys. Lett. **B429**(1998) 169.

CLEO Collaboration, S. Chen *et al.*, *Branching fraction and photon energy spectrum for* $b \to s\gamma$, Phys. Rev. Lett. **87**(2001) 251807, hep-ex/0108032.

BELLE Collaboration, K. Abe *et al.*, *A measurement of the branching fraction for the inclusive* $B \to X_s \gamma$ *decays with BELLE*, Phys. Lett. **B511**(2001) 151, hep-ex/0103042.

BABAR Collaboration, B. Aubert *et al.*, $b \to s\gamma$ *using a sum of exclusive modes* (2002), hep-ex/0207074.

BABAR Collaboration, B. Aubert *et al.*, *Determination of the branching fraction for inclusive decays* $B \to X_s \gamma$ (2002), hep-ex/0207076.

[142] F. A. Berends and R. Kleiss, *Initial state radiation at LEP energies and the corrections to Higgs boson production*, Nucl. Phys. **B260**(1985) 32.

[143] Particle Data Group Collaboration, D. E. Groom *et al.*, *Review of particle physics*, Eur. Phys. J. **C15**(2000) 1.

[144] M. Carena, S. Heinemeyer, C. E. M. Wagner, and G. Weiglein, *Suggestions for improved benchmark scenarios for Higgs boson searches at LEP2* (1999), hep-ph/9912223.

M. Carena, S. Heinemeyer, C. E. M. Wagner, and G. Weiglein, *Suggestions for benchmark scenarios for MSSM Higgs boson searches at hadron colliders*, Eur. Phys. J. **C26**(2003) 601, hep-ph/0202167.

[145] Muon g-2 Collaboration, G. W. Bennett *et al.*, *Measurement of the positive muon anomalous magnetic moment to 0.7-ppm*, Phys. Rev. Lett. **89**(2002) 101804, hep-ex/0208001.

[146] M. Frank, S. Heinemeyer, W. Hollik, and G. Weiglein, *The Higgs boson masses of the complex MSSM: A complete one- loop calculation* (2002), hep-ph/0212037.

[147] S. Heinemeyer, W. Hollik, and G. Weiglein, *Precise prediction for the mass of the lightest Higgs boson in the MSSM*, Phys. Lett. **B440**(1998) 296, hep-ph/9807423.

S. Heinemeyer, W. Hollik, and G. Weiglein, *QCD corrections to the masses of the neutral CP-even Higgs bosons in the MSSM*, Phys. Rev. **D58**(1998) 091701, hep-ph/9803277.

S. Heinemeyer, W. Hollik, and G. Weiglein, *Constraints on* $\tan\beta$ *in the MSSM from the upper bound on the mass of the lightest Higgs boson*, JHEP **06**(2000) 009, hep-ph/9909540.

[148] M. Carena, M. Quiros, and C. E. M. Wagner, *Effective potential methods and the Higgs mass spectrum in the MSSM*, Nucl. Phys. **B461**(1996) 407, hep-ph/9508343.

[149] M. Carena, S. Mrenna, and C. E. M. Wagner, *MSSM Higgs boson phenomenology at the Tevatron collider*, Phys. Rev. **D60**(1999) 075010, hep-ph/9808312.

[150] M. Carena *et al.*, *Reconciling the two-loop diagrammatic and effective field theory computations of the mass of the lightest CP-even Higgs boson in the MSSM*, Nucl. Phys. **B580**(2000) 29, hep-ph/0001002.

[151] J. R. Espinosa and R.-J. Zhang, *MSSM lightest CP-even Higgs boson mass to O(alpha(s) alpha(t)): The effective potential approach*, JHEP **03**(2000) 026, hep-ph/9912236.

[152] LEP Higgs Working Group Collaboration, R. Barate *et al.*, *Searches for the neutral Higgs bosons of the MSSM: Preliminary combined results using LEP data collected at energies up to 209 GeV* (2001), hep-ex/0107030.

[153] ALEPH, DELPHI, L3 and OPAL Collaboration, P. Bock *et al.*, *Searches for Higgs bosons: Preliminary combined results using LEP data collected at energies up to 202 GeV* (2000), CERN-EP-2000-055.

[154] ALEPH Collaboration, D. Decamp *et al.*, *ALEPH: A detector for electron - positron annihilations at LEP*, Nucl. Instrum. Meth. **A294**(1990) 121.

[155] DELPHI Collaboration, P. A. Aarnio *et al.*, *The DELPHI detector at LEP*, Nucl. Instrum. Meth. **A303**(1991) 233.

[156] L3 Collaboration, B. Adeva *et al.*, *The construction of the L3 experiment*, Nucl. Instrum. Meth. **A289**(1990) 35.

[157] ALEPH Collaboration, A. Heister *et al.*, *Final results of the searches for neutral Higgs bosons in e+ e- collisions at* $\sqrt{s}$ *up to 209 GeV*, Phys. Lett. **B526**(2002) 191, hep-ex/0201014.

[158] DELPHI Collaboration, J. Abdallah *et al.*, *Final results from DELPHI on the searches for SM and MSSM neutral Higgs bosons*, Eur. Phys. J. **C32**(2004) 145, hep-ex/0303013.

[159] L3 Collaboration, P. Achard *et al.*, *Search for neutral Higgs bosons of the minimal supersymmetric standard model in e+ e- interactions at* $\sqrt{s}$ *up to 209 GeV*, Phys. Lett. **B545**(2002) 30, hep-ex/0208042.

[160] B. C. Allanach *et al.*, *The Snowmass points and slopes: Benchmarks for SUSY searches*, Eur. Phys. J. **C25**(2002) 113, hep-ph/0202233.

[161] P. Bechtle, K. Desch, and P. Wienemann (2004), available from http://www-flc.desy.de/fittino.

[162] ECFA/DESY LC Physics Working Group Collaboration, J. A. Aguilar-Saavedra *et al.*, *TESLA technical design report pt. III: Physics at an e+e- linear collider* (2001), hep-ph/0106315.

[163] H. U. Martyn, *Width effects in slepton production* $e^+e^- \to \tilde{\mu}_r^+ \tilde{\mu}_r^-$ (1999), hep-ph/0002290.

[164] P. Skands *et al.*, *SUSY Les Houches accord: Interfacing SUSY spectrum calculators, decay packages, and event generators* (2003), hep-ph/0311123.

[165] W. Porod, *SPheno, a program for calculating supersymmetric spectra, SUSY particle decays and SUSY particle production at e+ e- colliders*, Comput. Phys. Commun. **153**(2003) 275, hep-ph/0301101.

[166] F. James and M. Roos, *'MINUIT' a system for function minimization and analysis of the parameter errors and correlations*, Comput. Phys. Commun. **10**(1975) 343.

[167] K. Desch, J. Kalinowski, G. Moortgat-Pick, M. M. Nojiri, and G. Polesello, *SUSY parameter determination in combined analyses at LHC/LC*, JHEP **02**(2004) 035, hep-ph/0312069.

[168] P. M. Zerwas *et al.*, *Reconstruction of fundamental SUSY parameters* (2002), hep-ph/0211076.

[169] W. Porod, *Phenomenology of stops, sbottoms, staus and tau-sneutrino* (1998), PhD thesis Univ. Vienna, hep-ph/9804208.

[170] M. Drees and K. Hikasa, *Scalar top production in e+ e- annihilation*, Phys. Lett. **B252**(1990) 127.

[171] H. Baer, F. E. Paige, S. D. Protopopescu, and X. Tata, *Isajet 7.48: A monte carlo event generator for p p, anti-p p, and e+ e- reactions* (1999), hep-ph/0001086.

[172] T. Kuhl (2004), private communication.

[173] M. Drees, *Intermediate scale symmetry breaking and the spectrum of super partners in superstring inspired supergravity models*, Phys. Lett. **B181**(1986) 279.

[174] W. Porod (2004), private communication.

[175] N. Buncic *et al.*, *ROOT. an interactive object-oriented framework and its application to NA49 analysis* (1997), Talk given at Computing in High-energy Physics (CHEP 97), Berlin, Germany, April 7th-11th.

Danksage

Es war einmal ein Jüngling, der kam aus dem tiefen Süden, wo der Wein wächst, und landete vollständig freiwillig in der Stadt im Norden, wo nieseliger Regen fällt und wo auf dem Berge Bahrenfeldia HERA, ZEUS und HERMES hausen. Dort wäre er vollständig verloren gewesen, und zwar nicht nur ohne seine wasserdichte und atmungsaktive GoreTex-Jacke, sondern insbesondere ohne all diejenigen, die ihm die Bewältigung der Aufgaben ermöglichten, die ihm aufgetragen wurden. Denn bald nach seiner Ankunft in der Stadt, wo nieseliger Regen fällt, beauftragte ihn der sagenumwobene König Rolf, eines der noch sagenhafteren MSSM-Higgs-Bosonen zu fangen, die in den Tiefen des OPALs herumspuken sollten. Dazu stattete ihn der König mit vielen zauberhaften Hilfsmitteln aus und gab ihn zum großen Helden Klaus in die Lehre, als daß er das kunstvolle Handwerk der Boson-Jagd erlerne. Der brachte ihm alles bei, was er brauchte, beschützte ihn wider die Ablenkungen und Versuchungen des Alltags und befragte mit ihm die Pythia des Orakels.

Schließlich war es so weit, und mit dem Segen des vertrauenswürdigen Confidence Levels stieg unser Jüngling hinab in den OPAL, überwand den dreiköpfigen Mischungshund, setzte über den Strom der Daten, ging fast unter in hadesionischen Ereignissen und jagte das Higgs, um zumindestens 95 von 100 seiner Teile in die Hände zu bekommen. Fast erlag er dabei der CP-Verletzung, die er sich zuzog und die alles vor seinen Augen verschwimmen ließ, doch unter großen Verlusten an Sensitivität rang er diese Krankheit nieder. Doch das Higgs war nicht zu finden, und so trat er vor König Rolf mit 17 halbtoten Szenarien in seinen Händen, die er mit Hilfe der Kombinationsfalle erlegt hatte. Und der König sah die Ausbeute und war traurig, daß kein Higgs-Boson in seinem Reich herumspukte, aber zufrieden genug mit dem Jüngling und seiner Jagd.

Und so dankte unser Jüngling all den Gefährten, die ihn auf seinem Wege in den OPAL und wieder zurück unterstützt hatten und ihn und seinen spärlichen Humor am Leben gehalten hatten. Es waren dies natürlich König Rolf und der große Held Klaus, sowie Thorsten K., der immer für alle und alles da war, Niels, der dafür sorgte, daß der Jüngling nicht zu dick wurde, Markus B., mit dem er wider die Gefahren in der Welt außerhalb des OPALs focht, Peter, mit dem er weitere wundersame Abenteuer in der Welt des Fits überstand, Götz und Wolfgang, die ihn viele Zauberkünste lehrten, Sven, Gudi und Werner, die ihm zu wundersamen Orakelsprüchen verhalfen und sie ihn deuten lehrten, Arnulf und Tom, von deren Jagd auf das Higgs er viel lernte, PIK, David, Christoph, Pippa, Thorsten W. und Gabi, die ihm halfen, sich tief im OPAL zurecht zu finden, sowie Ties und Felix, Steve, Jenny, Karsten, Gerald, Filip, Erika, Nabil, Marius, Markus H., Andreas, Matthias, Tatsiana, Thomas, Thorsten L., Ramona, Hendrik, Roman, Alexei, Jörgen, Blanka, Bernhard und Oliver, ohne die er nicht halb so erfolgreich gejagt und ohne die es gar keinen Spaß gemacht hätte.

Und so sank er schließlich in die Arme seiner Miriam, die ihm dankenswerterweise seine Leidenschaft für die brotlose Jagd auf unschuldige Bosonen verzieh, und sogar seine Mutter vergab ihm, die noch immer darauf beharrte, unsichtbare Teilchen zu jagen sei schlecht für die Psyche. Diese Göttin aber hatte er gar nicht getroffen auf seiner Reise in den OPAL.

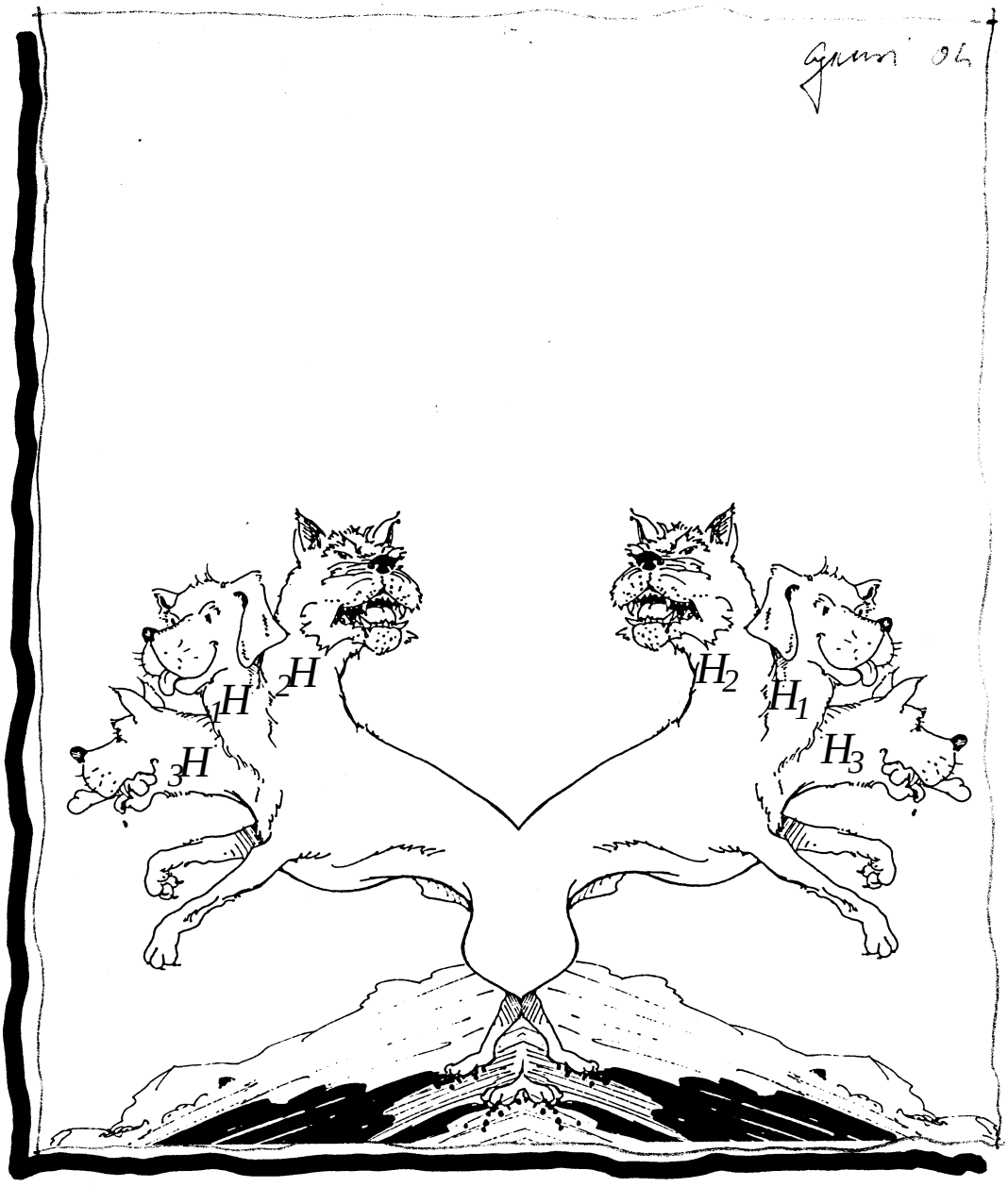
$_1H$
$_2H$
$_3H$
H_2
H_1
H_3